Generation of H-Atom Pulses
and
Associative Desorption of Hydrogen
Isotopologues from Metal Surfaces

Dissertation
zur Erlangung des mathematisch-naturwissenschaftlichen Doktorgrades
"Doctor rerum naturalium"
der Georg-August-Universität Göttingen

im Promotionsprogramm Chemie
der Georg-August University School of Sciene (GAUSS)

vorgelegt von
Sven Kaufmann
aus Neustadt a. Rbge.

Göttingen, 2017

Abstract

Part I of this work introduces a technique for the generation of H-atom pulses with unprecedented time resolution. In part II an extensive study of the associative desorption reaction of hydrogen isotopologues from metal surfaces is presented.

Generation of H-Atom Pulses   Short intense pulses are of fundamental importance for scientific studies of dynamics. Equivalent-time experiments relying on the pump-probe technique are conducted routinely in physics, chemistry and biology. In contrast to the light pulses often utilized in such studies, chemical reactions are generally initiated by collisions. While methods for the generation of matter pulses exist, their performance is significantly inferior to modern laser pulses. Here, a new photolysis technique is introduced to produce pulses of neutral matter, which relies on well-known simple physical principles. This technique is implemented for the first time and achieves an H-atom pulse duration of ~1.2 ns (time resolution of 0.03 %), which corresponds to an improvement by one order of magnitude compared to established photolysis methods. From the full mathematical description of the concept presented here further improvements are predicted. These include the reduction of the pulse duration below the nanosecond timescale as well as a significant increase in the absolute pulse intensity. This new method extends the scientific toolbox and enables a new class of future experiments which involve time-resolved collisions of neutral matter.

Hydrogen Permeation   The interaction of hydrogen with metal surfaces is one of the most fundamental reactions in surface chemistry. The H_2/Cu(111) system serves as a benchmark for theoretical studies, which are nowadays able to describe the reactivity of certain systems with an accuracy of $1\,\mathrm{kcal\,mol^{-1}}$, often referred to as "chemical accuracy". This study reports an extensive set of experimental data of the post-permeation associative desorption of H_2, HD and D_2 from single crystal surfaces of Cu(111), Cu(211) and Au(111). By invoking the principle of detailed balance initial state resolved reaction probability curves are obtained, which are compared to selected studies.

For the H_2/Cu(111) system small but significant deviations to the literature are found which are attributed to an improved calibration procedure in this work. The Cu(211) data revealed systematic differences to the Cu(111) sample on the order of the calibration

i

uncertainty, which necessitated the direct comparison of both copper facets under the same experimental conditions. Furthermore, evidence for an additional desorption channel on both facets is presented and analyzed quantitatively. Several possible reaction mechanisms are speculated upon which include argumentations as to why this had not been reported in previous work.

Finally, for the highly activated $H_2/Au(111)$ system the presented results provide a quantum-state-resolved experimental data set to which theoretical studies can be compared. In this data set an isotope-specific effect is observed, which questions the general validity of the adiabatic approximation generally assumed in description of the interaction of hydrogen with noble metal surfaces.

Acknowledgments

During the last few years I had a wonderful time working together with great people. Foremost, I would like to thank Prof. Dr. Alec M. Wodtke for the opportunity to work in his group and under excellent conditions. For his continuous support, many ideas and his motivation I am really thankful. I also owe huge thanks to Prof. Dr. Dirk Schwarzer for his mentoring and the countless helpful discussions over these years. Their supervision and assistance guided me during our projects and really expanded my scientific expertise in so many directions.

I further thank Prof. Dr. Jürgen Troe, Prof. Dr. Jörg Schröder, Prof. Dr. Ricardo Mata and PD Dr. Thomas Zeuch for being members of my examination board. Also I would like to express special gratitude to Prof. Dr. Daniel J. Auerbach for our many inspiring conversations, vivid discussions and his advice during our very fruitful teamwork. His limitless curiosity often led us both to a deeper understanding of the challenges at hand.

I also thank the members of the MPI workshops for their quick, precise and uncomplicated solutions to our experimental efforts. Without them none of this work would have been possible. I would also like to thank our technicians F. Lange and R. Bürsing for their excessive contributions in planning and construction of the apparatuses and, of course, for occasionally unlocking their cabinets of well-guarded equipment.

My thanks go to all the members of the group who made these past few years so enjoyable. So many colleagues accompanied me on my path, and I am truly thankful for all your company, friendship and help, especially the MPI bunch for the warm and family-like atmosphere. I will never forget our motivational after-dinner conversations and all the times we went to have a quick match of *kicker* to take our minds off life's daily struggles. My special thanks go to Svenja, for always brightening the mood with our cheerful conversations covering abysmal topics.

Special gratitude goes to my parents and brother, for their everlasting support and their faith in me. And last but not least Katharina, you will have my eternal gratitude for all your love, encouragement and support. And for your patience with me whenever I had too little time for you. I could not have done it without you.

Thank you all so very much.

Contents

Part I

Generation of H-Atom Pulses

Chapter 1

Introduction

This part of the work is dedicated to the introduction and description of a new method for the generation of H-atom pulses, which is well termed "bunch-compression photolysis" (BCP). It is based upon tailoring of a photodissociation process such that fragments generated in an extended volume comprise a certain space-velocity distribution. This distribution caused the bunch of neutrals to compress during their propagation, until arriving in a given spot at the same time. This spot is several centimeters away, clearly separating the source from the target. A large fraction of the contents presented in this part have already been published[1].

1.1 Pump Probe Methods

The field of chemical dynamics benefited greatly from the application of short intense laser pulses. The whole field of pump-probe spectroscopy emerged when short-pulsed laser systems became available. Today, femtosecond laser driven equivalent-time experiments have become a central tool in physics, chemistry and biology for studying inter- and intramolecular dynamics[2–9]. This scientific toolbox has been extended by short electron pulses[10–13] as well as other charged particles[14–16].

One disadvantage of these methods is the type of interaction they are based upon. When studying chemical dynamics, the interactions of interest are often initiated by collisions of neutral particles, e.g.[17–20]. In these works the neutral atom beams have been prepared by mechanical means, e.g. chopping of an effusive beam. Also, photolysis into neutral photofragments has been employed (e.g. ref. 21–24), but this method is so far restricted to nanosecond timescales and allows only limited control over the pulses. This lack of influence over the pulse characteristics is one of the main disadvantages which restricts the use of neutral particle beams. For pump-probe studies, extensive control of the pulse attributes, including intensity, duration and energetics are necessary. The latter also depends on the application and the energy necessary to induce the process to be studied.

1.2 Matter Pulses

The widespread use of laser pulse induced timing experiments is not only based upon the good availability of intense ultra-short pulses. There are more advantages, for example the easy tailoring of the spatial pulse dimensions, control of the propagation and additional characteristics, e.g. polarization. Also, the propagation with the speed of light is a benefit for timing experiments, since it is constant in a given homogeneous medium. In timing experiments the spatial position is related to the time as well as their uncertainties. This relationship is generally determined simply by the propagation velocity. For light pulses, this is very advantageous, because it gives a small timing difference for spatial uncertainties.

In contrast, particle pulses lack many of these benefits. Generally, their velocity is about five orders of magnitude slower than the speed of light, which increases the effect of spatial uncertainty on timing deviations. Therefore, when these pulses are generated by photolysis, the photolysis volume is also fundamentally limiting the temporal duration of the pulses. An additional problem is the often broad velocity distribution of matter pulses. This leads to an increasing spread of the pulse in direct proportion to the propagation distance, while light pulses do not spread in non-dispersive media. Furthermore, for pulses of charged particles, the duration and intensities are fundamentally limited by space charge.

In the following sections matter pulses will be described in more detail, separately for charged and neutral particles.

1.2.1 Charged Matter Pulses

The propagation of charged particle pulses can be influenced by electric and magnetic fields, which allows pulse compression via several techniques. In principle, the achievable pulse durations are limited by space charge effects and the maximum variation gradients of the time-dependent electrical fields that are used for compression. This will be illustrated by two examples of short pulses of charged particles.

Short electron pulses can simply be created by employing ultra-short laser pulses to induce photoemission[10], but the control of the generated electron bunch proved to be difficult. If the control mechanism is too slow or weak to counteract space charge induced broadening the repulsion of the charged particles will limit the final pulse duration. Therefore, the particle pulses need to be accelerated significantly to overcome this limitation, e.g.[10,16,25,26]. Here, the kinetic energies of the particles significantly exceed the energy range relevant for chemical reactions, ~0.1–10 eV (e.g. ref. 27).

As second example, Cassidy *et al.*[25] shaped a short pulse from positrons held in an ion trap. Those were accelerated out of the trap by a time varying electric potential, which was tailored to bunch all particles within the whole trap volume in a certain distance.

Space charge close to the compression point was overcome by use of strong additional magnetic fields. For particles with a higher mass-to-charge ratio the field strength would need to be scaled accordingly. Thus this makes the method practically unfeasible for applications, even for H-ions.

1.2.2 Neutral Matter Pulses

In contrast to charged particle pulses the control over neutral matter is severely restricted. While the interaction of charged particles with electrical fields is strong and well controllable, the methods to steer and compress neutrals are based on much weaker interactions. These include Stark and Zeeman effects and examples can be found in [28–37] and a review in [38].

This lack of potent manipulation tools has restricted the applicability of neutral matter pulses in the last decades. Here, neutral matter pulses have mostly been generated by mechanically chopping of effusive beams, which resulted in pulses on the microsecond timescale, e.g. [17–20]. A different approach was the photolysis of a molecule into neutral fragments, e.g. [21–24]. This non-mechanical method profits from the attributes of pulsed laser sources, but is also limited by several related factors and will be elaborated in detail in section 2.3.

Chapter 2

Methods

2.1 Laser Principles

This section contains brief summaries of the well-established principles of laser pulses that will be required for the methods applied in this work.

Ultrashort Pulses The term "ultrashort" is nowadays used to describe laser pulses with pulse durations on the order of picoseconds or shorter. Those are usually generated via the mode-locking technique, which results in a broadband spectrum. A key attribute of such pulses is their time-bandwidth product, which cannot exceed a certain lower limit. For Gaussian shaped pulses, this relation is expressed by:

$$\Delta\tau \, \Delta\nu = {2\ln(2)}/{\pi} \approx 0.441, \tag{2.1}$$

where $\Delta\tau$ denotes the temporal full width at half maximum (FWHM) of the laser pulse and $\Delta\nu$ the FWHM of its intensity spectrum.

Geometrical Optics In geometrical optics, often referred to as "ray optics", light propagation is described in terms of rays instead of waves. Here, straight line paths describe the light propagation along an optical axis, unless the properties of the medium change, e.g. refraction at interfaces. This allows for easy, first-principle descriptions of optical elements. For example lenses are described in the "thin lens" approximation, which neglects their actual thickness and curvature and simply reduces its attributes to the focal length.

Also, often the paraxial approximation is included, where all rays propagate close to the optical axis of the system and deviate only small angles from its direction. This further allows to assume the following approximations: $\sin\theta \approx \theta$; $\cos\theta \approx 1$, and $\tan\theta \approx \theta$.

In geometrical optics, focusing lenses can be described by their f-number, often expressed as "f/#". Here, the "#" denotes the ratio between the focal length f and clear aperture CA of the lens:

$$f = {}^{\mathrm{f}}\!/_{\mathrm{CA}}, \tag{2.2}$$

with CA as the diameter of the beam on the lens. The main disadvantage of geometrical optics is its neglect of the wave properties of light. For example, diffraction restricts the size of real foci to a lower limit, as will be described in the following section.

Gaussian Beams This section presents the description of focal volumes in the Gaussian beam approximation. The definition of the beam diameters will be based on the points where the intensity has fallen to $1/e^2$ of the maximum. This Gaussian beam radius $w(z)$ is then described by:

$$w(z) = w_0 \sqrt{1 + \left(\frac{\lambda z}{\pi\, w_0{}^2}\right)^2}, \tag{2.3}$$

with z as distance from the plane of minimum beam waist, the wavelength λ, and w_0 the radius at the waist. Additionally, the Rayleigh length z_R is given as:

$$z_R = \frac{\pi\, w_0{}^2}{\lambda}. \tag{2.4}$$

The Rayleigh length gives the distance from the plane of minimal beam waist where the beam diameter corresponds to: $w(z_R) = \sqrt{2}\, w_0$. For a focused Gaussian beam the diffraction limited focal radius w_f is given by:

$$w_f = \frac{\lambda\,\mathrm{f}}{\pi\, w_{\mathrm{CA}}}, \tag{2.5}$$

where f is the nominal focal length of the lens and w_{CA} is the beam diameter at the lens position. Outside of the focal region ($z > z_R$), the beam diameter increases linearly with the distance from the focal plane and can be calculated from geometrical optics:

$$\sin(\theta) = \frac{\mathrm{CA}}{\mathrm{f}} = \frac{1}{(2 \cdot f\text{-number})}, \tag{2.6}$$

with the quantities from eq. (2.2).

For the Gaussian shaped laser pulses used in this work, the focal beam characteristics have been determined by the knife-edge method that is described in part II, section 8.2.5.3 and the results are given in table 3.1.

Ray-Pulse Formalism Another established technique for the description of light propagation is the "ray-pulse" or "ray-tracing" formalism. Here, beams are described by vectors including their attributes, and matrices describe the effects of optical elements on the rays. This description can be fully time-dependent (e.g. ref. 39,40) and was used in this work to determine the temporal characteristics of the laser pulses after propagation through

the optical setup. Briefly, the considered laser pulse is a Fourier-transform limited (FTL) Gaussian shaped pulse, with center frequency at 268 nm and a bandwidth of 10 THz. The optical setup includes dispersion at a grating, propagation along a certain distance and focusing with a f/114 geometry. As a result, each individual frequency component of the pulse is stretched to a duration of ~10 ps and focused to a size of ~5 µm.

2.2 Spectroscopy

In this work, hydrogen iodide as well as H-atoms were detected spectroscopically.

H-Atom Detection Two different techniques for H-atom detection were employed, The first method was resonantly enhanced multi-photon ionization (REMPI), employing a (2+1) scheme at ~205.15 nm via the Lyman-β state. Additionally, the power dependence of this transition was determined for D-atoms, which follows a ⅔ power law. This is described in more detail in part II, section 8.2.5.2 of this work. The pulse duration of the dye laser pulse was ~7 ns FWHM, thus also limiting the detectable H-atom pulse duration.

Thus, a second method was introduced, namely the strong field multi-photon ionization by an ultra-short laser pulse (e.g. ref. 41,42). Here, the signal had been determined[1] to depend on the laser intensity as I^6 in the current setup (see "Probe Beam" in table 3.1). H-atoms were also generated by strong-field dissociation induced by this pulse (e.g. ref. 42–44). But those H-atoms were separate from pulse-generated H-atoms by their kinetic energy and resulting time-of-flight (TOF), which could also be varied by rotation of the laser light polarization axis. In contrast to REMPI the temporal resolution of this method was not limited by the duration of the laser pulse but instead by the focal volume, as will be described in section 2.3.3.

REMPI of HI The molecular beams of HI were probed by (2+1) REMPI via the $g^3\Sigma^-(O^+)$ S-band for the vibrational ground state, with the spectral properties reported in references[45–47]. This allowed the determination of the rotational populations within the beams under various conditions. Generally, only molecules in the vibrational ground state and for rotational states $J < 6$ were detected. For pure HI beams a rotational temperature of (20 ± 2) K could be obtained, but this depended on the actual molecular beam setup as described in section 4.1.

2.3 Matter Pulses Generated by Photodissociation

Fundamentally, matter pulses generated by photodissociation are limited in their duration by several interconnected factors. As stated in section 1.2 the duration of matter pulses is connected to the particles velocity and thus their spatial extent. Compared to light the

propagation velocities of particles are about five orders of magnitude slower. Thus, even for particles generated in a 1 mm volume with a velocity of $1\,\mathrm{km\,s^{-1}}$ the resulting pulse duration is already 1 µs. These considerations show that for particle pulses generated by photodissociation the photolysis and detection volumes are also limiting factors for the duration, which will be discussed in more detail in section 2.3.3.

Photolysis is often a one-photon process and the fragments can be described easily by conservation of energy and momentum (see for example eqs. (2.7) and (2.8)). Thus, with knowledge about the fragmentation pattern of the induced reaction, the propagation of the fragments can be described classically. Furthermore, for monochromatic light sources the photofragments result with only one sharp velocity. Spectral width is directly connected to a velocity spread, which also spreads the matter pulse during its propagation. From this it is clear, that the geometric distance between generation and probe volume of such matter pulses are a concern. In addition the resulting distribution of solid angles between dissociation and detection volumes can be significant as well, because the angular distribution of the fragmentation process needs to be considered. Furthermore, the laser pulse duration is connected to its spectral width, which will be discussed in detail in section 2.3.2.

In the following sections these aspects will be treated in more detail with H-atom pulses generated via photodissociation of hydrogen iodide as an example.

2.3.1   HI Photodissociation

The photodissociation of HI after adsorption via the continuous A-X band ($280\,\mathrm{nm}>\lambda >190\,\mathrm{nm}$) has been studied thoroughly[22,48–53]. There are two dissociation channels, both generating fragment atoms with well-defined velocities:

$$\mathrm{HI} \rightarrow \mathrm{H} + \mathrm{I}(^2\mathrm{P}_{3/2}), \tag{A}$$

$$\mathrm{HI} \rightarrow \mathrm{H} + \mathrm{I}^*(^2\mathrm{P}_{1/2}). \tag{B}$$

Here, the reaction channel A results from transitions perpendicular to the laser polarization and obtains H-atoms with a $\sin^2\theta$ angular distribution[22,49,54], with θ as the angle between the polarization vector of the radiation and the H-atom recoil angle. Channel B obtains H-atoms with a $\cos^2\theta$ angular distribution from parallel transitions. The branching ratio depends on the dissociation wavelength, which for 268.3 nm results in 45 % of channel B.

Conservation of momentum and energy allows the calculation of final fragment energies. Thus, for channel B one obtains the H-atom fragment velocity[50,52] as:

$$v_{\mathrm{H}} = \sqrt{2\,E_{\mathrm{kin}}\frac{m_{\mathrm{I}}}{m_{\mathrm{H}}(m_{\mathrm{H}} + m_{\mathrm{I}})}}, \tag{2.7}$$

with the masses of the fragment atoms $(m_\mathrm{I}, m_\mathrm{H})$ and the kinetic energy release as:

$$E_\mathrm{kin} = h\nu + E_\mathrm{HI} - D_0 - E_{\mathrm{I}^*}. \tag{2.8}$$

The single contributions are: the photon energy $h\nu$, the electronic energy of the resulting iodine atom $(E_{\mathrm{I}^*} = 7603\,\mathrm{cm}^{-1})$[45] in the $(^2\mathrm{P}_{1/2})$-state, and the HI bond dissociation energy $(D_0 = 24\,632\,\mathrm{cm}^{-1})$[50]. The last contribution is the internal energy of the HI molecule E_HI, which is zero for the ro-vibrational ground state. Measurements on the HI in the molecular beam expansion showed that the rotational cooling was insufficient to populate only the ground state. Thus, the rotational energy of the HI has to be considered. This is given as:

$$E_\mathrm{HI}(J) = B_0\, J(J+1) - D\, J^2(J+1)^2, \tag{2.9}$$

with the rotational quantum number J, the rotational constant $B_0 = 6.341\,96\,\mathrm{cm}^{-1}$, and the centrifugal distortion constant $D = 2.069 \times 10^{-4}\,\mathrm{cm}^{-1}$[55]. Experimentally, only rotational states with $J < 5$ were observed, which corresponds to a reduction in dissociation energy of up to $\lesssim 15\,\mathrm{meV}$. For the nominal H-atom kinetic energy of ~625 meV used in this work this corresponds to a reduction of 2.5 %.

2.3.2 Pulse Broadening by Spectral Bandwidth

The following considerations have been published previously[1]. By illustratively inserting a central frequency of the photolysis laser pulses used in this work (e.g. 268.3 nm) into eq. (2.7), a H-atom velocity of $v_\mathrm{H} = 10.89\,\mathrm{km\,s}^{-1}$ is obtained, which corresponds to a kinetic energy of $E_\mathrm{kin}(\mathrm{H}) = 0.625\,\mathrm{eV}$[50,52]. When assuming the volumes of source and detection volumes as points, one would obtain a H-atom pulse (HAP) whose temporal duration Δt would be limited only by the duration of the dissociation laser pulse $\Delta\tau$. The duration of laser pulses is coupled to their bandwidth $\Delta\nu$, and for FTL pulses with a Gaussian shape this is given by eq. (2.1). But the laser bandwidth is also connected to the atom-pulse duration, via eq. (2.8). In order to determine a quantitative way to describe those two effects, for now the broadening effect of the bandwidth will be summarized in a single factor Δt_BW. For the remainder of this work, a Gaussian quadrature will be assumed for convolution of both effects:

$$\Delta t = \sqrt{\Delta\tau^2 + \Delta t_\mathrm{BW}{}^2}. \tag{2.10}$$

For the quantification, the derivative of the H-atom velocity (eq. (2.7)) with respect to the photolysis frequency ν is considered as:

$$\frac{\mathrm{d}v_\mathrm{H}(\nu)}{\mathrm{d}\nu} = h\,\sqrt{\frac{m_\mathrm{I}}{2\,m_\mathrm{H}(m_\mathrm{H} + m_\mathrm{I})(h\nu + E_\mathrm{HI} - D_0 - E_{\mathrm{I}^*})}}. \tag{2.11}$$

For small deviations, this can be approximated to obtain a velocity spread Δv_H as:

$$
\begin{aligned}
\Delta v_H \approx \Delta \nu \, \frac{\mathrm{d}v_{\mathrm{H}}(\nu)}{\mathrm{d}\nu} &= \Delta \nu \, h \, \sqrt{\frac{m_{\mathrm{I}}}{2 \, m_{\mathrm{H}}(m_{\mathrm{H}} + m_{\mathrm{I}})(h\nu + E_{\mathrm{HI}} - D_0 - E_{\mathrm{I}^*})} \\
&= \Delta \nu \, h \, \sqrt{\frac{m_{\mathrm{I}}}{2 \, m_{\mathrm{H}}(m_{\mathrm{H}} + m_{\mathrm{I}}) \, E_{\mathrm{kin}}}}
\end{aligned}
\tag{2.12}
$$

To obtain the temporal effect from this velocity spread, the distance between photolysis and detection point X_0 needs to be considered. The resulting TOF is given by:

$$
t = X_0 / v_{\mathrm{H}},
\tag{2.13}
$$

and the first derivative as:

$$
\frac{\mathrm{d}t}{\mathrm{d}v_{\mathrm{H}}} = \left| \frac{-X_0}{v_{\mathrm{H}}{}^2} \right| = \frac{X_0}{v_{\mathrm{H}}{}^2}.
\tag{2.14}
$$

Now, again approximating a finite difference, yields:

$$
\Delta t_{\mathrm{BW}} \approx \frac{X_0}{v_{\mathrm{H},0}{}^2} \Delta v_{\mathrm{H}},
\tag{2.15}
$$

with $v_{\mathrm{H},0}$ being the H-atom velocity generated by the central frequency of the photolysis pulse. Now, combination of eqs. (2.12) and (2.15) yields:

$$
\begin{aligned}
\Delta t_{\mathrm{BW}} &= \frac{X_0}{v_{\mathrm{H},0}{}^2} \, \Delta \nu h \, \sqrt{\frac{m_{\mathrm{I}}}{2 \, m_{\mathrm{H}}(m_{\mathrm{H}} + m_{\mathrm{I}}) \, E_{\mathrm{kin}}}}, \\
&= \frac{X_0}{v_{\mathrm{H},0}{}^2} \, \frac{\Delta \nu h}{2 \, E_{\mathrm{kin}}}.
\end{aligned}
\tag{2.16}
$$

Equation (2.1) can be inserted into eq. (2.16):

$$
\Delta t_{\mathrm{BW}} = \frac{X_0}{v_{\mathrm{H},0}} \, \frac{h \, \ln(2)}{\pi \, \Delta \tau \, E_{\mathrm{kin}}},
\tag{2.17}
$$

and this result can be inserted in eq. (2.10) to obtain:

$$
\Delta t = \sqrt{\Delta \tau^2 + \frac{m_{\mathrm{H}}}{2 \, E_{\mathrm{kin}}{}^3} \left(\frac{h \, \ln(2) \, X_0}{\Delta \tau \, \pi} \right)^2}.
\tag{2.18}
$$

Equation (2.18) is the general solution for the HAP duration for a FTL pulse with Gaussian shape. In order to obtain the shortest pulse duration Δt_{min} within the current approximations the broadening effects of Δt_{BW} and $\Delta \tau$ need to be balanced since they are oppositional. The result is given as:
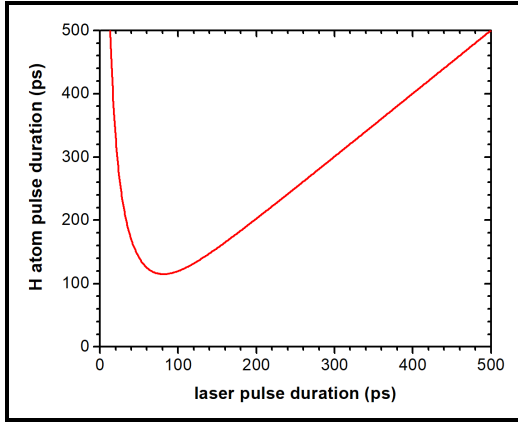
Figure 2.1: Illustration of the interplay of laser pulse duration and bandwidth of FTL Gaussian laser pulses. The effective H-atom pulse duration was calculated by eq. (2.18) for the following realistic parameters: $X_0 = 10\,\text{cm}$ and $E_\text{kin} = 1\,\text{eV}$. Here, an absolute minimum is yielded for a 80 ps laser pulse generating a 110 ps H-atom pulse. For shorter laser pulses, the increased bandwidth leads to longer H-atom pulse durations.

$$\Delta t_\text{min} = \sqrt{\frac{2\,\ln(2)\,h\,X_0}{\pi}} \cdot \sqrt{\sqrt{\frac{m_\text{H}}{2\,E_\text{kin}{}^3}}}. \tag{2.19}$$

For illustrative purposes, realistic numbers can be inserted: $X_0 = 10\,\text{cm}$ and $E_\text{kin} = 1\,\text{eV}$ result in $\Delta t_\text{min} = 110\,\text{ps}$, for an optimum laser pulse duration of $\Delta\tau = 80\,\text{ps}$. Additionally, the result of eq. (2.18) is depicted in fig. 2.1 for these parameters as well. Clearly, the broadening effect of the bandwidth severely limits the minimum pulse duration for such systems.

2.3.3 Finite Focal Sizes

To elucidate the effect of laser foci on H-atom pulses, the fundamental connection is simply given by:

$$t = {}^{d}\!/v, \tag{2.20}$$

with the particle velocity v, the length of the volume in propagation direction d, and the resulting TOF. In other words, the particles created at the far end of the photolysis volume need to travel the additional distance d, which separates them by a "transit time" t from the particles generated at the other end.

For a given H-atom pulse duration, this limits the reasonable focal volume. For example, a 100 ps H-atom pulse can originate only from a volume smaller than ~1 μm when the H-atom velocity is $10\,\text{km}\,\text{s}^{-1}$. In the geometrical optics model the f-number of the photolysis system would simply need to be reduced in order to produce smaller foci. But focal volumes are principally diffraction-limited, and therefore also dependend on the frequency of the radiation. Thus, the argumentation will now be expanded to Gaussian beam foci, which were described in section 2.1.

Another limiting factor is given by the HI photodissociation as a one-photon process which is proportional to the laser beam intensity. Therefore, the fragmentation will occur over the whole beam propagation volume when a homogeneous HI distribution is assumed.

Figure 2.2: Illustrative H-atom pulses generated under various focal conditions using a nanosecond pump and probe pulses at ~266 nm. The black line shows the signal from an unfocused pump pulse with ~11 mm diameter. The residual signals were generated using a lens with focal length of 250 mm, but with the lens displaced along the propagation direction by 30 mm (green), 10 mm (blue) or close to the correct position (red line). The decreasing width of the resulting H-atom pulses shows the effect of the illuminated volume of the molecular beam. The shift of the peak positions is due to a small misalignment of the laser beam direction.
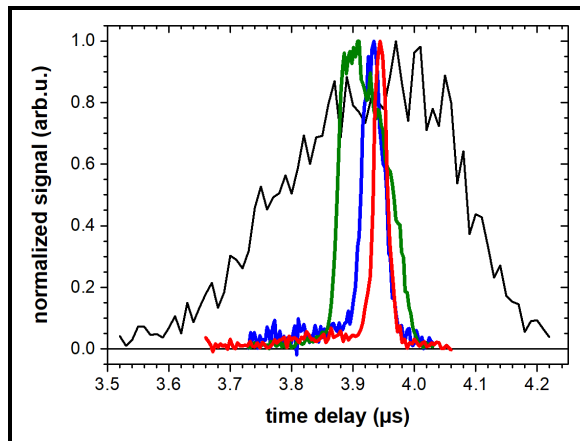
However, in applications molecular beams of HI are used which are geometrically restricted by apertures. When focusing the dissociation laser in the center of such a molecular beam, its outer diameter restricts the interaction volume along the laser propagation direction. Now, when the f-number is reduced, not only the focal waist becomes smaller but also the Rayleigh length decreases. Therefore, if the width of the molecular beam is not matched properly to the f-number, the temporal resolution of the H-atom pulse is governed by the laser beam size outside the focal region. Within this limit, the light propagation can again be approximated by geometrical optics, increasing the laser beam diameter linearly to the distance from the focus (see eq. (2.6)).

In conclusion, the photodissociation volume is defined in two dimensions by the laser cross section along the propagation direction and by the molecular beam dimension in the third dimension. To illustrate the effect of illuminated volume of the molecular beam on the resulting H-atom pulses, fig. 2.2 shows a few normalized H-atom pulses, each generated under different focal conditions. The black line gives the measured H-atom pulse from a non-focused dissociation laser with a FWHM diameter significantly larger than the molecular beam. The other three lines show H-atom pulses generated by focused laser beams. Here, the focal plane was displaced from the molecular beam center by ~30 mm (green), ~10 mm (blue) and $\lesssim$ 1 mm (red). The resulting variation in the illuminated volume directly affects the duration of the H-atom pulses.

2.4   Bunch Compression Photolysis

In this section the concept of bunch-compression photolysis (BCP) will be introduced[1], also based on the photodissociation of hydrogen iodide. The underlying calculations will be presented extensively, but it should be pointed out again that this information was already published elsewhere[1].

For the photolysis step, a "Pump" laser beam is used with the following core attributes: (1) a wavelength in the region of the A-X absorption band of HI (see section 2.3.1), here

~268 nm. (2) short FTL pulse with a sufficient bandwidth, here ~10 THz and ~116 fs[56] (both as FWHM). (3) Gaussian shape intensity profile. (4) linear polarization.

In this work, the detection of the formed HAP is restricted to laser ionization of the atoms by a second laser pulse ("Probe"). Thus, the temporal limitation depends on the spectroscopic method employed (see section 2.2) and was either the laser pulse duration itself (for REMPI) or the focal characteristics. However, for the conceptual treatment presented here, the laser foci are treated as idealized points. The broadening effects of finite focal sizes on H-atom pulses have been discussed in section 2.3.3.

2.4.1 Concept

A schematic drawing of the BCP concept is given in fig. 2.3. The photolysis or "Pump" laser beam (A) is dispersed on a grating (B). Due to the bandwidth of the FTL pulse the resulting, chirped beam is divergent and is focused by a spherical lens (D, with focal length f). In the focal plane each frequency component of this beam is focused onto an individual spot with spatial detuning $\Delta X(\nu)$ relative to its center frequency, forming a focal line of ~1.5 mm length. With the considerations presented in section 2.4.2, the detuning was tailored in such a way that the fragments produced by photodissociation are compressed spatially and temporally in a certain point (F). The nominal flight distance X_0 is measured from the focal spot of the center frequency of the pump pulse to the compression point.

The key point of this scheme is the spatial distribution of the foci for all frequency components. This is adjusted such that the resulting differences in kinetic energy of the photofragments compensate their initial spatial detuning ($\Delta X(\nu)$). In other words, faster fragments are generated in a larger distance from the target. Thus, the whole bunch of fragments with different velocities compresses during their propagation until all arrive at the same time in the same spot. Therefore, this method was termed bunch-compression photolysis (BCP).

2.4.2 Mathematical Description

The mathematical treatment of BCP that will be presented in this section was already published[1]. Here, the concept will be explained in detail, building on the results shown in sections 2.3.1 and 2.3.2. A few assumptions to simplify the treatment need to be included. As first approximation, the foci of the photolysis and detections lasers are assumed to be points, separated by a given distance (X_0). Then, the optimum distance between photolysis and detection point depends on the photolysis frequencies. For all fragments to arrive at the same target at the same time, the individual drift distances are given by:

$$X(\nu) = X_0 \, \frac{v_{\mathrm{H}}(\nu)}{v_{\mathrm{H}}(\nu_0)}. \tag{2.21}$$
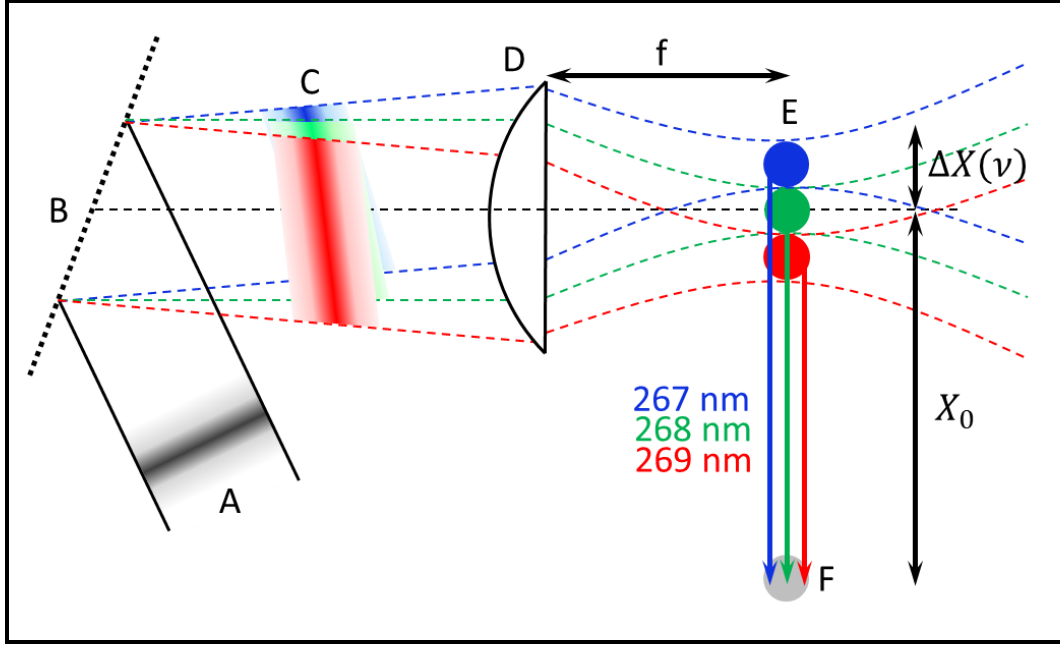
Figure 2.3: Schematic view of the optic setup for BCP. The Pump laser beam (A) is dispersed on a grating (B). The resulting chirped, divergent beam (C) is focused with a lens (D, focal length f). Each individual frequency component is focused onto a spot and due to the chirp those components are displaced $\Delta X(\nu)$ relative to the central frequency. This is illustratively depicted by three separated spots forming an approximately linear focus (E). By matching the photolysis energies with the correct spatial detuning, the photofragments are temporally focused onto a single spot (F) in the nominal distance (X_0). Reprinted with permission from [1]. Copyright 2014 Macmillan Publishers Limited.

Considering eqs. (2.7) and (2.8) this results in:

$$X(\nu) = X_0 \sqrt{\frac{h\nu + E_{\mathrm{HI}} - D_0 - E_{\mathrm{I}^*}}{h\nu_0 + E_{\mathrm{HI}} - D_0 - E_{\mathrm{I}^*}}} = X_0 \sqrt{\frac{E_{\mathrm{kin}}(v)}{E_{\mathrm{kin},0}}}, \tag{2.22}$$

with $E_{\mathrm{kin},0}$ as the kinetic energy of the fragments generated by the center frequency ν_0 of the pump beam. Henceforth, eq. (2.22) will be termed the *"ideal spatial frequency distribution"*, since it results in the optimal bunch-compression. For later considerations, a spatial detuning will be defined as:

$$\Delta X(\nu) := X(\nu) - X_0 = X_0 \left(\sqrt{\frac{E_{\mathrm{kin}}(v)}{E_{\mathrm{kin},0}}} - 1 \right). \tag{2.23}$$

Now that the goal is defined mathematically, the setup presented in fig. 2.3 needs to be characterized as well. Here, the combination of grating and lens result in the spatial chirp of the pump beam. Thus, the grating is treated first and its frequency-dependent diffraction angle $\beta(\nu)$ is given as:

$$\beta(\nu) = \sin^{-1} \left[m_g \, k_g \, {}^c\!/\nu - \sin(\alpha) \right], \tag{2.24}$$

with the grating constant k_g, the grating diffraction order m_g, the speed of light c, and

the incidence angle α. Thus, a nominally parallel incident beam with a given frequency spread is transformed to an angularly chirped, thereby divergent beam. In other words, each frequency component progresses at a different deflection angle, which can be defined as an angular deflection $\Delta\beta(\nu)$ relative to the central frequency:

$$\Delta\beta(\nu) = \beta(\nu) - \beta(\nu_0). \tag{2.25}$$

When such a chirped beam is focused by a spherical lens the spatial position of the focus for each frequency component $X_g(\nu)$ can be calculated within the paraxial approximation by:

$$
\begin{aligned}
X_g(\nu) &= X_0 + \Delta X_g(\nu), \\
&= X_0 + \mathrm{f}\left[\beta(\nu) - \beta(\nu_0)\right], \\
&= X_0 + \mathrm{f}\left[\sin^{-1}\left(m_g\, k_g\, \frac{c}{\nu} - \sin[\alpha]\right) - \sin^{-1}\left(m_g\, k_g\, \frac{c}{\nu_0} - \sin[\alpha]\right)\right].
\end{aligned}
\tag{2.26}
$$

This expression gives the experimentally resulting distribution of foci and will henceforth be termed "*grating spatial frequency distribution*". Now, the experimental conditions need to be chosen such that the *grating spatial frequency distribution* matches the *ideal spatial frequency distribution* (eq. (2.22)).

Practically, this matching condition needs to be fulfilled only over the frequency range of the pump pulse. In a first approximation the *ideal spatial frequency distribution* can be represented by a Taylor series:

$$X(\nu) = X_0 + \frac{X_0\, h}{2\, E_{\mathrm{kin},0}}(\nu - \nu_0) + \cdots, \tag{2.27}$$

with the first expansion coefficient, which will henceforth be referred to as *ideal linear spatial dispersion*:

$$\left(\frac{\mathrm{d}X(\nu)}{\mathrm{d}\nu}\right)_{\nu_0} = \frac{X_0\, h}{2\, E_{\mathrm{kin},0}}. \tag{2.28}$$

Analogue, the *grating spatial frequency distribution* (eq. (2.26)) can also be expressed by a Taylor series, with the first expansion coefficient, or *grating linear spatial dispersion*, as:

$$\left(\frac{\mathrm{d}X_g(\nu)}{\mathrm{d}\nu}\right) = \frac{c\, \mathrm{f}\, m_g\, k_g}{\nu_0\, \sqrt{\nu_0{}^2 - (\nu_0\, \sin[\alpha] - c\, m_g\, k_g)^2}}. \tag{2.29}$$

An illustration of the linear dispersion as function of the grating incidence angle α is shown in fig. 2.4 for the experimental conditions (table 3.2). Clearly, both dispersions match at 25° and 60°. For experimental purposes, the angle with the highest reflection

Figure 2.4: Dependence of the *grating's linear spatial dispersion* on the incidence angle (black line), calculated by eq. (2.29) and the experimental conditions (table 3.2). The red line shows the required *ideal linear spatial dispersion* (eq. (2.28)) for $X_0 = 44.6\,\text{mm}$ and both curves match at 25° and 60°. Experimental arguments, like the absolute reflectivity, then govern the choice of the angle for applications. Reprinted with permission from [1]. Copyright 2014 Macmillan Publishers Limited.
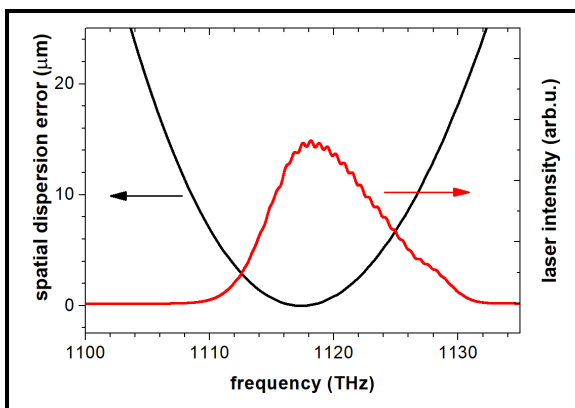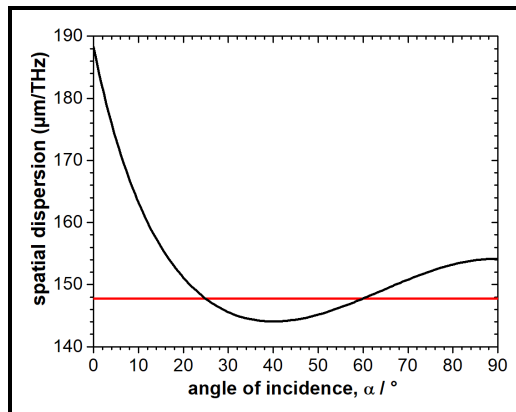
Figure 2.5: Illustration of the spatial dispersion error (numerator in eq. (2.30), black line) for the experimental conditions. Also shown is the measured intensity spectrum of the pump laser pulse (red line). Reprinted with permission from [1]. Copyright 2014 Macmillan Publishers Limited.
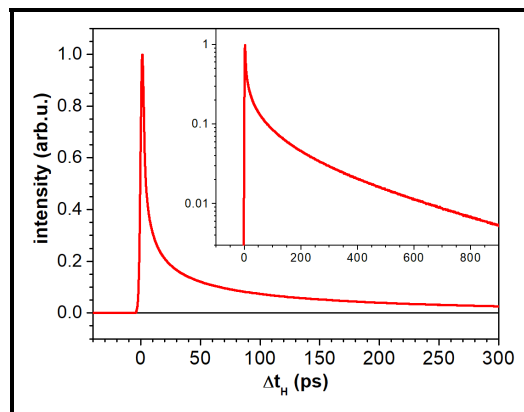
Figure 2.6: The temporal profile of the H-atom pulse as calculated from experimental conditions and eq. (2.30). Pump and probe laser foci were assumed as points and more details are given in the text. The inset shows the same curve on a logarithmic scale, to improve the illustration of the long tail. Reprinted with permission from [1]. Copyright 2014 Macmillan Publishers Limited.

was chosen, thus 60°.

In order to determine the impact of deviations between the *ideal spatial frequency distribution* and *linear grating spatial dispersion*, the H-atom pulse was simulated for experimental conditions. This still excludes finite laser focal sizes, but includes the pump laser spectrum $v_{\text{H}}(\nu)$. The resulting H-atom pulse shape is then given by:

$$\Delta t_{\text{H}}(\nu) = \frac{X_g(\nu) - X(\nu)}{v_{\text{H}}(\nu)}.$$ (2.30)

These results are presented in figs. 2.5 and 2.6, where the first figure shows the spatial dispersion error (black line) and the pump pulse intensity profile (red line) and the second figure the resulting H-atom pulse. The inset gives a logarithmic scale to illustrate the long tail of the pulse. In this example, the FWHM gives a pulse duration of $<10\,\text{ps}$ but ignores the long tail. Considering instead the integrated signal, the first 50 % (75 %) of the pulse would extend over a length of 94 ps (~300 ps).

2.4.3 Numerical Simulation

In addition to the treatment of BCP presented in section 2.4.2, numerical simulations were carried out. This treats the pump and probe laser pulses as Gaussian beams instead of ideal points. Hence, the broadening effects discussed in section 2.3.3 are included in this model.

In the presented model the photolysis pulse is approximated as instantaneous. The actual grating/lens combination of the setup broadens the pump pulse from ~116 fs to <10 ps by dispersion[1], as calculated from the ray-pulse formalism described in section 2.1. Thus, the instantaneous laser pulse approximation is reasonable as long as the H-atom pulse duration is considerably longer. Also, from the H-atom velocity the propagation distance during this pulse duration is calculated as ~0.1 µm and is therefore neglected for the simulation. A second approximation is made with regard to the molecular beam, which is simply assumed as a homogeneous distribution of HI molecules over a total length of 1 mm. This corresponds to the width of the experimental apertures (see (E) in fig. 3.1) and the laser focal plane is considered as positioned in the center.

For the simulation, the Cartesian coordinate system is defined by the propagation directions of the molecular beam (y), the laser pulses (z) and the resulting H-atom pulse (x), as is also indicated in fig. 3.1. Taken as the origin of this coordinate system is the center of the focus of the central frequency of the pump pulse. By using the Gaussian beam parameters that have been determined experimentally (table 3.1) both laser beams are described within the Gaussian beam model, which was already treated in detail in part II, section 8.2.5.3. Because the photodissociation employed here is a one-photon process (cf. section 2.3.1), the H-atom fragments are generated within the spatial profile of the pump beam intensity as:

$$ I\left(x, y, z, \nu\right) = \frac{I_0}{\left(w_{\text{Pump}} \sqrt{1 + \left[\frac{z}{z_{\text{Pump}}}\right]}\right)^2} \cdot \exp\left[\frac{-2\left(\left[x - \Delta X_g(\nu)\right]^2 + y^2\right)}{\left(w_{\text{Pump}} \sqrt{1 + \left[\frac{z}{z_{\text{Pump}}}\right]}\right)^2}\right]. \qquad (2.31) $$

Here, due to the small solid angles within the given setup, the angular dependence of the photolysis process for a linearly polarized laser beam was neglected. The quantity $\Delta X_g(\nu)$ was defined in eq. (2.26). It is pointed out, that the (x)-axis is correlated with the frequency dependent spatial dispersion. Thus, the spectrum of the pump laser (see fig. 2.5) was included in the simulation by sequential calculations for fixed frequencies, and for each frequency the value $\Delta X_g(\nu)$ was determined.

For the probe beam the non-resonant multi-photon ionization process for H-atoms had been determined with a power dependence of I^6 (section 2.2). Thus, the ionization probability in the focused probe beam is given as:

$$I\left(x,y,z\right) = \left(\frac{I_0}{\left(w_{\text{Probe}}\sqrt{1+\left[\frac{z}{z_{\text{Probe}}}\right]}\right)^2} \cdot \exp\left[\frac{-2\left([x-X_0]^2+y^2\right)}{\left(w_{\text{Probe}}\sqrt{1+\left[\frac{z}{z_{\text{Probe}}}\right]}\right)^2}\right]\right)^6 . \quad (2.32)$$

Now two sets of random points (x,y,z coordinates) were generated, one for the pump pulse volume and one for the probe pulse volume. For each point within the pump volume the distance to all points in the probe volume was calculated. Then for each distance and the frequency-dependent velocity (eq. (2.7)) an arrival time was determined. From the product of eqs. (2.31) and (2.32) at the corresponding coordinates a weighting factor was calculated for each point pair. By repeating this for a high total number of point-pairs, on the order of 10^6, and binning of the obtained results in 10 ps bins, an arrival time distribution is obtained.

This procedure is conducted for the whole spectrum of the pump laser pulse, where each distribution is weighted with the intensity at the given photolysis frequency. Additionally, this whole simulation was conducted for the rotational states of HI with $J < 5$, because those had been observed (section 2.3.1). The only free factor in this simulation were the relative amplitudes of the rotational states of HI.

In order to determine a better estimation of the H-atom pulse duration which excludes the broadening effects of the applied detection method the simulation was modified. Instead of a probe beam volume, a surface was assumed at X_0 with an area of 1 mm x 1 mm and a homogeneous detection efficiency. This approach was considered justified to simulate the H-atom pulse for possible future applications of BCP in the field of surface science. In contrast to a point probe volume, this approach took geometrical broadening effects into account in a meaningful manner.

Chapter 3

Experimental Setup

In this chapter the experimental setup will be described in detail and separate for laser and vacuum assemblies.

3.1 Vacuum Assemblies

3.1.1 Schematic Overview

A schematic diagram of the experimental setup is presented in fig. 3.1, with the coordinate system used throughout this work indicated in the lower right corner. This setup contained a set of three differentially pumped vacuum chambers. In the first two chambers a molecular beam is generated by a solenoid valve (A), propagating along the y-axis in fig. 3.1. In the third chamber were the ion optics setup, the detection MCP and the laser windows. Both laser beams propagated along the z-axis perpendicular to the shown plane. The pump laser beam crossed the molecular beam at (I), generating an H-atom pulse. The H-atoms that propagated along the x-axis were ionized by the probe laser beam at (J) and accelerated by the ion optics towards the detector.

3.1.2 Vacuum Chambers

All three differentially pumped vacuum chambers were designed and home-built in the workshop of the institute. These chambers were connected to the neighboring ones by apertures with $2\,\mathrm{mm}$ diameter ($\varnothing$) and pumped by one turbomolecular pump (STP-301C, Edwards) each. The molecular beam generation and shaping is described in detail in section 3.1.3 and the ion optics setup in section 3.1.4. Under operation conditions the pressures in the three chambers were $1 \times 10^{-4}\,\mathrm{mbar}$, $4 \times 10^{-6}\,\mathrm{mbar}$ and $4 \times 10^{-8}\,\mathrm{mbar}$. The third chamber also held the laser entry and exit windows, which consisted of laser polished magnesium fluoride ($18\,\mathrm{mm}$ diameter, $2\,\mathrm{mm}$ thickness, Korth Kristalle GmbH). These were mounted on home-built viewports and sealed by Viton® o-rings. This assembly allowed regular replacement of the window crystals, which was necessary due to the optical

21

A: Nozzle (0.5 mm Ø)
B: Skimmer (2 mm Ø)
C: Aperture (2 mm Ø)
D: Electrode (GND, 6 mm Ø)
E: Entrance Slit (1 mm width)
F: Electrode (+100 V, 6 mm Ø)
G: Electrode (GND, 6 mm Ø)
H: Grid (GND, 12 mm Ø)
I: Pump Laser Beam (268 nm)
J: Probe Laser Beams (805 nm)
K: MCP Detector (-2.1 kV)

125.2 mm

44.2 mm

44.2 mm

1st chamber p ~1E-4 mbar   2nd chamber p ~4E-6 mbar   3rd chamber p ~4E-8 mbar

241 mm
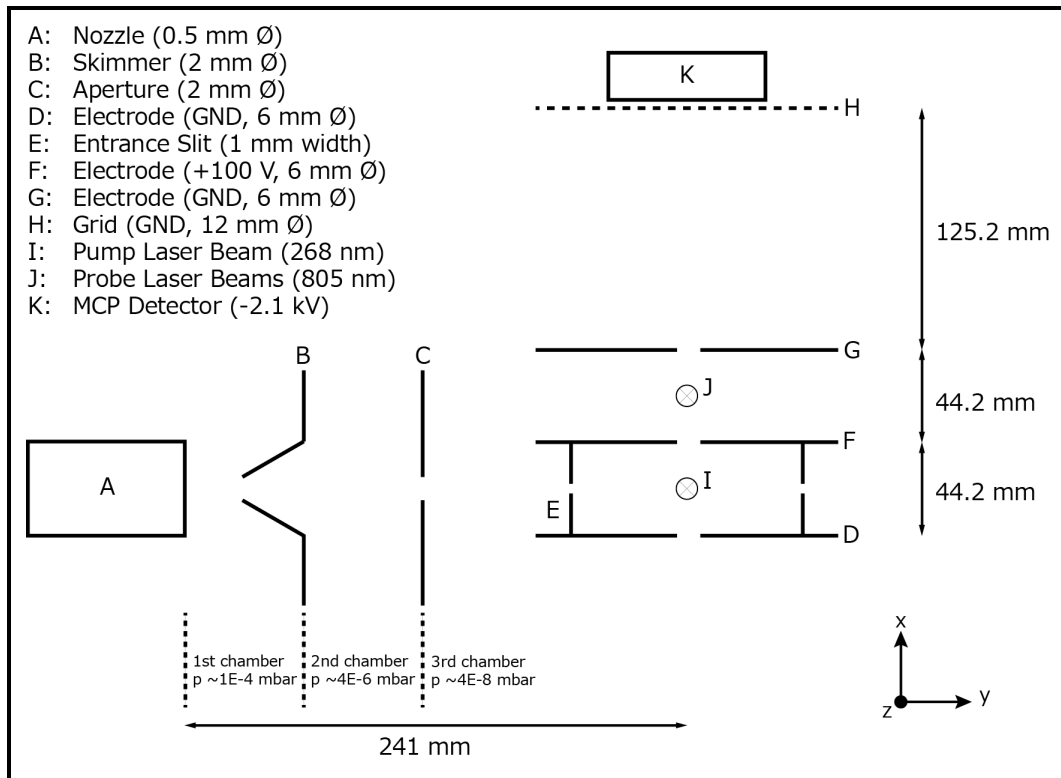
Figure 3.1: Schematic drawing of the experimental vacuum setup, which consisted of three differentially pumped vacuum chambers. These are set up for molecular beam expansion and shaping (A,B,C,E) and the third chamber contained the ion optics setup (D,F-K). The coordinate system used throughout this work is indicated in the lower right corner. The HI molecular beam generated in the nozzle (A) passed along the y-axis from (A) to (I). Pump and probe laser beams (I and J) progressed along the z-axis and the H-atom pulse along the x-axis from (I) to (K). All significant parts are indicated by the letters and the relevant dimensions are presented as well. A more detailed description is given in the text and the according subsections. Reprinted with permission from [1]. Copyright 2014 Macmillan Publishers Limited.

damages induced by the high-power ultraviolet (UV) radiation.

3.1.3 Molecular Beam Setup

In this work two different molecular beam nozzles were used. First, a commercial solenoid valve (Pulse Valves Series 9, Parker) was used with a 0.5 mm nozzle diameter (∅). This operated sufficiently to align and optimize the ion optics setup and laser beams and produced molecular beams with low rotational temperatures [(20 ± 2) K]. But this valve turned out to be unsuitable for long term operation under the harsh corrosive conditions in the setup, where pure HI gas was supplied to the valve with a stagnation pressure of 2 bar.

Thus, a home-built solenoid valve had been designed to reduce the exposure of HI to the moving parts, and a schematic of the result is shown in fig. 3.2. This design was stable over long operation times, operated with a repetition rate of 50 Hz, and produced molecular beams with a duration of ~200 μs FWHM. Only the necessary water cooling of the valve and the non-thermal rotational distributions of HI in the molecular beam were
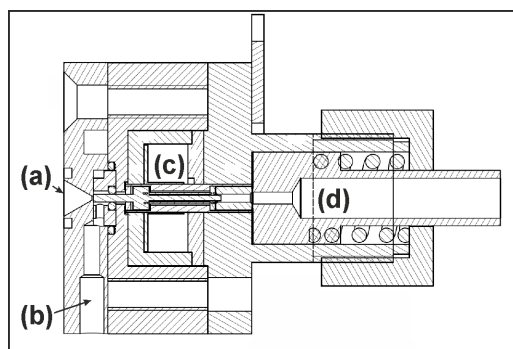
Figure 3.2: Schematic view of the solenoid valve design for reactive gases. The expansion cone had an angle of 60° starting from the 0.5 mm ⌀ hole (a). The gas was supplied from a connection at the side (b) to a small volume sealed by the poppet. Seal materials were a Viton® o-ring separating the poppet from the solenoid region (c) and a thin (120 μm) Kapton® sheet at the tip of the poppet with a hole of according size. The force of the spring (d) pressing on the poppet was adjustable by the fixation mechanism.
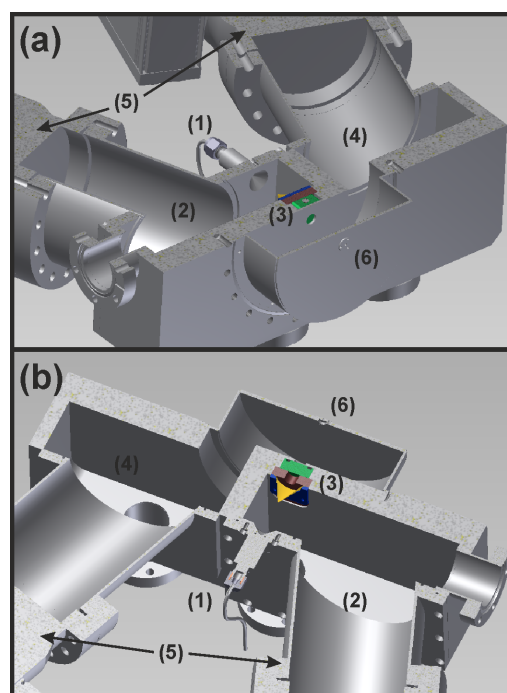
Figure 3.3: Cut through views of the molecular beam source chambers from two perspectives (panels a and b). The molecular beam valve and nozzle (1) is mounted on the source chamber (2). A collimating electro-formed skimmer (2 mm ⌀, Beam Dynamics) and a slide valve (3) for separately sealing the source chamber from the differential pumping stage (4). Both chambers are pumped by turbomolecular pumps (5, STP-301C, Edwards) and connected to the main chamber by a small aperture (6) with a diameter of 2 mm.

disadvantages.

The molecular beams were generated in two differentially pumped chambers and an overview is shown in fig. 3.3. Both solenoid valves were mounted on a nozzle diameter of 2 mm and the beams were collimated by an electro-formed skimmer (2 mm ⌀, Beam Dynamics). A slide valve allowed separation of the source from the residual chambers, e.g. for daily maintenance on the valve. The differential pumping stage was connected to the main chamber by a small aperture of 2 mm ⌀, which was aligned to allow the molecular beam to pass through.

3.1.4   Ion Optics

Figure 3.4 gives a schematic view of the main part of the optics setup, as it was used for BCP. Here, the round electrode plates (grey) are the parallel electrodes, each 1.5 mm thick, 108 mm outer diameter and 6 mm inner diameter. Those electrodes were fixed with nuts on insulated rods, which allowed for parallel alignment and supply of individual potentials. On the lowest electrode, two slit apertures (1 mm x 10 mm) were added to limit the width

Figure 3.4: Schematic view of the ion optics relevant for BCP. The round electrode plates (grey) were parallel and aligned to their central apertures, insulated from the holding rods via ceramics (white). For BCP, the lower and upper electrode were set to ground potential and to the center electrode a repulsion potential of $+100\,$V was applied. The two slits on the bottom electrode restricted the width of the incoming molecular beam (black), which was dissociated with the chirped pump laser (blue). The *neutral* photofragments (green) that passed the aperture bunched at a given distance and were ionized there by the probe laser (red). Then, the nascent H^+-ions (blue) were accelerated towards the detector. For both laser beams the polarization plane is indicated by black arrows.
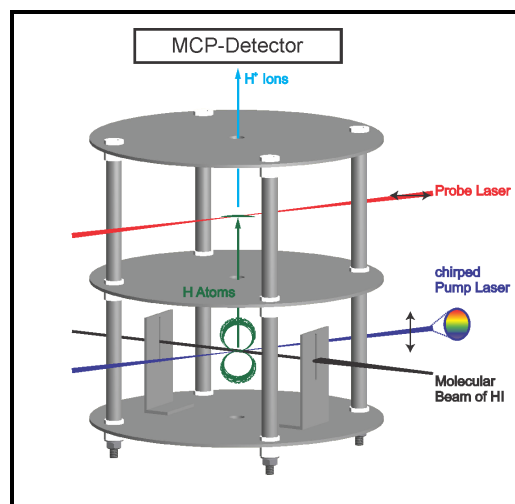
of the HI molecular beam (black). For BCP experiments, the lower and upper electrodes were kept at ground potential and the middle electrode at $+100\,$V. When the pump laser (blue) intersected the HI molecular beam, the *neutral* photodissociation fragments (green) spread undisturbed while ions generated by multi-photon ionization were repelled from the detection region. In the optimal compression distance, the compressed H-atom pulse was ionized by the pump laser beam (red), and the nascent H^+-ions (blue) are accelerated towards the MCP detector. The space between the last electrode and the grid (G and H in fig. 3.1) allowed field-free drift of the accelerated ions and thus TOF measurements.

Variation of the polarization axis (black arrows) of the probe laser allowed the control over the recoil direction of ions generated from residual gas molecules (e.g. HI, H_2). These originated from strong-field dissociation and successive ionization (e.g. ref. 42–44) with broad fragment velocity distributions. Variation of the recoil vector perpendicular to the H-atom pulse propagation direction then allowed to distinguish these products by their arrival TOF.

For REMPI experiments, the electrode potentials were slightly different. Here, the bottom electrode was set to $+1\,$kV while all others were set to ground potential. Thus, all ions generated from the molecular beam were accelerated towards the detector.

Not shown are two additional electrodes which were integrated into the setup at a larger distance from the bottom electrode. Those were each displaced by $5\,$mm from the calculated optimal compression distance for BCP via channel A, which was $111\,$mm from the photolysis spot. In this work, these electrodes were only used for H-atom pulses generated by nanosecond laser dissociation.

3.1.5 Acquisition Equipment and Procedure

A home-built program in the LabView programming environment (LabView2011, National Instruments, Austin) controlled all laser systems as well as the data acquisition and handling. Ion signals from the MCP (two plates in chevron setup, Burle) detector were

recorded by an oscilloscope (DPO 3034, Tektronix), averaged over 512 acquisitions and the resulting TOF distributions transferred to a computer. Then, the signals of the TOF ranges corresponding to certain particles were integrated and the results stored. Due to their high velocity the H-atoms from the generated pulses could be distinguished from H-atoms produced by other sources (see section 2.2). The repetition rate of the experiments was 10 Hz or 50 Hz, as limited by the laser or molecular beam valve repetition rates.

All timings in the experiment were controlled by delay generators (DG535, Stanford Research Systems Inc.; SDG Elite, Coherent Inc.), which were managed by the control program. For each given delay time between the two laser pulses, background noise was acquired as well, which was subtracted from the signals. For this, the molecular beam nozzle delay time was increased by 500 µs, such that the laser beams passed through the chamber before the molecular beam. In general, reproducibility measurements were conducted on different days to verify the BCP results. Additionally, a certain range of delay times was measured repeatedly in each single acquisition. This range of delay times was determined by the different settings within the optical delay stage, which allowed to realize the same time delay (see section 3.2.2.2).

As a result from this method the density of acquired data points for varied between certain time-delay ranges. Thus, for the signal processing the smoothing of the BCP data was not based on regular averaging methods. Instead a low pass fast Fourier transform filter with a cutoff frequency of 320 MHz was applied.

3.2 Laser Setups

In this work five different laser setups were used, each chosen by their characteristics for a given purpose. Because this work was the proof-of-principle for the BCP concept the setup was first characterized, aligned and optimized using nanosecond pulsed lasers. For BCP too a nanosecond probe laser was employed first for alignment purposes. After this optimization, the H-atom pulse duration was characterized by the setup with two femtosecond lasers.

3.2.1 Nanosecond Lasers

The applications of narrow bandwidth neodymium-doped yttrium aluminium garnet (Nd:YAG) laser beams in this experiment had several advantages. Especially beneficial were the high-pulse powers which provided strong signals for alignment of the ion optics, characterization of the HI molecular beam and optimization of the detection setup. Of course, the detectable H-atom pulse duration was fundamentally limited by the duration of these laser pulses.

3.2.1.1 ns Pump Beam

To determine the duration of H-atom pulses that could be achieved with the present experimental geometry the established method of HI photodissociation was applied. For this, a narrow bandwidth UV laser beam was required. In this work, the fourth harmonic of a Nd:YAG (Quanta-Ray Lab-170-10, Spectra-Physics) at 266 nm was employed. This laser had a repetition rate of 10 Hz, pulse energies of ~75 mJ and a pulse duration of ~7 ns.

3.2.1.2 ns Probe Beam

For probing H-atoms, the same setup was used that is described in detail in part II, section 9.1.2. Using (2+1) REMPI of H-atoms via the Lyman-β state using ~205.15 nm radiation was described in section 2.2. Here it is simply pointed out, that the pulse duration of ~7 ns FWHM limited the time resolution but also allowed for easier detection of the H-atom pulses. Thus, this laser beam was beneficial for determination and characterization of the experimental delay time between pump and probe lasers as well as for the TOF window for H-atoms in the acquisition setup.

3.2.1.3 REMPI of HI

For the (2+1) REMPI of HI via the $g^3\Sigma^-(O^+)$ S-band (see section 2.2) the setup described in part II, section 9.1.2 was modified slightly. Here, the required wavelength range of 302–303 nm was achieved with the second harmonic of the dye laser. Thus, this beam was separated from the fundamental wavelength before the third harmonic setup and directed onto the molecular beam using a plano-convex lens with a focal length of 250 mm.

3.2.2 Femtosecond Lasers

The two femtosecond laser beams that were used to realize BCP were produced by a common Ti:Sapphire oscillator (Vitesse, Coherent Inc., 116 fs pulse width) amplified in two separate regenerative Ti:Sapphire amplifiers (RGA). Each RGA was pumped by a neodymium-doped yttrium lithium fluoride (Nd:YLF) laser with a repetition rate of 1 kHz. Further modification of the two resulting synchronized laser beams to the used 'Pump" and "Probe" radiation will be described in the following sections. Figure 3.5 presents a schematic overview of the setup and table 3.1 summarizes the relevant properties of both shaped beams.

3.2.2.1 fs Pump Beam

The photolysis RGA (Libra, Coherent) is frequency tripled producing 0.45 mJ per pulse at the center wavelength of 268.3 nm. This photolysis pulse is dispersed with a ruled 2400 lines mm^{-1} grating (P2400 UV, Spectrogon) optimized for a 50° angle of incidence.
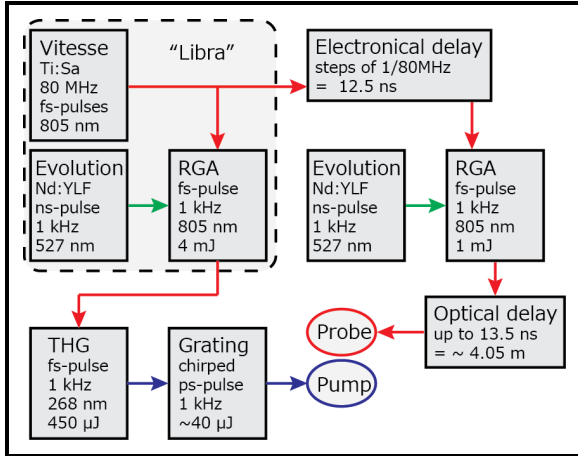
Figure 3.5: Schematic view of the laser setup used for BCP. Briefly, a common Ti:Sapphire oscillator is amplified in two separate RGAs, which allows to vary the time delay between both beams over a wide range with great precision. The radiation of one pulse is frequency tripled and dispersed on a grating to form the "Pump" pulse for BCP. The second pulse is delayed relative to the Pump beam, first in steps of the reciprocal oscillator frequency (12.5 ns) and subsequently via an additional optical delay stage, forming the "Probe" beam for H-atom detection. The RGA of the probe beam was a home-built device, but the RGA of the pump beam was a part of the commercial "Libra" system (Coherent Inc.).

Table 3.1: Summary of the femtosecond laser pulse properties used in the experiment. It is pointed out that for the pump beam the focus characteristics correspond to the non-chirped pulse.

Parameter	Pump Beam	Probe Beam
ν_0	1117.4 THz	372.4 THz
$\Delta\nu$ [a]	10 THz	10 THz
f [b]	250 mm	200 mm
w_0	(8.5 ± 0.6) µm	(125 ± 5) µm
FWHM [c]	(10.2 ± 0.7) µm	(150 ± 6) µm
z_R	0.85 mm	1.8 mm

[a] as Gaussian FWHM

[b] nominal focal length for 268 nm and 800 nm, respectively.

[c] of the beam intensity profile

This "Pump" radiation is focused onto the molecular beam with an anti-reflection coated fused silica lens with a focal length of 250 mm and 50.8 mm ∅. After these optics only ~40 µJ per pulse reached the photolysis volume.

It is pointed out that the focal conditions reported in table 3.1 for the pump beam correspond to a beam that was not diffracted on the grating. The focal volume of such an angularly dispersed beam was ~1.5 mm (FWHM) along the dispersion direction and the focal size of the individual frequency components were undeterminable. Table 3.2 gives a summary of the experimental details relevant for the H-atom pulse generated with this radiation.

3.2.2.2   fs Probe Beam

The 80 MHz output of the oscillator served as a clock for the whole system and triggered the Pockels-cells of both RGAs. This allowed a delay of the input to the home-built probe RGA relative to the output of the photolysis RGA. This electronically controlled delay was up to ~900 µs, in steps of 12.5 ns ($80\,\mathrm{MHz}^{-1}$). The output of the probe RGA passed an optical delay stage with a continuously tunable delay of 0–13.5 ns. This delay stage

consisted of a 30 cm translation stage (LTS300, Thorlabs Inc.) where the beam passed eight times, corresponding to a time delay of ~8 ns. The residual delay was realized by a flip-mirror allowing access to an additional, fixed optical delay length, which corresponded to ~5.5 ns. Successive acquisitions for the whole variation range of the translation stage with and without this fixed distance led to an overlap of certain delay times in regular intervals, which allowed a certain degree of reproducibility verification.

Such a long total optical delay was necessary to create an overlap with the next oscillator pulse, which ultimately made equivalent-time experiments of sub-ns resolution over a ~900 µs range possible. These detection pulses, with a pulse energy of ~1 mJ and a center wavelength of 805 nm, were focused with an anti-reflection coated fused silica lens with a focal length of 200 mm. This allowed H-atom detection via strong-field ionization, as described in section 2.2.

An additional challenge was the accompanying strong-field dissociation and successive ionization of the residual gases, mostly HI and H_2. This also generated H-atoms, but those could be separated in the detection according to their TOF. Using a waveplate, the polarization of the probe laser could be rotated to influence the recoil direction of unwanted dissociation reactions.

Table 3.2: Summary of the experimental conditions the presented BCP H-atom pulse was acquired under.

Parameter	Value
X_0	44.57 mm
$\nu_{H,0}$ [a]	$10.89 \, \text{km}\,\text{s}^{-1}$
k_g	$2400 \, \text{lines}\,\text{mm}^{-1}$
m_g	1
α [b]	60.0°

[a]velocity of H-atoms produced by photolysis laser central frequency

[b]incidence angle of probe beam on grating

Chapter 4

Results

4.1 HI REMPI

Figure 4.1 shows an illustrative REMPI spectrum of a pure HI molecular beam. Here, the experimental conditions had not been optimized for rotational cooling in order to determine the range of transitions that could be obtained. Clearly, the $g^3\Sigma^-(O^+)$ S-band was best suitable for the task with well-resolved lines for $J < 6$.

The molecular beam conditions were generally optimized to obtain a maximum flux in the generated H-atom pulses. For example, variation of the stagnation pressure (1–4 bar) controlled the rotational temperature in the beam over the range of 20–75 K. The timings of the valve were also crucial, because the HI intensities and the rotational distributions varied within the molecular beam pulse. Furthermore, the different valves used (see section 3.1.3) produced very different distributions in the pulses, i.e. the home-built valve generated non-thermal rotational distributions.

Additional tests of seeding HI in helium gave lower total H-atom yields. While the rotational distributions collapsed to obtain a beneficially higher relative population of $J = 0$, this advantage was overcompensated by an absolute dilution of HI molecules.
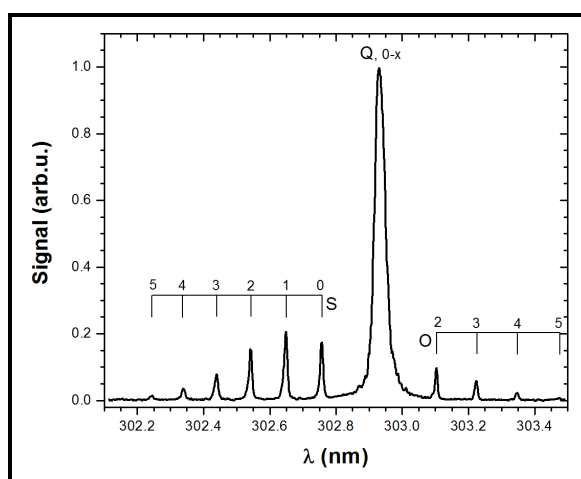
Figure 4.1: Illustrative REMPI spectrum of a molecular beam of HI. The signal obtained by using (2+1)-REMPI via the $g^3\Sigma^-(0^+)$ state ($v' = 0$) is shown[47]. From the integrated line intensities of the S-band the rotational temperature was determined as $(55 \pm 5)\,\mathrm{K}$. Transitions of the Q-band were not resolved for rotational states and the O-branch contained not enough information to determine the rotational temperature reliably.
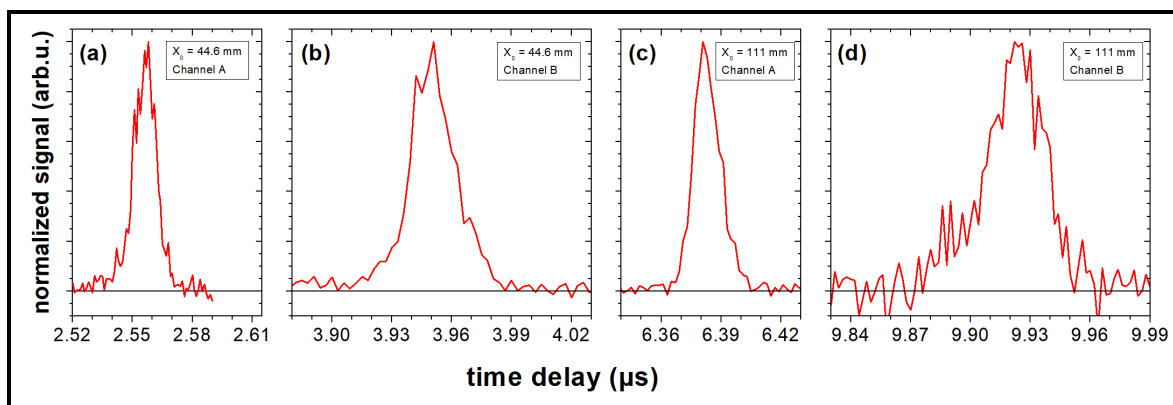
Figure 4.2: Several H-atom pulses generated and detected by nanosecond laser pulses under different conditions. For two different distances between pump and probe foci, $X_0 = 44.6$ mm and 111 mm for panels (a,b) and (c,d), respectively. In panels (a,c) the laser polarization was perpendicular to the H-atom pulse, thus corresponding to channel A. Panels (b,d) show the results for the parallel transition channel B.

4.2 H-atom Pulses by Nanosecond Photolysis

As shown in fig. 2.2 H-atom pulses were generated by ns lasers to align and optimize the experimental setup. Additionally, these serve as benchmark to which the BCP method can be compared. A summary of the optimized H-atom pulses obtained from ns photodissociation is given in fig. 4.2. Each of the four panels shows the results for different conditions, namely reaction channels A and B, and two distances. These distances correspond to the optimal distances for BCP by the two reaction channels for the available optical setup. Generally, all pulses have a non-symmetric shape and due to the velocity spread of the H-atoms are the pulses temporally broadened for increased propagation distances. Here, the FWHM of the time profiles increase from 12 ns to 16 ns and from 24 ns and 32 ns. Furthermore, comparison of the two reaction channels clearly shows broader pulses for H-atoms with lower kinetic energy.

4.3 H-atom Pulses by Femtosecond Photolysis

4.3.1 Bunch-Compression Photolysis

Figure 4.3 shows a direct comparison of two H-atom pulses generated by fs-laser photodissociation. Here, the black line shows an H-atom pulse obtained by focusing of the pump pulse onto the molecular beam, as for the ns setup. Due to the bandwidth of the dissociation laser pulse the H-atom pulse broadened to a Gaussian-FWHM of ~135 ns (blue line). This is six orders of magnitude longer than the initial laser pulse duration. In contrast to this pulse the temporal width of the BCP-H-atom pulse (red line) is reduced to a few ns and actually results in a "pulse train". These individual pulses originate from different rotational states of the HI molecules prior to photodissociation, as indicated in fig. 4.3. Their internal energy is directly converted to kinetic energy upon fragmentation
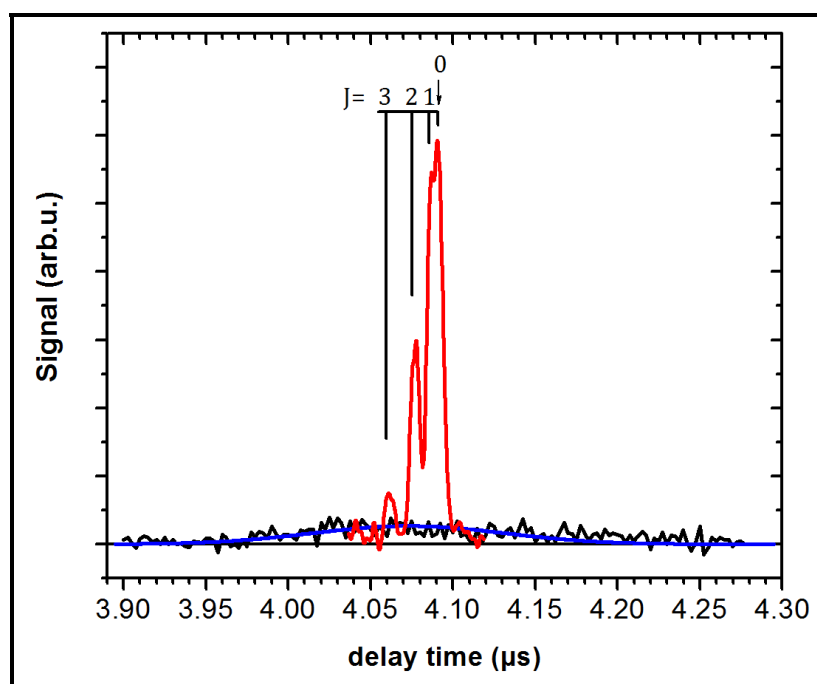
Figure 4.3: Comparison of H-atom pulses generated by BCP (red) and conventional fs photolysis (black), both scaled to pump laser intensity. Focusing a fs laser pulse for photolysis results in a large initial-velocity spread and the resulting H-atom pulse has a Gaussian-FWHM of 135 ns (blue). In contrast, BCP (red) gives a pulse width low enough to resolve individual pulses originating from the different rotational states of HI. Furhermore, the peak intensity is much higher, partly due to the compression and partly due to improved photodissociation conditions, as described in the text. Reprinted with permission from [1]. Copyright 2014 Macmillan Publishers Limited.

(see eq. (2.8)), thus higher excited molecules have larger velocities. The observed width of the separate H-atom pulses in the pulse train is 5.8 ns, which was determined from the resolved $J = 2$ signal.

In fig. 4.3 the pulses have been corrected for the power of the dissociation laser pulses. Simply focusing the laser pulse results in saturation of the dissociation accompanied by a substantial amount of multi-photon ionization. In contrast, the BCP is ~20 times below the saturation limit and shows no multi-photon processes. This is not only due to the lowered beam intensity by the limited efficiency of the grating-lens combination. Instead, the pulse energy is spread over a much larger volume, ~1.5 mm along the dispersion direction. Clearly, BCP results not only in shorter H-atom pulses but also in higher pulse intensities. This is partly due to the compression of the same number of H-atoms into a shorter time interval and partly due to the increased focal volume, which allows better dissociation conditions.

4.3.2 Numerical Simulations

The BCP signal from fig. 4.3 is shown enlarged in fig. 4.4 as black circles. The result of the numerical simulation for the experimental conditions is shown by the red line (see section 2.4.3). It shuold be pointed out that the only adjustable parameter in this model
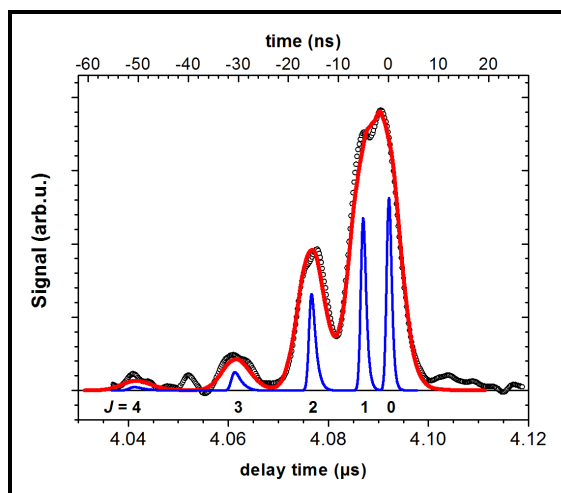
Figure 4.4: Comparison of the BCP-signal (black circles) to the result of the numerical simulation (red line) according to the experimental conditions (section 2.4.3). Additionally shown is the simulation result (blue lines) for a hypothetical experiment where the probe laser pulse was replaced by a surface of 1 mm x 1 mm. The uncertainty of this simulation is ±0.3 ns and thus well represented by the thickness of the line. Reprinted in part with permission from [1]. Copyright 2014 Macmillan Publishers Limited.
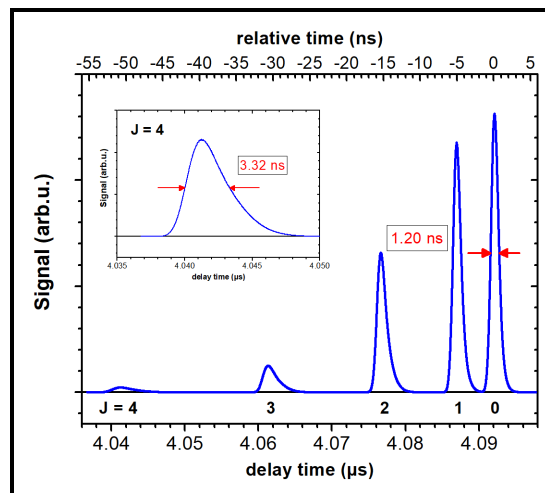
Figure 4.5: Detailed view of the numerical simulation results for the H-atom pulse duration impinging on a flat surface (blue). The inset shows the enlarged pulse train member corresponding to HI in the $J = 4$ state upon photodissociation. Although all those pulses are clearly not symmetrical are the FWHM values indicated by red arrows for the $J = 0$ and 4 signals. Reprinted in part with permission from [1]. Copyright 2014 Macmillan Publishers Limited.

were the relative partitions of the rotational states. Clearly, the model reproduces the temporal distribution of the H-atom pulse train wery well.

Additionally, the model had been modified to determine the actual H-atom pulse time profile without the broadening effects of the detection method. For this, the probe laser pulse was replaced by a hypothetical surface of 1 mm x 1 mm in the simulation (see section 2.4.3) and the result is shown by the blue lines in fig. 4.3. This demonstrates that the individual H-atom pulses are actually significantly broadened by the detection method.

The simulation result is also shown enlarged in fig. 4.5. Here the non-symmetrical shape of the H-atom pulses in the pulse train is distinguishable, and the FWHM durations are indicated (red arrows) for the $J = 0$ and $J = 4$ members of the signal. While the expected H-atom pulse duration for $J = 0$ is (1.2 ± 0.3) ns, thus significantly shorter than the measured 5.8 ns, is the $J = 4$ signal about twice as broad. This effect is a simple result of the optimization of experimental setup, especially the grating, for BCP of HI in the ro-vibrational ground state (see eq. (2.26)). The reduction in dissociation energy (eq. (2.9)) is small but sufficient to broaden the individual pulses of the pulse train. This effect increases with the rotational energy of the parent HI molecule, but the experimental time resolution was insufficient for a direct measurement of this effect.

Chapter 5

Discussion

In this chapter the presented results will be discussed elaborately.

5.1 Experimental Aspects

This section treats the influence of all experimental aspects on the H-atom pulses and discusses possible improvements.

5.1.1 HI Molecular Beam

One limiting factor of the achievable H-atom pulse intensities was the applied vacuum system, which ultimately limited the operation conditions of the molecular beam. For example, when expanding HI at higher stagnation pressures (6 bar), the HI rotational population distribution would collapse to only the $J = 0$ state. Furthermore, improved vacuum systems would allow an increase of the repetition rate of the experiment from 50 Hz up to a maximum of 1 kHz limited by the laser pulse repetition rate.

Expansion of gas mixtures of seeded HI in e.g. helium would also lead to lower rotational temperatures in the molecular beams. But this would be compensated by dilution of the total HI amount. It would also be necessary to tailor the expansion conditions to prevent cluster formation in the beam.

From REMPI of the HI in the molecular beam the rotational populations could be determined. But due to the corrosive properties of the gas the valve and nozzle had to be maintained on a daily basis. After few hours of experiment, the valve was diassembled, rinsed in ethanol, and the sealing parts were replaced. As a result, the exact conditions within the molecular beam, i.e. pulse duration and rotational distribution, varied slightly. Due to the considerable alignment effort necessary for BCP it was not possible to conduct REMPI and BCP experiments within the same day and thus nozzle conditions. An improved experimental design would have been necessary for that.

5.1.2 Laser Alignment

In this experiment, the alignment, timing and focusing of the laser beams was most crucial to obtain the shortest H-atom pulses possible. Even slight misalignments instantly manifested in longer matter pulse durations.

5.1.2.1 Pump Laser

For the simple focusing method the alignment and optimization of the focusing conditions was feasible by observation of the total ion yield obtained from multi-photon ionization of the molecular beam. Unfortunately, this method could not be used for the BCP pump beam, and the alignment to iris-apertures outside the chamber was not accurate enough. Thus, the exact focal position for BCP had to be aligned successively by repeated H-atom pulse measurements.

5.1.2.2 Probe Laser

For the H-atom pulse duration the alignment of the probe laser was also crucial. Especially the multi-pass optical delay stage (eight times 30 cm) required additional equipment to verify the correct alignment. This was realized by a camera which recorded the fraction of the laser pulse that was transmitted through a high-reflective mirror. The center of the beam for all positions of the translation stage was recorded.

The alignment of the residual optical delay length (total of ~4 m) was verified as described in section 3.2.2.2 . A camera was used to verify the translation stage alignment and iris-apertures for the residual optical delay. In this setup, a certain time delay range could be realized for different translation stage positions, which allowed some degree of verification of the temporal overlap.

For alignment of the focal position the actual distance to the probe beam was calculated from the difference between a measured and the expected time delay of an H-atom pulse. Then, the focus position was corrected by using a translation stage with a resolution of 10 μm. It is emphasized that a misalignment of the total pump-probe distance also results in a significant broadening of the H-atom pulse duration. From the principles presented in section 2.4.2 the H-atom propagation was modeled for the BCP conditions. This simulation was extended to determine the H-atom pulse profile expected when probing in a distance displaced by Δx from the nominal compression distance X_0. These results are presented in fig. 5.1 and clearly show that the H-atom pulses are significantly broadened to the ns timescale. Even for an error of ~1 % in the propagation direction, the effect is substantial for the given setup. In contrast to these errors are the asymmetry and broadening effects resulting from the spatial dispersion error negligible (figs. 2.5 and 2.6). In conclusion, the BCP method requires substantial effort for alignment of the probe technique and deviations manifest directly in an increase of the pulse duration.
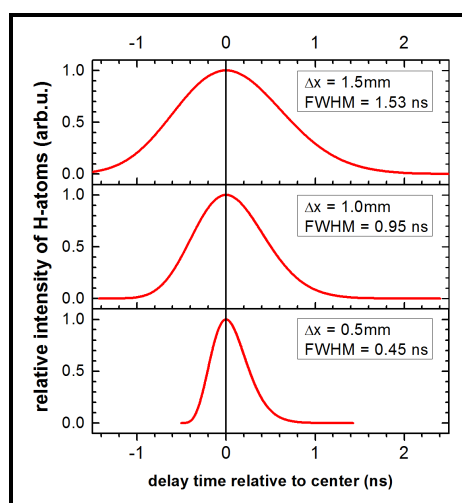
Figure 5.1: Simulated H-atom pulses for displaced probe distances. Indicated in each panel are the displacement and the resulting FWHM of the asymmetric H-atom pulse. For this simulation, point foci for pump and probe laser were assumed and an *ideal spatial frequency distribution* [eq. (2.22)]. The nominal optimum compression distance was $X_0 = 44.62\,\mathrm{mm}$, and the displacement from this is indicated in each panel. More details of the method are given in section 2.4.2.

5.2   H-atom Pulses

In this section the obtained H-atom pulses will be discussed in detail.

5.2.1   Photodissociation Methods

A direct comparison between "conventional" ns photodissociation by focused laser beams to the new BCP method is shown in fig. 5.2. Here, the result of the conventional method was shifted along the time axis in order to compare more easily. The deviation of time delays resulted from the difference in photon energy for the center wavelength of the pump pulses.

In contrast to the conventional ns-pulse the temporal resolution of the BCP-signal is improved and even allows to distinguish various rotational states of the parent HI molecules. Table 5.1 summarizes the relative time resolutions obtained by the three different H-atom pulse techniques studied in this work. Here, the resolution is defined as the ratio between the pulse FWHM and its delay time of the main ($J = 0$) peak. All three compared methods were conducted for the same X_0 and reaction channel B, only the pump laser frequency was higher for the ns laser. Thus, the photon energy was ~35 meV higher than for the fs pump pulses, which is considered negligible since here relative numbers were compared.

Obviously, focusing of a fs pump pulse gives the worst resolution of the three methods, by one order of magnitude. Comparing BCP and the ns laser dissociation shows an improved resolution for BCP by a factor of four. The result of the numerical simulation corresponds to a realistic H-atom pulse duration, which is not limited by the detection method. Here, the resolution is enhanced by one order of magnitude compared to the ns laser dissociation.

Considering other pulse properties like the total H-atom flux, the conventional ns method benefits from the high pulse energies that are achieved routinely. But this topic is

Figure 5.2: Direct comparison of normalized H-atom pulses generated by different techniques under otherwise similar experimental conditions. In both cases reaction channel B was employed, the distance between pump and probe was $X_0 = 44.6\,\text{mm}$ and comparable molecular beam conditions were used. The red line shows the H-atom pulse produced by bunch-compression photolysis (see fig. 4.4) and was detected with a femtosecond probe pulse. For comparison the black line shows a H-atom pulse generated and detected by nanosecond laser pulses. This signal has been shifted by $+140\,\text{ns}$ to improve the comparability.
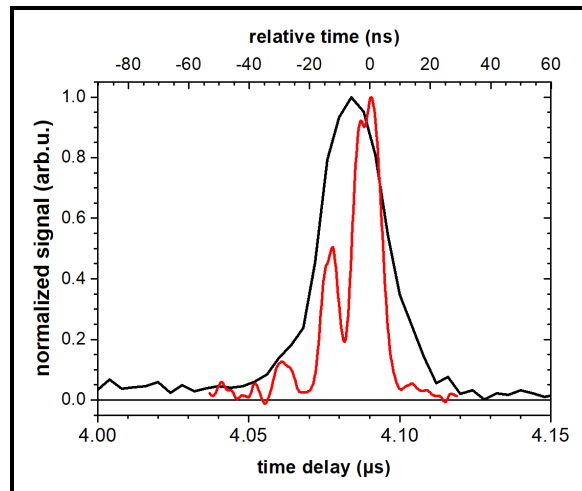
Table 5.1: Temporal resolution of the H-atom pulses generated by different techniques. The relative resolutions are determined from the quotient of pulse-FWHM and delay time.

H-atom pulse method	delay time / µs [a]	FWHM / ns	Resolution / %
ns pump pulse, focused	3.9440	24	0.61
fs pump pulse, focused	4.0905	135	3.30
fs pump pulse, BCP	4.0905	5.8 [b]	0.14
fs pump pulse, BCP	4.0905	1.2 [c]	0.03

[a] for the center of the peak corresponding to HI initially in $J = 0$.

[b] determined from the resolved peak corresponding to HI initially in $J = 2$.

[c] result of the numerical model presented in fig. 4.5, corresponding to HI initially in $J = 0$.

more complex and thus treated in section 5.2.2.3 in more detail. Here, another unfavourable property of both fs methods is pointed out. The initial energy spread from the dissociation laser bandwidth is retained in the fragments, resulting in a kinetic energy distribution with a FWHM of 7 % for the presented system. In principle, this can be problematic for some applications like energy resolved scattering (see section 5.2.2.5).

5.2.2 Bunch Compression Photolysis

The comparison of BCP to other photodissociation techniques was presented in section 5.2.1. Here, the determined properties of the H-atom pulses and the general limitations of the method will be discussed.

5.2.2.1 Measured Pulse Train

The BCP signal presented in fig. 4.3 clearly demonstrates that the technique is applicable and offers several advantages. The temporal resolution is improved compared to established methods, but is still on the order of ns. This was limited by the detection method in this work and determined by the probe laser focal volume.

From the measured focal dimensions (table 3.1) and the strong field ionization techni-que (see section 2.2) an effective probe pulse focal size can be estimated as ~60 μm. As shown in section 2.3.3 an effective minimum temporal width of ~5.5 ns for the H-atom pulse train can be approximated from the H-atom velocity of $\nu_{H,0} = 10.89 \, \mathrm{km \, s^{-1}}$ (table 3.2). This effect considers the probe pulse focal volume only.

In this work BCP was demonstrated only for the given experimental geometry and reaction channel B. For reaction channel A a BCP pulse was not measured, because the larger optimal compression distance ($X_0 = 111 \, \mathrm{mm}$) would lead to a decrease of signal in-tensity. Also the time resolution would still be comparable since it was limited by the probe technique. For variation of the focusing optics to lower f-numbers a substantial amount of re-design of the vacuum apparatus would have been required. Thus, improvements from such changes can only be estimated as is presented in the following sections.

5.2.2.2 Numerical Simulations

Figure 4.4 showed that the obtained H-atom pulse is well described by the numerical simulation method that had been introduced in section 2.4.3. From the uncertainty of the measured pump laser focal volume an error of ±0.3 ns was estimated for the H-atom pulse duration, thus smaller than the line thickness in figs. 4.4 and 4.5. It should be borne in mind that the only variable parameter in this model was the relative population of the rotational states. While those could principally be determined via REMPI, it was not possible to conduct BCP experiments under exactly the same conditions, as explained in section 5.1.1. Here it is simply pointed out that the rotational populations are comparable to certain REMPI results within the determination accuracy.

When assuming a surface as probe instead of the laser focal volume the simulated H-atom pulse duration is severely reduced, as shown in fig. 4.5. Here, the probe surface dimensions (1 mm x 1 mm) were chosen to represent a realistic geometry for a hypothetical application. This also prevented an excessive reduction of the broadening effects for the current experimental geometry and yielded an FWHM of $(1.2 \pm 0.3) \, \mathrm{ns}$ for the $J = 0$ member of the H-atom pulse train. This corresponds to an improvement of the H-atom pulse time resolution by a factor of five (see table 5.1), which shows that in this work the probe method is the limiting factor. Simulations for improved setups for BCP will be presented in section 5.2.2.4.

In the results presented in fig. 4.5 the FWHM of the individual members of the H-atom pulse train increases with rotational state. This is easily explained by the optimization of the setup for the dissociation of HI in the $J = 0$ state. While the rotational energy of HI is only on the order of a few meV not negligible deviations result in the *ideal spatial frequency distribution* [eq. (2.22)]. But this effect is only observable in the simulation, the experimental signals are not temporally resolved.

Other simulations studied the broadening effects resulting from the spatial disper-

sion error and were presented in figs. 2.5 and 2.6. Here, the asymmetry of the expected H-atom pulse led to a temporal spread on the order of 1–100 ps. Furthermore, the effect of displacement of the probe pulse was simulated and already discussed in section 5.1.2.2.

5.2.2.3 H-atom Pulse Intensities

In the comparison of focused photolysis and BCP (see fig. 4.3) the different H-atom pulse intensities are clearly discernible. Despite the fact that both pulses had been scaled according to the photolysis pulse power is the integrated intensity of the BCP-pulse significantly larger. To explain this, the differences in the focal volumes will be considered.

For the simple focusing method the focal properties had been determined experimentally (table 3.1). From the beam radius in the focus w_0, the Rayleigh length z_R and the molecular beam width of 1 mm, the focal volume is well described. For the comparison to BCP only the variation along the H-atom propagation direction (x axis) induced by the grating/lens combination must be considered. Here, the focal volume extends over a length of ~1.5 mm, thus is simply enlarged by a factor of ~150. This spread of the pulse energy results in several advantages. The saturation of the adsorption which can occur in the focused pump pulse was considered first. In BCP the larger illuminated volume allows higher absolute pulse energies without saturation. An accompanying effect is the reduction or suppression of multi-photon processes, e.g. non-resonant ionization, which was detected by simple focusing but not in the BCP setup. A third advantage is the higher absolute number of illuminated HI molecules in the enlarged focal volume. In conclusion, all these effects increase the number of H-atoms in the pulses generated by BCP, additionally to compressing them into a short time interval.

It should be pointed out that the duration of the H-atom pulses is also limited by the focal volume and the experimental geometry (section 2.3.3). While focusing optics with a lower f-number (eq. (2.2), f/114 for this setup) decrease the focal radius for the individual frequency components of the beam, their Rayleigh length is also reduced. If the molecular beam radius is not adapted to the Rayleigh length the resulting H-atom pulse duration is governed by the illuminated photolysis volume outside the actual focus region. In conclusion, the focusing optics, molecular beam dimensions and experimental geometry need to be adjusted to obtain the shortest possible H-atom pulse duration. It should also be pointed out that for diffraction limited foci the focal radius is proportional to the wavelength, thus shorter H-atom pulses can be obtained with dissociation at higher laser frequencies.

Based on these considerations the photolysis volume could also be enlarged without further degrading the H-atom pulse duration by use of a cylindrical lens for focusing. The intention is to focus only along the H-atom propagation direction (x) while the pump beam is unmodified (or only reduced in its width) along the molecular beam propagation direction (y). If the illuminated width along (y) is matched to the molecular beam width

along the laser propagation direction (z), the total focal volume for BCP could be increased by another factor of ~100 without influencing the H-atom pulse duration.

From the laser pulse intensity, the focal volume and the HI molecular absorption coefficient the fraction of illuminated molecules which dissociate can be calculated. Here, a molecular beam density on the order of $1 \times 10^{13} \, \text{cm}^{-3}$ is assumed, which reflects the realistic intensities for pulsed nozzles running close to their physical limits, which are imposed by the formation of shock waves at the skimmers used for collimation. Then, H-atom numbers on the order of 1×10^7 are obtained and from these the reaction channel B makes up for ~45 %. Considering the small solid angle probed in this experiment, which is estimated as ~1.4 mrad, and the $\cos^2 \theta$ recoil distribution, the number of H-atoms in the probe volume is estimated to be ~20 per laser pulse. For the reaction channel A, the larger optimal compression distance results in an even smaller solid angle, which leads to an expectation of less than ten H-atoms per laser pulse. This was one reason for not testing this approach with the available setup, next to the probe pulse limiting the time resolution. It is also pointed out that the density of the molecular beam has actually not been measured and could therefore be even lower. Furthermore, the population of several rotational states in the HI molecular beam distributes the absolute signal intensity over the single members of the pulse train.

5.2.2.4 Optimization

In this section, feasible improvements for BCP will be listed. These include arrangements to increase the H-atom pulse intensities as well as ways to reduce the duration of the pulses. Previously mentioned were changes of the vacuum setup (section 5.1.1) to increase the HI($J = 0$) fraction within the molecular beam and the repetition rate of the experiment. In section 5.2.2.3 the complex interplay of the focal geometry was discussed, which requires matching the molecular beam width and f-number (thus w_0 and z_R) to each other. Replacing the spherical lens used in this work by a cylindrical lens provides a relatively easy means to increase the H-atom pulse intensity without degrading its duration. Another promising approach to improve the intensity of the pulses would be the alignment of the HI molecules by an intense IR-laser field prior to dissociation[29,30,33].

For characterization of the temporal evolution of H-atom pulses below the ns limit an improved detection method is necessary first . From the numerical simulation result it is clear that a surface-based approach would be beneficial, since this would not extend along the H-atom propagation axis in contrast to volume-based methods (see section 2.3.3).

With the numerical model presented in section 2.4.3, the H-atom pulse duration for varied setups can be simulated accurately. For example, simply applying optics with a f-number of $f/13$ and a matched molecular beam width of 250 µm would yield H-atom pulses with a duration of 690 ps impinging on the probe surface. To make progress below this, one must simultaneously improve the focusing of the photolysis light and more

perfectly produce the *ideal chirp* in the laboratory by correcting for the higher order expansion coefficients in eq. (2.27). The latter is experimentally feasible in principle by prisms or a deformable mirror setup[1].

Considerably shorter H-atom pulses are possible only at shorter wavelengths, which combines several beneficial factors. With increasing photon energy the H-atom velocity is higher, reducing the dependence on focal size and the velocity spread due to the laser bandwidth. Furthermore scale diffraction limited focal diameters with the wavelength, thus lead directly to shorter H-atom pulses. Also, the HI photodissociation properties vary with the photolysis frequency, i.e. the A-X absorption band maximum is around ~220 nm[53]. Additionally, the branching ratio between the two reaction channels favours channel A for higher photon energies[52], which also results in higher fragment energies.

As an example for these considerations a hypothetical experiment employing a wavelength of 157 nm will be discussed. Wang *et al.*[57] studied this reaction in detail and obtained the corresponding branching ratio (82 % channel B), angular distribution and fragment energies. Also, the absorption coefficient was reported by[53] and is higher than for 268 nm. Now, BCP will be modeled with the additional assumptions of Gaussian beam shape, ideal focusing by f/17 optics and realization of the *ideal spatial frequency distribution* [eq. (2.22)]. As detector, a 0.5 mm x 0.5 mm surface placed at $X_0 = 44.6$ mm is assumed and the molecular beam width was restricted to 250 µm. This simulation obtains a H-atom pulse duration of FWHM 110 ps. The kinetic energy of these H-atoms would be 3.8 eV, which is still on the order of chemically relevant energies.

5.2.2.5 Possible Applications

Finally, possible applications for short H-atom pulses will be discussed. The advantages of the bunch-compression technique relative to the established nanosecond laser photodissociation technique include not only the reduction of pulse duration but also the increased H-atom flux. Thus, the presented method provides the possibility to study time-dependent dynamics induced by collisions with neutrals. While the achieved timescale is still considerably longer than that of motion on the atomic scale several other problems can be studied, of which a few will be pointed out here.

Utilizing the H-atom pulse as probe for laser-excited surfaces is one option. The H-atom scattering products would depend strongly on the lifetime of excited surface states, if the lifetime of the latter is on the same order of magnitude or longer. For example, the kinetics of metal-insulator-metal devices producing chemicurrents are of considerable interest in current research[20,58,59]. The kinetics of the electronic structure as well as the chemical kinetics need to be determined to unravel the underlying reaction mechanism for such non-adiabatic reactions, as elaborated in part II, section 11.2.3. But it should be remembered that the lifetimes of electronic excitation are on the order of ps for metals (e.g. ref. 6) and thus might not be probable with H-atom pulses. In contrast, lifetimes for surface states

on the order of µs are known for specific systems[60].

Another possible application of H-atom pulses would be direct scattering experiments, e.g.[24,61–63]. Here, the improvements would primarily comprise the increased flux by using the bunch-compression method, while the energy resolution is comparable and the time resolution already sufficient.

More sophisticated experiments can also be speculated upon, for example the reaction of incident H-atoms on a deuterated silicon surface. Studying the reaction products with laser spectroscopy would allow the identification of Langmuir-Hinshelwood (LH), Eley-Rideal (ER) or hot atom Eley-Rideal (HA-ER) reaction mechanisms or speculatively D-atoms produced via ballistic exchange. The lifetime of excited H-atoms in the HA-ER mechanism could possibly be many nanoseconds on a semiconductor like silicon.

For direct studies of kinetics on the nanosecond timescale, systems with high activation energies are necessary. For example, the atomic hydrogen desorption from surfaces, probably from high temperature refractory materials like tungsten. Temperature dependent experiments would reveal the kinetics from time resolved measurements, similar to the NO/Pt(111) system. Here, experiments were successfully carried out at lower temperatures and with millisecond time resolution[64,65]. Furthermore, timing experiments initiated by bimolecular collisions directly are considered possible. For example, short H-atom pulses possibly allow direct measurements the of lifetimes of collision-complexes[66].

Chapter 6

Conclusion

In this work the method of bunch-compression photolysis (BCP) was presented and also realized experimentally. This method is described in good approximation by well-known fundamental physics. Although the intensity of the obtained H-atom pulse train is low for the given setup and the individual pulse duration is still on the order of nanoseconds, the temporal resolution is enhanced relative to the established photodissociation method by approximately one order of magnitude. Information about the population of rotational levels of the parent molecule is already accessible and several further improvements to reduce the pulse duration are feasible. An additional advantage of BCP is the drastic reduction of undesired multi-photon processes within the dissociation volume, which occur in the conventional method. A further advantage is the photodissociation volume, enlarged by several orders of magnitude, which principally enables higher absolute H-atom fluxes.

In conclusion, the presented BCP method expands the scientific toolbox by enabling a new class of time-resolved experiments based on the interaction with neutral matter.

Part II

Hydrogen Permeation

Chapter 7

Introduction

Heterogeneous catalysis of gas phase molecules on metal surfaces is of tremendous importance in industrial scale chemistry. Production of most synthetic compounds involves one or more steps with liquid or gas phase molecules on a metal catalyst. The most prominent reaction is the ammonia synthesis via the Haber-Bosch process, due to its vast significance and scale: a world wide total production of 1.46×10^8 t in 2015[67,68]. G. Ertl characterized the sequence of elementary reactions involved in this process[69] and was awarded the Nobel Prize in Chemistry for this work in 2007.

One of the most simple reactions in heterogeneous catalysis is the dissociative adsorption of gas phase molecules on a metal surface. Even with the smallest molecule, H_2, quantitative modeling is still challenging for modern theoretical methods (e.g. ref. 70,71). Due to the restricted scope of this work, only the interaction of hydrogen molecules with selected transition metals will be treated. Nevertheless, it is pointed out that a wide range of other studies is available, including studies on nickel (e.g. ref. 72–74), silicon (e.g. ref. 75,76) and tungsten (e.g. ref. 77) surfaces as well as adsorption of other small molecules like methane (e.g. ref. 78–85) or oxygen (e.g. ref. 86–89).

Variation of the considered metal results in a change of the barrier height to dissociative hydrogen adsorption. Systems are usually categorized in one of three branches, depending on the height of this barrier: (i) non-activated, like palladium[73,90–96] or platinum[89,97–101]; (ii) weakly activated, like ruthenium[102–104] or cobalt[105,106] and (iii) strongly activated (barrier $\gtrsim 0.1$ eV) like the coinage metals copper (see section 7.4.1), silver[107–113] and gold (see section 7.4.2).

In this study, the applied experimental method restricts the reactions on the surface to the LH mechanism (cf. section 7.1) in the regime of low adsorbate coverage. Therefore, all adsorbates are equilibrated with the surface, which limits the control over initial conditions of the reactants. Furthermore, the surface has to provide the energy to overcome the barrier to reaction from its thermal reservoir[114,115]. All systems studied in this work have an activation barrier for desorption which exceeds the thermally provided energy, resulting in a low probability of adsorbate excitations into the reactive transition state. Unfortunately,

this excitation processes cannot be probed directly. However, information can be gained from determination of the energy distribution of the nascent products: For several decades, the dynamics of gas-surface interactions have been studied by characterization of desorbing molecules and accompanying theoretical investigations (e.g. ref. 70,114–118). Nowadays, a challenge for this methodology is the non-adiabacity observed in several systems, which is discussed in more detail in section 7.3. Thus, in this work several different systems were studied to improve the current level of understanding of gas-surface dynamics, each with regard to a different aspect as described in section 7.4.

7.1   Reaction Mechanisms in Heterogeneous Catalysis

Nowadays, three fundamental molecule-surface reaction types are distinguished. First is the Langmuir-Hinshelwood (LH) type[119], where two reactants adsorb and equilibrate on a surface. Reactions then take place between these adsorbates diffusing on the surface. The second type is the ER reaction[120], where only one reactant is adsorbed and equilibrated on the surface while the other reactant is impinging from the gas phase. Here, the reaction is immediate and the product desorbs, therefore surface diffusion is not relevant. The third type is termed HA-ER, a modification of the ER mechanism. Here, the gas phase reactant neither impinges directly on its counterpart nor does it scatter off the surface. It rather samples an increased surface area, partly dissipating its energy. Before it is fully equilibrated, it reacts with another adsorbate and the nascent molecule desorbs. The difference between ER (e.g. ref. 121) and HA-ER has been demonstrated by reaction cross sections larger than expected for ER reactions alone[122] and by kinetic considerations in abstraction reactions[123]. HA-ER reactions have also been differentiated further: a "secondary" reaction mechanism was found, where the impinging particle transfers a part of its energy to an already adsorbed atom, which then reacts successively with another adsorbed atom[124].

7.2   Activated Dissociative Adsorption

As stated in chapter 7, the dissociative adsorption of H_2 can be characterized into three categories depending on the necessary activation energies. The barrier to adsorption originates from the one-dimensional picture established by Lennard-Jones[125]: An avoided crossing of the potential energy curves (PECs) of H_2 physisorption and chemisorption on a given metal surface.

Figure 7.1 illustrates this schematically (e.g. ref. 116,125,126), where the PECs for molecular physisorption (dotted, light blue) and H-atom chemisorption (dotted, dark blue) are shown. Dependent on their relative position, the resulting curves (red and green lines) form a barrier to reaction E_{ad}, and systems are characterized by its magnitude: non-

activated for negative values and activated for positive ones. Systems are termed weakly activated when $E_{ad} \lesssim 0.1\,\mathrm{eV}$, which is the same order of magnitude as thermal energy of the surface. Also schematically illustrated is the effect of the barrier by the inset (light blue $n(E)$ axis), depicting a Maxwell energy distribution for molecules impinging on the surface at a given temperature (orange line) and the fraction of those which can react (shaded orange region). By detailed balance (see section 8.3.1), this is also the energy distribution that would be observed for desorbing molecules.
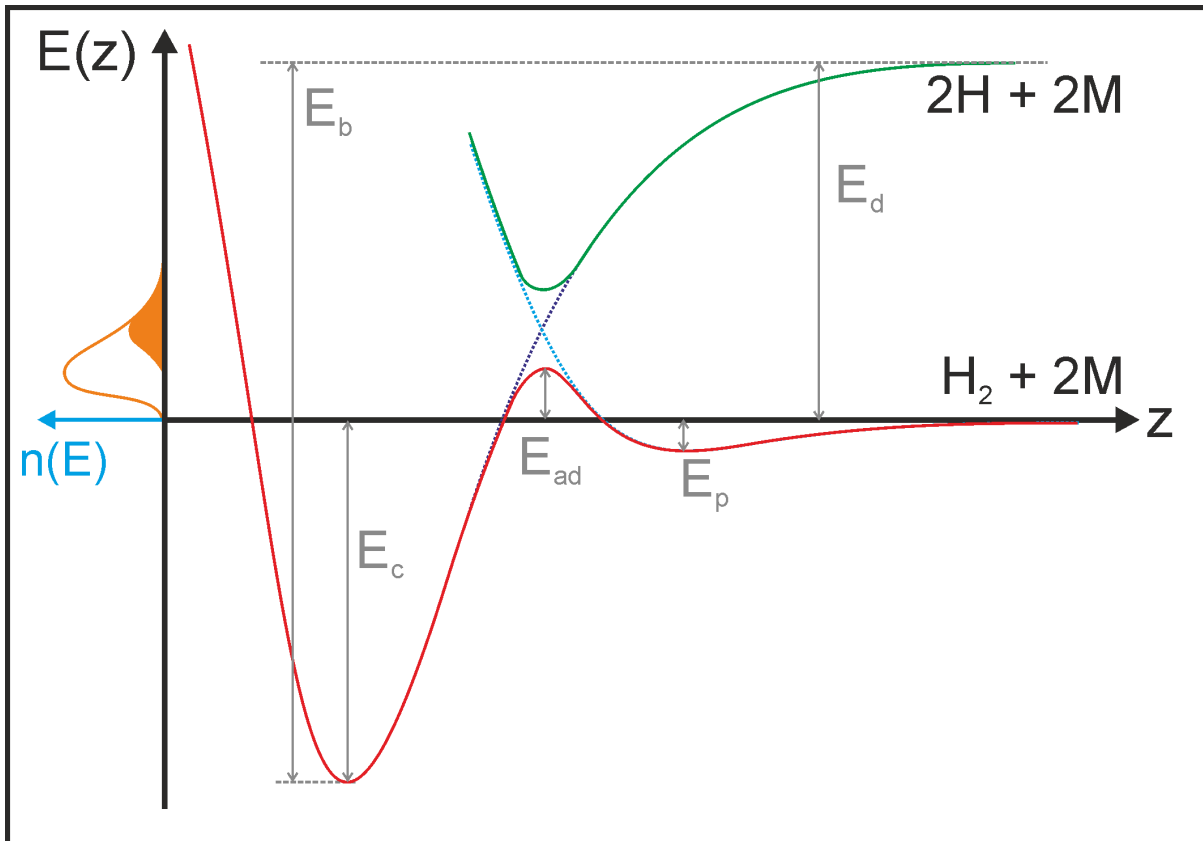
Figure 7.1: Schematic representation of the Lennard-Jones model illustrating activated adsorption processes on metal surfaces [116,125,126]. Dotted curves illustrate the PECs for molecular physisorption (light blue) and H-atom chemisorption (dark blue), while the solid curves give the resulting PECs formed by the avoided crossing (red and green). The height of the resulting barrier for adsorption, E_{ad} is determined by the relative position of the curves. Other indicated quantities are: E_p, the molecular physisorption well, E_b the energy of the two formed H-metal bonds, E_d the dissociation energy of H_2 and E_c the chemisorption energy. The effect of the barrier on the desorption distribution is additionally illustrated by the inset $n(E)$ axis (blue). Here, the Maxwell energy distribution at the surface temperature is given schematically (orange line) and the shaded region (orange) depicts the fraction of this distribution, which is able to cross the barrier.

7.2.1 Adsorption Energies

The chemisorption energy E_c according to fig. 7.1 can be calculated using the energy balance of the adsorption reaction from the H_2 dissociation energy E_d and the energy of the two H-metal bonds $E_{HM} = 1/2 \cdot E_b$, via:

$$E_c = 2 \cdot E_{HM} - E_d. \tag{7.1}$$

The dissociation energy for gas-phase H_2 is $4.52\,eV$[127]. Ferrin *et al.*[112] calculated binding energies for hydrogen atoms on metals for various facets using density functional theory (DFT). By inserting their values into eq. (7.1) one determines an exothermicity of ~$0.38\,eV$ for Cu(111), but for Au(111) the process is endothermic by ~$0.16\,eV$.

7.3 Non-Adiabacity in Surface Reactions

While the Born-Oppenheimer approximation (BOA) proved to be adequate for the description of many gas-surface dynamics, systems exist which cannot be described with this model. Especially metal surfaces do show non-adiabatic behaviour (e.g. ref. 128–130) and have been the subject of research over the last decades (e.g. ref. 59,70,131–137).

As to hydrogen-metal interactions, it has been proven that the non-adiabatic effects manifest in scattering and adsorption of H-atoms[61,138–141] as well as in associative desorption processes, where "chemicurrents" were observed in the hydrogen desorption from coinage metals[18–20,58,131,133,142,143]. This term describes measurable currents induced in metal-insulator-metal devices as a result of hydrogen recombination reactions under hydrogen atom exposure.

Further studies showed plasmon-driven H_2 dissociation on gold nanoparticles with a proposed mechanism involving electron-hole pair excitation[144]. Another study predicts non-adiabatic interactions for the H_2/Au system[145] and for H_2/Ag a recent study predicted non-adiabatic effects dependent on the methodology used[137]. In contrast is the H_2/Cu system seen as a model for adiabatic behaviour[146–149].

7.4 Studied Systems

The systems studied in this work are H_2/Cu(111), H_2/Cu(211) and H_2/Au(111). Each is surveyed for the three isotopologues H_2, HD and D_2, respectively. The three surfaces were chosen for dedicated purposes, as described below.

7.4.1 Copper

Because the H_2 dissociation on metal surfaces is considered simple in many regards, the H_2/Cu(111) reaction has achieved the status of a benchmark system, investigated in many theoretical[112,150–175] and experimental[87,90,117,121,176–194] studies. The main advantages of this system are the small, closed-shell gas phase molecule, the well ordered surface structure of a single crystal lattice and the proposed adiabacity of the reaction[146–149].

The experimental studies cover desorption studies[90,121,176,177,182,189–193,195], which are related to the activated adsorption process via the principle of detailed balance[73,90,118,126,175],

as well as direct adsorption measurements[121,178–180,195]. Desorption experiments differ in the way the hydrogen is supplied to the surface and accordingly in the temperature range studied, which is elaborated in section 8.2.2.

Due to the large number of available studies, the knowledge of the dynamics in the dissociative adsorption of hydrogen on copper is quite comprehensive. Detailed, quantum state specific information on the reaction probability in the zero coverage limit and its dependence on various conditions is available[117,121,179,182,185,186,189,190,192,196]. The increase in sticking probability with kinetic energy is quantified[117,175,185,189] as well as the dependence on alignment[190–192].

The role of vibrational excitation of the impinging molecule is also quantitatively understood[117,155,159,161,166,167,175,179,180,185,187,189,194,195]: the elongation of the molecular bond is directly connected to the reaction coordinate of dissociation. Rotational excitation has a more complex influence on the reaction probability[155,170,185,189,191]. Briefly, as J is increased from 0, the rotation of the molecule initially hinders the dissociation; this is understood as an alignment effect: the molecule is not able to align to the minimum energy path, which shifts the dynamical distribution of barriers to higher energies[185,189,190,193,197].

It was shown that the further increase of the rotational energy ($J > 5$) leads to a reduction of the barrier distributions. Due to the induced bond elongation at the transition state the rotational energy can couple to the reaction coordinate and reduce the barriers to reaction. This effect of alignment at low rotational states was captured partly in calculations by Darling and Holloway[155] using reduced dimensionality, but not in more recent adiabatic theoretical works[167,175].

There is a claim that the barriers of the hydrogen-Cu(111) reaction is described in the limit of "chemical accuracy"[70,167,175] (see section 8.1.4). But there is still a disagreement between experiment and theory for the reaction probabilities at high kinetic energies as well as for the desorption energies found in several experimental studies[176–178,185,193]. Also, in 2014 the study of Nattino et al.[175] aimed to compare their theoretical results for D$_2$/Cu(111) to permeation experiments of Michelsen et al.[182,185]. During their cooperation the authors realized errors in the original permeation data analysis program, which led to complications and errors in the results on the same order of magnitude as the accuracy of the theory. Thus, this work aimed to provide experimental data with an improved accuracy as new benchmark for this system.

An additional question is posed by the reactivity at surface step sites and defects. Calculated reaction barriers for defect sites[198] on copper's (111) and (211) facets strongly suggest that the reactivity on these surfaces is dominated by defects altogether, while experimental evidence[178,189] points into another direction. In contrast to that, it was shown for hydrogen adsorption on stepped platinum surfaces[101,199], that the reaction mechanism depends on the surface site. This allowed the decomposition into separable, site-dependent mechanisms[200] and the quantitative prediction of reactivity depending

on the step and defect densities of several surface facets. In order to determine whether similar effects occur in the highly activated H_2/Cu system, crystals with the (111) and (211) facets are studied here.

7.4.2 Gold

The dissociative chemisorption of gas phase hydrogen on gold surfaces is subject of current research, since it addresses several interesting topics. One is the high barrier to reaction predicted by theory [97,112,201], presenting a fundamental test for the semi-empirical specific reaction parameter (SRP)-DFT method (see section 8.1.1), to determine if it is applicable to predict other systems. Providing such a benchmark dataset is one of the immediate goals of this study. So far, only desorption barriers from adsorption and temperature programmed desorption (TPD) off polycrystalline gold films [202,203] and TPD of Au(111) [204] have been reported. An experimental, quantum state resolved dataset as for H_2/Cu(111) is not available.

The most recent predictions by Wijzenbroek $et\ al.$ [201] include quantum state specific reaction probability curve (RPC) for both H_2 and D_2. The minimum barrier height for reaction is found to be significantly larger (1.25 eV) than for H_2/Cu (0.49 eV [167]). Furthermore, their results are analyzed in terms of rotational and vibrational efficacies (see section 8.3.3.5), which are also found to be higher than for H_2/Cu. Surprisingly, in these results the rotational alignment effect found for H_2/Cu for ($J < 5$) (cf. section 7.4.1) is not apparent in the H_2/Au system. Wijzenbroek $et\ al.$ performed their calculations for a perfect crystal lattice in the 0 K limit as well as an estimate of the effect of the Au(111) surface reconstruction (see section 8.2.1).

In addition, non-adiabatic effects have been proposed to play a role in the reaction by DFT calculations from Takagi $et\ al.$ [145], while Wijzenbroek $et\ al.$ found no such hints [201]. Experimental evidence for non-adiabacity in hydrogen interaction with gold has also been found and was presented in section 7.3. Clearly, experimental data is needed to further investigate this system.

Chapter 8

Methods

This chapter is subdivided into three main sections, with the first dedicated to modern theory methods applied to describe gas-surface reactions. In the second section, descriptions of experimentally necessary concepts are introduced. Finally, the third section elaborates the methods for analysis of experimental data.

8.1   *Ab Initio* Model for Gas-Surface Interaction

For some gas-surface systems, modern *ab initio* based theory is on the verge of describing interactions quantitatively. Such sophisticated models need to be validated by comparison to experimental results, as acquired in this work. The following subsections give a brief summary of this topic.

8.1.1   Specific Reaction Parameter Functional

Molecular reactions on metal surfaces are best described using DFT with functionals relying on a generalized gradient approximation (GGA) to describe the electronic structure[160,205]. Widely used functionals to describe molecule-metal interactions have been Perdew and Wang 91 (PW91)[206,207], Perdew-Burke-Ernzerhof (PBE)[208] as well as revised Perdew-Burke-Ernzerhof (RPBE)[209]. An improvement in accuracy has been achieved by implementation of the SRP. This semi-empirical method was originally developed by Truhlar and coworkers[210] to describe gas phase reactions. Transfer of this approach to gas-surface interactions was successfully demonstrated by Díaz *et al.*[167] for the highly activated H_2/Cu system. In contrast, the SRP approach has not yet been successfully applied to H_2/Ru or H_2/Pd[70].

The SRP expresses the exchange correlation by a weighted average of two chosen density functionals. Then, the exchange correlation (E_{XC}) of the SRP functional is defined as[167]:

$$E_{XC}^{SRP} = x \cdot E_{XC}^{F1} + (1 - x) \cdot E_{XC}^{F2}, \tag{8.1}$$

where x is the adjustable SRP, E_{XC}^{F1} and E_{XC}^{F2} are the exchange correlations of previously chosen functionals. In the first implementation of this approach[167], the SRP was composed of RPBE as $F1$ and PW91 as $F2$. In order to yield a good model for the H_2/Cu(111) system, this SRP was adjusted to best describe experimental[182,185] sticking of D_2 from a molecular beam on Cu(111), at a surface temperature of 120 K. With $x = 0.43$, the resulting "SRP43" functional was found to describe experimental reaction probabilities within "chemical accuracy" (cf. section 8.1.4). This approach was refined later[170] by replacing PW91 with PBE as $F2$, thus yielding a SRP of 0.48 and improving the agreement.

8.1.2 Dimensionality of Calculations

The high computational cost of quantum mechanical calculations requires the reduction of the dimensionality of complex systems. Dependent on the number and severity of assumptions, calculations are accelerated at the expense of quality and accuracy of the results.

Starting from the full quantum mechanical treatment of the Schrödinger equation, the first and most successful simplification is the BOA, which separates the motion of electronic degrees of freedom from those of the nuclei. This allows the treatment of the nuclear motion with classical mechanics, as is done by *ab initio* molecular dynamics (AIMD). Here, the relevant forces of the system are computed on the fly[211,212], allowing to pursue molecular dynamics in small time steps and with high accuracy.

Further reduction of the complexity of the system is achieved by introduction of accurate potential energy surfaces (PESs) obtained by DFT methods. The main complexity in this approach is the construction of the PES, on which the molecular dynamics are carried out afterwards. This reduces the computational cost for the molecular dynamics greatly, which allows to a huge amount of simulations to be carried out with little additional effort. Besides, other approximations can be employed, for example the quasi-classical trajectory (QCT) method[213], where the zero point vibrational energy is added to the system (e.g. ref. 175,201).

An even stronger approximation is the Born-Oppenheimer static surface (BOSS) model[167,168], where the nuclear positions of the surface lattice are kept fixed. Usually, these positions have been obtained by preceding simulations of a slab: starting with the nuclei on their nominal bulk lattice positions at 0 K, they are allowed to relax in order to compensate for the surface energy. Moreover, in order to estimate thermal effects or the role of surface reconstructions, other positions have been applied as well (e.g. ref. 201). Using those fixed positions, the dimensionality for the PES is greatly reduced, which is often necessary considering the huge amount of atoms in gas-surface systems.

Despite many other approaches used in the field of gas-surface dynamics, it is referred to the corresponding literature, treating those in more detail (e.g. ref. 70,71).

8.1.3 Barrier Distributions

For calculations of activated adsorption processes (see section 7.2), a diatomic molecule approaching a single crystal surface and adsorbing dissociatively is examined. A first, most severe simplification when calculating a corresponding PES is the exclusion of molecular rotational and vibrational degrees of freedom. Considering only specific incidence conditions thus yields a PES from which a barrier to reaction can be obtained.

Now, the incidence conditions need to be averaged for all possible surface sites and initial molecular orientations, each giving a different energy barrier for reaction. These can be summarized in a "barrier distribution function" giving the obtained minimum reaction barriers as function of kinetic energy. The kinetic energy E_{kin} dependent reaction probability for the system is then derived by the classical hole model[214,215] from the barrier distribution function:

$$S(E_{\text{kin}}) = \int_0^{E_{\text{kin}}} N(E') \, \mathrm{d}E'.$$

(8.2)

The progression of this integration over the whole kinetic energy range yields the RPC of the system. In this model, several other assumptions are included. Only collision energy is available for the reaction, tunneling effects are neglected, and there is only a purely classical mechanism to overcome the barrier.

In the past, the first approximation of RPCs has mostly been of sigmoidal and symmetric form[79,117,182,185,189,193,194,216–219]. Theoretical descriptions on the other hand have demonstrated that symmetry is not intrinsic for the distribution of barriers[167,168,175,201]. Therefore, an improved description can be achieved by using more sophisticated functions and might even be necessary, as was shown for the D_2/Cu(111) system[175,193]. Thus, this section introduces several functions to describe the RPCs. Note that generally the RPCs are quantum state dependent and so are their parameters. For clarity, the notation has been simplified in this section. Furthermore, in this work the terms RPC and sticking function are used synonymously.

When no information of the shape of the barrier distribution function is available, it is often assumed to be of Gaussian shape. Then, for the RPC obtained from eq. (8.2) follows[175,218]:

$$S(E) = \frac{A}{\sqrt{\pi} \cdot W} \int_0^E \exp\left[-\left(\frac{E' - E}{W}\right)^2\right] \mathrm{d}E'. = \frac{A}{2} \cdot \left[1 + \mathrm{erf}\left(-\frac{E - E_0}{W}\right)\right].$$

(8.3)

Considering only kinetic energy to participate in the reaction, this error function (ERF)-form is the one historically applied most often (e.g. ref. 79,117,182,185,189,193,194,216–220):

$$S_{\mathrm{Erf}}\left(E_{\mathrm{kin}}\right) = \frac{A}{2} \cdot \left[1 + \mathrm{erf}\left(\frac{E_{\mathrm{kin}} - E_0}{W}\right)\right], \tag{8.4}$$

with three, ro-vibrational state dependent parameters: A, the saturation value, W, determining the width of the curve, and E_0 giving the point of inflection as well as the kinetic energy where $S\left(E_{\mathrm{kin}}\right)$ is half of the saturation value.

The asymmetric function applied by Nattino *et al.*[175] to analyze the D_2/Cu(111) data of Michelsen *et al.*[182,185] was the generalized logistic function (LGS):

$$S_{\mathrm{LGS}}\left(E_{\mathrm{kin}}\right) = A \Big/ \left[1 + \nu \cdot \exp\left(-\frac{E_{\mathrm{kin}} - E_0'}{W'}\right)\right]^{1/\nu}. \tag{8.5}$$

Here, the additional parameter ν determines the asymmetry of the curve. Due to this asymmetry, the parameter W' is not the same as W in eq. (8.4). Therefore, redefinition was necessary for comparison[175].

An even more flexible function is the five parameter curve (FPC), which was also introduced by Nattino *et al.*[175] and recently applied by Wijzenbroek *et al.*[201]:

$$S_{\mathrm{FPC}}\left(E_{\mathrm{kin}}\right) = A \cdot \exp\left[\frac{-\exp\left(-\frac{E_{\mathrm{kin}} - E_0'}{W'}\right)}{1 + \exp\left(-\frac{E_{\mathrm{kin}} - E_0''}{W''}\right)}\right]. \tag{8.6}$$

Again, the five parameters are similar but not equal to eq. (8.4). Their detailed meaning can be found in[175]. Only the amplitude factor, A, still gives the saturation value.

For fundamentally different systems, like hydrogen adsorption on stepped platinum surfaces, the reactivity needs to be described for several reaction pathways or channels. Groot *et al.*[101] were able to disaggregate the adsorption reactivity in the H_2/Pt system into three independent and additive channels: (1) direct reaction at defect sites (constant with E_{kin}), (2) reaction at terraces (linear increase with E_{kin}) and (3) reaction at steps. The reactivity of the last channel was found to decrease exponentially with E_{kin}:

$$S_{\exp}\left(E_{\mathrm{kin}}\right) = A \cdot \exp\left(-\frac{E_{\mathrm{kin}}}{\gamma}\right). \tag{8.7}$$

Here, A is the amplitude and γ a parameter tuning the decay with kinetic energy, the $1/e$ width. This reaction channel was found to depend on the step density[101] and such qualitative behaviour of the sticking function has also been explained by dynamical steering[101,221–225].

Furthermore, Poelsema *et al.*[99,100] studied H_2 adsorption on Pt(111) and found a dependence on the surface step density. They were able to assign a precursor-mediated mechanism to this dependence, where physisorbed molecules diffuse to reactive step sites. This mechanism was found to be competing with direct reaction at step sites and dependent on defect density and adsorbate coverage.

Carlsson and Madix[78] found an even more complex adsorption mechanism for methane on pre-covered Pt(111), which is based on the modified Kisliuk model[226]: the extrinsic precursor model. Here, a surface adsorbate creates a physisorption well for another adsorbate, which then diffuses to a reactive site.

Another system including several reaction pathways is the methane dissociation on iridium, where Dombrowski *et al.*[84] found a precursor-activated mechanism for vibrationally excited methane.

For now, it can be concluded that detailed studies are necessary to fully understand and describe the reactivity of adsorption. It cannot be easily determined if several reaction pathways coexist on a given surface[84,101], or if the barrier distribution function is just more complex than assumed[175,193]. In this study, the choice of sticking functions is based on the experimental data and described in section 8.3.3.1.

8.1.4 Chemical Accuracy

The term "chemical accuracy" is used in comparison of theoretically predicted reaction probabilities to experimental ones. In general, a theoretical description is considered chemically accurate, if the deviations to experiment are smaller than $1\,\text{kcal}\,\text{mol}^{-1} \approx 43\,\text{meV}$[167,168]. For these comparisons, the mean absolute error (MAE) is calculated.

When considering RPCs, as in this work, not the whole shape of the curve can be compared. Rather, specific representative points are considered. Assuming symmetric sigmoidal shaped functions to describe the sticking probabilities (see section 8.1.3), the point of inflection is one of the characteristic points of the curve, E_0 (see eq. (8.4)). In theoretical descriptions, this corresponds to the point where the sticking probability reaches half of the saturation value. In order to compare experimental to theoretical results, the deviation in kinetic energy for those respective points is taken as the MAE (e.g. ref. 167,168,175). This direct comparison is a severe oversimplification, since it ignores the symmetry considerations and various models to describe the RPCs elaborated in section 8.1.3. Another disadvantage follows directly from this consideration: the reactivity value to compare experiment with theory is completely arbitrary. Results depend on this parameter, which becomes a more serious problem the stronger both RPC descriptions deviate from each other.

8.2 Experimental Aspects

In this section, several experimentally relevant principles are elaborated. These include spectroscopic and geometrical aspects as well as methods and descriptions of the studied surfaces.

8.2.1 Crystal and Surface Structure

Copper and gold both crystallize within a face-centered cubic (fcc) unit cell. The layer stacking is described as ABC, i.e. that three layers are distinguishable by their lateral positions before the stacking is repeated. In the second layer the atoms are placed below half of the hollow sites of the first layer and in the third layer they are placed below the residual half. This results in two kinds of hollow sites: the hexagonal close packed (hcp) hollow site with an atom in the layer directly below, and the fcc hollow site with an atom in the second layer below. The surface facets studied here are described by the Miller indices (111) and (211). Schematic drawings are presented in fig. 8.1. The perspective views are from the top (panels (a) and (c)) and from the side (panels (b) and (d)). A (111) facet is shown in panels (a) and (b) and a (211) facet in panels (c) and (d). The unit cells of each surface are indicated in red. Additionally panel (c) shows the crystallographic directions parallel and perpendicular to the steps. In panel (b) the numbers indicate the "ABC"-layer structure with additional color coding used throughout fig. 8.1. Highlighted in panel (d) are the exposed microfacets: Terraces of {111} (blue), consisting of three rows of atoms, followed by a single {100}-step (green). The {111} terraces are tilted relative to the surface normal by 19.5° and the {100}-steps are tilted with approximately 35.3° relative to the surface normal.

An additional feature of the Au(111) surface is its well studied reconstruction[227–236]. Here, the ideal Au(111) surface is compressed by forming domains of $\left(22 \times \sqrt{3}\right)$ along the [110] direction. Alternating domains of the $\left(22 \times \sqrt{3}\right)$ reconstruction form a secondary structure termed "herringbone" or chevron phase, with a periodicity of ~30 nm[231]. Also, "u"-like[227] patterns have been observed.

The nature of reconstruction lifting under adsorption[235] and the energetics of the interaction with chemisorbed hydrogen atoms[236] are still subject of investigation. The enormous size of the reconstructed unit cell impedes DFT calculations, and reaction barriers for H_2 with the reconstructed Au(111) surface have been calculated only tentatively by Wijzenbroek et al.[201]. They obtained reaction barriers for certain sites by simulating a frozen lattice of the reconstructed surface, resulting in barriers increased by ~25–100 meV.

Due to the high sample temperatures necessary for permeation experiments, the thermal stability of the reconstruction needs to be considered. Surface pre-melting has been observed by Hoss et al.[237] at a transition temperature of (1070 ± 20) K using medium energy ion scattering (MEIS). Huang et al.[228] and Sandy et al.[229] utilized X-ray scattering and observed reconstruction lifting above 880 K, which results in a discommensuration fluid. Here, the discommensurations and kinks are disordered while the atomic positions themselves are well defined. Thus, the former reconstructed layer becomes an isotropically compressed phase. Watson et al.[233] also studied the Au(111) structure at high temperatures (480–1225 K) with X-ray scattering and obtained similar results.

Thermal evolution of a Cu(111) facet has also been studied using MEIS by Chae

et al.[238]. They observed changes in the attributes of the surface layer at elevated temperatures ($T \gtrsim 900\,\mathrm{K}$), such as an increase in the thermal expansion coefficient, interlayer spacing and changes in the vibrational amplitudes of the top layer. Evidence for surface pre-melting was not observed. Various attempts to simulate copper facets using molecular dynamics and effective medium theory (e.g. ref. 239–241) have been conducted with varying agreement to experiment. However, effects for surface facets less densely packed than (111): anharmonicity, vacancy-adatom formation, restructuring of micro facets and surface pre-melting. While no simulations were carried out for the Cu(211) facet directly, the thermal stability of the facets does scale with packing density, which predicts strong effects for the (211) facet.

8.2.2   Supply of Hydrogen to the Surface

Two methods have commonly been applied to provide hydrogen atoms to a surface for desorption experiments. One is permeation through the bulk of the sample (e.g. ref. 90,182,242,243), which has also been applied in this work and is described in detail in section 8.2.3. Briefly, this method is advantageous with regard to the continuous supply without interfering with the desorbing flux, therefore restricting the recombination reactions on the surface to the LH mechanism. The main disadvantage is the high sample temperature required ($\gtrsim 900\,\mathrm{K}$) to achieve measurable flux, impeding the comparability to theoretical work, which is usually restricted to low temperature or perfect crystal lattices.

In addition, quantitative comparisons between reaction rates for H_2, HD, and D_2 are not possible in post permeation desorption experiments, due to the varying permeation rate of the isotopologues. Also, deviations in sample manufacturing, like channel diameter or membrane thickness, render quantitative comparison between samples impossible. Only relative comparisons can be made, which is a severe drawback when the limits of quantitative theoretical predictions on surface facets of different metals are to be tested. On the other hand, the post permeation desorption approach benefits from the intrinsic restriction to the LH desorption mechanism and quantum state selective product detection.

Another viable method to supply H-atoms to the sample is by dosing the surface directly with atomic beam sources. This has been achieved by thermal dissociation of an effusive beam of H_2 (e.g. ref. 108,133), plasma or discharge driven dissociation (e.g. ref. 18,107) and H_2 dissociation at heated filaments (e.g. ref. 202,244). In principle, H-atom beams could be applied as well (cf. part I), but this method would require considerable experimental effort. A major disadvantage of H-atom dosing is the competition of ER and HA-ER abstraction reactions with the LH desorption. To exclude ER and HA-ER contributions, the H-atom beams are mechanically chopped on the µs timescale. This allows to separate LH desorption signals from other sources by temporal delay: ER based reactions are fast in contrast to LH reaction. Therefore, the delay between the end of dosing and the detection has to be long enough for clear separation, but short enough to

obtain significant signal. The residence time of atoms on the surface depends on the surface temperature, which allows the probing of a range of intermediate ones ($\sim$300–900 K)[193].

8.2.3 Permeation Theory

A general description of hydrogen permeation through metals is given in a review by S. A. Steward[245]. In this section, the fundamental assumptions presented by Steward are summarized briefly and relevant quantities for the systems studied in this work are given. Diffusion is considered as starting point for the quantitative characterization of the permeability of hydrogen through solid materials. The diffusion flux J_{diff} along a spatial concentration gradient $\partial c/\partial x$ is given by Fick's first law:

$$J_{\text{diff}} = -D_{\text{diff}} \cdot \frac{\partial c}{\partial x}, \tag{8.8}$$

with the material dependent constant D_{diff}. The concentration of a gas in another medium can be related to the pressure above the given solution, which is described by Henry's law. Considering molecules which dissociate upon dissolution, like hydrogen uptake in metals, requires a varied version, Sievert's law:

$$S_{\text{diss}} = \frac{C_H}{\sqrt{p_{H_2}}}, \tag{8.9}$$

with the proportionality constant S_{diss}, which is referred to as solubility. Equation (8.9) can be inserted in eq. (8.8). Successively assuming a constant gradient over the whole metal membrane Δx allows expression of the flux-dependence on the total pressure difference, Δp_{H_2}:

$$J_{\text{diff}} = -D_{\text{diff}} \cdot S_{\text{diss}} \cdot \frac{\partial \sqrt{p_{H_2}}}{\partial x} \approx -D_{\text{diff}} \cdot S_{\text{diss}} \cdot \frac{\sqrt{\Delta p_{H_2}}}{\Delta x}. \tag{8.10}$$

Equation (8.10) is valid for systems in a steady state and with a constant concentration gradient over the length Δx. Further simplification can be achieved by definition of the permeability Φ as product of S_{diss} and D_{diff}, as well as by omitting the minus sign, since it is meant to determine the direction of the flux. To characterize a time-dependent flux $Q_{\text{perm}}(t)$ through a metal membrane with the area A, eq. (8.10) is modified to:

$$Q_{\text{perm}}(t) = J_{\text{diff}} \cdot A \cdot t = \Phi \cdot A \cdot t \cdot \frac{\sqrt{\Delta p_{H_2}}}{\Delta x}. \tag{8.11}$$

Differentiation now gives the steady-state flow rate, which can be measured to ultimately obtain the permeability:

$$\frac{\mathrm{d}\,Q_{\text{perm}}}{\mathrm{d}\,t} = \Phi \cdot A \cdot \frac{\sqrt{\Delta p_{H_2}}}{\Delta x}. \tag{8.12}$$

Table 8.1: Constants describing hydrogen permeation (cf. eqs. (8.11) and (8.13)) through several metals[245]. The values given for iron, copper and silver describe the permeation of H_2, while the ones for gold describe D_2.

Parameter	Iron[246]	Copper[247]	Silver[248]	Gold[249]
Φ_0 / $\mathrm{mol\,m^{-1}\,s^{-1}\,Pa^{-0.5}}$	4.1×10^{-8}	8.42×10^{-7}	2.21×10^{-7}	1.14×10^{-6}
E_Φ / K	4200	9290	10 440	13 800
T_{melt}[127] / K	1538	1358	1235	1337

Since S_{diss} and D_{diff} are temperature dependent, the permeability is also a function of temperature, which is first approximated by Arrhenius-like behaviour:

$$\Phi = \Phi_0 \cdot \exp\left(- E_\Phi / [R \cdot T] \right), \tag{8.13}$$

with a new quantity, the Arrhenius activation energy for permeation E_Φ, which is commonly expressed directly in units of temperature to omit the R from eq. (8.13). For several metals the quantities relevant for this work (Φ_0, E_Φ and melting temperature T_{melt}) can be found in table 8.1. Furthermore, simulated permeation fluxes are presented in fig. 8.2 for experimental conditions; i.e. a membrane thickness Δx of 0.3 mm and pressure difference Δp_{H_2} of 1 bar.

8.2.4 Velocity Measurement of Ions

In this work, information from desorbing hydrogen molecules is acquired. This includes their quantum state as well as their kinetic energy distributions, and the methodology to obtain the latter is described in the following subsections. It is pointed out, that a fundamental requirement for determination of the kinetic energy of a molecule is a collision-free environment preventing energy transfer between particles. Generally, this is achieved by conducting experiments under vacuum conditions.

8.2.4.1 Experimental Methods

Several methods to determine particle velocities are viable. They vary widely in their (dis-) advantages. However, most methods include TOF measurements after transversing a certain distance. They differ only in the way in which the start and end time points are marked. For streams of neutrals, mechanical chopping at two positions (e.g. ref. 72) with successive detection has been applied. Quantum state resolved detection has been achieved by laser ionization, also marking the starting time point for this ionized subset of molecules. The end time point is generally coupled with ion detection, this allows direct TOF determination. This method has been demonstrated in two variants: the first leaves the velocity distribution unaltered by having the ions drift in an electric field-free environment (e.g. ref. 91,182); the second uses a weak and well defined extraction field (e.g. ref. 108,250).

Both methods require the transformation of the obtained TOF into a kinetic energy distribution. The ion extraction variant requires profound knowledge of the field parameters and distances for this transformation, as well as careful subtraction of the background, since ions will be detected irrespective of their initial flight direction. The field-free drift method applied in this study requires only two parameters for the transformation (cf. section 8.2.4.2), but suffers from a disadvantageous Jacobian. The inverse quadratic relationship between kinetic energy and TOF of the ions results in a strong dispersion of the sampling rate. Low kinetic energy ions are stretched over long TOF intervals, lowering the total detection amplitude and therefore decreasing the signal to noise ratio (SNR). In contrast, higher energy intervals are compressed to a small TOF range by sacrificing resolution for signal intensity. Additionally, slow ions spend longer times in the drift region, this results in increased effects of distortions on them. This is treated extensively in section 8.2.6.2.

8.2.4.2 Free Ion Drift

All results presented in this study rely on measuring the TOF distributions of ions drifting in a nominally field-free environment. This subsection presents the fundamentals of the transformation to obtain the kinetic energy from TOF measurements.

In the setup presented here, particles with an initial velocity distribution are ionized inside a non-perturbing environment, the Faraday cage assembly (FCA) (see section 9.1.1.6). For all these ions, the distance to the exit of this FCA is the same. Accordingly, this drift length in the FCA x_0 is the first relevant parameter, which varies with the actual ionization position and drift trajectory. From the initial velocity of a particle, v_p, the TOF, t', results simply as: $t' = x_0/v_p$.

As soon as an ion exits the FCA it is accelerated by an electric extraction field and directed onto an ion detector. For traversing this ion optic setup a certain TOF is needed, which results in an offset in the obtained TOF distribution. If the potential of the extraction is significantly larger than the initial kinetic energy of the ions, this time becomes independent of the latter and therefore constant. This constant TOF of ions in the detection setup t_{shift} is the second relevant parameter and allows the TOF inside the FCA to be obtained from the measured one, t, by: $t' = t - t_{\text{shift}}$. How these parameters x_0 and t_{shift} are obtained is described in section 8.2.4.3.

It is noteworthy that in the presented experiment the flux of neutral molecules is constant, and timing information is provided only due to the pulsed ionization of this flux. Therefore, the laser pulse duration (section 9.1.2) ultimately determines the time resolution of the setup. A description of the detection geometry is given in section 9.1.1.9.

8.2.4.3 Calibration Methods

In order to determine the kinetic energy of the drifting particles, the TOF axis had to be calibrated to translate accurately into velocity. Generally, this is achieved by measuring a known velocity distribution which allows to obtain corresponding calibration parameters.

Here, these are (see section 8.2.4.2) x_0 and t_{shift}. While x_0 varies with the exact laser focal position, t_{shift} is constant in first approximation. Actually, the t_{shift} parameter is independent of the initial kinetic energy of the ions, but it varies with the mass-to-charge ratio (m/z). Here, as reference for scaling the t_{shift} of H_2 is used:

$$t_{\text{shift}} \left(m/z \right) = t_{\text{shift}}^{H_2} \cdot \sqrt{\frac{(m/z)}{(m/z)_{H_2}}}, \tag{8.14}$$

with $t_{\text{shift}}^{H_2} = (3.2 \pm 0.1)\,\mu s$ for $(m/z) = 2$ amu, determined as described in section 8.2.4.3.

Knudsen A Knudsen cell was used to generate thermal Maxwell-Boltzmann distributions (MBDs) for calibration purposes. For each new build of the FCA and laser alignment, a sophisticated calibration dataset was acquired, including H_2 and D_2 TOF traces over a wide temperature range (~300–840 K). In this dataset, variations in the laser alignment and ion optics setup were negligible. Also, the assumption of no variation in FCA conditions - despite the necessary changes in the thermal environment - allows the analysis of this dataset by fitting the distributions with global parameters. The fitting procedure is described in section 8.3.2.1 and results are presented in section 10.1.1. Such a sophisticated fit is very constrained because it results in reliable parameters which were taken as "nominal" values describing the current setup. This model considers the velocity-dependent detection technique (section 8.3.4) and assumes a thermal, one-dimensional MBD from the Knudsen source. This yields the expected signal as function of the TOF t and the source temperature T_K, as:

$$I(t, T_K)\,\text{d}t = k \cdot \left(\frac{x_0}{t - t_{\text{shift}}} \right)^4 \cdot \exp \left(-\frac{m}{2 \cdot k_b \cdot T_K} \cdot \left[\frac{x_0}{t - t_{\text{shift}}} \right]^2 \right) \text{d}t, \tag{8.15}$$

with k as normalization constant and t_{shift} from eq. (8.14).

In contrast to the sophisticated method, daily calibration measurements were carried out only at a single temperature for H_2 and D_2, before and after the permeation experiment, respectively. Fitting these gave the calibration parameters, including the "cutoff" (see section 8.2.6.2). Comparison of those to the nominal values allowed the judgement of the status of the FCA. If the deviations were too severe, a new FCA had to be constructed.

While this probing of the "cutoff" is an advantageous property, which provides further information of the setup, the MBD method also has downsides. Most prominent is the deviation of the kinetic energy range from the one observed in the current permeation

experiments. A second disadvantage arises from the employed experimental method to detect the particles, relying on quantum state resolved ionization (cf. section 8.2.5.2). When the laser system is adjusted for detection of vibrationally excited hydrogen, it is not feasible to also detect ground state hydrogen at the same time. The high vibrational energy of hydrogen (appendix C) in combination with the thermal state population produced in the Knudsen cell makes a calibration under these conditions impossible. Therefore, another method is presented below.

Internal Calibration Standard   As noted above, calibration parameters are obtained by comparison of measurements to known TOF distributions. Because the Knudsen cell method (section 8.2.4.3) relies on thermal MBD, it cannot be used when the ionization laser is set to detect vibrationally excited hydrogen molecules. Fortunately, the range of both laser setups (section 9.1.2) covered the D_2 $(v = 1)$ $J-$sequence and thus allowed the designation of D_2 $(v = 1, J = 2)$ as "reference" state with its resonance at ~207.5 nm. Desorption data recorded from this reference were analyzed quantitatively according to the detailed balance model (section 8.3.1.2), i.e. RPC parameters (see section 8.3.3.1) were obtained carefully, using a Knudsen-calibrated setup.

This set of parameters allowed to employ this desorption distribution as new calibration standard. Keeping the permeation setup under the same conditions, the TOF distribution was acquired successively by using the second laser setup. Fitting these TOF distributions while keeping the detailed balance parameters fixed, required the variation of x_0 and the total amplitude only. Because the cutoff function (section 8.2.6.2) has negligible influence on the desorption data, this calibration methodology turned out to be reliable.

A disadvantage of this method is the sample and condition dependence of this internal calibration standard. For each sample surface, this had to be acquired carefully and under the same permeation conditions, e.g. surface temperature and sample position. Furthermore, this method did not permit the verification of parameters for the cutoff function, but enabled the acquirement of desorption data without the need of a Knudsen cell for calibration.

Independent t_{shift} Measurement   To measure the t_{shift} parameter independently, the extractor tube was equipped with a voltage switch (see section 9.1.1.7). When switching the extractor tube from ground to the extraction voltage several µs after the laser shot, the fastest ions had already left the drift region and entered the - still field-free - section between the FCA and the extractor. Upon switching, those were accelerated immediately. This resulted in a sharp initial peak in the measured TOF distribution, while the distribution of the particles still in the field free section was not disturbed. With several switch times and two hydrogen isotopologues (H_2, D_2), the velocity independent t_{shift} for each isotopologue was obtained (see section 10.1.4.1) by using this "delayed extraction" method. The ratio

Table 8.2: Nuclear spin statistical weights of hydrogen isotopologues.

$g_{ns}(J)$	$\mathbf{H_2}$	$\mathbf{HD}$	$\mathbf{D_2}$
$J = \mathbf{even}$	1	1	2
$J = \mathbf{odd}$	3	1	1

of those values was found to be consistent with the expected one scaling with mass to charge ratio, as given in eq. (8.14).

Accompanying simulations of this procedure are presented in section 10.1.4.2. The experimental results in section 10.1.4.1. This method to obtain a value for t_{shift} independent of other calibration parameters allowed the constrained fitting of the calibration data. Therefore, this method is more reliable than fitting $t_{\text{shift}}^{\text{H}_2}$ and $t_{\text{shift}}^{\text{D}_2}$ independently[182,185].

8.2.5 Spectroscopy and Laser Principles

8.2.5.1 Hydrogen Spectroscopy

In order to calculate the ro-vibrational energy levels of the hydrogen isotopologues in their electronic ground state, it is sufficient to approximate the molecule as linear rotor, including centrifugal distortion and the inharmonic oscillator model. In this model, the relevant quantities are: T_{eq}, B_{eq}, a_{eq}, D_{eq}, w_{eq}, $w_{eq}x_{eq}$ and $w_{eq}y_{eq}$. Their meaning and the values for the electronic states relevant in this work are given in appendix C. For each rotation - vibration level, the energy relative to the minimum of the potential energy curve of the given electronic state is now calculated as[251]:

$$E(v, J) = G(v) + F(v, J),$$
$$G(v) = w_{eq} \cdot \left(v + 1/2\right) - w_{eq}x_{eq} \cdot \left(v + 1/2\right)^2 + w_{eq}y_{eq} \cdot \left(v + 1/2\right)^3, \qquad (8.16)$$
$$F(v, J) = \left[B_{eq} - a_{eq}\left(v + 1/2\right)\right] \cdot J\left(J + 1\right) - D_{eq} \cdot J^2\left(J + 1\right)^2.$$

These energy levels are used for the calculation of Boltzmann population distributions (see section 8.3.3.3) and for REMPI transitions (see section 8.2.5.2).

Furthermore, the $^{ortho}/_{para}$ ratio of hydrogen is dependent on the nuclear spin statistical weight (g_{ns}) presented in table 8.2[251].

8.2.5.2 Resonantly Enhanced Multi-Photon Ionization

Quantum state selective ionization of hydrogen isotopologues is conducted using (2+1) REMPI in the wavelength range ~200–220 nm[252–256]. As applied in similar works, this transition utilizes the E,F $^1\Sigma_g^+$ double-well state for the resonant two-photon step[182,185,189,193]. In this study, only Q-branch transitions are probed:

E,F$^1\Sigma_g^+$ $(v' = 0, J'' = J') \leftarrow$ X$^1\Sigma_g^+$ (v'', J'').
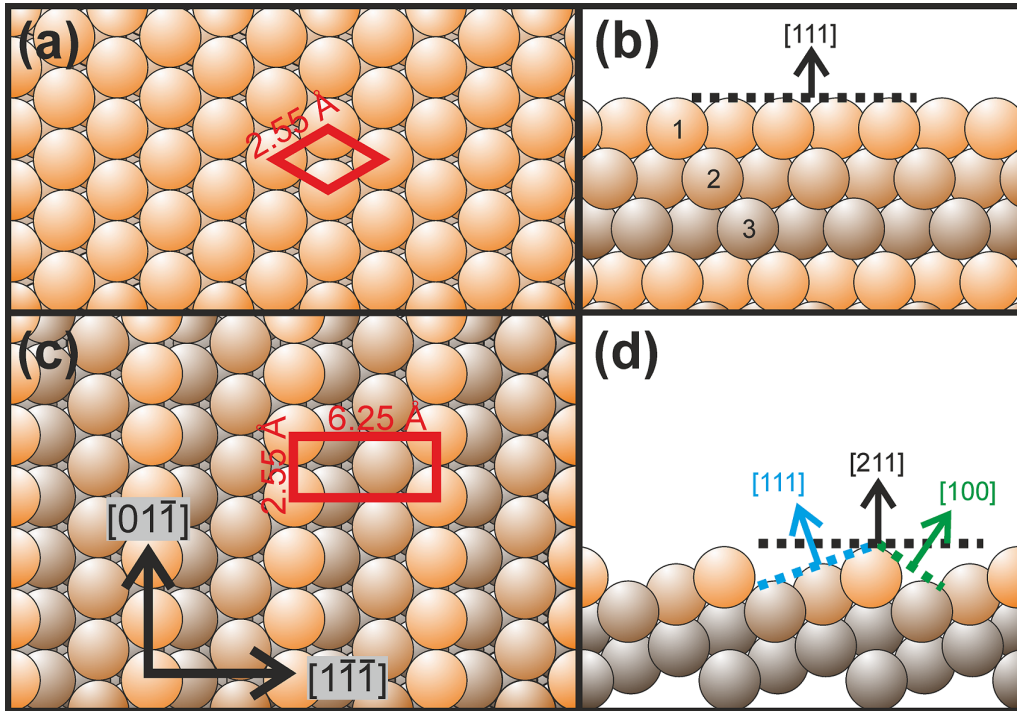
Figure 8.1: Schematic drawings of the crystal structures investigated in this study. The panels show the hard sphere models of a fcc (111) (panels (a) and (b)) as well as a fcc (211) facet (panels (b) and (c)). Panels (a) and (c) give a top view while (b) and (d) give a view of the side for the corresponding facets. The color of the spheres reflects the surface layer, from orange (1st) over brown (2nd) to dark brown (3rd). Gray spheres in panels (c) and (d) represent lower layers. The unit cells are indicated in red in panels (a) and (c). Highlighted in panel (b) by the numbers is the "ABC" layer structure of the fcc crystal lattice. Additionally shown in panel (c) are the crystallographic directions parallel and perpendicular to the steps. Panel (d) indicates the microfacets exposed on the surface: The {111}-terrace (blue) is tilted by approximately 19.5° to the (211) surface (black), while the {100}-step is tilted by ~35.3° (green) in the other direction.
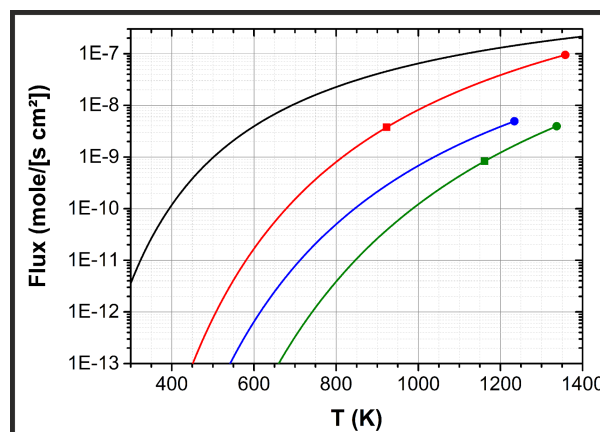
Figure 8.2: Temperature-dependent permeation fluxes of several metals simulated by using eq. (8.12) and assuming experimental conditions of a membrane thickness of 0.3 mm and a backing pressure of 1 bar. The filled circles mark the melting point of each metal and the filled squares the operating conditions used in this work. The colors correspond to the different metals: iron (black), copper (red), silver (blue) and gold (green).

Transition frequencies from Pomerantz *et al.*[255] were verified for the current setup using a wavemeter, which allowed the reproducible adjustment of the laser to the transition maximum. Transition line strength factors were also taken from Pomerantz *et al.*[255]. For the laser power dependence, saturation effects in the multi photon ionization (MPI) had to be considered. As shown for Gaussian beams focused by spherical lenses, a ¾ power law should be yielded[257], which results from the double-cone shape of the extended focal volume. In the current laser setup, measurements showed this power dependence as well[56] despite the deviation of the obtained laser focal volume (see section 8.2.6.3).

8.2.5.3 Gaussian Beams

A description of focal volumes in the Gaussian beam approximation was already given in part I, section 2.1. The experimental determination of Gaussian beam parameters has been demonstrated using mechanical choppers[258], movable slit apertures[259], optical fibers[260] and classical razor or knife edges[261–263]. Here, Gaussian beam shapes (cf. part I, section 2.1) are assumed which are separable into the horizontal (x) and vertical (y) transversal directions. The beam shape is described along the longitudinal (z) direction by the relative distance z to the beam waist or focal position z_0. The beam radius $w(z)$ is then given as:

$$w(z) = w_0 \cdot \sqrt{1 + \left(\frac{z - z_0}{z_R}\right)^2}, \tag{8.17}$$

with the beam radius at waist / focus position w_0 and the Rayleigh length z_R. Experimentally, $w(z)$ values are determined by the knife edge method, which has several advantages. It can be applied to both transversal directions separately, is easy to execute, works for all wavelengths and requires no expensive hardware. This method entails measurements of the total beam intensity behind the focus, while a razor edge is moved into the laser beam along one transversal direction and cuts away a fraction of the beam (e.g. ref. 261–263). The measured intensity is then given by the integral over the Gaussian beam up to the knife edge position, which is given by the ERF. Assuming the knife edge thickness to be smaller than z_R, no broadening should occur. Additionally neglecting interference effects, the measured intensity I is given as function of the knife edge position in horizontal direction x_{edge}, beam center in horizontal transversal direction x_c and total intensity I_0:

$$I\left(z, x_{\text{edge}}\right) = \frac{I_0}{2} \cdot \left[1 + \text{erf}\left(\frac{x_{\text{edge}} - x_c}{\sqrt{2 \cdot w(z)^2}}\right)\right]. \tag{8.18}$$

From such measured $I(z)$ distributions all focal parameters can be obtained by fitting eqs. (8.17) and (8.18), respectively. Measurement and analysis are analogue for the vertical beam direction. With this method, the focus of the REMPI laser beam (see section 9.1.2)

was characterized and the results are presented in fig. 8.3 and table 8.3. While the focal parameters are on the order of magnitude expected for a dye laser beam and differ only little for both transversal directions, a very strong astigmatism was found. The focal planes of the horizontal and vertical plane were offset by (25 ± 2) mm from each other.

Using the obtained parameters within the Gaussian beam approximation, a full three dimensional description of the laser beam can be given. Here, values are indicated for the horizontal direction by the superscript ^{x} and for the vertical direction by ^{y}, respectively. The model description follows as:

$$
w(z)^x = w_0{}^x \cdot \sqrt{1 + \left(\frac{z - z_0{}^x}{z_R{}^x}\right)^2},
$$

$$
w(z)^y = w_0{}^y \cdot \sqrt{1 + \left(\frac{z - z_0{}^y}{z_R{}^y}\right)^2}, \tag{8.19}
$$

$$
I(x, y, z) = \left[\frac{I_0}{w(z)^x + w(z)^y}\right] \cdot \exp\left[-2 \cdot \left(\left[\frac{x_{\text{edge}} - x_c}{w(z)^x}\right]^2 + \left[\frac{y_{\text{edge}} - y_c}{w(z)^y}\right]^2\right)\right].
$$

A visualization of the resulting spatial beam profile is presented in fig. 8.4, panels (a) and (e). Also given is a simulation of the same model without the offset of focal planes for comparison (panels (b) and (d)). Clearly, the intensity profiles for the center of the beams (panels (a) and (b)) show strong perturbations for the actual beam, with only little variation of the main intensity over several mm. This allows the anticipation of perturbation effects for the TOF distributions.

In conclusion, the spatial intensity distribution of the dye laser beam is best approximated by a long cylinder. Consequences for TOF measurements in this work are described in detail in sections 8.2.6.3, 9.1.1.9 and 10.1.5.

8.2.6 Aberrations in Time-of-Flight Distributions

As stated in section 8.2.4.3, several effects could distort TOF distributions. The following sections give an overview of the most relevant for this study.

8.2.6.1 Space Charge

Since the TOF method relies on field-free drift conditions after laser ionization, space charge effects can severely alter the distributions. The ions are generated in the laser focal region and therefore in a relatively small volume. Furthermore, in this study D_2 is the molecule with the highest mass. But with a D_2^+ mass to charge ratio of $(m/z) = 4$ amu it is still more susceptible to electric forces than most diatomic molecules.

The effect of space charge on the TOF distributions is shown in fig. 8.5, where D_2 Knudsen traces are shown. The conditions were chosen to operate close to the space charge
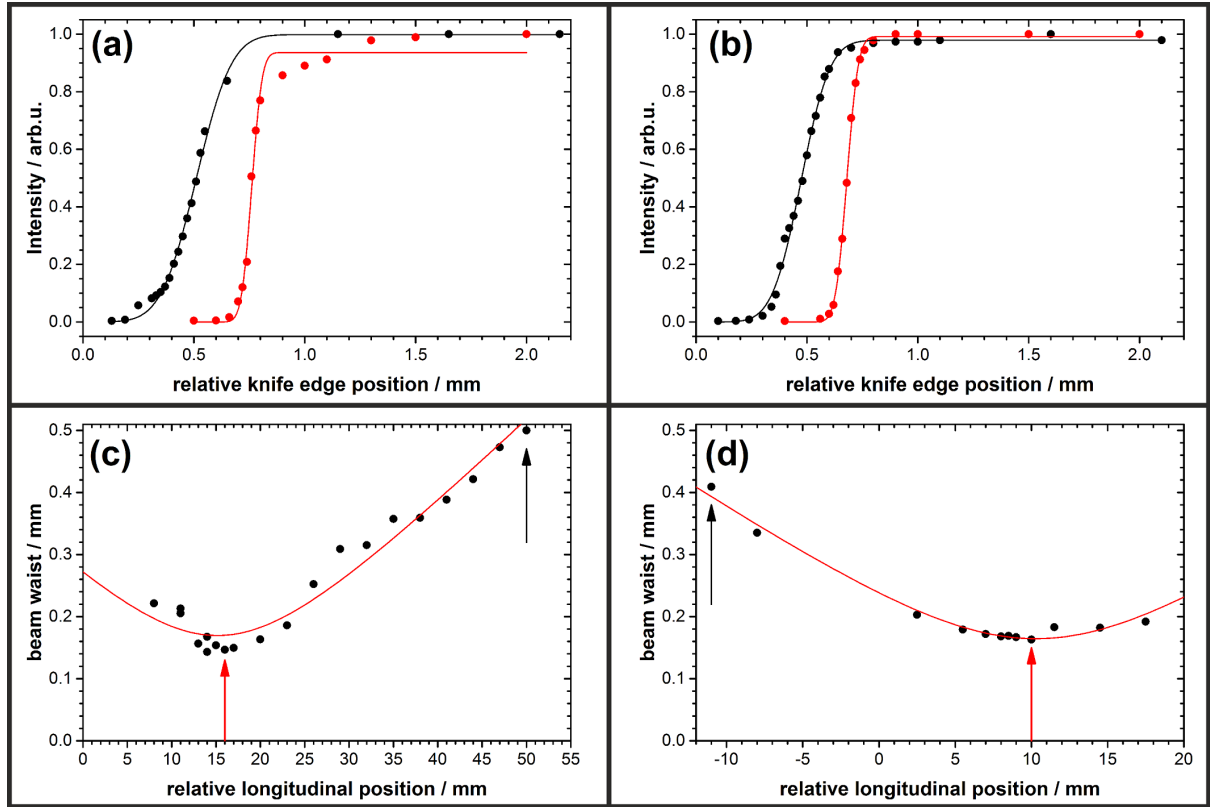
Figure 8.3: Measured Gaussian beam parameters using the knife-edge method. Panels (a) and (c) correspond to the horizontal, (b) and (d) to the vertical direction. Panels (a) and (b) show measured intensity data points and corresponding ERF-function fits (eq. (8.18)) for datasets near (red) and far away from the focus (black). The datasets are shifted in their x-coordinates for illustrative purposes. Panels (c) and (d) give the resulting beam waist parameters (points) for multiple measurements along the longitudinal beam axis, with arrows marking the datasets shown in panels (a) and (b). The x-coordinates are not on the same scale between panels (c) and (d). The red lines show fits of eq. (8.17) to the points. All results are presented in table 8.3.

Table 8.3: Parameters obtained from fits to the measurements of the REMPI laser focus shown in fig. 8.3 by using the knife-edge method.

Parameter	Value in mm	Shown in fig. 8.3 as	transversal direction
Distance to focus	34.8 ± 1.5	panel (a), black	horizontal (x)
Fitted $w(z)$	0.146 ± 0.016	panel (a), black	horizontal (x)
Distance to focus	0.8 ± 1.5	panel (a), red	horizontal (x)
Fitted $w(z)$	0.500 ± 0.018	panel (a), red	horizontal (x)
Distance to focus	21.3 ± 0.6	panel (b), black	vertical (y)
Fitted $w(z)$	0.409 ± 0.014	panel (b), black	vertical (y)
Distance to focus	0.3 ± 0.6	panel (b), red	vertical (y)
Fitted $w(z)$	0.162 ± 0.005	panel (b), red	vertical (y)
Fitted z_R	12.1 ± 1.1	panel (c), red	horizontal (x)
Fitted w_0	0.170 ± 0.008	panel (c), red	horizontal (x)
Fitted z_R	9.8 ± 0.5	panel (d), red	vertical (y)
Fitted w_0	0.164 ± 0.040	panel (d), red	vertical (y)

Figure 8.4: Simulated intensity distributions for Gaussian beams. Based on the determined properties of the dye laser beam (fig. 8.3, table 8.3) Gaussian beam assumptions were used to simulate the intensity-space profile along the propagation direction. Panel (a) shows the relative intensity in the center of the simulated beam, panel (b) the intensity of a hypothetical beam with the same parameters except the astigmatism. The space-intensity profiles of those beams are given in the sequences shown in panel (e) and (d), with the intensity legend given in panel (c). The single graphs in both sequences are shown for the propagation points indicated by red dots in panels (a) and (b), in the order from top to bottom. In each sequence, the left hand graphs give contour lines and the right hand graphs perspective views. The length axes reach from -0.5 to $+0.5$ mm in all cases.
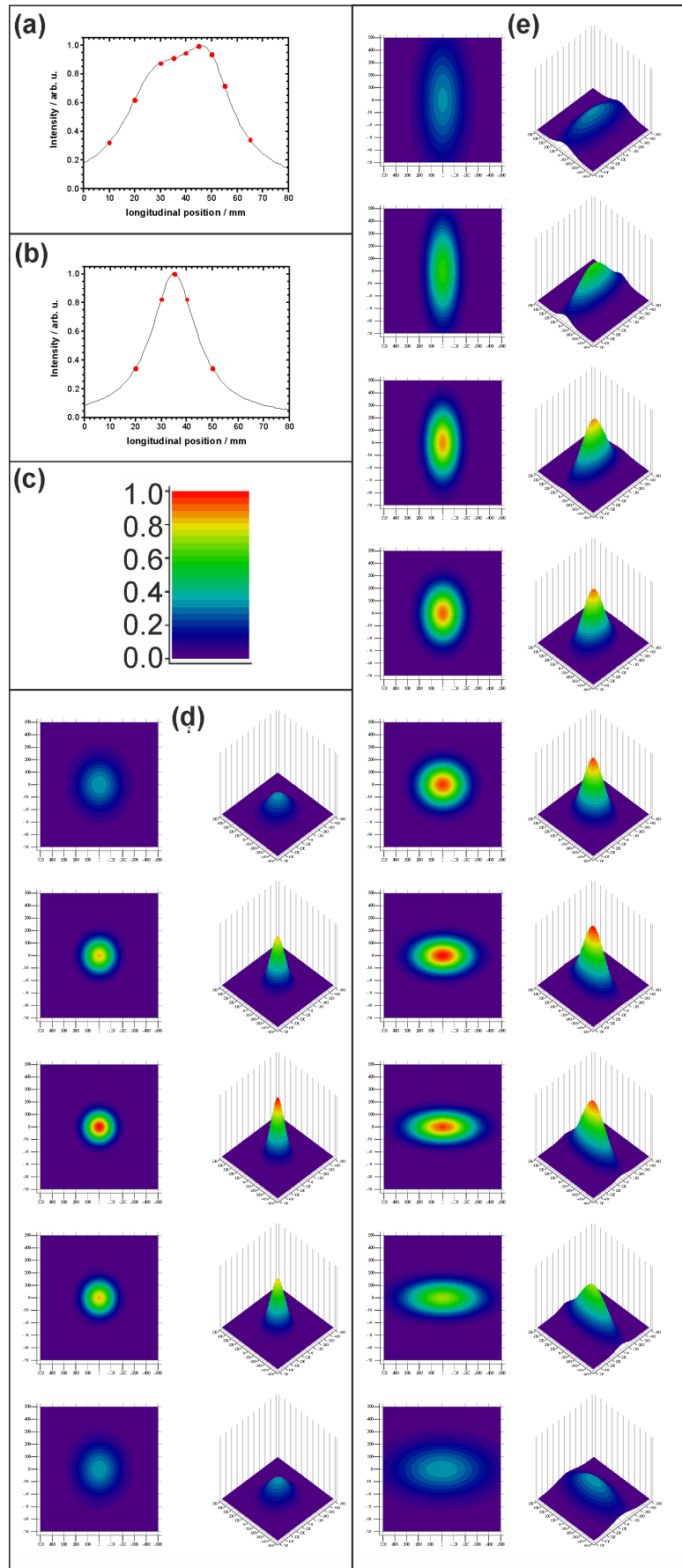
limit and traces without further data processing are shown. For each trace, the laser is tuned away in steps from the transition resonance (black), to reduce the total number of ions generated by the pulse. This detuning reduces the space charge effect, which is clearly apparent for traces near the resonance (black, red, blue) and yields distributions which are distorted and shifted to shorter TOF. Reducing the total number of ions further leads to distributions which are less disturbed (green, brown) until the expected distribution is obtained (orange). By calculating the average number of ions generated per laser pulse, an absolute limit was determined under which no space charge effects were apparent. This limitation was checked for each acquisition, so that effects on the measured data could be excluded.
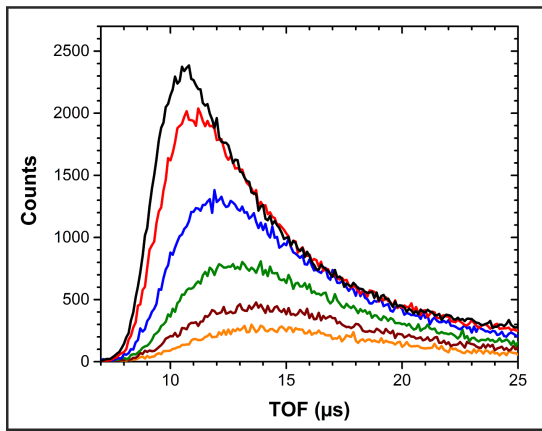
Figure 8.5: Illustration of Space Charge Effects on TOF distributions. Knudsen TOF distributions without any data processing are shown. The conditions are the same for all traces, only the laser frequency was changed for each trace. Starting on the resonance of the transition (black), the frequency was detuned increasingly (in the order: red, blue, green, brown, orange). This resulted in a reduction of the total number of ions generated by each laser pulse. With increasing ions per pulse not only the signal intensity is higher, but the TOF distributions become more strongly disturbed. Careful comparison to the expected distribution then allowed to determine the limit, at which space charge effects become significant.

8.2.6.2   Cutoff Functions

Since the FCA cannot be perfectly field-free, distortions had to be taken into account. Fundamentally, ions with low kinetic energies are influenced more strongly by small electric fields and as a result may not reach the detector. In order to describe this effect, a "cutoff function" was included in the fitting procedure, which simply acts as an energy dependent scaling factor ranging between unity (no distortions) and zero (absolute depletion). Previously, such a cutoff has successfully been described in TOF, relying on a function form based on the hyperbolic tangent function[185]. This function relied on two adjustable parameters: the center of the function t_c, and a width t_w:

$$\text{Cutoff}(t_i) = 1 - \tanh\big([t_i - t_c]/t_w\big). \tag{8.20}$$

In this work, a function form is introduced which is dependent on the E_{kin} of the ions and also uses two adjustable parameters: a minimal kinetic energy for cutoff E_{min} required for the ions to be able to pass the FCA and a slope parameter for cutoff E_{slope} describing how fast the cutoff approaches zero with decreasing E_{kin}. This function is given as:

$$\text{Cutoff}(E_{\text{kin}}) = 1 - \exp\big(-E_{\text{slope}} \cdot [E_{\text{kin}} - E_{\text{min}}]\big) \ \mid \text{for } E_{\text{kin}} \geq E_{\text{min}}. \tag{8.21}$$
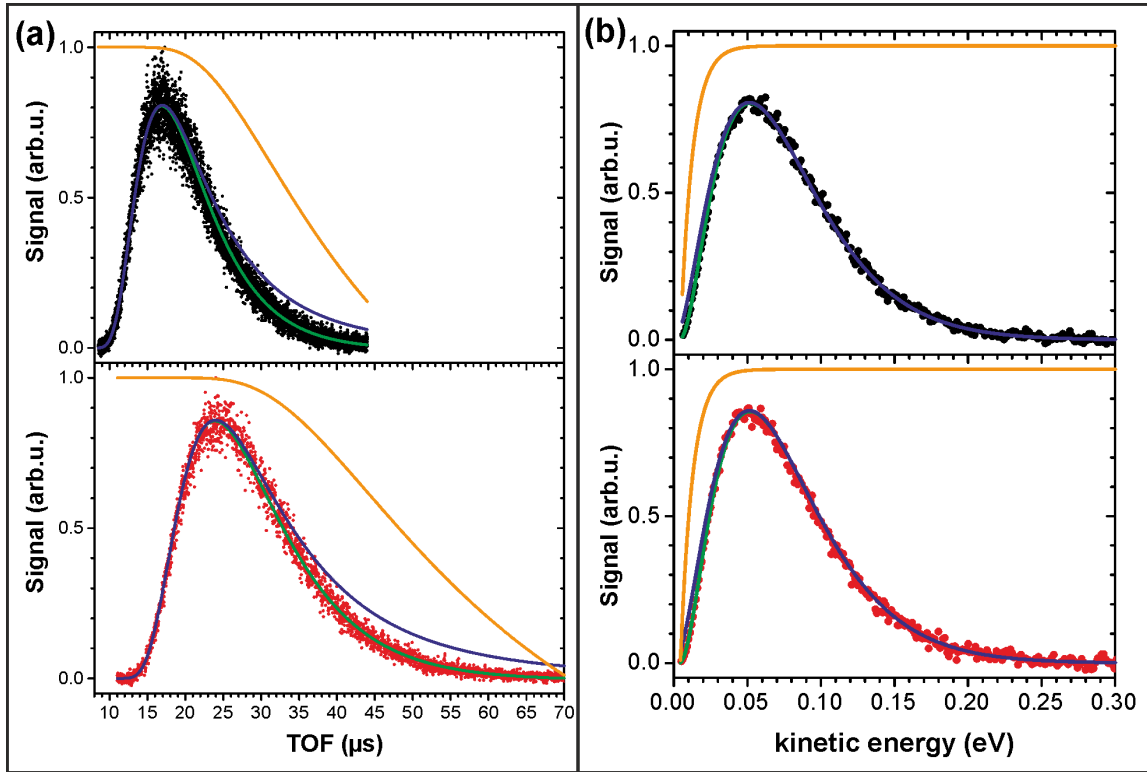
Figure 8.6: Instructive Knudsen cell traces used for calibration and comparison to the expected effusive TOF distributions at 298 K. Panels (a) show measured TOF distributions of H_2 (subpanel (i), black dots) and D_2 (subpanel (ii), red dots) at room temperature and the corresponding fits (green line) as well as the global cutoff function obtained (orange line). A hypothetical, unaffected effusion distribution is given by the blue lines. Panels (b) show the same datasets converted to kinetic energy scale. The obtained parameters are $E_{\mathrm{min}} = 4.4\,\mathrm{meV}$ and $E_{\mathrm{slope}} = 122.8\,\mathrm{eV}^{-1}$ for the cutoff function and $x_0 = 30.5\,\mathrm{mm}$ for the drift length.

An advantage of this function is the direct transferability to several isotopologues, which allows global - and therefore more reliable - fitting of several calibration datasets. Lacking a more sophisticated theoretical model, the functional form is still empirical, just as in eq. (8.20).

From the illustrative cutoffs shown in figs. 8.6 and 8.7 it is apparent, that the deviations generally do not extend to the energy range above 100 meV. In contrast, the desorption distributions from strongly activated systems exceed this kinetic energy region considerably and therefore are considered not to be biased in a significant way.

8.2.6.3 Laser Focal Volume

In this experiment the laser ionization generates the detectable ions via the REMPI technique (see section 8.2.5.2). Due to their non-linear intensity dependence, MPI processes are very sensitive to the spatial profile of the excitation radiation. Since high intensities are essential, the processes are often limited to a focal and adjacent regions[257]. Therefore, a laser focal volume as described in fig. 8.4 potentially alters the detection geometry of the setup severely. Since it increases the volume where ionization takes place, it would princi-

pally allow the reduction of the space charge effects (section 8.2.6.1) without reduction of the total number of ions. Another advantage would be the increased detection sensitivity for systems with low molecule density. Disadvantages are the imprecise spatial resolution and the resulting changes in experimental geometry.

From the determined spatial profile presented in fig. 8.4, a reasonable approximation of the laser focus is a cylinder which is several orders of magnitude larger than its diameter ($\gg$10 mm length and ~0.2 mm diameter). Sections 8.2.7.1 and 9.1.1.9 treat how this affects the detection geometry in the setup.

8.2.7 Angular Averaging

Even when treating the laser focal volume as a point, the experimental geometry will not correspond to a well-collimated system. Despite the use of limiting apertures the surface of a permeation sample will always need to be orders of magnitude larger than the laser focus, so that a sufficiently large flux of desorbing molecules can be detected. As a result, the detected signal is a superposition of several trajectories varying in the desorption angle relative to the surface.

In previous desorption experiments (e.g. ref. 175,185), such angular averaging has been treated assuming normal energy scaling and ignoring the strongly non-uniform angular distributions found for desorbing molecules (cf. section 8.3.2.3). The distribution of angles for ion trajectories able to reach the detection has been determined by using numerical simulations of the sample surface and laser focal volume as point. This is schematically shown in fig. 8.8. Comparing the results to a one-dimensional (1D) approximation yielded only small deviations, even when considering the laser focal volume as long line[175] (up to 9.4 mm). Using the approximation of a laser focal spot, the different geometry in our setup yielded a half-cone angle of ~7°, which is significantly smaller than the 20° in the setup of Michelsen *et al.*[182,185].

This simple cone approximation is contradicted by the measured spatial laser focus profile discussed in section 8.2.5.3, which is best approximated with a long cylinder. Apertures in the current setup geometrically limit the ion trajectories able to reach the detector (cf. section 9.1.1.9). One of these apertures is approximated as linear projection of the extractor tube aperture onto the shielding mesh (SM), as shown in fig. 9.9. This approximation might not be accurate, when considering non-ideal meshes and resulting non-homogeneous fields in the setup. Also assumed is that the region between FCA and SM is free of electric fields. Furthermore, the angular distributions of desorbing particles are strongly non-uniform (see section 8.3.2.3). Even for systems with known angular distributions, these angle dependent intensity factors have not been considered in any three-dimensional (3D) models so far.

For the current setup, the distribution of angles has been simulated including a long laser line and limiting apertures in the detection setup (see section 8.2.7.1). Taking into

account the averaging over these angles and the angle dependent drift length x_0 of each trajectory, and further assuming normal energy scaling (see section 8.3.1.1) gives the kinetic energy of a molecule as dependent on the polar angle relative to the surface normal θ and the TOF t:

$$E_{\text{kin}}(\theta, t) = \frac{m}{2} \cdot \left(\frac{x_0}{\cos(\theta)} \right)^2 \cdot \left(\frac{1}{t} \right)^2 \cdot \cos^2(\theta). \tag{8.22}$$

Here, m is the mass of the molecule and t the offset-corrected TOF (see section 8.2.4.3).

This expression must be used to replace the kinetic energy terms in the detailed balance model (see section 8.3.1.1). Also including the calculated angular distributions in the setup (see section 8.2.7.1), TOF distributions were analyzed in regard to the impact of this 3D model. This was achieved by simulating TOF distributions for both Knudsen and permeation using typical characteristics with the 3D model and successively fitting those with the 1D model. For the Knudsen cell, this procedure yielded an increased drift length x_0 by ~1.5 % (30.45 mm compared to 30.00 mm), which is similar to the results obtained by Nattino *et al.*[175].

A typical permeation TOF profile was simulated, excluding the actual angular desorption distributions, and assuming normal energy scaling, as shown in eq. (8.22). Fitting this 3D result with the 1D model yielded for the E_0 a reduction by ~2.5 % relative to the initial value. For the width parameter of the sticking curve W, the value was reduced by ~0.25 %.

Furthermore, we investigated the effects of mixing both models for calibration and permeation. When permeation data is determined by the 3D method and the drift length obtained from 1D calibration, the fitted parameters deviate by less than 2.5 %. Vice versa, the deviations are also ~2 %, which is well within the experimental uncertainty.

The effect of assuming uniform angular desorption distributions has been estimated by including the measured angle-dependent intensity factors for typical TOF data. Unsurprisingly, the resulting deviation between 1D and 3D was decreased: this effect reduced the weighting for trajectories with higher angles.

In conclusion, all results presented in this study have been obtained using the simple 1D model. Even the combined effects resulting from detailed considerations of the experimental geometry were determined to not alter the results significantly.

8.2.7.1 Acceptance Angle Distributions

In this section, the numerical approach to determine the angular distribution of the experimental geometry will be introduced. In contrast to the simple (see fig. 8.8) geometry for a laser focal point, the present geometry is more complex due to the laser focal line as well as several apertures preventing trajectories from reaching the detection region (see section 9.1.1.9). The geometry shown in fig. 9.9 for the permeation samples differs

from the Knudsen cell measurements only by the size of the source. Since the Knudsen is basically a point source with dimensions similar to the laser focus width, the distribution of angles for detectable trajectories is vastly different from the permeation source. These differences are determined by only two parameters, the source radius r, and the actual length of the laser line l. Other geometrical restrictions are the limiting apertures, which is either the sample area, tantalum shield aperture or the acceptance of the extractor tube projected onto the SM (see fig. 9.9).

In order to determine the distribution of acceptance angles for each given geometry, a numerical method is introduced in this section. Figure 8.10 illustrates the approach schematically. For each angle θ, a cone with its tip in the laser focal line and its base on the sample surface (radius r) is considered. The base circumference b, depends on its radius r' and is given as: $b = 2\pi r'$. As depicted in fig. 8.10 panel (ii) r' is defined by the distance between base plane and the tip at the laser focus d, as: $\theta = \tan(r'/d)$. Translating this cone along the laser focal line as shown in panel (iii) (blue, Δx) yields another cone with the same circumference and therefore number of trajectories. For high Δx, shown in panel (iv), the full circumference is not included on the sample surface, and only the length of the arc (green) can be added to the number of trajectories.

Therefore, the circumferences have to be calculated with a more sophisticated method. Generally, every point on the circumference of a circle is defined with the radius r' and the azimuthal angle around the base normal ϕ, as:

$$p_{\text{circ}}(r', \phi) = \sqrt{(r')^2 \cdot \sin^2(\phi) + (r')^2 \cdot \cos^2(\phi)}. \tag{8.23}$$

This expression can be expanded to describe the position for a cone offset along the laser line by Δx:

$$p_{\text{offset}}(r', \phi, \Delta x) = \sqrt{[-r' \cdot \sin(\phi) + \Delta x]^2 + (r')^2 \cdot \cos^2(\phi)}. \tag{8.24}$$

Now, this expression allows to test for each trajectory, if it is still included on the sample surface, by simply checking if $p_{\text{offset}}(r', \phi, \Delta x) \leq r$. Because the experimental geometry includes several limiting apertures, which have to be considered as well, we simply replace r with r_{limit} and yield:

$$p_{\text{incl}}(r', \phi, \Delta x) = \begin{cases} 1 & \text{if } p_{\text{offset}}(r', \phi, \Delta x) \leq r_{\text{limit}} \\ 0 & \text{if } p_{\text{offset}}(r', \phi, \Delta x) > r_{\text{limit}} \end{cases} \tag{8.25}$$

Now, integration over ϕ to 2π gives the length of the arc l_a, corresponding to trajectories passing the apertures:

$$l_a(r', \phi, \Delta x) = r' \cdot \int_{\phi=0}^{2\pi} p_{\text{incl}}(r', \phi, \Delta x) \ \mathrm{d}\phi. \tag{8.26}$$

In the case of the whole circle passing the apertures, the integral in eq. (8.26) amounts to $2\,\pi\,r'$, which is the circumference.

In order to consider the full geometry, a maximum radius r_{max}, is given by the maximum distance of start and end point of a trajectory projected onto the surface plane. Here, this is estimated by simply adding the radii of sample and limiting aperture: $r_{\mathrm{max}} = r + r_{\mathrm{limit}}$. Using this method to integrate the number of possible angles for each radius $0 \leq r' \leq r_{\mathrm{max}}$, and for offsets along half of the laser line length, $0 \leq \Delta x \leq {}^l\!/\!_2$, results in the geometric angular distribution:

$$n(\theta, r_{\mathrm{max}}, l) = \int_{\Delta x = 0}^{l/2} \int_{r'=0}^{r_{\mathrm{max}}} \int_{\phi=0}^{2\pi} p_{\mathrm{incl}}(r', \phi, \Delta x)\ \mathrm{d}\phi\ \mathrm{d}r'\ \mathrm{d}\Delta x. \qquad (8.27)$$

By means of this methodology, acceptance angle distributions were calculated for a detection geometry as shown in fig. 9.9 for both the Knudsen cell and the permeation sources. The results are shown in fig. 8.9, simulated by measured dimensions of the corresponding sources and limiting apertures, as given in the caption.

These very distinct distributions were applied to compare 3D considerations for the setup to a simple 1D model. Those results are presented in section 8.2.7.

8.2.8 Simulations using SIMION

The simulation package SIMION® (Scientific Instrument Services, Inc.), version "8.1.1.32-2013-05-20"[264], was used to simulate the results presented in this chapter. SIMION® is a simulation program for electrostatic and/or magnetic two-dimensional (2D) as well as 3D potential arrays. It is also capable to simulate ion propagation trajectories in these arrays and allows programmatic adjustments to include dynamic changes during these simulations. In this work it was used to determine details of the ion optics setup and to improve the design of the FCA.

8.2.8.1 Design of Faraday Cage Assembly

The design of the FCA was optimized over several versions in the experimental setup. This process started from a replication of the setup described by Michelsen *et al.*[185] and concluded in the design presented in section 9.1.1.6.

First, in the design described by Michelsen *et al.*[185] the FCA meshes were heated with attached ceramic tubes along the sides. A main disadvantage of this design is the indirect heating of meshes along the ion drift direction, which are the most relevant parts for the buildup of patch charges. The design presented in section 9.1.1.6 incorporates direct resistive heating of all relevant meshes, which results in the improved conditions presented in section 8.2.6.2. However, in this design there must be a small gap on the long mesh (see section 9.1.1.6 and fig. 9.7, panel (i)), in order to allow direct resistive heating. Also, the rods around which this mesh was wrapped are situated inside the FCA, and
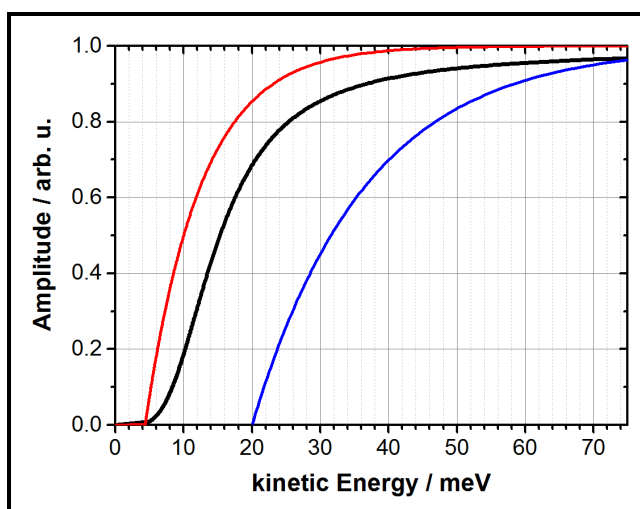
Figure 8.7: Detailed view of the exponential-based cutoff function eq. (8.21) as determined from experiment in fig. 8.6 (red). The result is directly compared to the tanh-function eq. (8.20) (black), with parameters as reported in the literature (red)[175,185]. The reported parameters are: $t_c = 19.5\,\mu s$, $t_w = 6.6\,\mu s$, $t_{\mathrm{shift}}^{D_2} = 1.79\,\mu s$ and $x_0 = 23.7\,mm$. Additionally shown is a cutoff-function with $E_{\min} = 20\,meV$ and $E_{\mathrm{slope}} = 60\,eV^{-1}$, to illustrate the range of FCA conditions relevant for experiments.
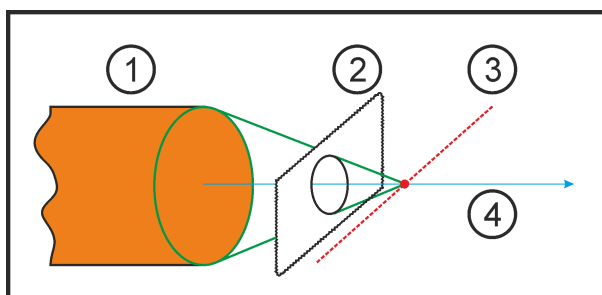
Figure 8.8: Schematic drawing of simple angular averaging assumptions for desorption experiments. In the first approximation, the detectable desorbing flux off a sample (1, orange) is limited by the surface area or apertures (2). In combination with a laser focal spot (3, red), a cone is formed (green). This cone contains all particle trajectories, which are ionized and propagate towards the detector (4, blue arrow). Summation over all angles in the cone then yields the angular distribution that is averaged about.
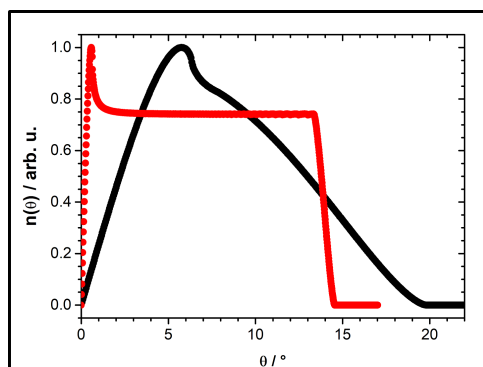
Figure 8.9: Angular distributions calculated with the numerical method presented here. These results correspond to the experimental geometry of the setup used in this work. As limiting apertures, the tantalum shield radius of 1.5 mm and the linear projection of the extractor onto the SM (cf. fig. 9.9), with 10 mm radius, were included. All distances and dimensions were taken as measured. The results for a permeation sample with a radius of 1.5 mm are shown as black dots, and for a Knudsen cell orifice with 0.15 mm radius as red dots.
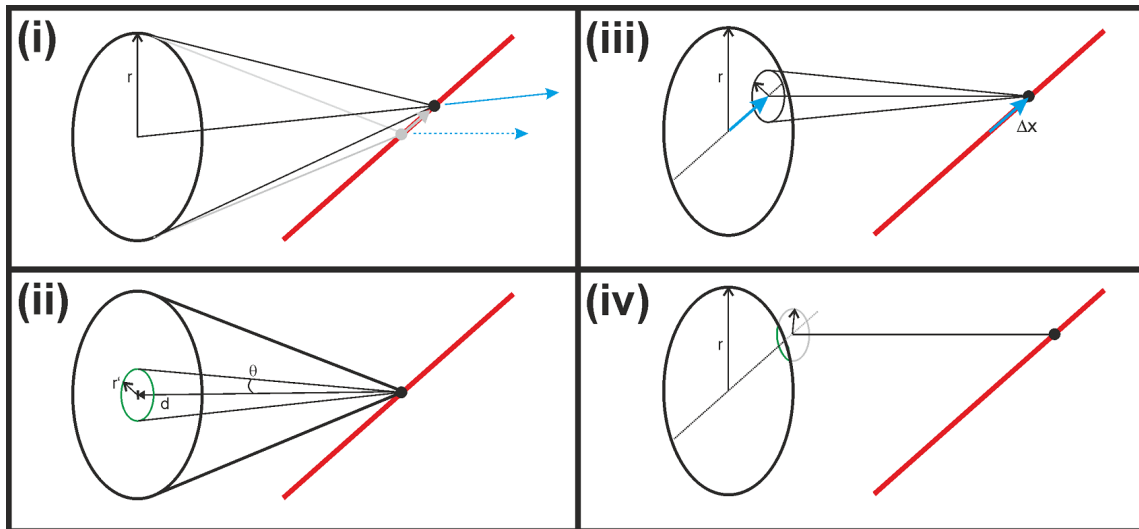
Figure 8.10: Illustration of the cone approach to simulate the angular averaging in the setup numerically. In panel (i) the gray cone indicates the acceptance of a symmetric setup, as depicted in fig. 9.9. If the base of the cone – which is the sample surface – is unchanged while its top is shifted along the laser focal line, an asymmetric cone (black) results with a new distribution of angles. Panel (ii) shows the approach to determine the angular distribution contained in a symmetric cone. For every angle θ, a circle with radius r' represents the base of the cone. All points on its perimeter represent a trajectory to the laser focus with the same angle and length. Integration with increasing r' until the outer sample radius is reached then yields the angular distribution of the cone. To determine the effect of a linear laser focus, panel (iii) illustrates a viable method: the top of the cone is translated (blue arrows) along the focal line and the integration is repeated for each offset Δx. Asymmetry is considered when the circumference of the base circle is not completely on the sample surface, as shown in panel (iv). Only points on the surface (green sector) can be included in the angular distribution. When considering other geometrical factors, e.g. limiting apertures, this method yields the angular distributions for a given setup.

might also cause perturbations. Especially, since the symmetry is broken by this design. SIMION simulations were used to estimate the effects on ion trajectories, but deviations were found to be negligible.

Simulations were furthermore employed to estimate the effect of available meshes for construction, e.g. wire diameter and separation, in terms of ion transmission and field penetration. While Faraday cages are theoretically field-free, the size of the gaps in the meshes does influence the transmission of external electric fields into the cage. SIMION simulations were employed to find the optimal mesh properties as well as optimizing the external dimensions of the FCA and the additional SM (cf. section 9.1.1.6).

8.2.8.2 Simulation of t_{shift}

In addition to the experiment to determine the t_{shift} presented in section 8.2.4.3, simulations were carried out. To determine the TOF in the ion optics, the setup was modeled as a simplified 2D potential array. All dimensions, alignments and potentials were simulated with their nominal values, and the FCA and SM were reduced to consist of perfect meshes only. Figure 8.11 shows the cut through the ion optics setup along the center of the ion flight axis, perpendicular to the laser beam propagation direction. Panel (a) gives the excerpt of a cut of a schematic Inventor[265] drawing. For clarification, panel (b) gives a

schematic accentuation of the parts relevant for the simulation: the outer chamber walls (grey), the FCA and SM (purple), extractor (blue), lens with baffles for stray light suppression (red) and the MCP detector (green). From the known dimensions of the parts, the simplified 2D setup given in panel (c) was constructed in SIMION. The potentials were set to the experimental values, i.e. $-30\,\text{V}$ for the extractor tube, $-1200\,\text{V}$ for the lens tube and $-2100\,\text{V}$ for the detector. All other surfaces were grounded. The colored lines in panel (c) give the equipotential lines calculated from SIMION with the following legend: the green lines show $0.2\,\text{V}$ steps from $0\,\text{V}$ to $-1\,\text{V}$, the blue $5\,\text{V}$ steps from $-5\,\text{V}$ to $-30\,\text{V}$ and the red $100\,\text{V}$ steps from $-100\,\text{V}$ to $-2000\,\text{V}$. Panel (d) gives the equipotential lines of the same 2D array as in (c) when the extractor voltage is set to ground as well. Finally, panel (e) gives a perspective view of the array presented in (c), where the vertical dimension corresponds to the electric potential.

Ion trajectory simulations were conducted with these arrays for the three isotopologues under otherwise constant conditions. The velocity distribution was simulated as 1D-MBD with $300\,\text{K}$ and along the nominal drift axis. The particles were defined as single charged ions, originating from a point source $29\,\text{mm}$ before the SM. During these simulations, the extractor voltage was switched from ground to $-30\,\text{V}$ several μs after the ions were generated. The switching was assumed to occur instantaneously and several simulations were conducted to investigate the effects of switching at varied time points after initialization. The corresponding potential arrays of both conditions are given in panels (c) and (d) of fig. 8.11.

In this simulation a certain fraction of the particles, from the high-velocity portion of the MBD had already left the FCA before the extractor was switched to its working potential. Therefore, this fraction of ions did already propagate further into the ion optic setup. Due to their immediate simultaneous acceleration, their arrival time on the detector varied only very little. As a result, a relatively sharp peak was generated in the arrival TOF distribution. For the fraction of ions still residing in the FCA the conditions did not differ from a regular experiment. They propagated as an undisturbed MBD through the whole setup. The ion trajectories recorded for each particle its initial velocity, the total TOF and the TOF between SM and detector. This last number corresponds to the t_{shift} of the simulated setup.

The results of this simulation are presented in section 10.1.4.2, the corresponding measurements in section 10.1.4.1.

Figure 8.11: Different views of the setup. Panel (a): Excerpt of the AutoCAD drawing of the setup, showing the FCA and ion optics as cut on the TOF axis. Panel (b): Schematic accentuation of the setup shown in panel (a), including color coding. The surrounding chamber walls are depicted in grey, FCA and SM in purple, the extractor in blue, the lens tube with baffles in red and the MCP detector in green. Panel (c): 2D potential array of the setup shown in panel (b). Also given are equipotential lines resulting from the experimentally used potentials: $-30\,$V for the extractor, $-1200\,$V for the lens and $-2100\,$V for the MCP detector. The equipotential lines are color coded as follows: red lines range from $-2000\,$V to $-100\,$V in steps of $100\,$V; blue lines from $-30\,$V to $-5\,$V in steps of $5\,$V and the green lines from $-1\,$V to $0\,$V in steps of $0.2\,$V. Panel (d): The same array as shown in panel (c) but with the equipotential lines resulting from setting the extractor to ground potential. Panel (e) gives a perspective view of the array and contour lines shown in panel (c), with the added vertical dimension corresponding to the relative potential. The light green mesh is added as a guide for the eye and the blue line in the center of the array shows a trajectory resulting for a typical particle.
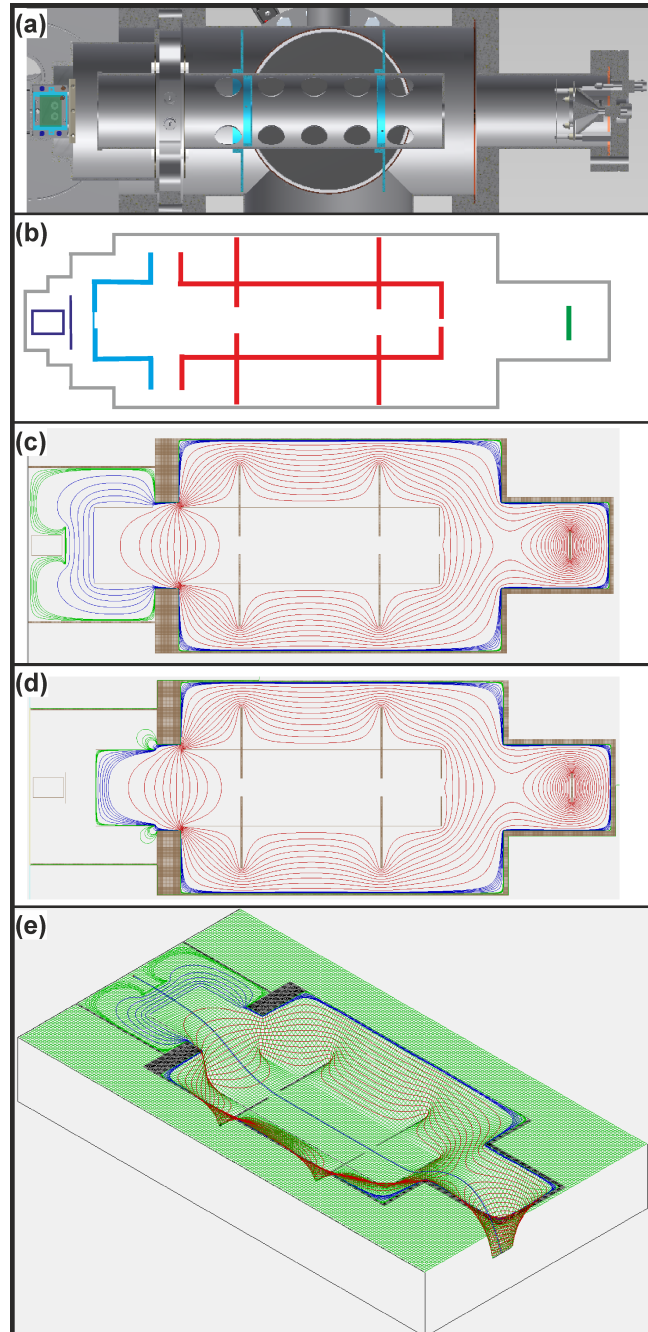
8.3 Analysis Methods

In this section, the various aspects of the analysis of acquired desorption data will be explained. This includes the fundamental assumptions of the detailed balance model as well as concrete analysis and interpretation methods.

8.3.1 Detailed Balance Model

The principle of detailed balance[73,117,118,126,175,182,185] has been used successfully to describe the desorption of molecules from metal surfaces[73,79,117,118,182,185,189,216,217,219]. It relates the associative desorption to the reverse process of dissociative adsorption. The detailed investigation of the Hydrogen/Cu(111) system by desorption as well as sticking experiments provides an excellent example of the validity of this model[175,186,189,193,195]. The following sections will illustrate the model in detail, including its assumptions and limitations.

Generally, the detailed balance model refers to systems maintained in an equilibrium or steady state. Systems described by this term need to have rate equality for each molecular process resulting in states distinguishable from each other and the corresponding reverse process. In classical mechanics, this has been referred to by "dynamic reversibility" (e.g. ref. 126). For quantum mechanical descriptions, the basic assumption is of statistical nature for all transitions, including the random phase. Conclusively, detailed balance allows deductions about processes by information acquired from the corresponding reverse process.

8.3.1.1 Assumptions and Limitations

Equilibrium For the detailed balance model, it is essential to consider the system in a steady state. For associative desorption experiments, the lack of adsorbing flux makes detailed balance a severe presumption. However, its validity is based on the assumption of equilibrium conditions for adsorbed particles. If those are thermally equilibrated with the surface, they are considered independent of their initial conditions which lead to their adsorption. Then, the desorbing flux can be described by the MBD at the surface temperature, independent of how the adsorbates were supplied to the surface, which allows the interpretation of such non-equilibrium measurements.

Now, to discuss the effect of a barrier to desorption, it is referred to fig. 7.1, which illustrates the Lennard-Jones PES. The inset (blue axes) depicts the thermal MBD and the shaded region the fraction of molecules which are able to desorb. By detailed balance, this desorbing flux corresponds to the flux which is able to adsorb from impinging molecules with the same MBD.

Energy Scaling As discussed by Van Willigen[242], a 1D reaction barrier would affect the angular distribution of desorbing particles. Dependent on the height of the potential barrier, narrower distributions than $\cos(\theta)$ are expected. Within the limit of 1D barriers, only the kinetic energy component of the particle motion parallel to the surface normal is participating in the reaction. This simple model is referred to as "normal energy scaling", and although the energy scaling law can vary for each system, it has been found to be applicable in many systems (e.g.[182,185,189]). One argumentation for this effect is that the PES appears uncorrugated for the impinging molecule or is of a shape resulting in approximately the same scaling[118,266].

Generally, the effective energy of particles to overcome the barrier, E_{eff} is related to the initial energy, E_i, the incidence angle relative to the surface normal, θ_i, and a scaling constant, n:

$$E_{\text{eff}}(\theta) = E_i \cdot \cos^n(\theta_i). \tag{8.28}$$

For $n = 2$, one obtains normal energy scaling, but there is no physical reason to constrain n. Even more, in an attempt to combine temperature dependent effects in the angular distributions and desorption energies found in the $H_2/Cu(111)$ system, Murphy and Hodgson[193] proposed an energy scaling model where the scaling factor is dependent on the incidence energy, $n(E_i)$.

Breakdown As stated in the paragraph above, one fundamental assumption is the equilibration of adsorbates with the surface prior to reaction. While this has been demonstrated for the $H_2/Cu(111)$ system by comparison of results using different H-atom supply techniques[189,193], this is not necessarily true for all systems. There are also cases for which the microscopic reversibility is impossible. One system where this was assumed for several years is hydrogen/silicon. Here, the de-/adsorption process is connected to a change in surface structure. Kolasinski *et al.*[75,76] studied $D_2/Si(100)$ and found strong deviations between de- and adsorption, which was attributed to surface reconstruction *accompanying* the desorption process.

Generally, desorption experiments are conducted far from equilibrium conditions: the gas pressure above the studied surface must be low, in order to not perturb the desorption flux. Consequently, the surface adsorbate coverage must be considerably higher than expected for equilibrium conditions at the apparent pressure. If the surface heat bath is the only energy source for reaction, detailed balance should hold. But if energy is also transfered by impinging particles, then the pressure above the surface will alter the mechanism for reaction. It is noted, that this argument is not restricted to ER or HA-ER reactions, but collision-induced desorption has also been observed in the methane/nickel system[267] using argon as projectiles. On the other hand, the collision rates between adsorbates and the surface are substantially higher than between gas phase molecules and the surface, thus results in much lower impact.

Surface Coverage In post permeation desorption experiments, the surface coverage is usually much lower than a monolayer (ML). An estimate for the experimental conditions for D_2/Au(111) yielded a steady state concentration of 2.4×10^{-3} ML. This is advantageous because it allows direct comparison to theoretical work, which is usually conducted for the zero coverage limit as well.

In contrast, the surface coverage dependence of reactivity cannot be studied with this method. This limits its applicability. In permeation experiments, permeation and desorption rates are both dependent on the surface temperature, and the range of applicable backing pressures is limited, resulting in little control over the surface coverage. H-atom dosing techniques (see section 8.2.2) have clear advantages in this regard, since the dosage is independent of T_s, although other practical limitations will prevent variations of the surface coverage over several orders of magnitude.

This is unfortunate, since the reaction probability (e.g. ref. 99) as well as the energetics (e.g. ref. 202) are functions of the coverage. Further complications may arise when the mechanism varies with coverage or the adsorbates form islands. In the latter case, the desorption distributions will depend heavily on the local structure, which does not correspond to the expected clean surface, despite the low average coverage.

8.3.1.2 Desorption Experiments

Application of detailed balance to the associative desorption of hydrogen off a metal surface allows relating a flux-weighted velocity distribution $f(v, J, T_s, E_{\mathrm{kin}})$ to the sticking probability curve $S(v, J, E_{\mathrm{kin}})$. When considering the desorption normal to the surface only, the relationship is given as[117,175,185]:

$$f(E_{\mathrm{kin}}, v, J, T_s)\,\mathrm{d}E_{\mathrm{kin}} = K \cdot E_{\mathrm{kin}} \cdot \exp\left(\frac{-E(v, J)}{k_b \cdot T_s}\right) \cdot S(v, J, E_{\mathrm{kin}})\ \mathrm{d}E_{\mathrm{kin}}, \qquad (8.29)$$

with the Boltzmann constant k_b, the surface temperature T_s, a constant factor K, and the sticking function $S(v, J, E_{\mathrm{kin}})$. The form of the sticking functions is discussed in sections 8.1.3 and 8.3.3.1. In order to apply eq. (8.29) to the interpretation of experimental measurements, the flux off the surface has to be described as function of TOF (t). Including the density dependent ionization probability then results in[117,185]:

$$f(t, v, J, T_s)\,\mathrm{d}t = K' \cdot \left(\frac{x_0}{t - t_{\mathrm{shift}}}\right)^4 \cdot \exp\left(-\frac{m}{2 \cdot k_b \cdot T_s} \cdot \left[\frac{x_0}{t - t_{\mathrm{shift}}}\right]^2\right) \cdot S(v, J, t)\,\mathrm{d}t, \ \ (8.30)$$

with a new constant factor K'. This scaling is principally inseparable from the corresponding amplitude parameter of the RPC(see section 8.1.3). However, a relative scale can be extracted for all quantum states of each specific isotopologue and surface. Under assumed

constant experimental conditions, the obtained absolute amplitude can be separated into several components: an unknown factor summarising all experimental conditions (K''), the quantum state dependent Boltzmann factor (see eq. (8.34)) and the RPC saturation value of interest. By correcting each signal for the corresponding Boltzmann factor, the state dependent saturation values can be extracted on a relative scale. Normalization is then achieved by arbitrary scaling of the unknown constant K'', e.g. such that the obtained values of the $v = 0$, J-sequences average to unity.

Previous D_2/Cu(111) desorption experiments[117,175,182,185] included averaging over several angles for a cone starting from the laser focal point as tip and base at the surface active area. In our setup, the experimental geometry reduces the angular acceptance to 7° half-cone angle, and the effect of angular averaging is found to be negligible (see section 8.2.7). Therefore, this is not included in the analysis and the desorption flux is treated as 1D.

8.3.2 Time-of-Flight Signal Processing

Each measured TOF distribution was subtracted by an "off-resonant" trace, which were obtained by tuning the probe laser away from the resonant transition and acquiring another TOF trace with all other parameters kept constant. This subtraction removed all laser-induced background, since the laser power did not vary from such small deviation of the wavelength. On- and off-resonant traces were obtained alternatingly to prevent effects from drifting parameters over longer timescales or more serious problems and failures.

These subtracted TOF signals were then corrected for laser power[257] and added up. The result was successively corrected for the total number of acquisitions and the corresponding transition line strength[255]. This yielded TOF distributions on a relative scale for each surface and isotopologue.

For H_2/Cu(111), the data acquisition was slightly different, since this dataset was acquired before experimental optimization. Here, the TOF resolution was 100 ns in contrast to 20 ns for Cu(211) and Au(111). Follow-up measurements directly comparing Cu(111) and Cu(211) under similar conditions showed no loss of relevant information by this resolution change.

Furthermore, the off-resonant traces were not acquired for each quantum state individually. Rather a representative off-resonant signal was acquired and smoothed, which was then scaled to match each on-resonant data in an early TOF range with no apparent desorption signal. These results were also compared with follow-up measurements for representative states and confirmed the applicability of the method.

8.3.2.1 Employed Programs

TOF data was analyzed with a Python[268] program, utilizing the Levenberg-Marquardt algorithm[269,270] implemented in the "lmfit" package[271]. Calibration measurements have

been analyzed with the model in eq. (8.15) for x_0, including the cutoff function parameters E_{slope} and E_{min} (cf. eq. (8.21)) and using a fixed t_{shift} value (eq. (8.14)). These calibration parameters were fixed for the analysis of the permeation datasets acquired on the same day.

In order to constrain certain fits, each parameter could be fitted as a global parameter, if reasonable. For example, the t_{shift} for each isotopologue is related by eq. (8.14), allowing the global fitting of both t_{shift} and x_0 for Knudsen calibration data of several isotopologues (see section 10.1.1). Furthermore the baseline level was not determined as free fit parameter. Instead, a TOF interval was chosen which contained no measurable signal, e.g. before the t_{shift} or $>50\,\mu\text{s}$. The averaged value of this interval then determined a fixed baseline.

All other data analysis and mathematical operations were conducted by using homebuilt programs for Python[268] and Mathcad[272]. Simulation of ion trajectories were conducted using SIMION8.1[264] (see section 8.2.8). Graphics in this work were produced using OriginPro[273] and CorelDRAW[274], technical drawings were produced using the AutoCAD program Inventor[265].

8.3.2.2 Quantum State Dependence of Parameters

Principally, the RPCs are unique for each quantum state. However, specific properties vary only within the noise level over the rotational sequences or between each isotopologue. Especially the width parameter of RPCs has been observed as independent from the rotational, but not the vibrational state (e.g. ref. 182,185,193). For each data set obtained in this work, possible dependences were tested by fitting the width parameter both individual for each J-state and "global" for the whole rotational sequence of each v-state. This constraint was found to improve the reliability for specific data with low SNR, while not degrading the overall fit quality of the whole sequence. Further details of this will be discussed in section 11.2.2.1.

As result, the data sets for both copper facets were each fitted using such global widths $[W(v)]$ for each isotopologue and vibrational state. However, the gold data suffered from worse SNR, especially for HD, and the high desorption energies found resulted in inadequate probing of the RPC's saturation regime. In order to achieve reasonable fit results and reliable parameter variation (see sections 8.3.3 and 11.2.2.1), the width parameter was obtained globally irrespective of rotational state and isotopologue. While this seems counter-intuitive, it is pointed out that the variation of individual widths for the three isotopologues lies well within their uncertainty, and only weak or insignificant variations have been observed before (see ref. 185,189,193).

8.3.2.3 Angular Distributions

Angular distributions for systems with activated desorption show strongly peaked behaviour, as was shown in several studies[73,107,178,195,196,242,243,275,276]. Furthermore, as stated in

section 8.3.1.1, only a certain fraction of the total energy is participating in overcoming the barrier. In this section, the analysis of the angular desorption distribution will be treated.

In general, integration of the desorption flux (eq. (8.29)) over energy and the assumed angular averaging gives the general expression for the angle dependent desorption flux as[117]:

$$f(\theta) = \int_0^\infty N_c \cdot E_{\text{kin}} \exp\left(-\frac{E_{\text{kin}}}{k_b \cdot T_s}\right) \cos(\theta)\, S_i(E_{\text{kin}}, \theta)\, \mathrm{d}E_{\text{kin}}, \qquad (8.31)$$

with N_c as normalization factor, usually taken as $N_c = f\,(\theta = 0°)$. It is pointed out that in this work the angular averaging is considered negligible (see section 8.2.7) and normal energy scaling (section 8.3.1.1) is assumed. Therefore, eq. (8.31) is simplified to:

$$f(\theta) = \int_0^\infty N_c \cdot E_{\text{eff}} \exp\left(-\frac{E_{\text{eff}}}{k_b \cdot T_s}\right) S_i(E_{\text{eff}})\, \mathrm{d}E_{\text{eff}}, \qquad (8.32)$$

with $E_{\text{eff}}(\theta)$ according to eq. (8.28) and $n = 2$. Now, with the considerations made by Anger *et al.*[178], this integrated desorbing flux, $P(\theta)$ is described by:

$$P(\theta) = \cos^n(\theta). \qquad (8.33)$$

This form of eq. (8.33) has been based on empirical results only (e.g. ref. 73,242) before Anger *et al.* found arguments to base it on physical properties[178]. To analyze experimental data, eq. (8.33) is fitted to the integrated flux for each angle. In the setup used in this work, a few complications arise. First, for some distributions the peak was not parallel to the surface normal, which was easily corrected by an angle-offset in eq. (8.33). Then, there are two apparent desorption channels for the desorption from copper (compare section 8.3.3.1). Assuming clear separation of these channels then allows independent integration and successive fitting.

8.3.3 Interpretation of Results

Due to the use of the same functional form in the fitting process for all quantum states, the RPC's characteristics can be described by the variation of the obtained parameters. As elaborated in section 8.3.2.2, the width of the curves shows little variation with rotational state and isotopologue.. Previous work found this parameter to vary strongest with T_s (e.g. ref. 118,181,185,186,193), which is not varied over a significant range in this study.

Mathematical functions describing the RPCs have been described in section 8.1.3 and those relevant to this work in section 8.3.3.1. For the fast reaction channel, fitted by using the ERF form (eq. (8.4)), the parameters are: the width $W(v)$ as described in the paragraph above, the point of inflection $E_0(v, J)$, and the amplitude, which is termed from now on $A_{\text{Erf}}(v, J)$. The slow reaction channel is described by the exponential function

(eq. (8.7)), with the decay parameter $\gamma(v, J)$ and an amplitude $A_{\mathrm{Exp}}(v, J)$. In order to describe the slow channel flux, the integrated flux will be analyzed instead of A_{Exp}.

8.3.3.1 Experimentally Relevant Sticking Functions

As demonstrated in section 8.1.3, the choice of mathematical function to describe the RPCs is non-trivial and of critical importance. It needs to be tested for each system, which is most suitable to describe experimentally obtained data. While more flexible forms, like LGS or FPC, will always give better agreement in fitting procedures, it remains to be verified if their use is justified. For over-parameterized functions it is impossible to deduce reliable information about the studied system, due to the correlation between parameters, which is discussed in more detail in section 11.2.2.1.

In order to determine reasonable RPCs, generic experimental curves were fitted using several model functions as well as linear combinations of those. Careful analysis of these fit results then yielded the most simple functions, which were still flexible enough to describe the datasets. While details will be given in section 11.2.2.1, the main arguments for the choices in this study will be presented here briefly.

For the Au(111) system, the high kinetic energies found in the desorption distributions illustrate a main problem in associative desorption experiments. The sampled energy range is determined by the surface temperature, which is fundamentally limited. The mismatch of RPC and thermal energy distribution leads to little sampling in the high-kinetic energy range. Therefore, the saturation regime of the RPCs is restricted to an upper limit, and no information about the shape of the curve can be extracted reliably. Fortunately, the shape of the distributions is well described by eq. (8.4).

For copper measurements, the data in this study is affected by a feature not clearly observed in previous studies. The desorption distributions show a component at kinetic energies below ~0.3 eV. Such a behaviour was not reported for almost identical experiments by Michelsen *et al.*[182,185] and Rettner *et al.*[189] In contrast, a similar feature was reported by Murphy and Hodgson[193], who explained their observations by thermally generated reaction sites with low barrier. A detailed discussion will be given in section 11.3.1.4, but here it is sufficient to conclude the occurrence of a second, additive reaction channel. While Murphy and Hodgson described their RPCs with approximately linear dependence at low kinetic energies, the data in this work is best described using an exponential decay as in eq. (8.7). Due to the overlap of this sticking component with the main desorption peak, the latter is approximated using the ERF (eq. (8.4)) to prevent parameter correlation (see section 11.2.2.1). In the course of this work, those two contributions will be termed "slow" and "fast" channel.

Generally, the measured TOF distributions include a thermal background (TB) for most acquisitions of molecules in their vibrational ground state. This contribution can be included during the fitting process, as described in detail in section 10.1.5. For measure-

ments on gold, this TB contribution is clearly separated in TOF from the main desorption feature, allowing direct fitting of the data without subtraction of the TB.

8.3.3.2 Trends in Derived Parameters

With regards to the fast channel, the interpretation of parameter variation is quite straightforward. An increase in E_0 marks a shift of the RPC to higher kinetic energies, i.e. a higher barrier to reaction. The width of the actual reaction barrier distribution is determined by $W(v)$, which only allows for comparison between vibrational states, surfaces and usually isotopologues. The relative amplitudes are best interpreted by obtaining quantum state population distributions, as described in section 8.3.3.3.

For the slow channel, the interpretation is less straightforward. As stated above, the amplitude is best analyzed regarding the integrated flux, which can then be compared to the fast channel. The decay parameter describes the shape of the RPC easily, but due to the convolutions in the detailed balance model (see section 8.3.1), the resulting form in TOF is not easily predicted. This is complicated even more by the overlap of TB in the low kinetic energy region. Qualitatively, larger values of $\gamma(v, J)$ result in a less pronounced decay with rising kinetic energy resulting in a broader shape of the slow channel peak. Therefore, it extends to higher kinetic energies and shorter TOF and increases the overlap to the fast channel.

8.3.3.3 Quantum State Population Distributions

As per the principle of detailed balance (section 8.3.1), the quantum state population distributions of the nascent molecules should follow a Boltzmann distribution at T_s. Deviations from this behaviour allow conclusions regarding the dynamics of the reaction. Including the rotational degeneracy and the nuclear spin statistical weight of the isotopologue and rotational state considered ($g_{ns}(J)$, see table 8.2), the Boltzmann factor at T_s is given as:

$$F(v, J, T_s) = C \cdot (2J + 1) \cdot g_{ns}(J) \cdot \exp\left(\frac{-E(v, J)}{k_b \cdot T_s}\right).$$
(8.34)

Here, C is a normalization constant, which scales the results to the experimental total flux. This constant includes all other factors for different sample surfaces and the isotopologues probed. The term $E(v, J)$ describes the internal energy of the given ro-vibrational state (see section 8.2.5.1).

In order to obtain quantum state population distributions from the measured TOF distributions, $I(v, J, t)$, the integrated flux of each quantum state $P_i(v, J)$ needs to be compared. This is achieved by employing the obtained RPC functions $S_i(v, J, E_{\text{kin}})$ in the integration over the kinetic energy E_{kin}[175,185,220]:

$$P_i(v, J)\,\mathrm{d}E_{\mathrm{kin}} = F(v, J, T_s) \cdot \int_{E_{kin}=0}^{\infty} \sqrt{E_{\mathrm{kin}}} \cdot \exp\left(\frac{-E(v, J)}{k_b \cdot T_s}\right) \cdot S_i(v, J, E_{\mathrm{kin}})\,\mathrm{d}E_{\mathrm{kin}}. \quad (8.35)$$

Since desorption measurements do not allow for determination of absolute reaction probabilities, the saturation values of the S_i functions are defined only on a relative scale. Corresponding procedures are given in the following section 8.3.3.4.

Normalization of the quantum state population distributions was achieved by scaling constant C in eq. (8.34) to result in the sum over all states to equal unity. The vibrational state population distributions were determined by summing the fluxes of all rotational states of the same vibrational level, if these rotational states were measured for all vibrational states considered.

8.3.3.4 Saturation Values

This section illustrates several methods to extract relative saturation values for RPCs form desorption data. It is pointed out, that this analyses are based on the ERF model in order to distinguish the two reaction channels, as described in section 8.3.3.1.

In previous studies (e.g. ref. 175,182,185,189), the measured quantum state population distributions were compared with simulations assuming saturation at unity for all (v, J)-states and thermal distributions (see section 8.3.3.3). Since little deviation was observed for rotational states, the saturation values were only compared in between vibrational states. Obtained results were successively normalized to the maximum values. For the D_2/Cu(111) system[182,185] these results varied only within a factor of approximately two. For H_2/Cu(111), the variation was even negligible[189] and resulted in the reasonable assumption of approximately constant saturation values for all states. In this study such saturation values were obtained by the same methodology and because this is based upon comparison of integrated and expected fluxes, these will be termed "A_{flux}".

Additionally, quantum state resolved saturation parameters were calculated from the TOF data directly. Here, the relative amplitude from each fit was divided by the Boltzmann factor (eq. (8.34), with $C = 1$). In a successive step these values were normalized for each isotopologue and surface, such that the average value of the corresponding $(v = 0)$ sequences resulted as unity. Because the fits are based on the ERF model, these results will henceforth be termed "A_{erf}".

8.3.3.5 Efficacy

Advanced analysis of results is conducted in regard to efficacy. This term describes the relative efficiency of translational energy to internal energy of a molecule to overcome the barrier to reaction. Efficacies greater than unity mean that the internal molecular degree of freedom is more efficient than translational energy in overcoming the reaction barrier.

Due to the ERF form fitted to all RPCs, and by assuming saturation values near unity, the RPC of different states can be compared simply by the $E_0(v, J)$ parameters. Since the W parameters are mostly temperature-dependent, the $E_0(v, J)$ parameters are the characteristic quantity for each RPC. Comparison of the difference from $E_0(v, J)$ of a certain (v, J) state to the ground state of a molecule, $E_0(v = 0, J = 0)$, to the molecular internal energy of that state, yields the internal efficacy $\varepsilon_{\text{int}}(v, J)$ as:[185,189]:

$$\varepsilon_{\text{int}}(v, J) = \frac{E_0(v = 0, J = 0) - E_0(v, J)}{E_{\text{int}}(v, J) - E_{\text{int}}(v = 0, J = 0)}. \tag{8.36}$$

For fully quantum state resolved data, the efficacy can be determined for rotational and vibrational energy independently, given as:

$$\varepsilon_{\text{rot}}(v, J) = \frac{E_0(v, J = 0) - E_0(v, J)}{E_{\text{int}}(v, J) - E_{\text{int}}(v, J = 0)}. \tag{8.37}$$

$$\varepsilon_{\text{vib}}(v > 0, J) = \frac{E_0(v - 1, J) - E_0(v, J)}{E_{\text{int}}(v, J) - E_{\text{int}}(v - 1, J)}. \tag{8.38}$$

Efficacies have been determined using this method for Cu(111) and D_2[117,185] and H_2[189]. Recently, a similar method was applied to theoretical predictions of the H_2/Au(111) system[201]. Here, the RPCs were described using the FPC (eq. (8.6)), which does not contain a point of inflection similar to the E_0 parameter of the ERF (eq. (8.4)). Instead, an arbitrary value of reaction probability was chosen, and the kinetic energy of each RPC at this value was compared. Disadvantages of this approach are the arbitrary choice and the complex variation of RPC shape with T_s. In order to circumvent these problems, a new method to determine efficacies independent of the mathematical function form is introduced in section 8.3.4.4.

8.3.3.6 State Averaged Desorption Energies

It is also informative to determine the mean desorption energy averaged over all ro-vibrational states. This allows comparison to experiments without state resolution, e.g. Comsa and David[176]. When assuming normal energy scaling and a Boltzmann population distribution at surface temperature T_s, the weighted average of the mean kinetic energy of the desorbing flux $\langle E_{\text{kin}} \rangle$ is given as[117,175]:

$$\langle E_{\text{kin}} \rangle = \frac{\sum_{v,J} F(v, J, T_s) \cdot \int_{E_{kin}=0}^{\infty} (E_{\text{kin}})^2 \cdot \exp\left(\frac{E_{\text{kin}}}{k_b \cdot T_s}\right) \cdot S(v, J, E_{\text{kin}}) \, \mathrm{d}E_{\text{kin}}}{\sum_{v,J} F(v, J, T_s) \cdot \int_{E_{kin}=0}^{\infty} E_{\text{kin}} \cdot \exp\left(\frac{E_{\text{kin}}}{k_b \cdot T_s}\right) \cdot S(v, J, E_{\text{kin}}) \, \mathrm{d}E_{\text{kin}}}. \tag{8.39}$$

For data acquired in this study, a complication to this approach arises. When the desorption flux is separated into two channels (see section 8.3.3.1), eq. (8.39) has to

be modified. For each channel $S(v, J, E_{\text{kin}})$ can be expressed by eq. (8.4) or eq. (8.7), respectively. For the total desorption flux S_{total}, both those contributions need to be added before insertion in eq. (8.39):

$$S_{\text{total}}(v, J, E_{\text{kin}}) = S_{\text{erf}}(v, J, E_{\text{kin}}) + S_{\text{exp}}(v, J, E_{\text{kin}}). \tag{8.40}$$

However, a serious assumption is required to justify this approach. The normal energy scaling assumed for the fast channel is not necessarily given for the slow channel. Because the quality of the presented data does not allow to determine an energy scaling law for both channels independently, normal energy scaling is assumed for both channels.

8.3.4 Conversion of Time-of-Flight Distributions

For several aspects of the analysis, it is necessary to convert the acquired TOF distributions to yield the desorption flux in the kinetic energy domain directly. The necessary considerations will be elaborated in this section. As mentioned in section 8.2.4.2, the velocity $v_p(t)$ of a particle in the FCA is determined as: $v_p(t) = {x_0}/{t - t_{\text{shift}}}$. Insertion in the 1D MBD (cf. eq. (8.15)) yields:

$$f(t, T)\,\mathrm{d}t = k \cdot v_p(t)^4 \cdot \exp\left(-\frac{m}{2 \cdot k_b \cdot T} \cdot v_p(t)^2\right)\,\mathrm{d}t, \tag{8.41}$$

Now, the transformation function from $[v_p(t)]$ to kinetic energy E_{kin} results in a factor of $[v_p(t)^{-3}]$. An additional factor of $[v_p(t)]$ is required to compensate for the density dependence of the detection, which is determined by the ionization step. Therefore, the complete Jacobian to transform the obtained TOF into kinetic energy dependent flux distribution is $[v_p(t)^2]$. This transformation also requires a new proportionality constant for the acquired kinetic energy distributions. In a successive step, the obtained distributions can be re-binned in the kinetic energy domain.

8.3.4.1 Kinetic Energy Distributions

In order to describe the measured flux without the detailed balance model, the kinetic energy distributions were also fitted as Gaussian peaks[220]. This allows to describe the measured results independent of the detailed balance model and excludes parameter correlation (see section 11.2.2.1). The results and methodology are given in appendix D.2. Here, the fits were restricted to exclude TB contributions for all samples, but it is pointed out that for both copper facets only the fast channel is fitted. Furthermore, for highly excited ro-vibrational states the overlap of fast and slow channel is extensive, which results in deviations from Gaussian shape. However, this effect is assumed to be small due to the low relative flux of the slow channel.

8.3.4.2 Numerical Sticking Probability Curves

For each ro-vibrational state, the measured TOF distribution, $I(v, J, t)$, can be numerically converted to obtain a reaction probability distribution. Because an absolute scale for the reaction probability cannot be obtained from desorption experiments, a comparison between isotopologues or different surfaces is impossible. However, it is possible to compare RPCs in between different ro-vibrational states by scaling the data relative to each other. After the fundamental data processing (cf. section 8.3.2) the reaction probabilities, $S(v, J, t)$, were obtained by dividing the TOF distributions, $I(v, J, t)$, by the Boltzmann factor (eq. (8.34)), and the MBD at T_s [175,189]:

$$S(v, J, E_{\text{kin}}(t))\, \mathrm{d}t \, \propto \frac{I(v, J, t)}{F(v, J, T_s) \cdot \sqrt{E_{\text{kin}}(t)} \cdot \exp\left(\frac{-E_{\text{kin}}(t)}{k_b \cdot T_s}\right)}\, \mathrm{d}t. \qquad (8.42)$$

Care has to be taken using this approach, since the inversion in eq. (8.42) is only valid if the sticking probability function is angle independent, as in this work (cf. section 8.2.7). The obtained RPCs, $S(v, J, t)$, were converted onto an energy scale, $S(v, J, E_{\text{kin}})$, and re-binned (section 8.3.4). For further analysis, the energy range for this analysis was limited to experimentally significant data points. Hence, the range was determined by the desorption peak already converted to flux as function of kinetic energy, $I(v, J, E_{\text{kin}})$. Data points were rejected when their relative amplitude in this distribution was less than $25\,\%$ of the maximum value of the peak. This restricted the result to data points with significant amplitude regardless of the actual RPC shape and energetic range.

Resulting experimental RPCs are on a relative scale for each given isotopologue and surface. Therefore, the ordinate values can neither be used to predict absolute reaction probabilities, nor to compare reactivity between different samples. However, further analysis is possible with regard to quantum state dependence for each data set, which is described in section 8.3.4.3 and section 8.3.4.4.

8.3.4.3 Threshold Offset

The relative energetic position of the derived experimental RPCs on their mutual intensity scale (see section 8.3.4.2) represents a shift of the dynamical reaction barriers for these states. This can be analyzed regardless of the functional form used to describe the RPC in the fitting process, which can be relevant as elaborated in section 8.1.3.

To introduce a quantitative value describing the effect of the internal energy of a molecule, a "threshold offset", $\Delta S(v, J)$, is defined [220]. This gives the shift along the kinetic energy axis, which results in the best overlap between the $S(v, J, t)$-curve (eq. (8.42)) with the curve of a certain reference state, ideally the ro-vibrational ground state of the corresponding isotopologue.

Figure 8.12 illustrates this method for selected curves from $D_2/Cu(111)$. The ΔS
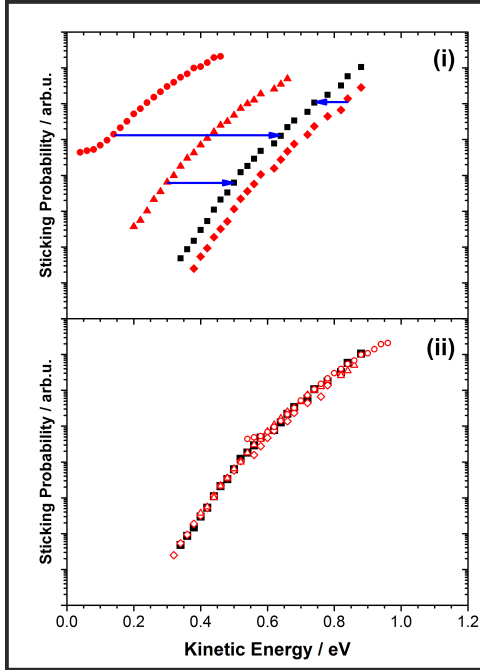
Figure 8.12: Determination of the threshold offset, $\Delta S(v, J)$, for selected ro-vibrational states. Presented is data from D_2/Cu(111), ($v = 0, J = 0$, black squares) and ($v = 0 - 2, J = 2$, red diamonds, triangles and circles, respectively) on a decadic logarithmic scale. Both graphs show the numerically determined reaction probabilities, derived directly from the measurements as described in section 8.3.4.2. Panel (i) directly gives the results on the same relative scale. Data points are restricted to ranges with sufficient SNR as determined by the acquired desorption flux and described in the text. Panel (ii) shows the same points shifted in kinetic energy (open red symbols), as indicated by red arrows in panel (i), to best match the reference state (black) over the whole range.

values are determined as follows: First, the $S(v, J, t)$ curves are obtained from the TOF data according to eq. (8.42), converted to the kinetic energy domain and re-binned into $20 \, \mathrm{meV}$ bins, E_i. The results are shown in panel (a) in fig. 8.12. Second, each considered curve is shifted in kinetic energy, in steps of the bin size (red arrows). Third, for each shift E_{shift}, the "root mean square deviation" (RMSD) is determined as:

$$\mathrm{RMSD}(v, J, E_{\mathrm{shift}}) = \frac{1}{n} \cdot \sum_{E_i} \left(\log_{10} \left[\frac{S(v, J, [E_i - E_{\mathrm{shift}}])}{S(v = 0, J = 0, E_i)} \right] \right)^2 . \tag{8.43}$$

Here, for each kinetic energy, the deviation in reactivity to the reference state is calculated and squared. These values are summed and divided by the total number n of comparable data points, i.e. the kinetic energy bins that contain data from both curves. The $\log_{10}$ was applied to weight the whole reactivity range similarly. From this procedure, the ΔS results from the E_{shift} value which obtains the smallest $\mathrm{RMS}(v, J, E_{\mathrm{shift}})$.

Despite the variation of curve shape and the vast differences in initial range between the curves, the resulting overall agreement is satisfactory (panel (b)). Advantageous in this method is the absolute independence of fitting functional form (section 8.3.3.1), which allows determination of deduced values numerically from experimental data (see section 8.3.4.4).

8.3.4.4 Efficacies from Threshold Offsets

Analogue to section 8.3.3.5, the ratio of the threshold offsets (section 8.3.4.3) to the internal energy E_{int} difference of the corresponding states can be defined as another internal efficacy, $\xi_{\mathrm{int}}(v, J)$[220]:

$$\xi_{\text{int}}(v, J) = \frac{\Delta S(v, J) - \Delta S(v = 0, J = 0)}{E_{\text{int}}(v, J) - E_{\text{int}}(v = 0, J = 0)}. \tag{8.44}$$

Also, subsets of these internal efficacies are given when considering rotational or vibrational energy separately:

$$\xi_{\text{rot}}(v, J) = \frac{\Delta S(v, J) - \Delta S(v, J = 0)}{E_{\text{int}}(v, J) - E_{\text{int}}(v, J = 0)}. \tag{8.45}$$

$$\xi_{\text{vib}}(v > 0, J) = \frac{\Delta S(v, J) - \Delta S(v - 1, J)}{E_{\text{int}}(v, J) - E_{\text{int}}(v - 1, J)}. \tag{8.46}$$

As stated above (section 8.3.4.3), the efficacies determined by this method do not rely on the RPC model fitted to the obtained TOF data. This eliminates artifacts related to the functional form used to describe the sticking, and correlations between fitted parameters.

8.3.4.5 Extrapolation to Equilibrium Conditions

From the obtained state resolved RPC, the activation energy for adsorption of a thermal, isotropic gas sample can be estimated. This was demonstrated for the $H_2/Cu(111)$ system by Rettner *et al.*[186], with the goal to estimate reaction rates under equilibrium conditions. Since the ultimate goal of fundamental research in this field is tha ability to predict properties of heterogeneous catalytic processes, their analysis is adapted to all data obtained in this work. This is supposed to give at least an approximation of the activation energies for the studied systems.

Obviously, the methodology has to include several assumptions, amongst which the most severe is the direct transferability of the system properties over vast pressure ranges. The RPCs have been determined under ultra high vacuum conditions, but are applied to the pressure range relevant in industrial processes: a change bridging 11–13 orders of magnitude! Thus, the RPC obtained in the low coverage limit are assumed to be actually coverage independent, and the mechanism of the reaction needs to be unaltered.

Furthermore, the model chosen to represent the RPC was the ERF (see eq. (8.4)), and for all systems this is assumed to be the only reaction channel. All three ERF parameters are considered constant over the given temperature range, and the saturation values are averaged over rotational states for each vibrational state. Also assumed is normal energy scaling and conservation of the thermal equilibrium between the respective surface and gas.

For the calculations, the obtained quantum state resolved dynamical information of the system, such as the dependences on T_s, E_{kin} and collision angle, needs to be combined into a mean absorption probability $\langle S_0(T_s) \rangle$. This can then be related to the activation energy E_{act} of the system by assumption of an Arrhenius-like relationship[186]:

$$\langle S_0(T_s)\rangle = A_{\text{pre}} \cdot \exp\left(-\frac{E_{\text{act}}}{k_b \cdot T_s}\right), \tag{8.47}$$

with A_{pre} as a pre-factor. Now, simulation of $\langle S_0(T_s)\rangle$ over a certain temperature range allows extraction of E_{act} from a fit to eq. (8.47).

The main effort of the model by Rettner $et\ al.$[186] is to obtain $\langle S_0(T_s)\rangle$ by averaging the RPCs properties over incidence conditions. In order to achieve this, the gas above the surface is described by a thermal equilibrium, resulting in a MBD of the kinetic energies and a Boltzmann population of the quantum states. Furthermore, collisions of the gas with the surface are considered as isotropic, and normal energy scaling is assumed (see eq. (8.22)). Then, the averaging over incidence conditions for each quantum state specific RPC $[S_0(v, J, T_s, E_{\text{kin}}[\theta], \theta)]$, and including the detailed balance model (see section 8.3.1.2), results in the mean reaction probability as[186]:

$$\langle S_0(v, J, T_s)\rangle = \frac{\int\limits_0^{\pi/2}\int\limits_0^{\infty} S_0(v, J, T_s, E_{\text{kin}}[\theta], \theta)\ \mathrm{d}E_{\text{kin}}(\theta) \cdot \cos(\theta)\sin(\theta)\,\mathrm{d}\theta}{\int\limits_0^{\pi/2}\int\limits_0^{\infty} E_{\text{kin}}(\theta)\exp\left(-\frac{E_{\text{kin}}(\theta)}{k_b T_s}\right)\ \mathrm{d}\theta\ \cos(\theta)\sin(\theta)\,\mathrm{d}\theta}. \tag{8.48}$$

From these, averaging over quantum states is obtained by[186]:

$$\langle S_0(T_s)\rangle = \frac{\sum\limits_{v=0}^{v=v_{max}}\sum\limits_{J=0}^{J=J_{max}} F(v, J, T_s)\cdot\langle S_0(v, J, T_s)\rangle}{\sum\limits_{v=0}^{v=v_{max}}\sum\limits_{J=0}^{J=J_{max}} F(v, J, T_s)}, \tag{8.49}$$

with $F(v, J, T_s)$ as given in eq. (8.34), while v_{max} as well as J_{max} indicate the highest states for which RPCs have been determined. Using this model and methodology, E_{act} values have been simulated for all studied systems, and are presented in sections 10.2.1.10 and 10.2.2.9.

Chapter 9

Experimental

This chapter contains the description of the experimental setup as well as detailed descriptions of the procedures and techniques to conduct these experiments.

9.1 Setup

9.1.1 Vacuum Setup

The following sections describe several aspects of the experimental vacuum setup. The stainless steel chambers were homebuilt by the workshop of the institute according to custom design decisions, which will not be elaborated here.

9.1.1.1 Overview

The vacuum setup consists of two differentially pumped stages in three adjacent chambers. An overview is given by Inventor[265] drawings presented in fig. 9.1. All highlighted aspects will be described in more detail in the following subsections. Overviews of the total setup are given in panels (i-iv), and cuts in panels (v-vii). The layout of the system is highlighted in panel (iii): the system is built onto a table, with the ion pumps (yellow) as the mount for the vacuum chambers. The detection chamber (red, section 9.1.1.5) contains the whole ion optics and detection setup and is connected to the permeation chamber (green, section 9.1.1.4) via a differential pumping wall. Mounted on top of the permeation chamber are the surface preparation chamber (blue, section 9.1.1.3) and the manipulator (orange).

Ultra high vacuum UHV conditions are achieved in the setup by several ion getter and turbomolecular pumps. It is pointed out that the numbers in the following designations represent the nominal pumping speed for N_2 in $(l\,s^{-1})$. The detection chamber is equipped with a single ion getter (HP-100, Thermionics Laboratories, Hayward) at the bottom and two turbomolecular pumps (Turbovac 450 i / Turbovac SL 80 H, Oerlikon Leybold vacuum, Köln) attached to the side, where the smaller pump was used as compression stage for the larger pump. Working pressures were in the range of $(0.1\text{–}2.0) \times 10^{-9}$ mbar.

Due to the direct connection of the other two chambers, their working pressures were the same. These chambers were pumped with one ion getter pump (HP-500, Thermionics Laboratories, Hayward) and one turbomolecular pump (HiPace 80, Pfeiffer Vacuum GmbH, Asslar). Working pressures were in the range of $(0.3\text{–}2.0) \times 10^{-8}$ mbar. During the surface sputtering procedure, the ion getter pump had to be deactivated to prevent sputtering reactions inside the pump itself. Therefore, the working pressure in those chambers reached ~4×10^{-8} mbar, which was considered insignificant in contrast to the argon induced pressure rise to 1×10^{-6} mbar. After this procedure, the argon was pumped away before the ion pump was started again.

Attached to the permeation chamber is an O-ring sealed holder for the laser entry window (see section 9.1.1.4), which was also differentially pumped using a small ion getter pump (HP-045, Thermionics Laboratories, Hayward, not shown), resulting in pressures of $(0.5\text{–}2.0) \times 10^{-6}$ mbar.

9.1.1.2 Sample Mount

For sample handling in UHV, a four axis manipulator (VG Scienta Ltd., St. Leonards-on-Sea, UK) was used. The degrees of freedom included the three translational axes and the rotation around the vertical axis, which corresponds to the sample's θ. The azimuthal angle around the surface normal (ϕ) could only be aligned during the sample assembly in the mount. In this section the sample mount, the sample, the Knudsen cell as well as their heaters are described in detail.

Mount Assembly An Inventor drawing[265] of the sample mount assembly is shown in fig. 9.2. Panel (a) gives a perspective view and panel (b) a cut through the center. Highlighted by numbers are specific parts on the mount on the manipulator axis (1) and the supply lines for permeation gas (6) and cooling water (5). Not shown are the spiraled tubes attached to these supply lines, which allow enough flexibility for rotation of the mount around the vertical axis by $\pm > 90°$. The gas supplies are sealed by 1/8 inch $\varnothing$ Swagelok VCR® connectors using copper gaskets (3). The sample and Knudsen cell (2) are fixed by this mount as well. As heat sink, a copper block (4) is cooled by the water supply (5).

An advantage of the identical mount design for both Knudsen cell and permeation samples is the increased flexibility. Instead of the Knudsen cell and sample combination presented here, two samples could be mounted in this assembly simultaneously. This allowed direct comparison of desorption data acquired under the same experimental conditions.

Single Crystal Samples Figure 9.3 panel (a) gives the cut through view of a schematic drawing of a permeation sample. All samples were machined using the same layout and were delivered already assembled as shown in panel (a) (MaTeck Material-Technologie &
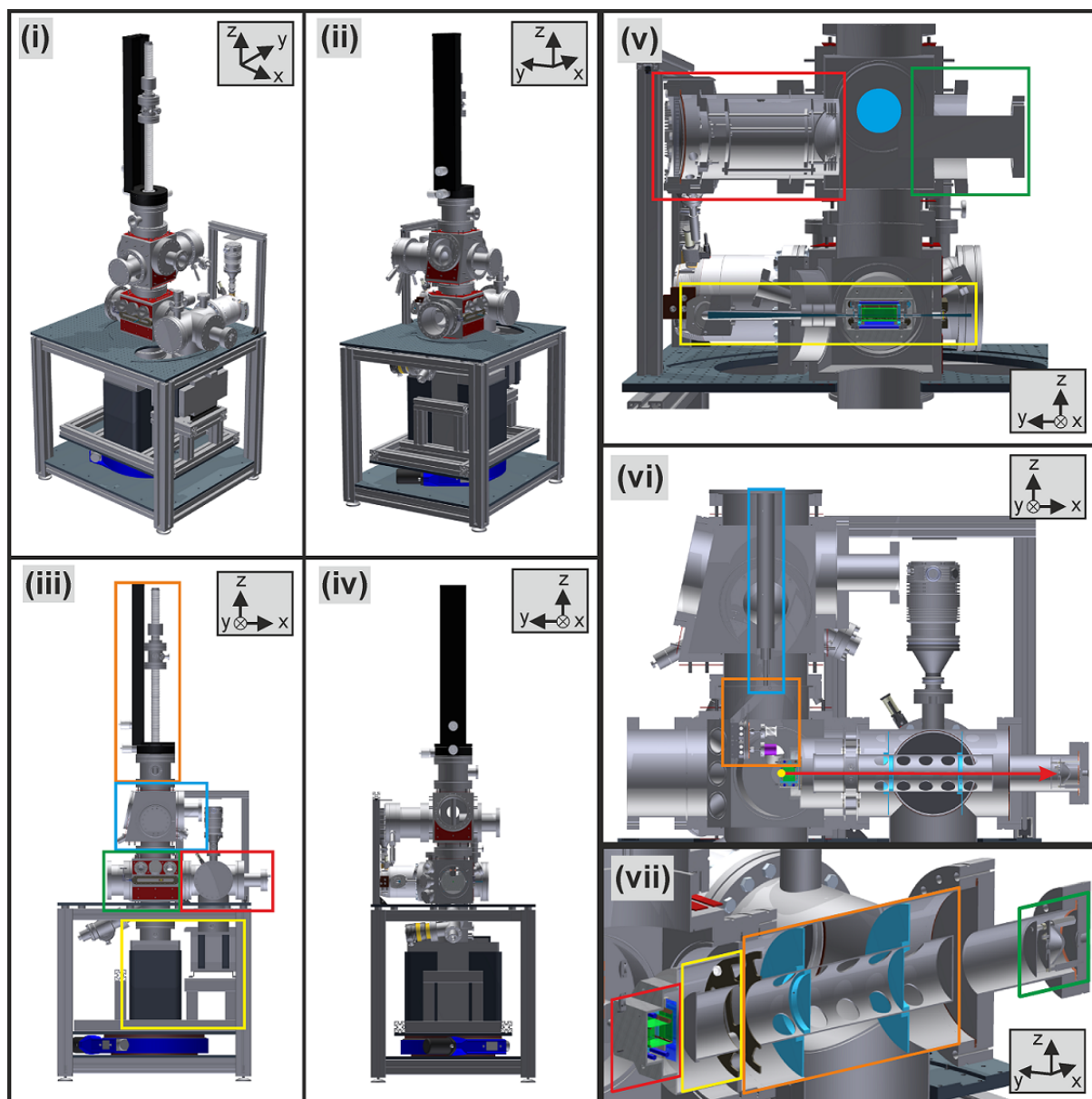
Figure 9.1: Several views showing the total vacuum setup as schematic Inventor[265] drawings. A general coordinate system is indicated in each panel: (x) is the ion flight direction, (y) the laser propagation direction and (z) the vertical axis. Panels (i) and (ii) give perspective overviews of the complete setup, panels (iii) and (iv) views along two axes. In panel (iii), several subassemblies are indicated by colored boxes: the manipulator (orange), surface preparation chamber (blue), permeation chamber (green), detection chamber (red) and the ion pumps (yellow). In the residual panels cuts through the setup are given to illustrate several aspects. For panel (v) the cut is through the plane of laser beam and vertical axis. Highlighted are the devices for LEED (red), Auger (green) and Ar^+ ion sputtering (blue circle); also indicated is the laser beam path (yellow). Panel (vi) shows a cut through the plane of ion propagation (red arrow) and vertical axis. Here, the laser focus point (yellow circle), the sample mount assembly (orange) and the manipulator rod (blue) are highlighted. Finally, panel (vii) gives a perspective view of the same cut and with zoom into the detection chamber. Here, the boxes highlight the parts of the ion optics assembly: the FCA (red), extractor tube (yellow), lens tube (orange) and the MCP detector.
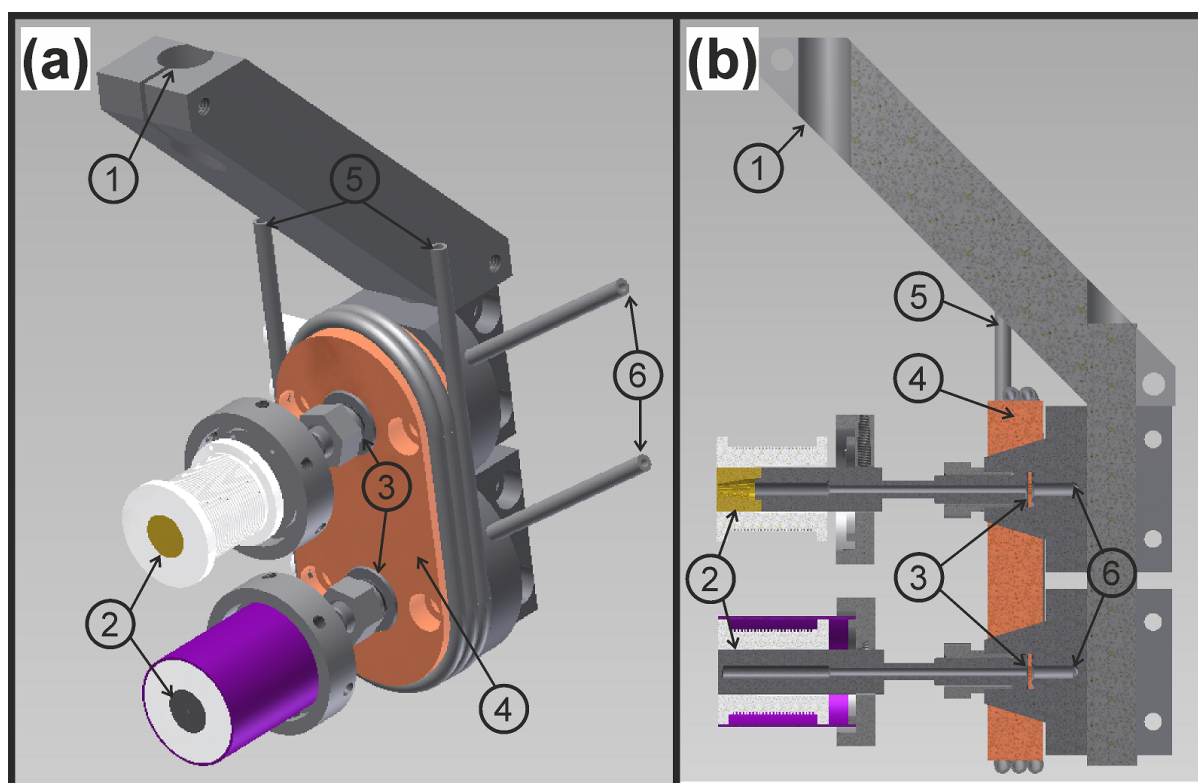
Figure 9.2: Inventor drawing of the sample holder. Panel (a) shows a perspective view, panel (b) a cross cut. The designations are the same in both panels: (1) marks the mount to the manipulator axis, (2) the sample and Knudsen cell assemblies. Those are fixed on the holder using seals with copper gaskets (3, Swagelok VCR® fitting, 1/8 inch ⌀), which is also the connection to both gas supply lines (6). The cooling block (4, orange) was chilled by room temperature water flowing through a tube loop (5).

Kristalle GmbH, Juelich, Germany). Each single crystal (1) was of cylindric shape (8 mm long and 8 mm ⌀), and the front surface was cut and polished to an accuracy of <0.1° to the nominal plane. The inner part of the crystal was eroded to form the depicted channel by electrical discharge machining, until only a ~0.3 mm thin membrane (2) separates the supplied gas from the UHV environment. A hole (3, 1 mm ⌀, ~1.5 mm deep) was eroded into the side of the crystal to hold a thermocouple. All thermocouples used in this work were type K and protected by a stainless steel mantle of 1 mm ⌀. Each sample was brazed with the sample material (4) to a stainless steel support tube (5), which allowed mounting to the sample holder and gas supply (6).

Heater Assembly Figure 9.3 panel (b) shows a cross section drawing of the homebuilt heater assembly design. The main body of the assembly is a homebuilt shape machined from a BN block (3, light grey). It is of cylindrical shape and formed to fit directly on the samples (1, gold). While providing mechanical contact to the sample side, its front was left open in order to avoid interference with the polished facet. BN was chosen as material because it is easily machinable, UHV compatible, with high thermal conductivity and electrically insulating. Spiraling groves held a tantalum wire (99.9 % purity, 0.25 mm

$\varnothing$, Goodfellow, Cambridge Limited, Huntington), which was resistively heated. In order to prevent this heating wire from losing the contact upon thermal expansion, additional BN parts (4, brown) held it in place. These parts were held together using a tantalum tube (2, purple), which also served as heat shield. A groove in the inner opening allowed to fit and fix the thermocouple (5, turquoise) to the sample. This assembly was mounted on a stainless steel ring-shaped part (6, dark grey), which then allowed for attachment on the samples. This was done by pressing screws on stainless steel parts of the samples and thus also allowes for exact adjustment of their relative position.

Panel (c) of fig. 9.3 shows a photograph of a mounted sample without the heater assembly as well as a Knudsen cell with attached heater (6). The sample (1) shown is Au(111), with the thermocouple already attached (2). In order to prevent permeation of hydrogen through the stainless steel support cylinder (cf. section 8.2.3 and fig. 8.2), this had to be cooled efficiently. As stated above, cooling is provided by the copper block (5) and thermal condition through the stainless steel tube. Therefore, copper clamps (3, 4) were attached to the sample and cooling block which were connected by copper wires, greatly enhancing the cooling rate.

Knudsen Cell A Knudsen cell was employed to produce beams with Maxwell-Boltzmann velocity distributions for calibration of the experiment. For this, hydrogen and deuterium was supplied alternatively to the Knudsen cell at several temperatures and in the range of ~300–800 K.

The Knudsen cell design consisted of a hollow copper cylinder capped with a molybdenum aperture (A0610M, Plano GmbH, Wetzlar). This aperture had a thickness of 125 μm and a hole $\varnothing$ of 300 μm. The hole diameter increases to the outer side at an angle of 90°, in order to avoid any channeling effects for the effusion flux. Figure 9.4 gives a cross section view of the schematic Knudsen cell design. Like the samples, it is mounted via a 1/8 inch $\varnothing$, Swagelok VCR® seal with copper gasket (4). A stainless steel gas supply tube is attached (3), onto which the cylindrical copper body (2) was brazed. With its outer dimensions similar to the samples, this allowed the use of the same heater assembly design as for the samples. The gas supply tube inside the copper cylinder (3) had holes perpendicular to the main aperture, which ensured that no direct flux from the stainless steel to the front aperture was possible (1). Thermocouples were fixed into a small hole in the side of the copper body, as for the samples.

9.1.1.3   Surface Preparation Chamber

In the upper part of the machine, a cross shaped chamber was set up for surface preparation and handling. The manipulator was mounted on top so that the sample holder could be translated vertically to the permeation chamber below and rotated around the vertical axis. This allowed positioning the sample relative to the three surface preparation and
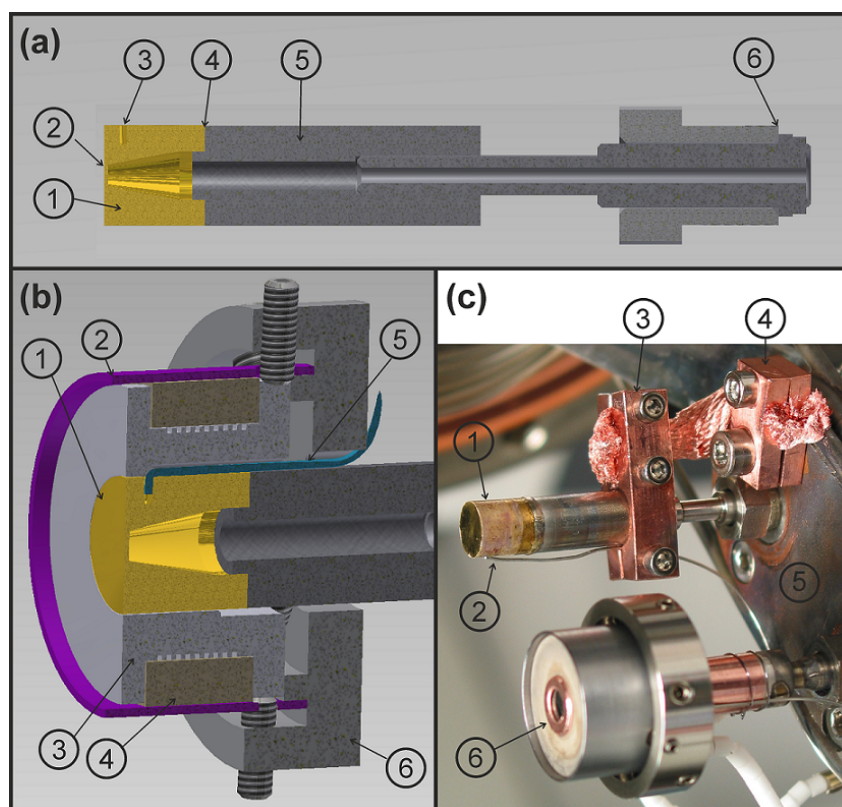
Figure 9.3: Panel (a): schematic cross section of the inventor drawing of the sample geometry. The single crystal cylinders (1, gold) were eroded to contain a channel from the gas supply to the polished surface (2). The residual membrane was specified as ~0.3 mm thick. In the side of each sample, a hole (1 mm $\varnothing$, ~1.5 mm deep) was eroded to serve as mount for the thermocouple (3). The connection to the stainless steel gas supply tube (5, grey) was achieved by brazing with the sample material. This assembly was fixed in the sample mount using a seal (6, 1/8 inch $\varnothing$, Swagelok VCR®) with copper gaskets. In panel (b), the cross section of the sample heater assembly is shown as schematic. The sample (1, gold) is surrounded by a homemade BN (3, light grey) part, leaving the front surface open. This BN part had mechanical contact to the sample and served as electrical insulation to and holder for the tungsten heating wire, which was coiled into the shown grooves. Additional BN parts (4, brown) were machined to keep the wire inside these grooves upon thermal expansion. These were held together by a tantalum tube (2, purple) which also served as heat shield. Another groove was eroded into the BN part (3) to fixate the thermocouple (5, turquoise). This assembly was mounted onto a stainless steel holder (6, dark grey), which consisted of a ground plate and a ring. The mounted heater assembly (2-4) was fixed with screws onto the holder and the holder itself was restrained on the stainless steel part of the sample by additional screws, so that the heater position on the sample could be adjusted. Panel (c) shows a photograph of the sample holder during the mounting process. The Au(111) sample (1) is fixed in the sample holder and the thermocouple (2) is already attached. Copper clamps (3, 4) and wires are used to improve the thermal conduction between sample mount and cooling block (5) in the holder assembly. (6) marks the Knudsen cell, which is already equipped with a heater assembly.
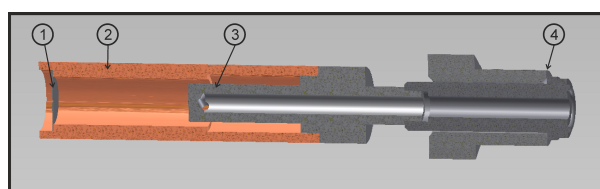
Figure 9.4: Cross section of the Inventor drawing of the Knudsen cell. The front aperture (1, grey, 150 µm $\varnothing$) used in this setup was a commercially available molybdenum plate (A0610M, Plano GmbH, Wetzlar). The aperture is held by a copper body (2, orange) which also serves as the gas reservoir. It was brazed to the cylindrical gas supply and mounting tube (3, grey) which had a connection hole perpendicular to the effusion direction. This assembly was fixed in the sample mount using a seal (4, 1/8 inch $\varnothing$, Swagelok VCR®) with copper gasket.

validation devices mounted on the horizontal connections along with a viewport. The surface device are an Ar^+-ion gun (Ion Source IQE 11/35, SPECS GmbH, Berlin) for sputtering. For annealing of the sputtered surfaces the heater on the sample was used. Absence of surface contaminants was successively checked by Auger electron spectroscopy (AES) (ESA100, STAIB Instruments GmbH, Langenbach) and the surface structure by LEED (ErLEED 3000 D, SPECS GmbH, Berlin).

9.1.1.4 Permeation Chamber

This chamber served as central connection to the other chambers and held the main vacuum pumps. It further mounted a hot filament ion gauge for pressure measurement, a viewport and the laser windows. In this chamber, the samples were positioned in front of the tantalum shield aperture mounted before the differential pumping wall to the detection chamber. This allowed pressure reduction in the detection chamber during permeation experiments as well as thermal shielding of the FCA from the sample heater radiation. Furthermore were this chamber's dimensions big enough to rotate the sample for angular measurements.

In fig. 9.5 panel (d), a cut through the horizontal plane shows the laser pathway (turquoise, vertical shape) through the main chamber, with the outer chamber walls hidden for clarity. The grey bar at the bottom shows the position of the holder for the laser entry window. As windows, MgF_2 crystals [(15.0 ± 0.1) mm $\varnothing$, (1.5 ± 0.1) mm thickness, polished for laser applications using UV light] were employed (Korth Kristalle GmbH, Altenholz). The holder design allowed exchange of these o-ring (Viton) sealed windows as soon as optical damage was observed. A differential pumping stage in the holder allowed achievement of UHV conditions in the main chamber. After passing through the FCA, the diverging laser beam passes an assembly of light baffles, each with increasing aperture diameter to block light which is reflected from the exit window and propagates back to the FCA region. To reduce this back-scattering, the laser exit window (CaF_2 viewport) is mounted on a flange in the Brewster angle corresponding to the employed wavelength range (58.6° for 205 nm). It is shown here rotated by 90°. For better illustration. Behind the laser exit window, the residual light was dumped outside the chamber.

9.1.1.5 Detection Chamber

This chamber held the devices for detection and measurement of the permeation flux. It was connected to the permeation chamber (section 9.1.1.4) by a differentially pumped wall with holes for the desorbing flux and laser propagation. Figure 9.5 shows Inventor[265] drawings of this chamber. Panel (a) gives an enlarged section of the cut through view of the differential wall, also holding the FCA, which is described in detail in section 9.1.1.6. The capped tube on the right-hand side represents the extractor tube of the ion optics,
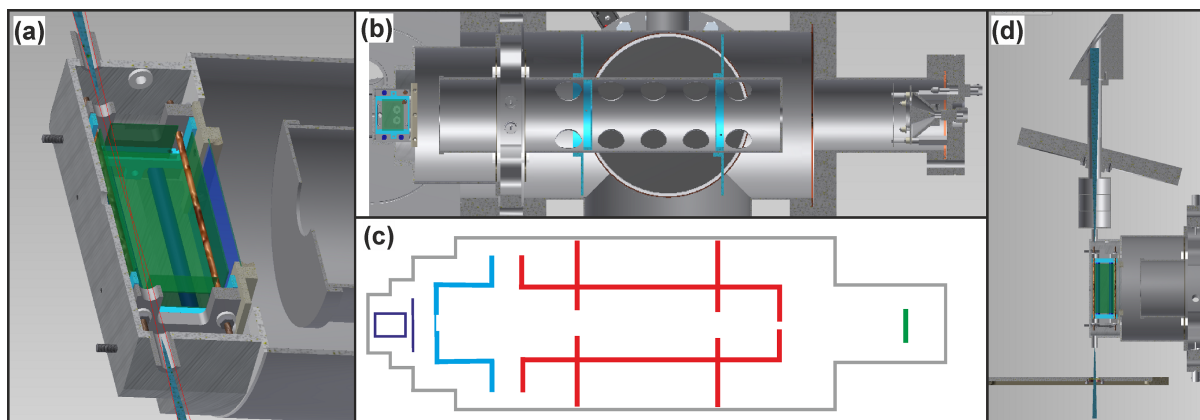
Figure 9.5: Cross section of Inventor [265] drawings of the detection chamber layout. Panel (a) shows a cut through the FCA, which is discussed in detail in section section 9.1.1.6. The capped tube on the right hand side represents the extractor; the assumed laser focus is indicated by the red lines. Panel (b) gives the center cross section through the detection setup in the plane perpendicular to the laser beam. For better contrast, panel (c) gives a schematic representation of the relevant parts. The grey lines represent the borders of the detection chamber, purple the FCA and SM. The extractor tube is shown as blue lines, the lens tube and the light baffles (light blue in panel (b)) in red and finally the MCP detector in green. Panel (d) gives a cross section in the plane of laser beam and ion flight path, showing the laser path through the setup. The outer chamber walls have been faded out for clarity. While the detection chamber is recognizable from the cut already shown in panel (a), the main chamber is only limited by the laser windows. The grey line at the bottom shows the holder for the laser entry window. The laser beam, indicated by the vertical turquoise area, is focused into the FCA (compare panel (a)) and passes through as diverging beam. Behind the FCA a tube including light baffles with increasing aperture diameters is situated, which blocks light reflected from the exit window. The assembly is shown in panel (d) above the FCA. To reduce backscattering, the laser exit window is mounted on a flange in the Brewster angle corresponding to the employed wavelength range. Here, it is shown rotated by 90° for better illustration.

and the laser propagation is indicated by the red lines. The tantalum heat shield (50 mm × 50 mm, 1.2 mm thick, 3 mm aperture diameter) on the differential wall is not depicted.

Panel (b) gives a cross section through the center of the detection setup in the plane perpendicular to the laser beam. In panel (c) the same view is represented schematically, in order to highlight the relevant parts. The grey lines represent the outer borders, purple lines the FCA. The ion optics consisted of two stainless steel tubes with 75 mm outer diameter, held at attractive potentials for cations. The first tube (blue, "extractor", $-30\,\text{V}$) was capped with a plate and 20 mm ∅ aperture. This was covered with a mesh, in order to extract the ions emerging from the FCA with a homogeneous electric field. A second tube (red, "lens") was held at a higher potential ($-1200\,\text{V}$) to accelerate and focus the particles onto the MCP detector (green, $-2100\,\text{V}$). The lens was equipped with light blocking baffles, holes in the main body for better pumping and an aperture at the end (10 mm ∅). Finally, panel (d) shows the permeation and detection chamber connection as a cut through the plane of laser beam and ion propagation, and was already described in section 9.1.1.4.

9.1.1.6 Faraday Cage Assembly

To obtain almost distortion free conditions, a Faraday cage assembly (FCA) of rectangular parallelepiped form was constructed from tungsten meshes, which were coated with graphite. Based on the design by Michelsen *et al.*[182,185], several improvements were implemented. The resulting design, coating method and heating are described in detail in the following paragraphs.

As main requirements, the drift length inside the FCA was sufficiently long (~30 mm) to allow the resolution of the velocity distributions. During acquisition, the number of ions generated by each laser pulse was kept low enough to exclude space charge effects (cf. section 8.2.6.1).

Design Figure 9.6 shows Inventor[265] drawings during several stages of assembling of the FCA design in perspective view. In addition, fig. 9.7 shows schematic cuts through the FCA.

The ion drift region of the FCA was limited by tungsten meshes (Advent Research Materials Ltd, Oxford, England, 99.95 % transmission, 0.025 mm wire $\varnothing$). Their coating with graphite is described in a paragraph below. This mesh was used to build the Faraday cage and an additional shielding mesh (SM) (43 mm × 53 mm). This SM increased the field homogeneity to the ion optics, elongated the drift length, and improved the electrical shielding along the lateral direction.

In fig. 9.6, these meshes are shown as green shaded region for the Faraday cage, and as dark blue shaded region for the SM. Four sides of the Faraday cage are composed of a single, large mesh (panel (iv), ~105 mm long and ~60 mm wide). The other two sides along the laser propagation direction were closed by additional, smaller meshes (panel (ii), ~30 mm × ~30 mm).

To form the Faraday cage, the main mesh was wrapped around metal rods (brown in panels (iii and iv), 2 mm $\varnothing$, WCu alloy), tightened by end rods and fixed there. Since this mesh was resistively heated, the side meshes had no direct contact to it and were simply grounded by their holding frames (grey and light blue, panels (i-iii), aluminium). Holes for laser propagation (4 mm $\varnothing$), the small gap between both ends of the main mesh, and the non-contacted side meshes are shown in the cut in panel (iii). Also shown in panels (ii and iii) is a lever screw (brown, behind mesh), fixing the rotation angle of the main mesh end rod and thereby allowing the tightening of the whole mesh.

Panel (iv) and panel (v), respectively, show the FCA with and without the SM mounted on top of the main frames (grey). The aluminium rods (dark blue), which fix the separation of both frames and give the assembly a total length of 102 mm along this direction are also shown. Finally, panel (vi) shows the FCA mounted inside the holder, which also served as differential pumping wall.

In this design, the total dimensions of the drift region, as limited by the meshes, were:

32.5 mm in ion drift direction, 60 mm along the laser propagation direction and a width of 20 mm. Ions generated inside were only exposed to meshes and holding rods but not to the supporting frame or insulating ceramics.

This is shown more clearly in fig. 9.7. In each panel, the lower right corner gives the coordinate system of three axes: (x) the ion drift direction, (y) the laser propagation direction and (z) the remaining direction. In panel (i), some features are highlighted: (1) marks the rods shaping the main mesh (2) to form four sides of the Faraday cage. (3) gives the approximate laser focal position where the ions are generated, (4) the SM and end of the ion drift region. Finally, (5) marks the nuts of mounting screws, which allow accurate positioning of the FCA relative to the laser. Panels (i to iii) show the FCA itself and panels (iv and v) how it is mounted on the differential wall. In panel (iv) the following are highlighted: the nuts on the mounting screws (1), which position and adjust the FCA on the differential wall relative to the laser focal position (2, red dot). Because the laser position is determined by the vacuum chamber design, the alignment of the final ion drift length (3, green arrow) can only be achieved by these nuts (1).

Coating Methods   In order to improve the FCA properties, the tungsten meshes were coated with graphite. Three different methods were employed for further optimization. First, dipping the meshes in an aqueous suspension (Aquadag E, Henkel Corporation, Michigan) and subsequent drying was tested[182,185]. While this method proved employable, some properties emerged as disadvantageous. Additionally to coating the wires with a rather thick layer were some holes in the mesh closed by the coating, which reduced the overall transmission. Furthermore, the coated layer was very brittle and hence sensitive to deformation. During the assembly, parts of the coating simply fell off and reduced the homogeneity of the coating and quality.

Following Kummer and Kirchhoff[277] a pyrolysis method was also employed. Here, the meshes were resistively heated under a stream of acetone in argon gas, resulting in pyrolysis and carbon deposition on the hot regions. Unfortunately, this method proved unsuitable for our design: due to the significant upscaling of the mesh size, the effect of inhomogeneities in the mesh structure became significant. These were unavoidable during the assembly and led to hotspots in the resistively heated meshes and successive damage during the coating process up to total destruction.

Finally, a spray coating method using isopropanole-based colloidal graphite (Graphit 33, CRC Industries Europe) proved as most effective to form a thin, homogeneous graphite layer. By adjustment of the distance between mesh and spray source, homogeneity and layer thickness could be varied to satisfaction. Due to the reduced thickness, the coating was less brittle and sensitive to mechanical deformation during further assembly.

This graphite coating improved the drift conditions greatly in contrast to the pure mesh, supposedly due to the enhanced surface roughness, which allowed patch charges

induced by adsorbed particles to discharge more easily. While the total transmission of ions was not reduced significantly, the coating had a different disadvantage, i.e. reduced thermal stability. Despite the meshes being heated during experiments (see paragraph below), excessive heat from other sources (like the sample heater) led to the destruction of the coating structure. This could clearly be seen in the obtained TOF distributions (see section 10.1.2) and by loss of mechanical adhesion between coating and meshes.

Heating   Heating of the main FCA mesh and the SM proved necessary to prevent adsorption of molecules on the meshes, probably water or hydrocarbons. Adsorbates could create patch fields due to their different work functions or by charging, resulting in distortion of the TOF distributions. The presented design allowed for direct, resistive heating (~6–7 W) of these meshes by driving current through them. Both meshes were grounded on one of the metal frames. In order to not disturb the ion drift, the heating current needed to be switched off before the laser pulse (300 μs), and switched back on after sufficient time for all ions to leave the drift region (150 μs after laser pulse).

9.1.1.7   Voltage Switch Device

For independent determination of the t_{shift} parameter (see section 9.2.2.2), the extractor tube in the ion optics was equipped with a homebuilt HV switch device. This device was driven with the laser repetition rate of 50 Hz and each time switched the extractor voltage from ground level to ~30 V. The time response of this device was characterized by probing the output voltage under experimental conditions, recorded the curves with an oscilloscope in different time resolution settings. Results are shown in fig. 9.8, where each panel corresponds to a different time resolution, indicated in red, and shows the switch output in yellow as well as the trigger pulse in blue (with y-scale 1 V). The relevant device properties derived from these measurements are summarized in the following paragraph.

The decay time constant of the device is ~800 μs (fig. 9.8 panel (a)), which is sufficient for the 20 ms time interval between two laser shots. In contrast, the variation of the potential over the time range of the experiment (<100 μs) is sufficiently small (panel (b)): ~3 V / 10 % over 100 μs. The slight overshoot (~5 V) of the voltage level is in the order of ~15 %. The time response of the rising voltage varies strongly over the first microsecond and is overlaid by an oscillation on the timescale of tens of nanoseconds (panels (c) and (d)). The initial rise on the course of ~20 ns reaches ~67 % of the nominal value and completes after ~400 ns. Panel (d) clearly shows a delay between trigger pulse and rising edge of ~100 ns, which has to be taken into account when analyzing the experimental traces (section 10.1.4.1).

The described deviations of the HV-switch properties from ideal behavior result in an error estimate of 0.1 μs for these measurements and an additional delay of 0.1 μs.
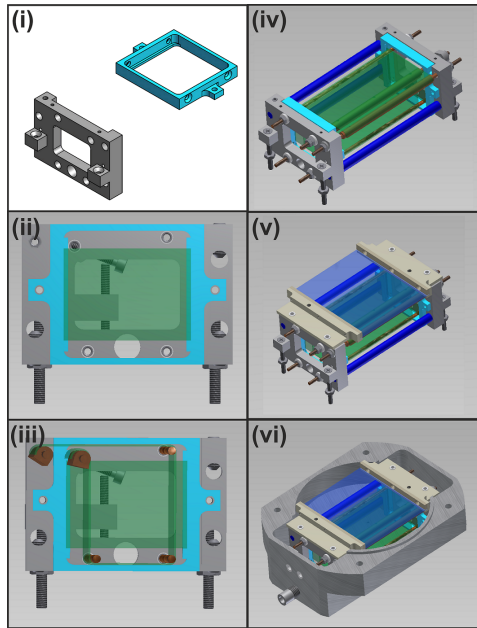
Figure 9.6: AutoCAD[265] drawings of the FCA in different steps of detail and assembly. (i) One of the main frames (grey) and holders for the side meshes (blue). These meshes close the FCA in the plane perpendicular to the laser propagation direction. In panel (ii) the assembled parts are shown with the mesh indicated by the green, semi-transparent area. The only open area reaching into the FCA is the hole at the bottom through which the laser beam propagates. In panel (iii) the WCu rods (brown) and the main mesh (green) are added. This view is cut after few mm inside the FCA. Panel (iv) gives a perspective view with the same elements as before and no cut. Rods are shown which separate both frame parts (dark blue) and fix their distance. The white parts are ceramics for electrical insulation. In panel (v), the SM (semi-transparent, blue) and its holders are added. Finally, panel (vi) shows the FCA when assembled into the differential wall.
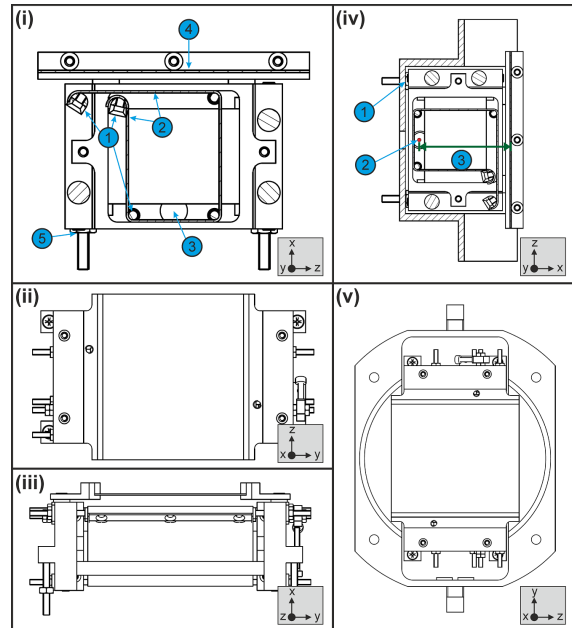
Figure 9.7: Schematic drawings[265] of the FCA from different perspectives. The coordinate system is given in the lower right corner of each panel. The axes show the directions of the ion drift (x) and the laser propagation (y) with (z) being perpendicular to both. The FCA is shown from different perspectives in panels (i)-(iii) with additional highlights in panel (i). (1) points to the WCu rods mounting the main mesh (2), which is electrically insulated from the holding frame. The position of the laser focus is indicated by (3). (4) points to the SM which marks the end of the free drift region. The last highlighted (5) parts are the mounting screws used to fix the FCA in the holder which is also the differential wall. The mounted assembly is shown in panels (iv) and (v). Finally, panel (iv) highlights points of the assembly responsible for the total drift length. Using nuts on the mounting screws (1) allows the adjustment of the exact FCA position in the chamber. Since the laser beam path (2) is fixed by the laser windows and baffles, the resulting drift length (3) can be varied by this adjustment.

Figure 9.8: Measured time response of the homebuilt HV switch device. The output of the switch was probed under experimental conditions and recorded with an oscilloscope using different time resolution settings. The results are shown in panels (a) to (d). The corresponding time resolution is indicated in red. In each panel the blue curve gives the trigger pulse supplied to the device and the yellow curve the response on the output of the HV switch.
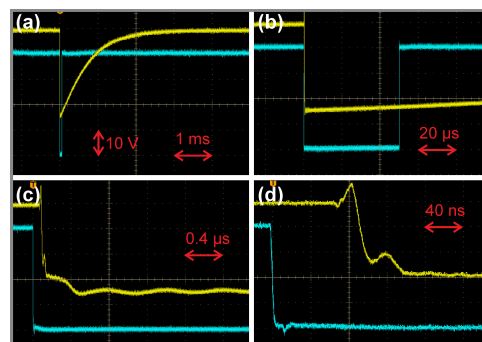
9.1.1.8 Other Devices

Several devices in this experiment were managed by a computer using a homebuilt program in the LabView programming environment (LabView2011, National Instruments, Austin). This program controlled the laser system as well as the data acquisition and handling. Ion signals were detected by an homebuilt MCP detector design with impedance matched output from commercial plates (MCP, Scientific Instruments GmbH, Gilching, Germany, Chevron setup). This electrical signal was preamplified and recorded by a multi channel scaler (EG&G Ortec, Turbo MCS). After each acquisition, the data was transferred to the control computer and stored in a file together with other relevant information, e.g. laser characteristics.

Other devices were controlled manually. Triggering and timing between devices was achieved by delay generators (DG535, Stanford Research Systems, Inc.). Ion optics were held at constant potentials by high voltage supplies (SRS PS350, Stanford Research Systems, Sunnyvale). All four heaters (FCA, SM, sample and Knudsen heaters) were controlled with a four channel power supply (HMP4040, Rhode & Schwarz, München).

9.1.1.9 Detection Geometry

Schematic views of the detection geometry relevant to TOF distributions are given in fig. 9.9. It shows the region between sample and extractor tube as projected onto two planes, with the coordinate system indicated in the lower right corner. Panel (a) shows the plane perpendicular to the laser beam propagation (y), panel (b) the plane defined by (y) and the ion flight direction (x). Several aspects are marked in both panels. Solid surfaces are the sample (orange, 1), the differential wall and tantalum shield (dark blue, 2), and the cap of the extractor tube (dark blue, 6). Meshes are indicated by dotted lines, as for the extractor (6). Nominally field-free regions are shaded, for the FCA (light gray, 4) and the SM (dark grey, 5). The laser focal line (red, 3) and the linear projection of the extractor tube aperture (blue dashed lines) are also shown. Green arrows indicate ion trajectories, chosen to show the maximum angles in each plane, which are detectable in this geometry.

It is pointed out that the resulting volumetric shape determined by all detectable trajectories differs vastly from the cone shape depicted in fig. 8.8. Another geometry is achieved for Knudsen cell measurements, where the sample surface in fig. 9.9 simply is replaced by one with the radius of the Knudsen orifice. In contrast, the geometric profile producing the TB is based on the laser volume as source (see fig. 10.7), which results in an increased amount of trajectories with higher θ. Numerical simulations to determine the distribution of angles for each setup are presented in section 8.2.7.1.
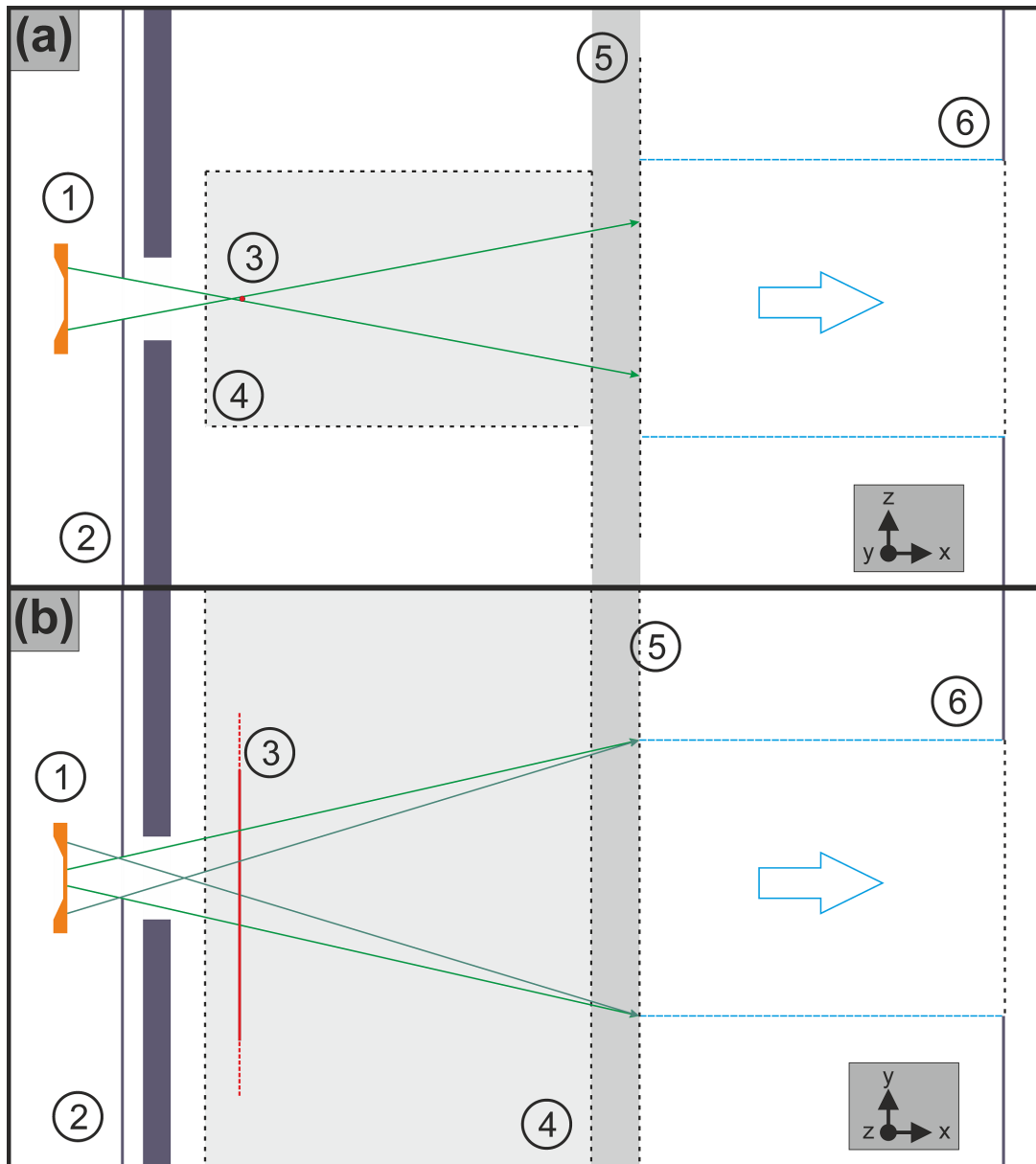
Figure 9.9: Schematic drawings illustrating how the angular acceptance of the setup is determined. Both panels show projections along a certain axis with the coordinate system given in the lower right corner. Panel (a) shows the plane perpendicular to the laser propagation axis (y) and panel (b) the plane containing the laser (y) and the ion flight direction (x). Both are to scale, corresponding to a certain build of the FCA, with the exact dimensions and the position relative to the laser beam could vary by few mm in each assembly. The legend is the same for both panels. Meshes are indicated by dashed lines. The sample (1, orange) is separated by the tantalum shield (2, thin purple line) and differential wall (2, thick purple line) from the FCA (4, light gray area). The laser focus (3) is a spot in both transversal directions (panel (a)) and a line - of not exactly defined length - in its longitudinal dimension (panel (b)). The region between FCA and SM (5, dashed line) is indicated by the dark gray area. Finally, the extractor tube (6, thin purple line and dashed line) is several cm away from the SM. When assuming a strong and homogeneous extraction field, the aperture on the extractor limits the trajectories which are able to reach the detector and can be projected (blue) onto the SM. In combination with the aperture in the tantalum shield (2), the experimental geometry causes well defined restrictions, resulting in the limiting trajectories indicated by green arrows.

9.1.2   Laser System

To generate the radiation necessary for the (2+1) REMPI a narrow bandwith dye laser (PrecisionScan, Sirah Laser- und Plasmatechnik, Kaarst) was employed. The dye laser was optically pumped by the second harmonic (532 nm) from a Nd:YAG (Powerlite 8050, Continuum, Santa Clara) at a frequency of 50 Hz and with pulse energies of ~190 mJ. The internal layout of the dye laser consisted of a single beam line and two dye capillaries optically pumped at three positions, thus generating three stages: resonator, preamplifier and main amplifier. Emission frequency of the dye laser was adjusted by a tunable grating in the resonator and verified using a wavemeter (WS-7, HighFinesse/Ångstrom, Tübingen). This laser radiation was frequency doubled in a beta-barium borate; β-BaB$_2$O$_4$ (BBO) - crystal and the generated second harmonic was successively mixed with the remainder of the fundamental radiation in a second BBO. This generated the third harmonic of the radiation, which resulted in UV pulses (200–220 nm) with energies of ~0.5–1.0 mJ and ~7 ns duration.

The radiation was guided to the UHV chamber via dielectric coated mirrors, which also separated the UV radiation from the residual fundamental and second harmonic. A spherical plano-convex lens focused the beam into the chamber with a 205 mm focal length. The desired beam path was defined by several baffles (section 9.1.1.4) to reduce the stray light on the detector. The correct alignment was additionally controlled by iris apertures next to the laser entry and exit windows, allowing to verify and reproduce the focal position to an accuracy of ~0.1 mm. Furthermore, a quartz wedge placed in the beam line allowed online measurement of the laser power.

In the course of this experiment a wavelength range of 200–220 nm had to be covered. This was achieved by two sets of laser dyes (appendix E) and accompanying dielectric coated mirrors. The set for the range of ~200–209 nm utilized a dye mixture of Rhodamines "101" and "B" in ethanol and was employed to detect molecules in the vibrational ground state as well as most of the D$_2$ ($v = 1$) $J-$sequence. As second setup, the dye "DCM" in ethanol was used and provided the wavelength range ~206–220 nm. This covered the detection range for vibrationally excited molecules, including the D$_2$ ($v = 1$) $J-$sequence as well.

For REMPI experiments (section 8.2.5.2), the maximum of each resonant transition was verified before TOF profiles were acquired. Wavelength reproducibility for successive experiments was provided by the wavemeter. Additionally verified was the required detuning for "off-resonant" acquisitions: the frequency of the laser was changed by ~140 GHz, corresponding to a wavelength shift of 20 pm at ~205 nm. For those traces, the laser power differed insignificantly and therefore most disturbing contributions were unchanged. Direct subtraction of these off-resonant traces allowed for correction of most noise signals.

Table 9.1: Table of the surface preparation procedures for each sample.

Procedure	Detail	Cu(111)	Cu(211)	Au(111)
Sputtering	Duration / min	20	30	25
	Ion Energy / keV	3	1	3
	Argon-pressure / 10^{-6} mbar	1	2	1
Annealing	Temperature / K	725	725	775
	Duration / min	20	20	20

9.2 Procedures

9.2.1 Surface Preparation

The single crystal surfaces had to be cleaned and prepared before the permeation experiments. Their cleanliness and structure had to be verified using AES and LEED. All studied samples were prepared by repeated cycles of sputtering and annealing until no contaminants could be detected on the surface. During the permeation experiment contaminants could diffuse from the bulk to the surface, due to the high sample temperature. After a few hours contamination levels rose to detectable amounts and needed to be cleaned again. In this way, the bulk contaminants were depleted over several cycles before the samples were used for experiments. Details of the cleaning procedure for each sample are given in table 9.1.

9.2.1.1 Auger Electron Spectroscopy

AES spectra are given in fig. 9.10 for Au(111) (panel (a)) and Cu(211) (panel(b)) Cu(111) spectra are not given since they are similar to Cu(111). In fig. 9.10, each panel gives an instructive spectrum of a contaminated (black) and sputter-annealed surface (red), which are representative of contaminant-free surfaces (cf. e.g.[278,279]). Relevant initial surface contaminants were carbon, nitrogen, oxygen and sulphur, with their strongest AES peaks at 275 eV, 389 eV, 510 eV and 153 eV, respectively[280]. For Au(111), the most persistent contaminant was carbon (as is apparent in fig. 9.10 panel (a)), which could be removed by repeated sputter-annealing cycles similar to the Cu(111) sample. In contrast, the Cu(211) sample was heavily contaminated with sulphur, which also easily segregated to the surface at higher temperatures. In fig. 9.10 panel (c) the strongest AES peaks of sulphur and copper are shown, which were used for a peak-to-peak analysis to determine the fraction of sulphur on the surface[280]. The sulphur concentration was decreased from 7.2 % of a monolayer (black) down to <0.8 %, which is close to the detection limit of the instrument. The preparation included sputter-anneal cycles as well as permeation at 925 K for several hours, which resulted in a total interval of two weeks in between the depicted spectra. Carbon contaminations were reduced to be less than 5 % of a monolayer before all permeation experiments.

9.2.1.2 Low Energy Electron Diffraction

The surface structure of the samples was verified using LEED and representative patterns are given in fig. 9.11, with electron energies 130 eV for the Au(111) pattern and 167 eV for all copper patterns shown. Panels (a), (b) and (d) show LEED patterns at ~300 K of Au(111), Cu(111) and Cu(211), respectively. The (111) facets show clear patterns expected from well ordered surfaces (cf. e.g.[281–283]). For the (211) facet shown in panel (d), the surface unit cell is also indicated (red, cf. e.g.[284]). In an attempt to obtain LEED patterns of the samples at elevated temperatures, we found the Cu(111) facet to be stable up to the permeation temperature (925 K, panel (c)). In contrast, the Au(111) pattern started to blur at elevated temperatures and disappeared at 925 K. For Cu(211), the pattern starts to blur at 650 K (panel (e)) and is completely vanished at 925 K (panel (f)). Assumptions regarding the surface structure cannot be made from the observed blurs in LEED measurements, since the Debye-Waller attenuation factors are not quantified for each facet[285].

9.2.2 Time of Flight Measurements

Generally, an off-resonant trace (section 9.1.2) was also acquired for each TOF trace under the same conditions and subtracted to correct most noise contributions. The number of laser shots for a single acquisition did not exceed 50 k, before the corresponding off-resonant measurement was conducted. If necessary, several successive runs were added to achieve a satisfactory SNR. This limitation ensured that slow drifts in experimental conditions could be identified and thus excluded in the analysis 50 k pulses correspond to an acquisition time of ~17 min.

While it was technically possible to obtain TOF traces with a resolution of 5 ns, it was found that restriction to a 20 ns bin width did not have a distorting effect but improved the immediate SNR substantially. The total number of bins varied slightly between measurements, but was chosen to always include the complete TOF signal and some noise afterwards (50–100 µs). Despite being redundant, later TOFs had the disadvantage to overlap with the heating current of the FCA (see section 9.1.1.6).

In the following subsections, additional information for several experimental techniques are given.

9.2.2.1 Knudsen Cell

For the calibration acquisitions using the Knudsen cell (see section 8.2.4.3), the experimental conditions were chosen carefully to avoid distortions on the TOF distribution. From the orifice of the Knudsen cell, the Knudsen condition could be calculated. The mean free path of the molecules inside the cell had to be significantly larger than the orifice diameter. Effusive flow was ensured by keeping the pressure inside the cell at least one
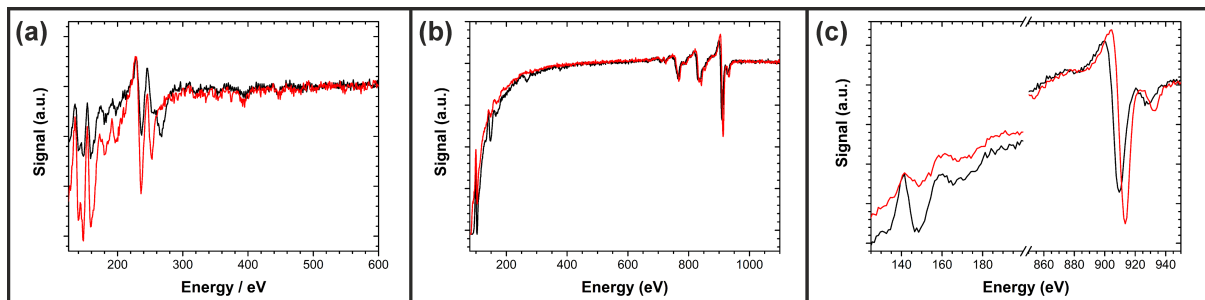
Figure 9.10: AES spectra of the studied samples acquired with 3 keV electron energy. Panel (a) gives Au(111) spectra of a contaminated (black) and a prepared surface (red). In panel (b), similar spectra for Cu(211) are given. Finally, panel (c) shows enlarged sections of panel (b) for analysis of the peak-to-peak ratio. Details are given in the text.
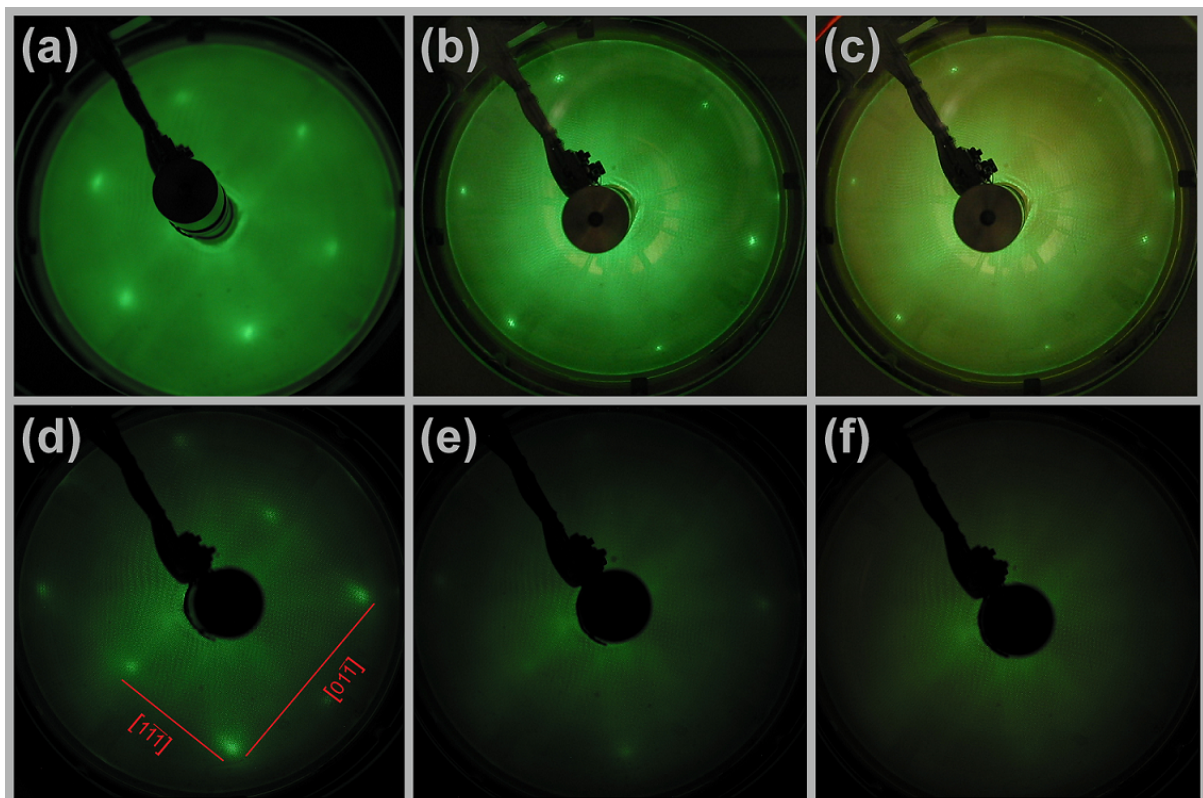
Figure 9.11: LEED patterns of the samples at different temperatures. Patterns of cleaned surfaces at ~300 K are shown in panels (a), (b) and (d) for Au(111), Cu(111) and Cu(211), respectively. In panel (d), the crystallographic directions of the (211) facet are marked (cf. fig. 8.1). At elevated temperatures, the Cu(111) facet remains stable up to the permeation temperature (925 K), as is shown in panel (c). For Cu(211), the pattern starts to blur at 650 K (panel (e)) and is completely vanished at 925 K (panel (f)). The electron energies were 130 eV for Au(111) and 167 eV for all copper patterns shown.

order of magnitude lower than this condition. Furthermore, as described in section 8.2.6.1, the total number of ions generated by each laser pulse had to be kept below the limit where space charge occurred.

With H_2 as probe, the $(v = 0, J = 1)$ state was sampled. Due to the favourable $ortho/para$ ratio and the high rotational quantum (section 8.2.5.1), the relative population of this state was very high. Therefore, the necessary pressure in the Knudsen cell (~5×10^{-2} mbar) and the number of laser pulses to accumulate (10 k) were relatively low. For D_2, $(v = 0, J = 2)$ provided the strongest signal. Here, the $ortho/para$ ratio is less favourable, which was compensated by accumulating signals for more laser pulses (30 k) at the same pressure.

An initial, sophisticated calibration was conducted whenever the alignment of the detection setup was varied, especially the FCA and the laser setup. For this, the temperature range of 300–835 K was probed in several steps using both H_2 and D_2. This gave a sophisticated dataset and allowed restrictive fitting with global parameters.

During regular measurement periods, daily calibration runs before and after each permeation phase were conducted. These included only room temperature measurements and were used to verify the x_0 parameter from the sophisticated calibration as well as to determine the cutoff function (section 8.2.6.2) parameters. It is pointed out that this calibration method was not possible for the laser setup using the "DCM" dye (section 9.1.2), because the quantum states available for probing with that setup were not thermally populated. This problem could be avoided by the introduction of the internal calibration method (see section 9.2.2.3), and application of both methods yielded satisfactory calibration for the setup.

9.2.2.2   Delayed Extraction

As described in section 8.2.4.3, a HV switch device (section 9.1.1.7) could be used to measure the t_{shift} parameter under experimental conditions. For these measurements, room temperature Knudsen cell experiments were applied, H_2 and D_2 just as for daily calibration purposes (see section 9.2.2.1). TOF distributions were acquired and compared for various delays of the HV switch relative to the laser pulse. The results are presented in section 10.1.4.1. Such measurements were only conducted after severe changes in the ion optics assembly, since variations in the detection setup were found to have negligible influence.

9.2.2.3   Internal Calibration Standard

As illustrated in section 8.2.4.3, the internal calibration standards had to be established for each surface and setup geometry. Thus, D_2 $(v = 1, J = 2)$ from each permeation source was measured for 50 k laser shots to provide sufficient SNR and at three temperatures: 873 K, 923 K and 975 K. Fitting this dataset with a global E_0 parameter allowed for a well restrained fit to characterize this internal calibration standard.

On successive measurements, the D_2 $(v = 1, J = 2)$ signal at $923\,K$ was acquired with $50\,k$ laser pulses as first and again as last signal for that respective day. These TOF traces were fitted with the fixed sticking function parameters obtained before and only x_0 and the amplitude as flexible parameters. While not able to characterize the cutoff (section 8.2.6.2), this allowed the determination of the x_0 on a daily basis.

9.2.2.4   Permeation Procedure

Generally, permeation data was acquired with 1 bar of the probe gas supplied to the sample. For HD, a $2 : 1$ mixture of D_2 :H_2 was provided to the sample. The statistic nature of the atomic recombination after permeation results in sufficient isotopic scrambling to produce HD. The ratio of the gases was chosen arbitrarily to compensate for the isotopologue-dependent rates[94]. During the measurements, the crystal surfaces were positioned in the chamber with a nominal distance to the laser focus of ~12.5 mm, resulting in a nominal angular averaging about a 7° half cone angle (see section 8.2.7).

For desorption measurements, the surface temperature for both copper crystals was $(923 \pm 3)\,K$, except for five specific data sets where the temperature was up to $11\,K$ higher. But successive measurements at $923\,K$ showed no distinguishable differences in the results. Acquisition at this temperature ensured adequate SNR, comparability to literature data[175,182,185,189], mechanical stability of the samples and sufficiently low working pressures in the chambers.

In contrast, Au(111) acquisitions had to be performed at a surface temperature of $1061\,K$, due to the lower permeation rates (see section 8.2.3). Problems arose from the increased thermal radiation which heated up the environment, thus leading to outgasing and possibly deterioration of the FCA (see section 9.1.1.6). While the mechanical stability of the crystal structure was high enough to withstand the backing pressure, macroscopic deformation of the sample occurred at higher temperatures. In the area of the thin membrane (~0.3 mm thick), the backing pressure had produced a bump facing towards the vacuum side. Successive LEED characterization still showed patterns corresponding to a (111) surface.

9.2.2.5   Angular Distribution Measurement

In order to measure angular distributions for the desorbing flux, the exact position of the sample surface on the mount assembly had to be determined first. Then positioning of the sample was possible by using the coordinate system on the manipulator axis, which is necessary due to the displacement of the sample surface relative to the rotation axis of the manipulator.

This calibration was performed using AES: the BN of the heater surrounding the sample had a distinctive different spectrum than the samples themselves. By scanning the translational axes of the manipulator the edges of the crystals were determined. Rotation

of the sample and repetition of this procedure then allowed to calculate the distance between the sample surface and the rotation axis of the manipulator by simple geometrical considerations. This information then defined the exact manipulator coordinates necessary to position the sample surface accurately for any given rotation angle.

In the given setup, only slight collimation (~7°) of the desorbing flux was provided. As a consequence, the whole active sample surface was probed in the acquisition of the angular distribution. Therefore, no correction was necessary for the probed surface area in the analysis of those. Geometrical restrictions in the permeation chamber limited the range of polar angles to $-30°$ to $30°$ around the surface normal, and the azimuthal angle could not be varied. Due to the aforementioned angular averaging of 7°, angular distributions were acquired with steps of 5°.

9.2.2.6   Perturbation Characterization

Additionally, tests verifying the influence of residual hydrogen gas in the chambers on other measurements were carried out. To allow comparison to experimental conditions, those tests were performed directly after permeation experiments without changing the source position in the chamber, the laser alignment or other factors like the temperature. Only the gas was pumped away behind the permeation sample, stopping the permeation flux.

First, the ratio of desorbing flux stemming from TB gas scattering off the sample surface was determined. For this, H_2 was bled into the permeation chamber until the same steady state pressure was reached as in the experiment. Repeated measurements for several quantum states yielded an estimate of $\lesssim 3\,\%$ of the total flux originating from such scattered gas. As far as the low SNR allows interpretation, the TOF profile does not differ significantly from the regular desorption distribution and thus is not considered further.

As second test, the TOF profile of TB gas in the detection chamber was obtained. Here, the gas was bled into the detection chamber to reach the steady state pressure $(8.9 \times 10^{-9}\,\text{mbar})$. H_2 and D_2 signals were acquired with $20\,\text{k}$ and $50\,\text{k}$ laser pulses, respectively. A detailed analysis of the acquired TOF traces is presented in section 10.1.5, which allowed successive correction of this contribution in all analysis steps.

Additionally, the desorption flux was checked for atoms. A (2+1) REMPI transition was accessible with the setup, using the Lyman-β transitions as resonant step. An isotopic shift of ~$26.62\,\text{cm}^{-1}$ [286] allowed the separation of H- and D-atoms, but no flux was observable under experimental conditions.

Chapter 10

Results

In the following sections the results of the measurements will be presented. In the first section, the calibration will be treated elaborately, while the second section contains all permeation results and their analyses. A detailed comparison of the latter to results from SRP-DFT theory[167,168,175,201] will be given in a succeeding section. It is pointed out, that some parts of this work have already been published elsewhere[220].

10.1 Calibration Results

Calibration results for the different techniques introduced in section 8.2.4.3 will be given in the following subsections. These treat the general Knudsen cell results, the observed aberrations, the introduced method of using permeation sources as internal calibration standard, and a last subsection for independent determination of the t_{shift} parameter.

10.1.1 Knudsen Method

How to use the effusive flux of a Knudsen cell to calibrate the experimental TOF axis has been described in section 8.2.4.3. Figure 10.1 shows a full calibration dataset obtained by measuring Knudsen TOF distributions at temperatures in the 300–835 K range, for H_2 and D_2. All traces were obtained successively within a few hours, in order to be independent of variations in the laser alignment and FCA conditions (see section 8.2.6.2). As described in section 8.2.4.3, the t_{shift} parameter scales with m/z (see eq. (8.14)) and the use of several temperatures influences the velocity distributions (see eq. (8.15)). This allows the fitting of the shown datasets for one set of global calibration parameters (x_0 and t_{shift}), and this restriction yields more reliable results.

The two parameters describing the cutoff (see eq. (8.21)) E_{slope} and E_{min} are also included globally for this dataset. While the resulting fit quality is satisfactory, this assumption might not be justified. An increased heating power for the Knudsen cell results in significant radiation, which heats up the environment of the FCA snd could easily result in a variation of these parameters. Thus, this approach might be an over-restriction of

Figure 10.1: Overview over several measured Knudsen TOF distributions. Each trace is normalized to the maximum and offset on the vertical axis. Measured (dots) distributions are presented as well as the fit results (purple lines) corresponding to a global x_0 parameter and fixed t_{shift}, as described in section 8.2.4.3. Traces for D_2 (black, red, green, dark blue) and H_2 (light blue, pink, orange, brown) are shown, each for the four different temperatures of 299 K, 490 K, 648 K and 835 K. The parameters describing the cutoff (see eq. (8.21)) in the setup were also obtained globally for the dataset shown. In conclusion the presented model (purple lines) is described by the following four parameters: $x_0 = (29.25 \pm 0.09)\,\text{mm}$; $t_{\text{shift}}^{H_2} = (3.2 \pm 0.1)\,\text{µs}$; $E_{\text{slope}} = (22.8 \pm 0.9)\,\text{eV}^{-1}$ and $E_{\text{min}} = (7.2 \pm 0.3)\,\text{meV}$.
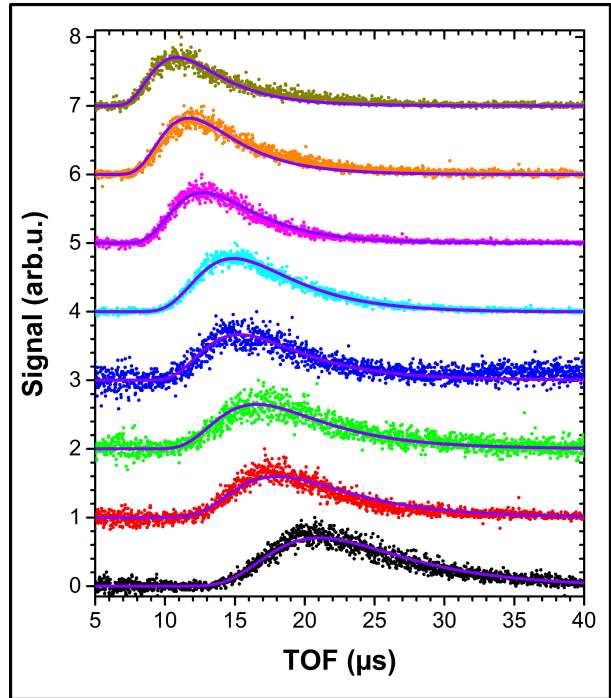
the model. In conclusion, the fitted model (purple lines in fig. 10.1) is described with the following parameters: $x_0 = (29.25 \pm 0.09)\,\text{mm}$; $E_{\text{slope}} = (22.8 \pm 0.9)\,\text{eV}^{-1}$ and $E_{\text{min}} = (7.2 \pm 0.3)\,\text{meV}$. Additionally, the t_{shift} was fixed to $t_{\text{shift}}^{H_2} = (3.2 \pm 0.1)\,\text{µs}$, as described in section 10.1.4.

Such a sophisticated calibration dataset was acquired for every build of the FCA. This gave "nominal" values for each current setup. Alignment of the laser using additional apertures outside the vacuum chamber roughly limited the accuracy to $\lesssim 0.3\,\text{mm}$. To verify the reproducibility, daily calibration measurements were carried out. For these measurements the effort was reduced to room-temperature Knudsen distributions using H_2 and D_2, each before and after the permeation experiments. Global fits of these distributions were then applied to determine daily calibration parameters, which could be compared to the nominal values.

Unfortunately, obtained results showed that degrading FCA conditions resulted in problems for this procedure: Unphysical large deviations in x_0 could be compensated by restrictive cutoff parameters, so that fitting of the model in wide ranges for x_0 was possible. Thus, this method became unreliable over the course of experiments. This was compensated by using the internal calibration method to obtain x_0 and the Knudsen traces to obtain the cutoff parameters only.

10.1.2 Cutoff Function

Some results of the obtained cutoff functions (section 8.2.6.2) were already presented in figs. 8.6 and 8.7, which show very little deviation from ideal behavior. In this section, the

range of possible cutoff function parameters and their influence on the TOF distributions is presented.

Since fig. 8.6 already illustrated the effect of small deviations on Knudsen traces, fig. 10.2 presents TOF distributions obtained from permeation experiments. As system $H_2/Cu(211)$ $(v = 1, J = 1)$ was chosen, due to the strong signal of both desorption channels. In both panels, the data (black points) was acquired at $1023\,K$ and fitted with the according model (red lines). The resulting cutoff functions are depicted by blue lines associated to the right hand y-scale. In panel (b), the measurement was conducted after overheating the FCA resulting in strong thermal degradation of the coating and thus cutoff conditions. This affects the slow channel significantly, while the fast reaction channel is almost undisturbed in its shape.

In contrast, the cutoff function shown in panel (a) does not rely on data points with significant amplitude. Therefore, the obtained values shown here are rather arbitrary, as long as the result does not affect data at TOF $\lesssim 30\,\mu s$. Figure 10.3 shows these cutoff functions in direct comparison as red and blue lines, with panel (a) in the TOF and panel (b) in the kinetic energy domain. Additionally shown (green) is the cutoff obtained from the sophisticated model result presented in fig. 10.1, showing a smoother but still significant perturbation influence. It is pointed out, that all these perturbations are considerable in the energy range below $120\,meV$, but negligible above. Therefore, the TOF distributions obtained in the permeation experiments should remain unaffected, at least for the fast desorption channel. Differences in FCA conditions were observed as slow sequences during experiments over the course of weeks. Therefore, obtained cutoff conditions were utilized to judge if the construction of a new FCA was necessary.

10.1.3 Internal Calibration

As described in section 8.2.4.3, a new calibration method was introduced in this work. Basically, this involved thorough acquisition of a specific TOF signal from a permeation source and its subsequent analysis. By using the obtained parameters from the corresponding model, successive measurements under similar conditions allowed the fitting of the signal for calibration parameters. In contrast to the Knudsen method (section 8.2.4.3), this does not allow determination of the cutoff parameters (section 8.2.6.2) because the relevant energy range was not probed sufficiently.

First, for each sample the FCA conditions were probed using sophisticated Knudsen measurements as described in section 10.1.1. Then, TOF traces from desorption of D_2 $(v = 1, J = 2)$ from the corresponding sample were acquired for three temperatures: the temperatures of the regular permeation measurements ($923\,K$ for both copper samples and $1061\,K$ for gold) as well as $\sim\pm50\,K$. These three traces were fitted globally using the detailed balance model, in order to increase the restrictions of the fit.

Successively, daily calibrations included measurements of D_2 $(v = 1, J = 2)$ in addition
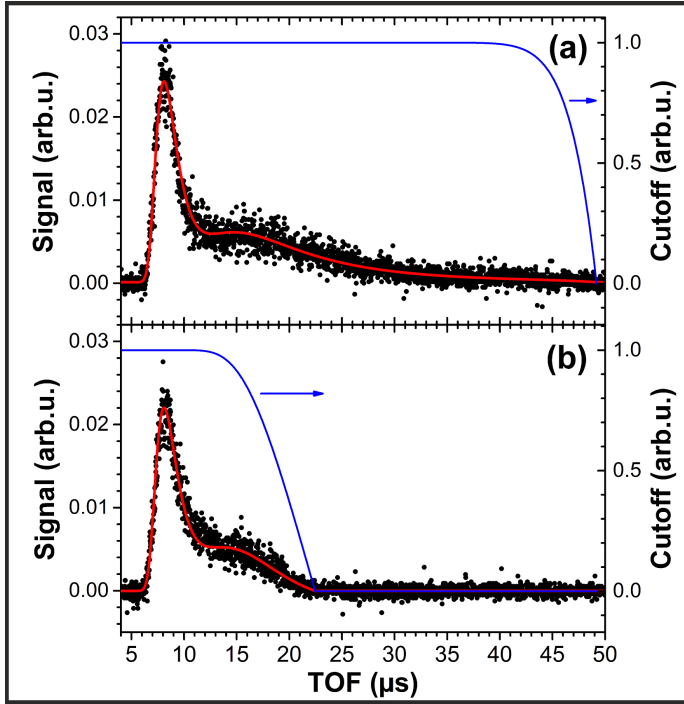
Figure 10.2: TOF distributions illustrating the influence of the cutoff function on desorption data. Both panels show data from Cu(211), H_2 ($v = 1, J = 1$) desorbing at $1023\,K$. The TOF data is shown as black dots, the obtained fit as red line and the applied cutoff function as blue line, corresponding to the right hand ordinate. The data in panel (b) was obtained after overheating the FCA, which resulted in more restrictive conditions for the ion drift. Clearly, the influence on the slow reaction channel is significant, while the fast reaction channel is almost undisturbed. In fig. 10.3 corresponding cutoff parameters are described with the curves are directly compared as red (for panel (a)) and blue (for panel (b)) lines.
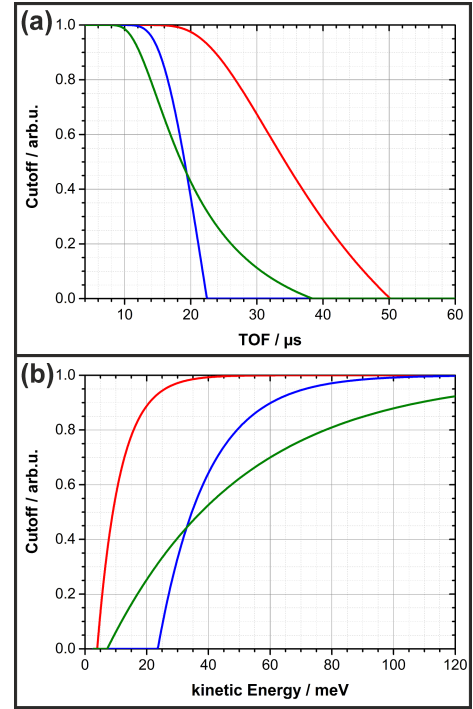
Figure 10.3: Illustration of various cutoff conditions using eq. (8.21). Resulting curves are shown in TOF for H_2 (panel (a)) and E_{kin} (panel (b)). Three sets of parameters are illustrated by colored lines, each showing the result of specific experimental conditions: red and blue for the cutoffs presented in fig. 10.2 and green for the calibration data set shown in fig. 10.1. The parameters are: t_{shift} globally as $3.2\,\mu s$, x_0 as $28.93\,mm$ for red and blue and $29.25\,mm$ for green. Cutoff-parameters for the red, blue and green curves were $E_{slope} = 2232\,eV^{-1}$, $62.7\,eV^{-1}$ and $22.8\,eV^{-1}$ and $E_{min} = 4.1\,meV$, $23.6\,meV$ and $7.2\,meV$.

Table 10.1: Results of the internal calibration procedures for the four different setups. Presented are the resulting x_0 values as well as the ERF parameters for D_2 ($v = 1, J = 2$).

Sample	x_0 / mm	E_0 / eV	W / eV
Cu(111)	28.59 ± 0.16	0.4583 ± 0.0021	0.1582 ± 0.0015
Cu(211)	28.11 ± 0.58	0.5448 ± 0.0030	0.2107 ± 0.0017
Au(111)	30.46 ± 0.45	1.0025 ± 0.0072	0.2932 ± 0.0027
Coppers	29.43 ± 0.33	see above [a]	see above [a]

[a]Using the same values as for the Cu(111) and Cu(211) sample, respectively.

to Knudsen acquisitions. This allowed determination of x_0 by internal calibration and using Knudsen calibration for E_{slope} and E_{min}. Comparison of the results to the established method yielded similar results and accuracy for x_0, when the FCA conditions were only weakly perturbing. Due to the different energy region probed by desorption experiments, the results of the nternal calibration method proved unaffected by degrading FCA quality, while Knudsen measurements suffered from the aforementioned problems. Therefore, the introduced method proved more reliable than the Knudsen method.

For the Au(111) sample, additional internal calibration parameters were determined for H_2 $(v = 0, J = 1)$ and $(v = 1, J = 1)$. These parameters were then used as calibration standard for H_2 permeation measurements for each respective laser setup, so that the probe gas behind the source did not need to be changed.

Table 10.1 summarizes the x_0 results obtained by the internal calibration method for each sample investigated in this work. For the setup allowing direct comparison of both copper surfaces (designated "Coppers"), no Knudsen cell measurements were possible and thus no information of the cutoff available. Fortunately, an overall check of the FCA quality could be obtained by daily observation of the slow peak found in permeation and TB acquisitions. Upon strong degradation, as shown in fig. 10.2, the measurements were stopped and a new FCA build had to be constructed.

10.1.4 Independent Determination of t_{shift}

In the following subsections, the elaborate determination of the t_{shift} parameter will be presented. Using the methodology of delayed extraction as described in section 8.2.4.3, the experimental results will be shown in section 10.1.4.1. These are compared to accompanying simulation results, presented in section 10.1.4.2. Thus, in this work the t_{shift} parameter was fixed to $t_{\text{shift}}^{H_2} = 3.2\,\mu\text{s}$ and scaled for other isotopologues according to eq. (8.14), in contrast to using it as adjustable parameter.

10.1.4.1 Delayed Extraction Measurements

In section 8.2.4.3 the method of delayed extraction was described in detail. Briefly, the ion optics setup had been modified to produce perturbed TOF distributions, which provide information over the t_{shift} parameter directly. Experimentally, Knudsen cell effusion at room temperature was employed, in order to produce especially broad TOF distributions (cf. section 8.2.4.3).

Figure 10.4 shows measured TOF distributions from this procedure for the isotopologues H_2 (panel (a)) and D_2 (panel (b)). Undisturbed MBD at $300\,\text{K}$ are shown as black curves in both panels. Panel (a) shows the results for several switching times: $8\,\mu\text{s}$, $12\,\mu\text{s}$ and $16\,\mu\text{s}$ for the red, blue and green curves. Clearly, all distributions show no intensity before the switching time, a sharp peak several μs later and converge to a similar shape as the undisturbed distribution for TOF a few μs after this peak. The sharp, high peaks

at the switching time are created by electrical noise from the device. For the distributions switched at long TOF (blue and green), an additional feature is observed, namely ~2 µs after the initial peak a second peak emerges. This is assumed to be an effect of the time response of the HV switch device, as presented in section 9.1.1.7.

The low signal occurring shortly before the initial peakis also noticeable in the green depicted distribution. These are ions which propagated far enough into the ion optics region to be accelerated by the lens tube and detected even before the extractor was switched. Therefore, the analysis is restricted to those distributions switched at timings where only few ions left the FCA, so that those two artifacts were absent. Finally, the insets show the enlarged excerpts of the initial TOF peaks of two distributions with arrows indicating the experimental determination of the t_{shift} values. Panel (b) of fig. 10.4 shows similar results for D_2 measurements, switched at 12 µs (red) and 15 µs (blue). The features of the traces are analogous to the ones in panel (a) and discussed above. Insets are also shown too, which indicate the points where the t_{shift} values were determined.

Unsurprisingly, the measured initial TOF peaks are significantly broader than the simulation results (see section 8.2.8.2) and do not fall off sharply. Therefore, the transition between biased and undisturbed TOF distribution is not exactly determinable. Furthermore significant anomalies are observed in the range of the following few microseconds (cf. fig. 10.4), which are ascribed to the voltage-time progression of the HV switch described in section 9.1.1.7. These effects increase with the actual switching time, as seen in the distributions shown in fig. 10.4(a). As outcome of this, the exact position to determine the t_{shift} values is debatable. The most reasonable option would be the base of the initial peak on the falling edge, where the distribution transits to the form of the undisturbed distribution. Other reasonable options are the peak or falling edge, which are both defined more clearly. The results of all these options are summarized in table 10.2 for the measurements in fig. 10.4. Fortunately, the t_{shift} scales with the mass to charge ratio, which allows the relating of the results for both isotopologues (see eq. (8.14)). Consequently, we determined the best agreement when using the values from the falling edge and for the shortest switch time, as given in table 10.2. Thus, throughout this work the t_{shift} values were referenced to the result of $t_{\mathrm{shift}}^{H_2} = (3.2 \pm 0.1)$ µs (cf. section 8.2.4.3).

10.1.4.2 Delayed Extraction Simulations

Results from the simulations described in section 8.2.8.2 are presented here. Due to the idealized conditions in a simulation, the t_{shift} parameters can be obtained directly from trajectories, that means taking the TOF interval of particles, which begins when passing the SM and ends when hitting the MCP. These values are dependent on the initial velocity of the ions, although the extraction accelerates all to the same final energies, which are orders of magnitude larger.

In these idealized simulations, the fast ions experience a shorter t_{shift}. To determine the
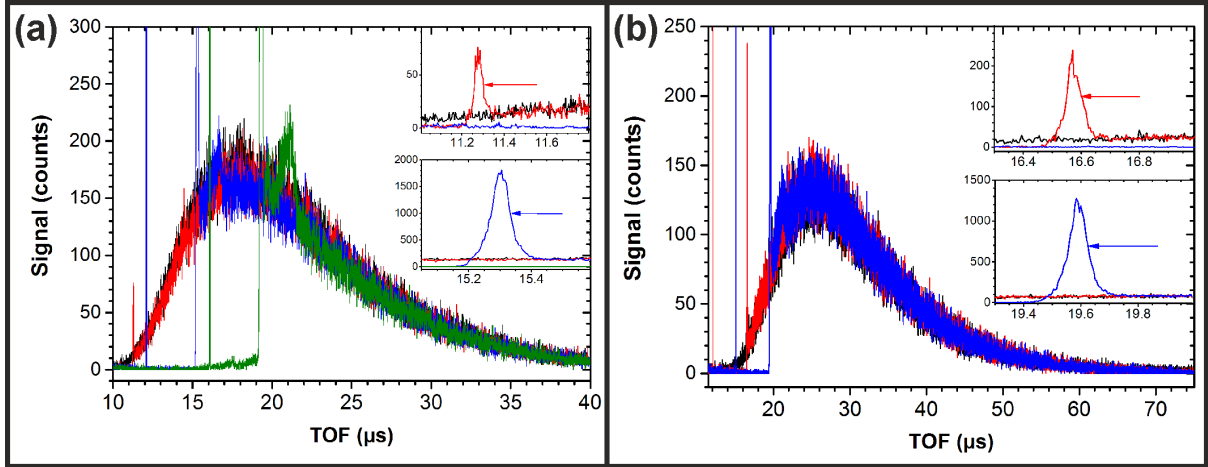
Figure 10.4: Results of the extraction switching experiment described in the text. Panel (a) gives TOF distributions for H_2 for several switching times relative to the time zero: non-switched (black), 8 µs (red), 12 µs (blue) and 16 µs (green). The insets show enlarged sections of the same graph with arrows indicating where the t_{shift} values were determined. In panel (b) TOF distributions for D_2, acquired with the same setup are shown. Here, the colors indicate switching times of non-switched (black), 12 µs (red) and 15 µs (blue). Again, the insets show enlarged sections of the same graph with arrows to indicate where the t_{shift} values were determined.

Table 10.2: Analysis of the data shown in fig. 10.4. The t_{shift} values were determined from the initial peaks shown in the insets and were corrected for the experimental delay of the HV switch discussed in section 9.1.1.7. More details can be found in the text.

Isotopologue	Switching time / µs	t_{shift} at Peak / µs	t_{shift} at Edge / µs	t_{shift} at Base / µs
H_2	8	3.18 ± 0.10	3.20 ± 0.10	3.24 ± 0.10
	12	3.21 ± 0.10	3.24 ± 0.10	3.24 ± 0.10
	16	3.21 ± 0.10	3.27 ± 0.10	3.39 ± 0.10
D_2	12	4.49 ± 0.10	4.50 ± 0.10	4.55 ± 0.10
	15	4.47 ± 0.10	4.53 ± 0.10	4.64 ± 0.10
D_2 simulated[a]		4.49	4.53	4.58

[a]value calculated by scaling the corresponding $t_{shift}^{H_2}$ value at 8 µs switching with the particle mass (see eq. (8.14)).

order of magnitude of this effect, the results obtained from simulation of undisturbed MBD for the three isotopologues are given in fig. 10.5, panel (a). All single trajectories were weighted for the MBD, re-binned for the resulting t_{shift} and normalized. These peaks are slightly asymmetric but can be fitted by Gaussian distributions, whose fitted properties are given in table 10.3. The FWHM of the peaks is below 50 ns which is significantly lower than the experimental accuracy. Therefore, the variation of the t_{shift} with ion initial velocity can be neglected in all following considerations.

To convert the simulated trajectories into TOF distributions, each single trajectory was weighted according to the MBD and re-binned for its arrival TOF. A selection of the resulting distributions is shown in fig. 10.5, panels (b) to (d). Panel (b) gives the TOF distributions of H_2 for three distinct switching times: $1\,\mu s$ (black), $10\,\mu s$ (red) and $15\,\mu s$ (blue). Clearly, the black points correspond to an undisturbed MBD, where no ions left the FCA before the extractor was switched. The two other distributions are clearly distorted, each showing a strong peak in the distribution ~2.8 µs after the switching time, before

continuing as undisturbed MBD. These are the two sets of ions during the simulation. The undisturbed fraction resides inside the FCA until the extractor is switched, while the residual fraction already propagates into the ion optics region and is accelerated immediately upon switching. Therefore, the latter fraction of ions arrive accumulated in a short time interval and form the observed peak.

Conclusively, the delay between switch time point and the sharp initial peak of the distribution is used as an approximation of the t_{shift} parameter, as shown in panel (b). This method is based on the argument that the sharp peak consists of ions which are disturbed from their regular MBD trajectories, i.e. those ions had already left the FCA when the extractor was switched. Thus, the TOF point where the undisturbed MBD and the sharp peak merge corresponds to ions passing the grid exactly at the switch time. Therefore, the precise t_{shift} should be determined from the delay between this TOF point and the time point of the switch. Due to broadening effects which occur under experimental conditions, the values measured at the falling edge of the peak had to be used for this (see section 10.1.4.1). The limit of the experimental accuracy was determined as $0.1 \, \mu$s and as consequence deviations below that range can be neglected. Performing these simulations for several switching times illustrates that the resulting t_{shift} is not dependent on this parameter within our degree of accuracy.

As described in section 8.2.4.3 and eq. (8.14), the t_{shift} scales with the mass to charge ratio of the particles. Simulation results of the three isotopologues H_2, HD and D_2 are given in fig. 10.5 panel (c), plotted as offset distributions (upper, intermediate and lower level, respectively). Results are given for switching at $1 \, \mu$s (black, red and blue points) and $15 \, \mu$s (red, blue and green triangles). This allows for direct comparison between the undisturbed (points) and biased (triangles) distributions. Figure 10.5 panel (d) gives an enlarged section of panel (c), including a line in the biased distributions which connects the last point of the peak with the first point that overlaps with the undisturbed distribution. Black arrows give the delay to the switching time (vertical brown bar), corresponding to the t_{shift} for each isotopologue. By using the result for H_2, $t_{\text{shift}}^{H_2}$, as reference point and scaling with isotopologue mass yields the results given in table 10.3. This shows that the methodology is suitable to determine the t_{shift}.

In summary, the t_{shift} parameter giving the TOF of ions in the extraction and detection of the setup can be estimated by simulations. Experimentally, this value can be determined by the introduced method of delayed extraction, biasing a known velocity distribution. The actual value depends on the exact FCA setup and the alignment of the ion optics as well as stray fields. This results in a less accurate determination of the value than the simulation, thus smaller effects can be neglected, e.g. the dependence on initial particle velocity.
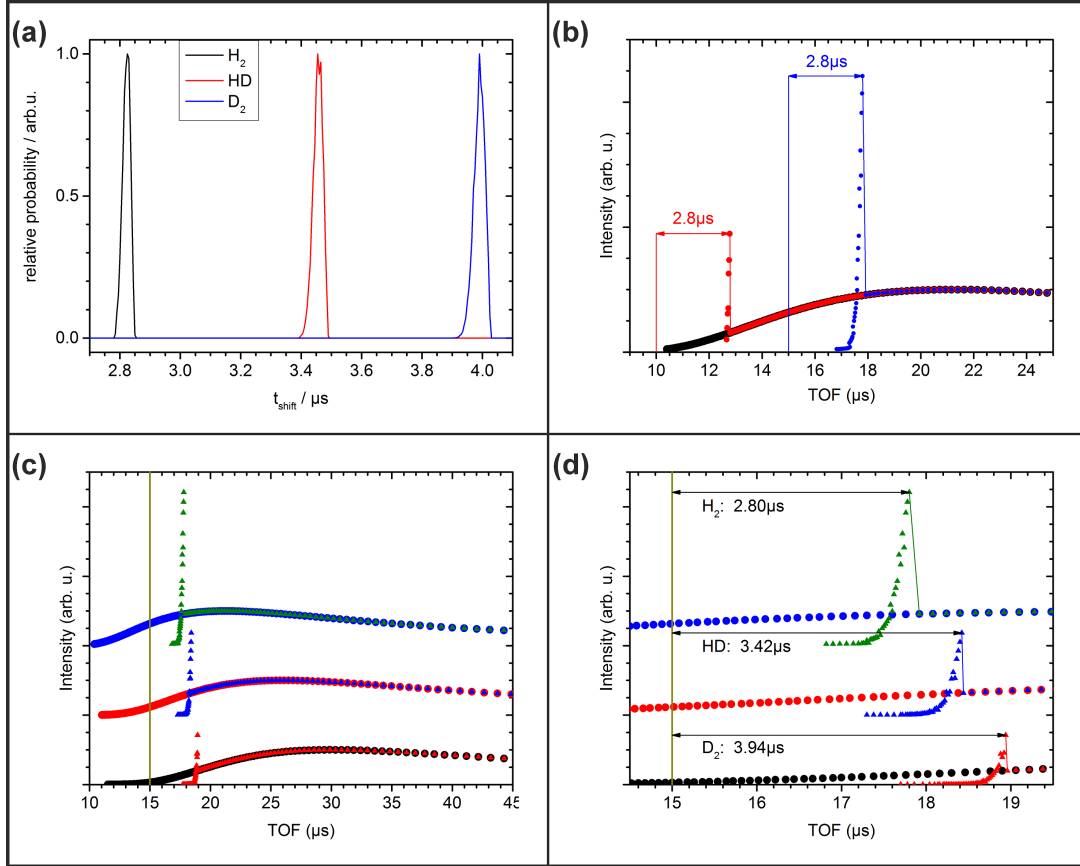
Figure 10.5: Summarized simulation results for different settings and isotopologues. Panel (a) gives t_{shift} distributions obtained directly from the simulation results of undisturbed MBDs. For each trajectory the TOF between the SM and the detector was recorded as t_{shift} and the results were weighted and re-binned to yield the shown distributions. Different colors denote distributions for the three isotopologues: black for H_2, red for HD and blue for D_2. Panel (b) shows simulated TOF distributions for H_2 at different switching times: $1\,\mu s$ (black), $10\,\mu s$ (red) and $15\,\mu s$ (blue). Vertical colored lines correspond to the switching time and the according peak in the TOF distribution and the resulting delay is indicated by the numbers and arrows. In panel (c) results for two switching times are presented offset for each isotopologue. Here, the results for switching at $1\,\mu s$ are shown as blue (H_2), red (HD) and black (D_2) points. Triangles show the results for switching at $15\,\mu s$, marked by the brown vertical line and coded as green (H_2), blue (HD) and red (D_2). Panel (d) gives an excerpt of the same data and color coding as panel (c). Here, colored straight lines connect the last point of the newly formed peaks and the first point of the regular distributions, respectively. Delay times between these peaks and the switching times are indicated by the black arrows and numbers for each isotopologue.

Table 10.3: Analyzed values from the SIMION results for the t_{shift} parameter. Gaussian fit parameters obtained from the peaks in fig. 10.5 as well as scaled t_{shift} parameters using the mass to charge ratio relative to the simulated $t_{\text{shift}}^{H_2}$ (see eq. (8.14)) are reported.

Quantity	$t_{\text{shift}}^{H_2}/\,\mu s$	$t_{\text{shift}}^{HD}/\,\mu s$	$t_{\text{shift}}^{D_2}/\,\mu s$
Gaussian center	2.823	3.457	3.991
Gaussian FWHM	0.031	0.038	0.043
From fig. 10.5, panel (d)	2.80	3.42	3.94
Scaled by mass to charge ratio	2.80	3.43	3.96

10.1.5 Thermal Background

Hydrogen molecules are always abundant, even in UHV environments. Therefore, hydrogen spectroscopy always encounters a certain contribution of TB, which has to be taken into account or subtracted.

For simulations of TB TOF distributions a MBD at room temperature is assumed. But in comparison to Knudsen cell or permeation measurements (see section 9.1.1.9), the geometry is very different. While for those experiments gas from a directed flow is restricted by apertures before ionization, background gas is ionized along the whole laser focus in the FCA. Due to the free-drift conditions inside the FCA not all of these ions can reach the detector. This rather depends on their initial trajectory and the limiting geometry, which is depicted schematically in fig. 10.7. Here, trajectories start on the laser line (red line) and have to end in a certain area to be detectable, which is ultimately limited by the circular aperture on the extractor tube. This is projected (blue lines) onto the SM, where the traversing ions are accelerated (blue arrow) immediately by the extraction field, regardless of their initial vector. Then, the distribution of angles under which ion trajectories (green arrows, generic) are able to reach the detection strongly dependes on the length of the laser line. Summing TOF curves over all possible ion flight paths which originate from such a line source then yields a reasonable simulation of the geometry relevant for the TB.

Experimentally, TOF distributions of the TB have been determined by leaking gas into the chamber under the same conditions as during permeation measurements, except for no gas being supplied to the source. A comparison of simulated and measured TOF distributions is given in fig. 10.6. Clearly, the distributions extend to longer TOF as the MBD based Knudsen traces, which allows scaling of the TB according to the signal in this range. In experimental data the resulting amplitudes were found to be negligible except for rotational states $J < 7$ in the vibrational ground state.
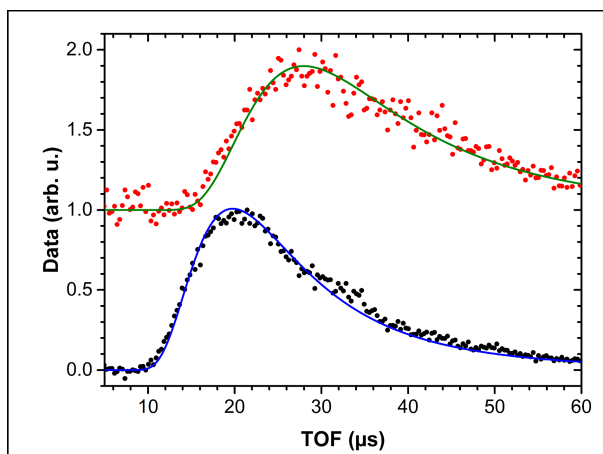
Figure 10.6: Normalized TOF distributions of TB gas measured for D_2 (red dots, offset) and H_2 (black dots) by leaking gas into the detection chamber. The lines give the result of the model described in the text and simulate the expected TOF distributions originating from a long laser line as shown in fig. 10.7. This background contribution is only found for molecules in the vibrational ground state and in low rotational states ($J < 7$).
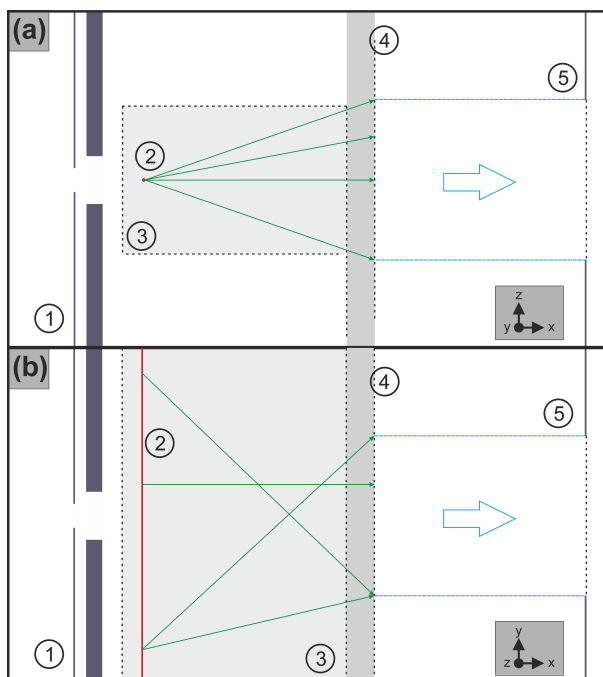
Figure 10.7: Schematic view of the origin of the thermal background signal. Both panels show projections onto a certain plane and indicate the coordinate system on the lower right. Panel (a) shows the plane perpendicular to the laser propagation axis (y) and panel (b) the plane containing the laser propagation (y) and the ion flight direction (x). Both are to scale and correspond to the FCA design described in section 9.1.1.6, with several details not depicted. It should be noted that the exact dimensions and positions relative to the laser beam vary by few mm in every build of the same setup. The legend is the same for both panels: Meshes are indicated by grey shaded regions bordered by dashed lines. Here, (1) marks the tantalum shield (thin purple line) and differential wall (thick purple line), the FCA (3, grey shaded areas), the SM (4) and (5) the extractor. In a first approximation, the aperture size of the extractor is projected (blue lines) onto the SM, to represent the area where traversing ions can be detected. Ions propagating through the SM are strongly accelerated by the homogeneous electric field and therefore propagate parallel to the x-axis (blue arrow), regardless of their previous trajectory. The laser focus (2) is approximated as a linear volume. In this geometry, the detectable trajectories (green arrows, generic) are only limited by these two geometric factors. Increasing the length of the laser focal line then results in addition of trajectories with drift lengths longer than the nominal (parallel to x-axis).

10.2   Permeation Results

For the presentation of the various analyzed aspects of the permeation measurements, the obtained data sets are separated in two sections. While the first includes the results of Cu(111) as well as Cu(211), the second presents the data obtained from Au(111). This sectioning simplifies the comparison of the copper data, because only slight differences were found between both facets. In a third section, the obtained results are compared to experimental and theoretical work in the literature. It is pointed out that significant parts of these results have already been published elsewhere[220].

10.2.1   Copper Crystals

In the following subsections the obtained Cu(111) and Cu(211) data will be compared directly to each other. Each subsection will present a certain aspect of the analysis, but comparison to literature results will be given in section 10.3.

All presented data was acquired at $(923 \pm 2)\,\mathrm{K}$ if not indicated otherwise. Experiments with varying sample temperatures were conducted, but due to experimental reasons this temperature range was restricted: too low permeation flux at low temperatures and irreversible degradation of FCA conditions at higher temperatures. Because it was the first sample to be probed, the majority of the obtained data of the Cu(111) facet had been acquired by a setup not yet optimized with regard to the FCA quality and acquisition procedure (cf. section 8.3.2). In order to verify the validity of those measurements, those were repeated for selected quantum states with the optimized settings, and successive comparison showed the differences to be insignificant.

Furthermore, both copper facets were compared directly by mounting both samples on the manipulator instead of the Knudsen cell. This allowed the observation of the permeation signals of different samples under the same experimental conditions, by alternating between the samples after each acquisition. For the copper systems, this even proved necessary because the differences between the TOF traces were found to be on the same order of magnitude as the absolute calibration uncertainty. Here, the calibration relied completely on the method of internal standard, which had been obtained for each facet and D_2 $(v = 1, J = 2)$. In the remainder of the document, these experiments will be referred to as "contrastable", while experiments basing the calibration on the Knudsen cell will be termed "conventional". The main advantage of the contrastable method is the ability to exchange the Knudsen cell on the sample mount with a different sample. This allows to acquire signals under the same experimental conditions, especially calibration parameters, for direct comparison of signals differing only little.

10.2.1.1 State Resolved Time-of-Flight Distributions

Illustrative data sets are presented in fig. 10.8, where panel (a) gives measured TOF distributions and panel (b) their conversion to flux in the kinetic energy domain and rebinned to 10 meV. Figure 10.8 presents a direct comparison of the data from both copper crystals using the contrastable method with Cu(111) data presented in black and manually scaled Cu(211) data in red. Each subpanel presents data for a different isotopologue and selected ro-vibrational states, as indicated in the caption, and for the data in subpanels (i) the TB contribution has been subtracted. Clearly, desorbing molecules behave similarly for both facets and the TOF distributions show only minor differences. More interestingly, in each trace two contributions are observable, which will be separated and explained in detail in section 10.2.1.2. In panel (b), these two contributions are clearly observable as distinct peaks, and they overlap in the range of ~0.1–0.3 eV. Due to the necessary conversions (section 8.3.4), the slow contribution is well identifiable in panel (b), while the TOF distributions in panel (a) show only low signals. This is due to the free ion drift method (see section 8.2.4.2) which disperses the energy range of 0.01–0.20 eV over a large TOF interval, e.g. 10–47.4 µs in panel (a, i).

Henceforth, these two contributions will be termed "slow channel" for the signal observed mainly below 0.2 eV and "fast channel" for the well known feature above 0.2 eV. Here, the latter is the regular signal observed in activated associative desorption and therefore comparable to literature results. In contrast, the slow channel suffers from several factors reducing its SNR: the aforementioned dispersion, but also the strong influence of FCA conditions (see sections 8.2.6.2 and 10.1.2). As will be presented later, this channel also shows a broad angular distribution which renders the measurable signal strongly dependent on the solid angle of the experimental detection. In the following subsection, the deconvolution of all contributions to the acquired signal will be elaborated in detail.

It is pointed out that there is some degree of correlation between the two reaction channels, due to their overlap in the kinetic energy range 0.1–0.3 eV. This is especially a concern for molecules with high internal energy, where the dynamical distribution of barriers is shifted to lower kinetic energies, resulting in stronger overlap between the two channels. As stated in section 10.2.1.2, the RPCs have been chosen to be described with relatively simple models to reduce this problem. Additionally, there is some correlation between the fast channel's parameters themselves, which will be discussed in detail in section 11.2.2.1.

In fig. 10.8 the shape of the desorption distributions of the two samples Cu(111) and Cu(211) is compared directly. Obviously, their differences are small but due to the use of the "contrastable" method they must be significant. Generally, the fast desorption peak is broader and shifted to higher kinetic energies for Cu(211). For the slow peak, differences are vague except for a stronger relative amplitude for the depicted H_2 data set. A quantitative analysis will be presented in section 10.2.1.3.
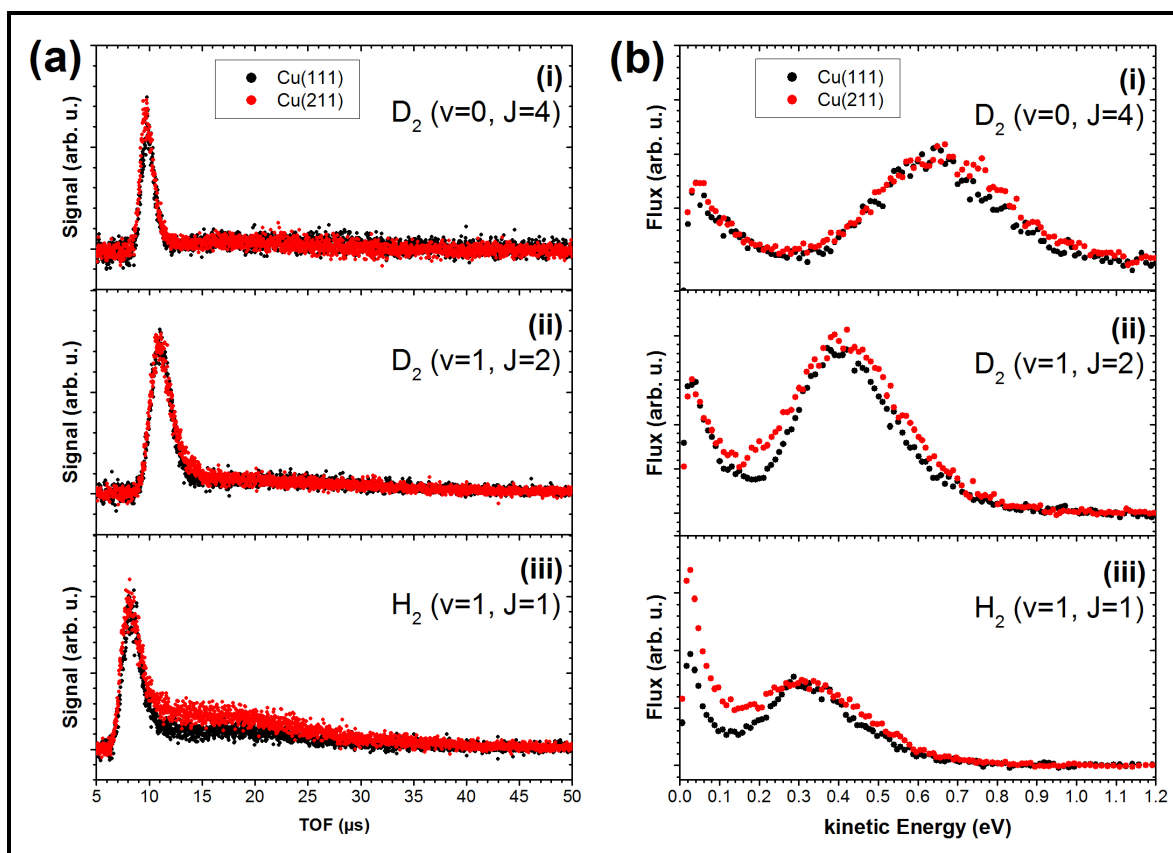
Figure 10.8: Illustrative desorption distributions obtained from Cu(111) (black dots) and Cu(211) (red dots). Panel (a) gives TOF traces and panel (b) their conversion to flux in the kinetic energy domain, rebinned to 10 meV. Each subpanel presents a different isotopologue and quantum state: (i) D_2 ($v = 0, J = 4$), (ii) D_2 ($v = 1, J = 2$) and (iii) H_2 ($v = 1, J = 1$). Here, the Cu(211) data has been scaled manually to allow easier comparison. For data in the vibrational ground state the TB contribution has been subtracted.

Figure 10.9: Normalized TOF traces for the J-sequence of the D_2 ($v = 0$) /Cu(211) data set. Each trace is plotted offset on the vertical axis and the orange line is inserted as guide for the eye through the peak of the $J = 0$ signal. In this illustration the effect of rotational energy can be observed directly. Beginning rotation ($J < 6$) shifts the peak to shorter TOF, and therefore indicates a shift of the reaction barrier distributions to higher energies, while above $J = 6$ this effect is reversed.
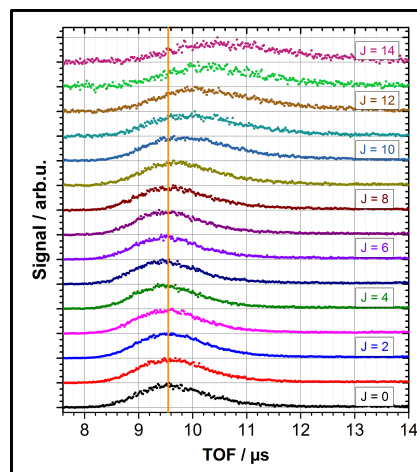
Additionally, fig. 10.9 shows normalized TOF traces for the $D_2/Cu(211)$ data set, explicitly the J-sequence of the vibrational ground state. Each signal is offset on the vertical axis and the orange line is inserted as a guide for the eye through the peak of the $J = 0$ signal. This presentation illustrates the effect of rotational excitation on the barrier distribution function without further analysis steps, up to $J = 6$. The distribution is shifted to higher energies and the peaks to shorter TOF before the effect reverses for higher J states. The quantitative analysis will be presented in section 10.2.1.3.

10.2.1.2 Signal Contributions

Instructive results of the decomposition into several reaction channels is shown in fig. 10.10, for selected states of D_2 desorbing from Cu(211). As in fig. 10.8, the distributions are presented as signal in TOF (panel (a)) and flux in kinetic energy domain (panel (b), rebinned to 5 meV). Vertical subpanels (i-iii) show the $J = 2$ data for vibrational states $v = 0 - 2$. In each graph, the data is represented by black dots and the model fit results as lines. Here, the red line gives the fit result summing all contributions, which are composed of up to three parts: (blue) TB for data in the vibrational ground state, (green) the fast channel and (purple) the slow channel.

While the TB has been determined by direct measurements (section 10.1.5), the other two channels need to be explained by the model of detailed balance (section 8.3.1.2). All following assumptions are based on the measured data and the best fit results of different RPC models, as described in section 8.1.3. An additional approximation is the complete separability of both reaction channels. Then, the slow channel has been found to be best fitted by a single exponential decay, see eq. (8.7). For the fast channel the ERF model (eq. (8.4)) was found to be sufficient. Other models (e.g. eqs. (8.5) and (8.6)) were also suitable, but resulted in significant over-parameterization. Furthermore, correlations between the two reaction channels became significant, due to the overlap of both contributions in the region of 0.1–0.3 eV. Thus, the eq. (8.4) model was used throughout this work for the fast channel.

It is pointed out, that the TB and slow channel overlap also, but the TOF profile of the TB had been determined independently (section 10.1.5) and extends to significantly longer TOF (>35 μs in fig. 10.10 panel (a, i)). Illustrative examples of the sticking probabilities from both channels are given in fig. 10.11. Here, measured data has been converted to sticking probability according to section 8.3.4.2 and the results were normalized to the saturation values of the corresponding H_2 ($v = 1$) and D_2 ($v = 2$) data sets. Further are the fitted RPCs of both reaction channels shown as lines and the thermal background contribution was subtracted in the ($v = 0$) data sets. A quantitative analysis of the fitted parameters of both channels will be presented below.
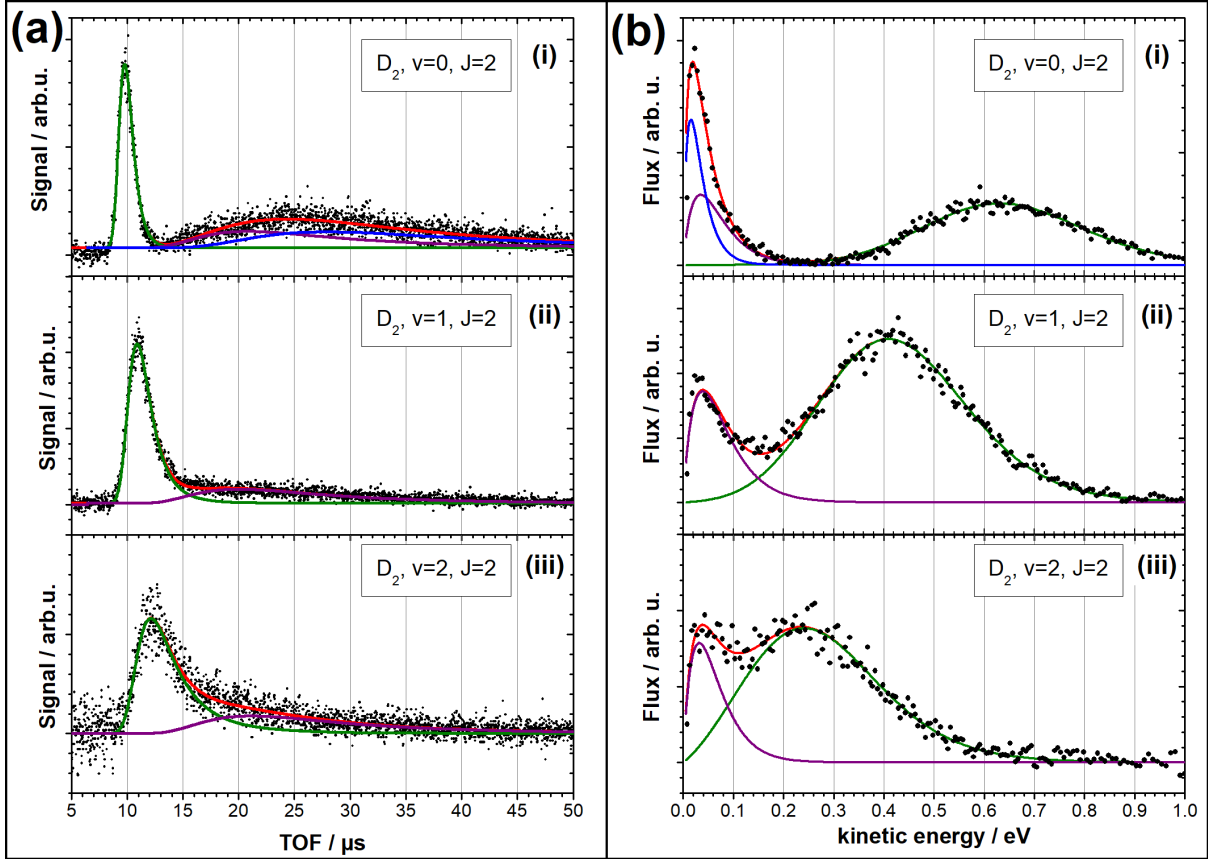
Figure 10.10: Instructive desorption data and fitted model contributions showing the signals in TOF (panel (a)) as well as the flux in kinetic energy domain (panel (b), rebinned to $5\,\mathrm{meV}$). All signals are from the D_2/Cu(211) data set, and $J = 2$, with the subpanels (i-iii) corresponding to the vibrational level ($v = 0 - 2$) of the presented signals. Black dots indicate the signal and lines the fitted contributions of the model described in the text: green for the fast channel, purple for the slow channel, blue for the TB and red as the sum of all those, as fitted to the data. TB contributions are only apparent for data of the vibrational ground state.

10.2.1.3 Obtained RPC Parameters

In the following paragraphs each fitted parameter will be presented in direct comparison for both copper facets. Here, the fast channel is described by the RPC in the form of eq. (8.4) with the parameters E_0, W and A_{erf}. For the slow channel, eq. (8.7) had been determined suitable with only two parameters: γ_{slow} and A_{slow}. Only results using the contrastable calibration method will be presented for the slow channel, since the FCA conditions had been least restrictive for those measurements. Thus, the SNR was improved relative to the Knudsen method and this resulted in lower uncertainties in the fitted parameters. In addition, all obtained parameters are also presented in tabular form in appendix D.1, for both methods.

E_0 **Parameter** All obtained E_0 values are presented in figs. 10.12, 10.13 and 10.14, as separated for rotational states of each isotopologue and with subpanels (a-c) for vibrational states ($v = 0 - 2$). Each figure gives the direct comparison for the two surface facets,
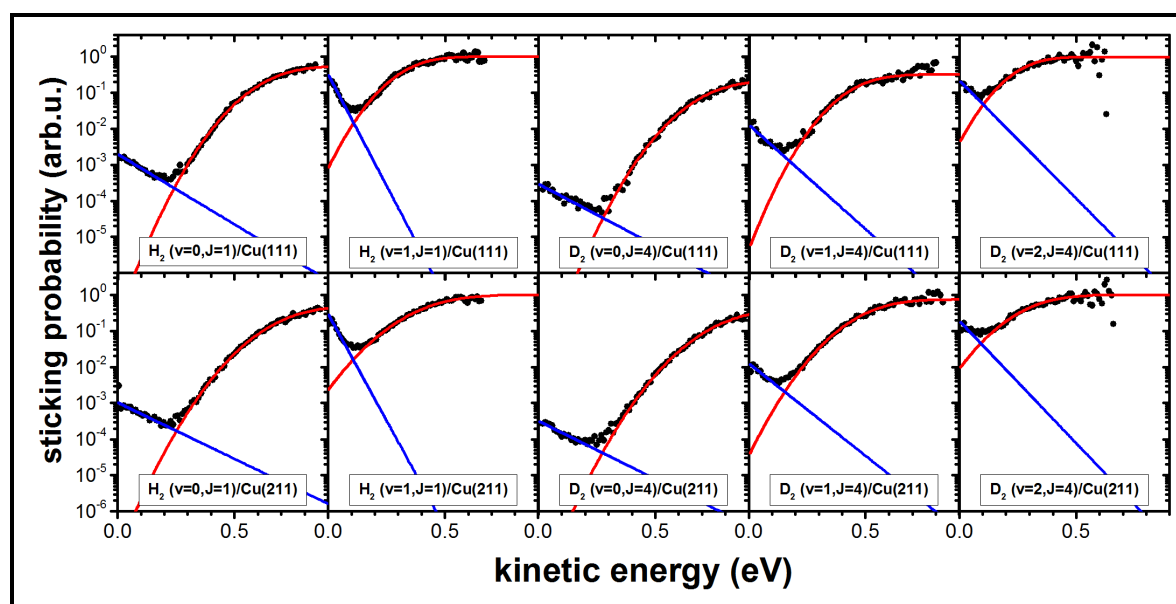
Figure 10.11: Illustrative data sets showing the composition of the reaction probability from both channels. In each panel the data set is indicated as molecule, surface and quantum state. Here, in each column the same molecule and quantum state are shown for Cu(111) (upper panels) and Cu(211) (lower panels). Measured TOF data from the contrastable method was numerically converted to reaction probabilities, rebinned (black points, see section 8.3.4.2) and restricted to the range where data had sufficient SNR, namely 5 % of the maximum flux. Results of the fitted RPCs models are shown for the fast (red, eq. (8.4)) and slow channel (blue, eq. (8.7)). The thermal background contribution was subtracted in the ($v = 0$) data sets and the data were normalized to the saturation value of the corresponding H_2 ($v = 1$) and D_2 ($v = 2$) sets.

with Cu(111) and Cu(211) being represented by solid and open symbols. Presented error bars were obtained from the fitting procedure and do not include the accuracy of the calibration. Black squares indicate data obtained using the conventional method, while the red circles show results from the contrastable method. Deviations between data from these two methods give a good representation of the calibration uncertainty.

Most interestingly, a global difference between the facets is observable: All E_0 values are significantly higher for Cu(211) throughout all isotopologues and quantum states. These differences cover the range of 30–130 meV, while the deviations between both calibration methods are a maximum of ~30 meV only. Between the facets these shifts do not correlate systematically with internal energy, but are rather constant. Thus, the dynamics are similar for both facets. For H_2 and D_2 the rotational sequences show an increase in the dynamical barrier distributions from the rotational ground states to intermediate states and a decrease at even higher rotational excitation. For HD, the E_0 values are approximately constant before decreasing in energy for higher rotational states ($J > 5$). Vibrational excitation leads to significant reduction of barrier distributions in all observed cases. Quantification of these effects will be presented in sections 10.2.1.5 and 10.2.1.7.

Width Parameters All obtained W values are summarized in table 10.4 and fig. 10.15. In this work, W parameters were fitted as global variable for all rotational states of each
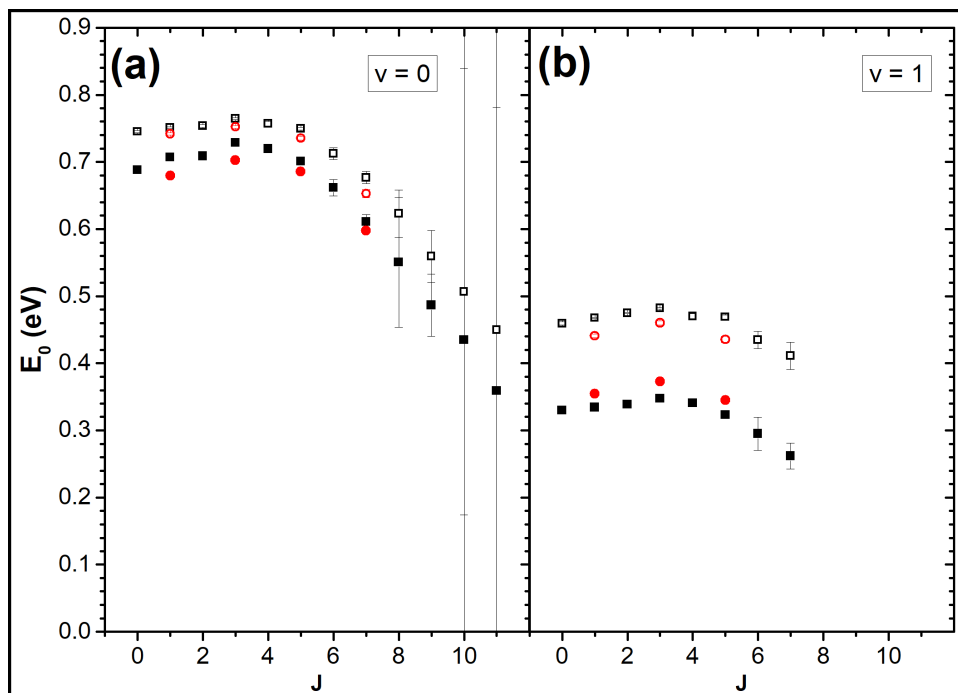
Figure 10.12: Overview of the obtained results for E_0 from H_2/Cu(111) (filled symbols) and H_2/Cu(211) (open symbols). Panels (a) and (b) show the results for the vibrational states ($v = 0$) and ($v = 1$), respectively. Black squares indicate data obtained with the conventional method and red circles data with contrastable method.
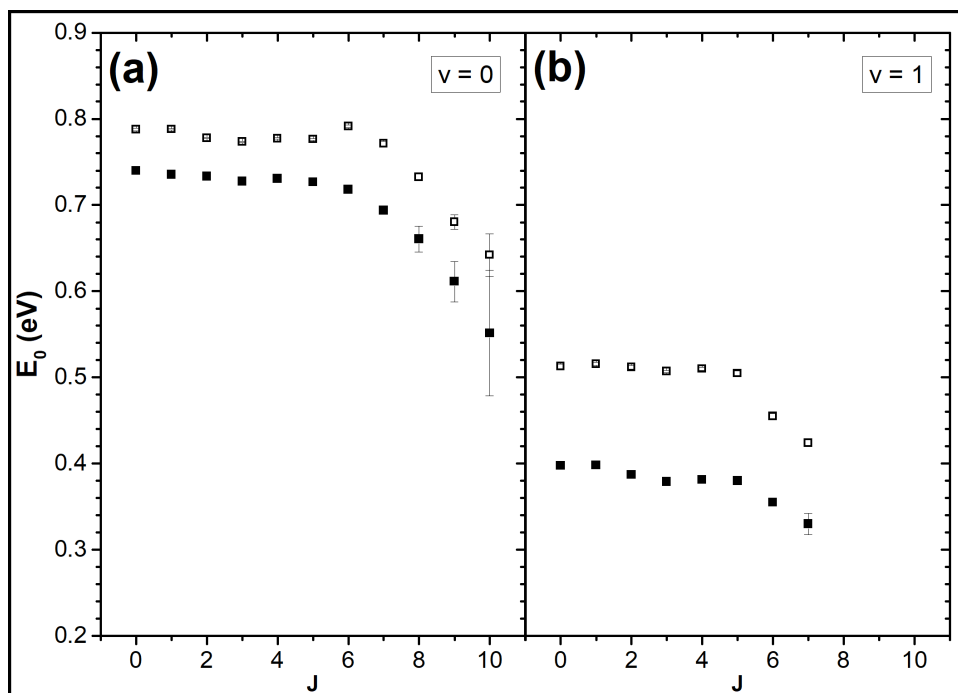
Figure 10.13: Overview of the obtained results for E_0 from HD/Cu(111) (filled symbols) and HD/Cu(211) (open symbols). Panels (a) and (b) show the results for the vibrational states ($v = 0$) and ($v = 1$), respectively. All data was obtained using the conventional method.
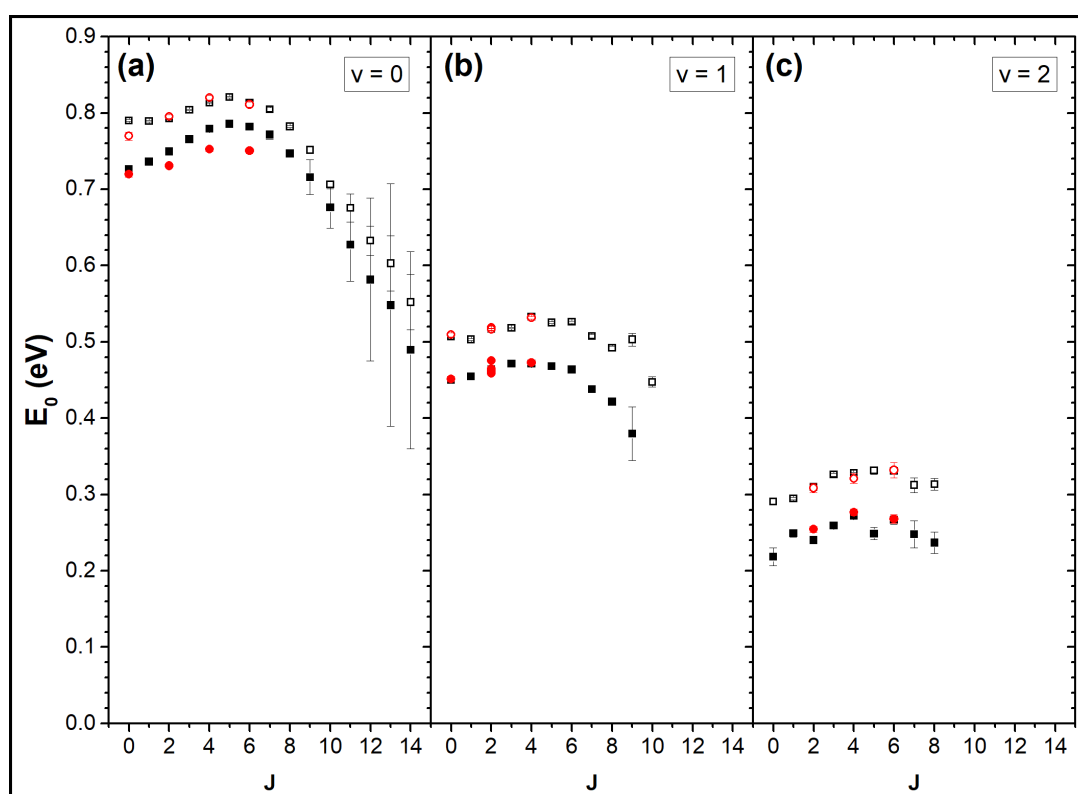
Figure 10.14: Overview of the obtained results for E_0 from $D_2/Cu(111)$ (filled symbols) and $D_2/Cu(211)$ (open symbols). Panels (a), (b) and (c) show the results for the vibrational states $v = 0 - 2$, respectively. Black squares indicate data obtained with the conventional method and red circles data with the contrastable method.

Figure 10.15: Obtained W values for both copper facets and different calibration methods, as described in section 10.2.1. Knudsen cell calibrated data is shown as black squares, data from the contrastable method as red circles. Cu(111) results are represented by filled symbols and Cu(211) results by open symbols, respectively. Results are seperated for the isotopologues H_2, HD and D_2 in the panels (i-iii).
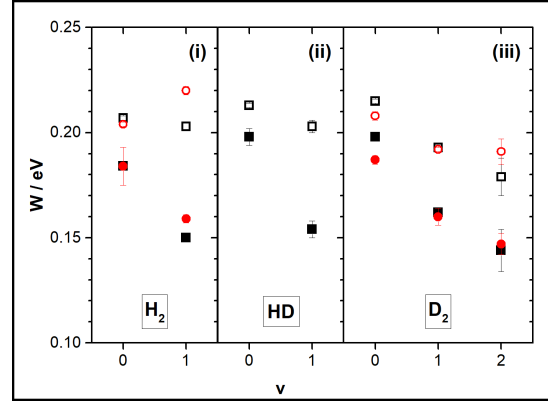
Table 10.4: Obtained W values for both copper facets and different calibration methods, as described in section 10.2.1. All W values are reported in meV.

Isotopologue	v	Cu(111)		Cu(211)	
		Conventional	Contrastable	Conventional	Contrastable
H_2	0	184 ± 9 [a]	184 ± 9	207 ± 1	204 ± 1
H_2	1	150 ± 2	159 ± 2	203 ± 2	220 ± 2
HD	0	198 ± 4	-	213 ± 1	-
HD	1	154 ± 4	-	203 ± 3	-
D_2	0	198 ± 1	187 ± 2	215 ± 1	208 ± 2
D_2	1	162 ± 1	160 ± 4	193 ± 2	192 ± 1
D_2	2	144 ± 10	147 ± 5	179 ± 9	191 ± 6

[a]Quantity fixed to value obtained by contrastable method, due to optimized setup.

isotopologue and vibrational state. Generally, the Cu(211) facet shows broader RPCs than the Cu(111) system, independent of the calibration method. A reduction of W with increasing vibrational state is found for all systems except one, i.e. H_2/Cu(211), using the contrastable method. It is pointed out that this specific system had the highest fraction of slow channel fluxes, which overlapped with the fast channel. For H_2/Cu(211) the W values obtained by the conventional method deviate on the order of determination accuracy. In general the observed reductions of W with vibrational excitation are significantly stronger for the Cu(111) facet.

Saturation Parameters   Saturation parameter results are presented as J-dependent A_{erf} in fig. 10.16, separated in panels for both facets and each isotopologue. The Cu(111) results cover the range 0–2 and agree well for different vibrational states, except for the HD ($v = 1$) rotational data for ($J = 0, 1$), which reaches up to ~3. In contrast, obtained A_{erf} values for Cu(211) had a maximum up to ~8 for excited vibrational states. The deviations from the range 0–2 increase in the order D_2 ($v = 1$), HD($v = 1$), H_2 ($v = 1$) to D_2 ($v = 2$), thus correlating with the vibrational energy.

In general, vibrational energy promotes the reactivity stronger for the Cu(211) facet than the Cu(111) facet. While rotational energy was expected to play only a minor role
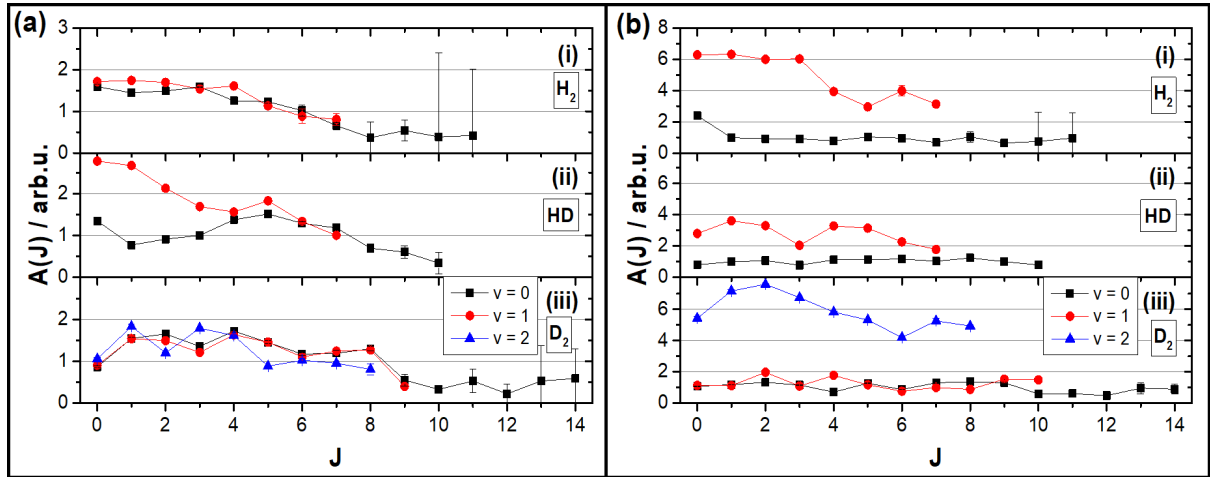
Figure 10.16: Obtained A_{erf} parameters of the fast channel. Here, the layout separates the results for copper facet in panels (a) (Cu(111)) and (b) (Cu(211)), while the subpanels correspond to the isotopologues, (i) H_2, (ii) HD and (iii) D_2. Vibrational states ($v = 0 - 2$) are indicated by black squares, red dots and blue triangles, respectively. Data sets have been normalized to obtain an average value of unity for each ($v = 0$) sequence.

Table 10.5: A_{flux} and A_{erf} parameters for both coppers facets and all three isotopologues. All values were averaged over the rotational sequences of the corresponding vibrational state.

-		Cu(111)		Cu(211)	
Isotopologue	v	A_{flux}	A_{erf}	A_{flux}	A_{erf}
H_2	0	1.00 ± 0.05	1.00	0.25 ± 0.02	1.00
H_2	1	0.77 ± 0.05	1.39	1.00 ± 0.06	4.83
HD	0	0.75 ± 0.06	1.00	0.45 ± 0.01	1.00
HD	1	1.00 ± 0.05	1.87	1.00 ± 0.07	2.77
D_2	0	1.00 ± 0.05	1.00	0.29 ± 0.01	1.00
D_2	1	0.76 ± 0.03	1.23	0.29 ± 0.02	1.26
D_2	2	0.55 ± 0.07	1.24	1.00 ± 0.09	5.83

deviations were found which are largest for $J < 5$. Table 10.5 presents the obtained A_{flux} results, which can be compared directly to literature results (see section 10.3.1.2). The A_{erf} values from fig. 10.16 averaged over the rotational sequences are shown additionally.

γ **Parameter** Figure 10.17 presents the obtained γ_{slow} parameters, which describe the fall-off of the sticking function with kinetic energy (eq. (8.7)). Here, the results are separated for the isotopologues and directly compared for both facets (open and filled symbols). A clear rotational state dependence is observed for H_2 ($v = 0$), showing a rise with increasing J. For D_2, this is also only observed for the ($v = 0$) sequence, while the results for $v > 0$ scatter in the range of 0.0–0.1 eV. In other words, the rotational excitation leads to an extended width of the sticking function. But between the surface facets no clear trends are distinguishable. A vibrational state dependence is only observed for H_2, which gives significantly higher values for ($v = 0$), while for D_2 the values are on the same order
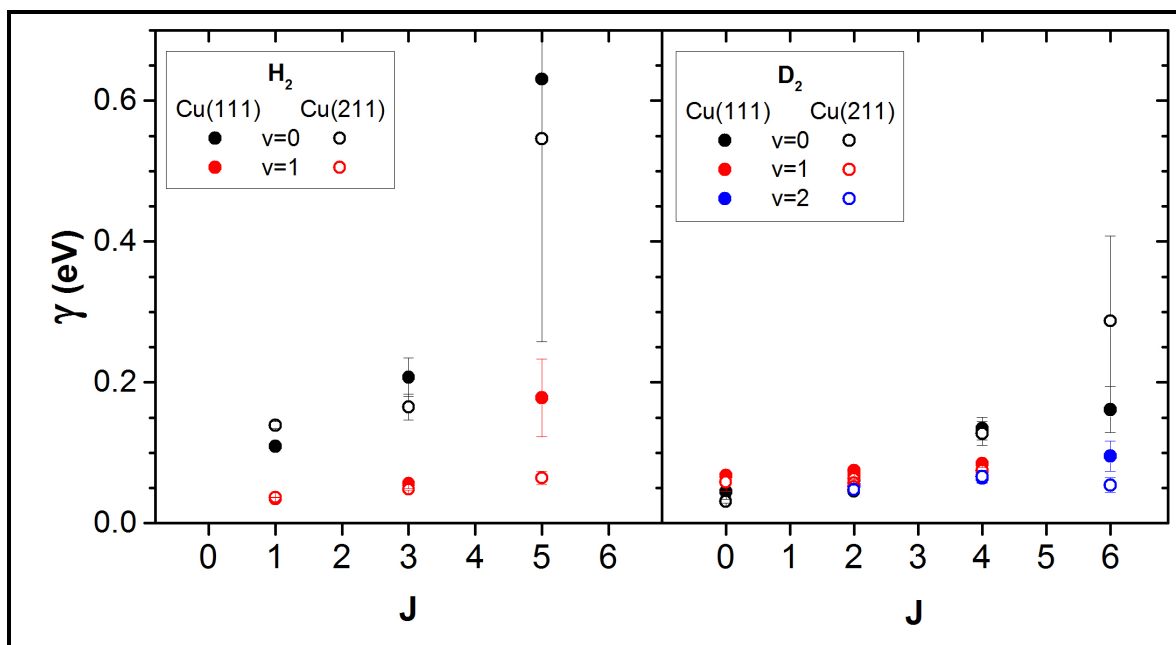
Figure 10.17: Summary of obtained γ_{slow} from both copper data sets. Only results using the contrastable method are given, because the other data sets have been less accurate due to worse FCA conditions. Panel (a) gives the results for H_2, panel (b) for D_2. Colors (black, red and blue) correspond to the different vibrational states ($v = 0 - 2$). Data for the Cu(111) facet is given by filled symbols, while Cu(211) is represented by open symbols.

of magnitude for all vibrational states. Thus, for H_2 vibrational excitation restricts the kinetic energy range where molecules can react.

Relative Flux   Due to the entanglement of the fitted A_{slow} parameters with γ_{slow}, here the integrated fluxes of the slow channel will be reported. These are more descriptive and presented in fig. 10.18 as the fraction of slow channel flux to total measured flux. The panels separate results for isotopologues and vibrational states but compare the surface facets directly. Similar to the γ_{slow} values, clear trends are observed only for the H_2 data. For D_2, the relative flux only decreases slightly with vibrational state, while showing no correlation with vibrational state or surface facet. In direct contrast the H_2 data set shows a clear reduction of the relative flux with increasing J, as well as generally higher fluxes for the Cu(211) sample.

It should be noted that the results presented here were obtained from TOF distributions that have been acquired normal to the surfaces. As will be shown in detail in section 10.2.1.8 the two reaction channels desorb with vastly different angular distributions. Therefore, the total flux from the surfaces in all directions is not represented by the results shown in fig. 10.18. In order to estimate the relative partitioning in the *total* flux from the surface, the observed angular distributions were integrated over all angles. For this, the n parameters in table 10.9 were averaged for slow and fast channel, respectively. This yielded an average $\cos^2(\theta)$-distribution for the slow channel and a $\cos^8(\theta)$-distribution for the fast channel. Successively, integration over all angles allows to scale the fluxes measured at the
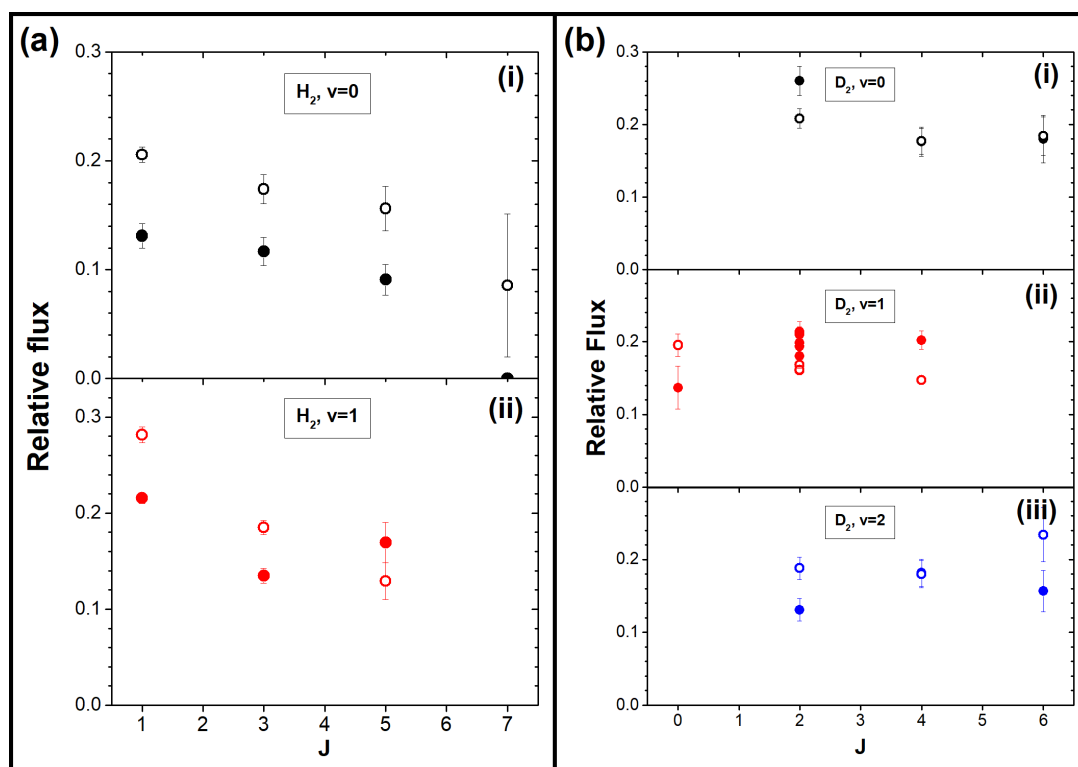
Figure 10.18: Summary of obtained relative fluxes for the slow channel from Cu(111) (filled symbols) and Cu(211) (open symbols). Panel (a) gives results for H_2 and (b) for D_2, with the subpanels (i-iii) corresponding to vibrational states $v = 0 - 2$. All data sets have been acquired *normal* to the surface.

surface normal to total fluxes. Averaging over isotopologues and all quantum states then yields a slow channel partition of (0.31 ± 0.09) for Cu(111) and (0.30 ± 0.07) for Cu(211).

Temperature Effects   Figure 10.19 shows how the slow channel is affected by temperature variations. Unfortunately the temperature range was limited to $(923 \pm 100)\,$K, because lower temperatures had insufficient flux. This is shown by the decrease in uncertainties for data sets at increased temperatures. At higher temperatures the FCA conditions degraded drastically by excess thermal radiation of the heating assembly, as described in fig. 10.2.

10.2.1.4   Quantum State Population Distributions

Quantum state population distributions derived from the measured fluxes are presented in fig. 10.20 in the form of Boltzmann plots with panel (a) for Cu(111) and (b) for Cu(211). Clearly, the distributions obtained for both reaction channels separately are for both facets in good agreement with each other. Deviations occur only for the Cu(211) facet and vibrationally excited states, but without a clear dependence on rotational state. Comparison to thermally expected rotational distributions are globally observed for high J-states only. Table 10.6 summarizes the results for vibrational state population distributions
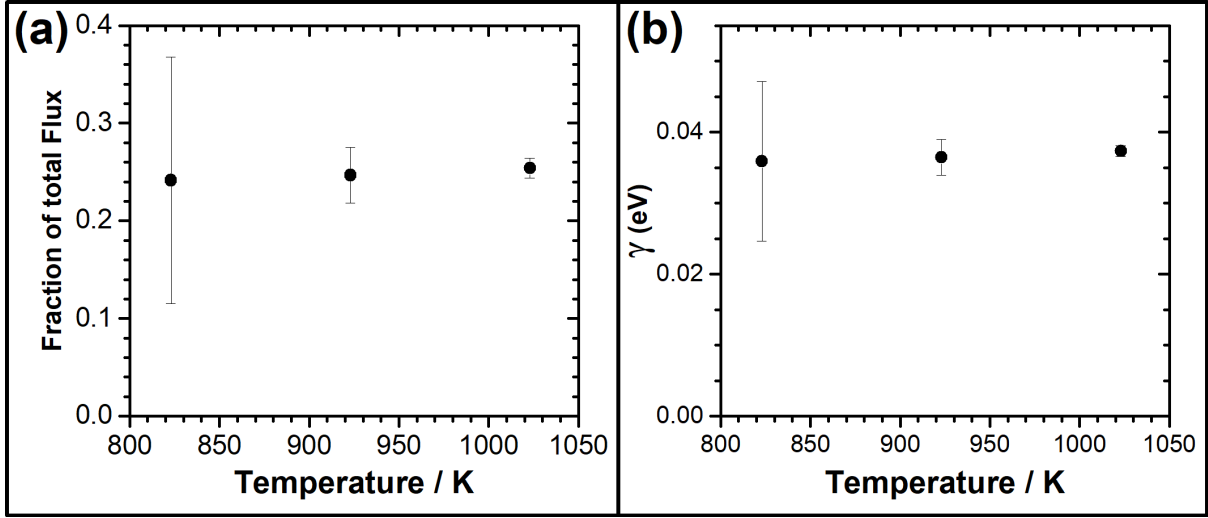
Figure 10.19: Temperature dependence of slow channel parameters obtained from the state with best SNR and high slow channel flux: H_2 ($v = 1, J = 1$)/Cu(211). Panel (a) gives the relative flux and (b) the γ_{slow} results. In the limited available range only three distinct temperatures were probed, but no dependences were observed. More details are given in the text.

Table 10.6: Obtained vibrational state population distributions for the hydrogen/copper system. Current results are presented for the total flux as well as subdivided for each reaction channel. Furthermore, thermally expected populations and literature values are presented.

System	Partition	H_2, $v=1/v=0$	HD, $v=1/v=0$	D_2, $v=1/v=0$	D_2, $v=2/v=0$
Cu(111)	**Total Flux**	0.059 ± 0.003	0.150 ± 0.007	0.148 ± 0.006	0.010 ± 0.001
	Fast Channel	0.058 ± 0.002	0.152 ± 0.005	0.150 ± 0.004	0.010 ± 0.001
	Slow Channel	0.063 ± 0.007	0.139 ± 0.016	0.136 ± 0.015	0.010 ± 0.002
Cu(211)	**Total Flux**	0.138 ± 0.005	0.158 ± 0.008	0.183 ± 0.005	0.050 ± 0.004
	Fast Channel	0.148 ± 0.005	0.163 ± 0.007	0.188 ± 0.005	0.053 ± 0.003
	Slow Channel	0.077 ± 0.012	0.115 ± 0.023	0.151 ± 0.008	0.028 ± 0.006
Lit. Cu(111)	**Ref.** [182,185]	-	-	0.25 ± 0.07	0.015 ± 0.004
	Ref. [189]	0.029 ± 0.007	-	-	-
	Ref. [177], 850 K	0.084 ± 0.030	-	0.35 ± 0.20	-
-	**Thermal**	0.0015	0.0035	0.0094	0.0001

with additional separation of the partitions for two reaction channels. Also literature values for Cu(111) from different sources are given as well as thermally expected populations. Evidently, enhanced partitioning of vibrational excitation is generally observed in the hydrogen/copper system. Since the exact partitioning varies between experiments, surface facets and isotopologues, no clear correlation can be observed. Breakdown in several reaction channels gives significant deviations mainly for the (211) facet, favouring the fast over the slow channel for all isotopologues.

Figure 10.21 gives the results for both copper facets using the contrastable method. While significantly fewer states have been obtained, the results are quantitatively the same as in fig. 10.20 and discussed above.
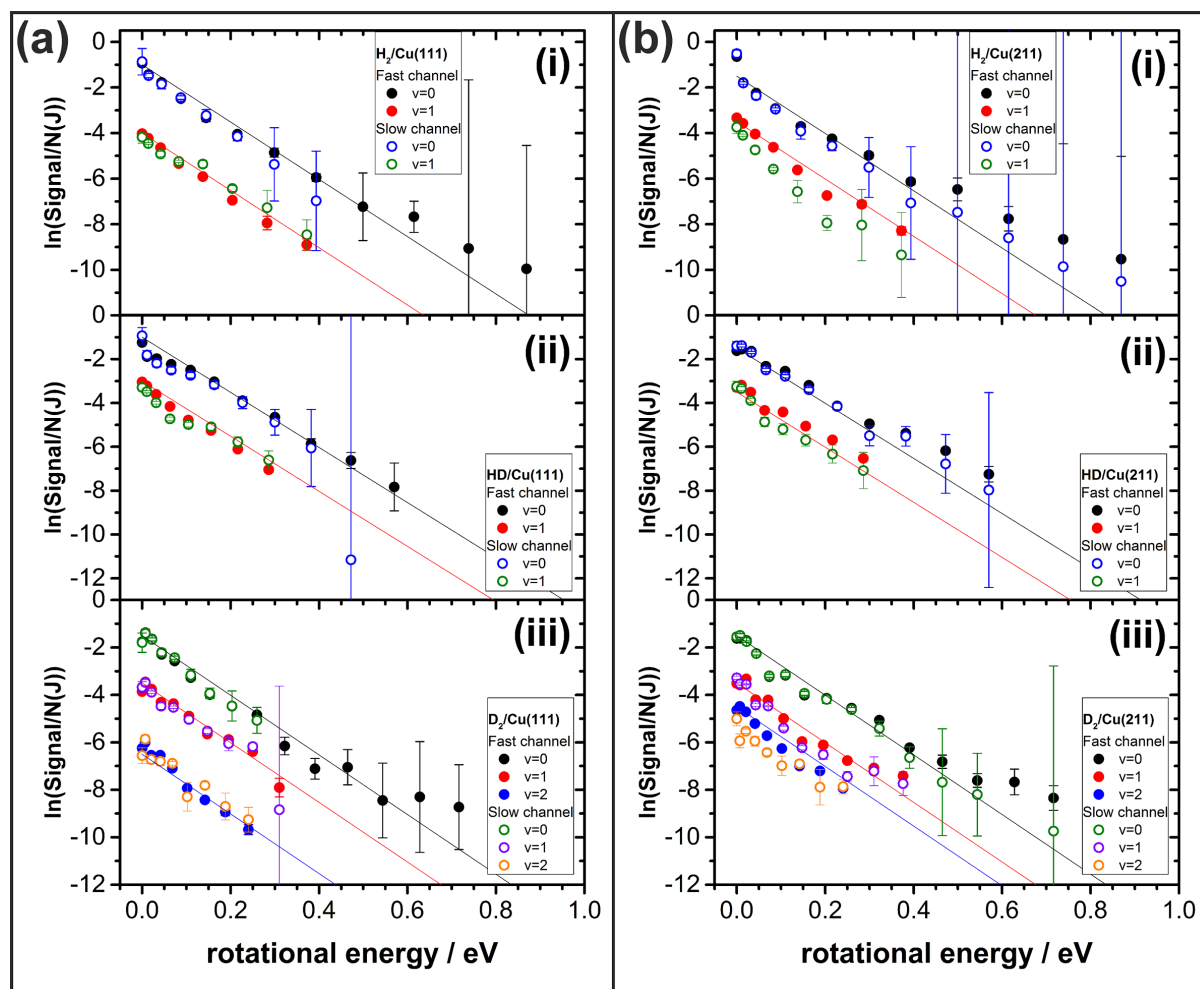
Figure 10.20: Boltzmann plots showing the quantum state population distributions for Cu(111) (panel (a)) and Cu(211) (b). Subpanels (i-iii) separate the results for the isotopologues (H$_2$, HD and D$_2$). Here, open symbols indicate results for the slow channel and filled symbols for the fast channel. Colors distinguish different vibrational states and are indicated additionally in a legend for each subpanel. Solid lines have been inserted to represent the slope expected from the surface temperature of (923 ± 2) K, their vertical positions are arbitrary.
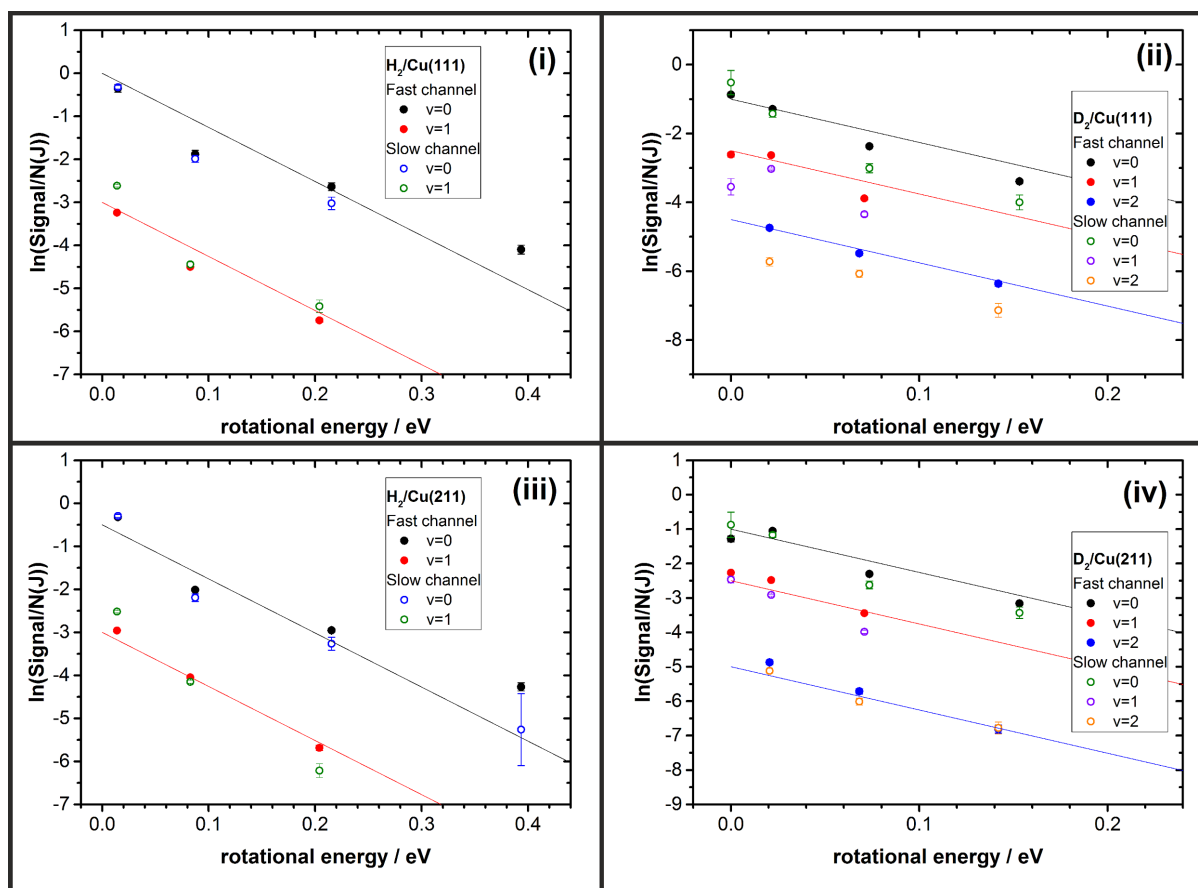
Figure 10.21: Boltzmann plots of quantum state population distributions using the contrastable method. Panel (i) gives $H_2/Cu(111)$, (ii) $D_2/Cu(111)$, (iii) $H_2/Cu(211)$ and (iv) $D_2/Cu(211)$. Again, open and filled symbols indicate results for the slow and fast channel, respectively. Colors distinguish different vibrational states and are indicated additionally in a legend for each panel and solid lines have been inserted as for fig. 10.20.

Table 10.7: Obtained efficacies for both copper facets based on E_0 as described in the text. Additionally, directly comparable literature values are presented in the last column.

Isotopologue	Efficacy	Cu(111)	Cu(211)	Lit. Cu(111) [a]
H_2	$\varepsilon_{\text{vib}}(v=1, J=0)$	0.69 ± 0.01	0.55 ± 0.01	0.51 ± 0.02
H_2	$\varepsilon_{\text{rot}}(v=0)$ [b]	0.51 ± 0.01	0.43 ± 0.02	0.45 ± 0.03
H_2	$\varepsilon_{\text{rot}}(v=1)$ [c]	0.28 ± 0.03	0.15 ± 0.04	0.39 ± 0.03
HD	$\varepsilon_{\text{vib}}(v=1, J=0)$	0.76 ± 0.01	0.61 ± 0.01	-
HD	$\varepsilon_{\text{rot}}(v=0)$ [d]	0.46 ± 0.04	0.39 ± 0.05	-
HD	$\varepsilon_{\text{rot}}(v=1)$ [e]	0.40 ± 0.02	0.33 ± 0.10	-
D_2	$\varepsilon_{\text{vib}}(v=1, J=0)$	0.74 ± 0.02	0.76 ± 0.01	0.54 ± 0.02
D_2	$\varepsilon_{\text{vib}}(v=2, J=0)$	0.65 ± 0.04	0.61 ± 0.02	0.54 ± 0.02
D_2	$\varepsilon_{\text{rot}}(v=0)$ [f]	0.59 ± 0.02	0.54 ± 0.04	0.41 ± 0.02
D_2	$\varepsilon_{\text{rot}}(v=1)$ [g]	0.42 ± 0.04	0.31 ± 0.05	0.32 ± 0.06
D_2	$\varepsilon_{\text{rot}}(v=2)$ [h]	0.16 ± 0.09	0.04 ± 0.05	0.36 ± 0.10

[a] Values from references [185] (D_2) and [189] (H_2).

[b] for data with $E_{\text{int}} > 0.48 \, \text{eV}$.

[c] for data with $E_{\text{int}} > 0.92 \, \text{eV}$ for Cu(111) and $E_{\text{int}} > 0.87 \, \text{eV}$ for Cu(211).

[d] for data with $E_{\text{int}} > 0.53 \, \text{eV}$ for Cu(111) and $E_{\text{int}} > 0.46 \, \text{eV}$ for Cu(211).

[e] for data with $E_{\text{int}} > 0.84 \, \text{eV}$ for Cu(111) and $E_{\text{int}} > 0.74 \, \text{eV}$ for Cu(211).

[f] for data with $E_{\text{int}} > 0.51 \, \text{eV}$.

[g] for data with $E_{\text{int}} > 0.71 \, \text{eV}$.

[h] for data with $E_{\text{int}} > 0.98 \, \text{eV}$.

10.2.1.5 Efficacies based on E_0 parameters

From the presented E_0 parameters efficacies were obtained using eqs. (8.37) and (8.38). All results are summarized in table 10.7 alongside with literature results for Cu(111) [182,185,189] to allow direct comparison. It is pointed out, that ε_{rot} values were not obtained from eq. (8.37) directly, due to the complex interaction at low J states in the H_2/Cu system. Instead, the method of linear regression through high J-state values plotted as function of internal energy was chosen (cf. [185]), yielding $\varepsilon_{\text{rot}}(v)$ values averaged over these states. As in the literature, low J data was excluded based on arbitrarily chosen values of internal energy, which are indicated for each ε_{rot} in table 10.7.

10.2.1.6 Threshold Reduction

Numerical determination of RPCs, as described in section 8.3.4.2, allows the determination of ΔS values as described in section 8.3.4.3. For illustrative purposes, fig. 10.22 gives numerical RPCs for both copper surfaces. Despite the generally similar results for both facets a larger contribution of the slow channel is noticeable in the D_2 ($v = 2, J = 2$)/Cu(211) data at $E_{\text{kin}} < 0.15 \, \text{eV}$.

All resulting ΔS values are presented in fig. 10.23, again separated in panels for both

Table 10.8: Obtained efficacies for D_2 and both copper facets using ΔS values (see eq. (8.46)).

System	Cu(111)	Cu(211)
H_2 $(v = 1, J = 0)$	0.81 ± 0.04	0.74 ± 0.04
$HD(v = 1, J = 0)$	0.76 ± 0.05	0.76 ± 0.05
D_2 $(v = 1, J = 0)$	0.70 ± 0.06	0.75 ± 0.06
D_2 $(v = 2, J = 0)$	0.95 ± 0.06	0.90 ± 0.06

surface facets. Similar to the E_0 presentation in references[185,189], the values are plotted as function of internal energy and for all isotopologues. The complex influence of rotational energy is easily seen in these graphs in the rotational sequences for all isotopologues and both facets. At low J the ΔS values are negative, but their variation with J decreases and approaches zero at intermediate J. Then, this trend reverses and the ΔS values become largely positive with an almost linear increase obtained at high J.

Also shown in fig. 10.23 are green lines, which were fitted through the ΔS values of all $J = 0$ states. The slopes of these lines show isotopologue-averaged vibrational efficacies similar to the rotational efficacy analysis established by Michelsen *et al.*[185]. Here, this method yields 0.81 ± 0.03 for Cu(111) and 0.79 ± 0.03 for Cu(211).

10.2.1.7 Efficacies based on ΔS parameters

As described in section 8.3.4.4 the ΔS values can be used to obtain efficacies by eq. (8.46) and the results are presented in table 10.8. Direct comparison to efficacies obtained by the established methodology (see table 10.7) shows strong deviations. The ξ_{vib} values show no systematic trends, i.e. some are lower than their corresponding $\varepsilon_{\mathrm{vib}}$ results [D_2 $(v = 1)$], some agree [HD $(v = 1)$ /Cu(111)], and most ξ_{vib} values are significantly larger. Because all values were determined from the same measured data sets, this shows that both methods are not equivalent. Thus ξ_{vib} results cannot be copared to literature values. In summary the ξ_{vib} values are on the order of ~0.7–0.8 for both facets and $(v = 1)$, but show values >0.9 for D_2 $(v = 2)$.

Rotational efficacies (ξ_{rot}, eq. (8.45)) are presented in fig. 10.24 in a different form. Here, the results are plotted as function of rotational energy. These plots ignore the vibrational energies and show that rotational effects are global for the three isotopologues studied here as well as for all vibrational states. Furthermore, it is indicated that rotational energy overcomes alignment effects at ~0.2 eV, irrespective even of surface facet. Finally, at high energies a value in the range 0.5–0.6 eV is reached asymptotically. This last result agrees well with the $\varepsilon_{\mathrm{rot}}$ results presented in table 10.7.
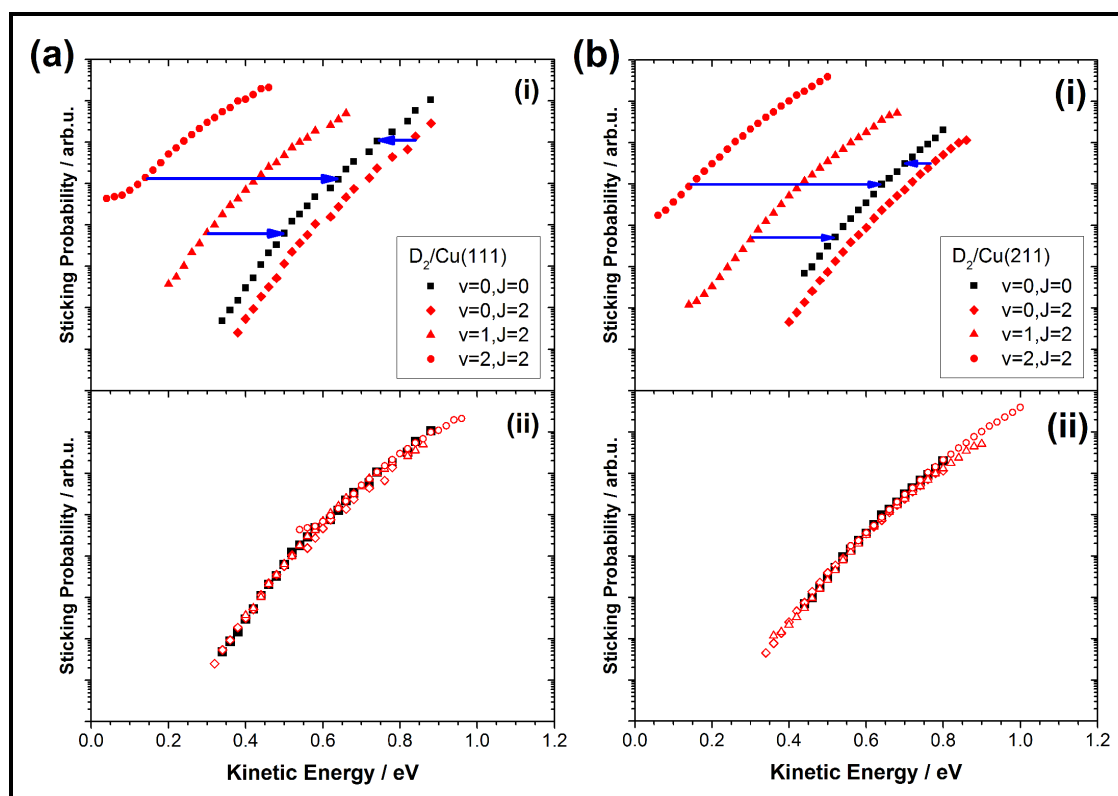
Figure 10.22: Illustration of numerically determined reaction probabilities according to section 8.3.4.2. Panel (a) gives D_2 data for Cu(111) and (b) for D_2/Cu(2111), with the black squares corresponding to the ground state serving as reference. Representative data for the states $(v = 0-2, J = 2)$ are given by the filled red diamonds, triangles and circles. Blue arrows in subpanels (i) indicate how the ΔS is determined, with the shifted RPCs given in subpanels (ii) as open symbols.
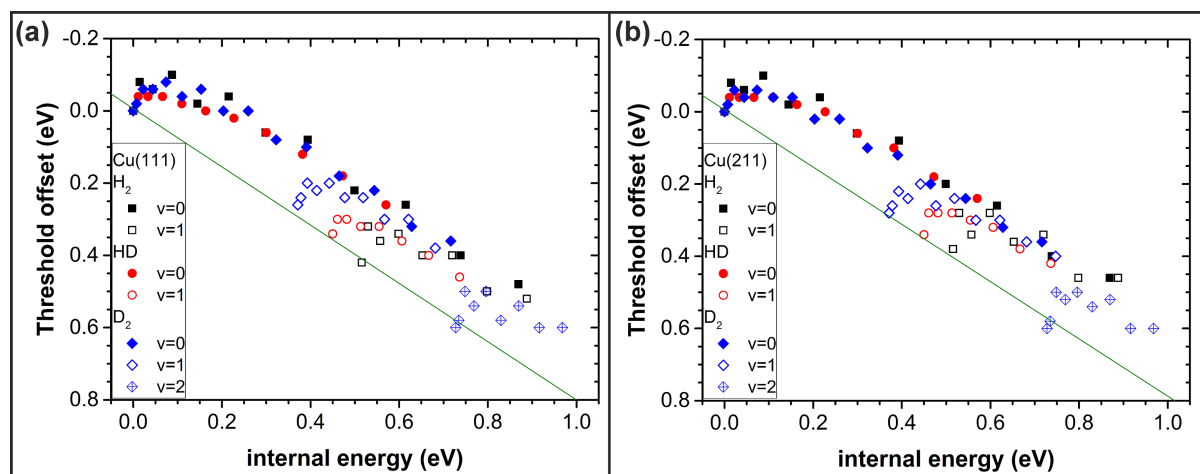
Figure 10.23: Summary of ΔS results for Cu(111) (panel (a)) and Cu(211) (b) plotted as function of internal molecular energy. Isotopologues are indicated by color and different symbols: H_2 as black squares, HD as red circles and D_2 as blue diamonds. The vibrational states are represented by symbol fills: filled, open and open with cross for $v = 0-2$. Additionally given are fits through all available $J = 0$ data points, as green lines. This method yields an isotopologue-averaged vibrational efficacy from the slopes: 0.81 ± 0.03 for Cu(111) and 0.79 ± 0.03 for Cu(211).

Table 10.9: Summary of angular distribution results from both copper facets. The first three columns describe the specific system, and the last two give the fit results of eq. (8.33). The model treated both reaction channels separately and thus obtained n parameters for both.

Surface	Isotopologue	Quantum State	n(Fast channel)	n(Slow channel)
Cu(211)	H_2	$v = 0, J = 1$	7.6 ± 0.5	0.8 ± 0.4
Cu(211)	D_2	$v = 0, J = 2$	9.1 ± 1.5	0.4 ± 2.6
Cu(211)	D_2	$v = 1, J = 2$	5.9 ± 0.9	4.0 ± 0.7
Cu(111)	D_2	$v = 0, J = 2$	9.2 ± 0.5	1.7 ± 0.5
Cu(111)	HD	$v = 0, J = 3$	8.6 ± 0.8	2.9 ± 0.9

10.2.1.8 Angular Desorption Distribution

The analysis of angular distributions was described in section 8.3.2.3 and the experimental procedure in section 9.2.2.5. Resulting TOF traces were fitted with the model for both reaction channels (eqs. (8.4) and (8.7)) and their respective integrated fluxes were obtained. From those, angular distributions were fitted using eq. (8.33). Table 10.9 summarizes all obtained n parameters and fig. 10.25 shows illustrative subsets of the obtained distributions. For the fast channel highly directed flux ($n \gg 1$) is observed along the surface normal (panels (a) and (c)). For the slow channel the distributions are rather broad ($n = 0.4$–4.0) and can also be described well by simple cosine distributions ($n = 1$), as illustrated in panels (b) and (d) by green lines. It is pointed out that the relative partition between the channels depends strongly on the direction of detection, as illustrated in panel (a), where results for both channels are given on the same scale. An estimate for the *total* flux off the crystals was presented in section 10.2.1.3.

10.2.1.9 Averaged Desorption Energies

As described in section 8.3.3.6, the state averaged desorption energies can be obtained based on eq. (8.39). Because the data set using the contrastable method contains significantly fewer quantum states, it was excluded from this analysis. Results for both copper facets are presented in table 10.10, which also gives the results as separated for isotopologue and reaction channels.

As expected from the similarity of fitted RPC parameters, the results vary only little between the surface facets. Also, differences between the isotopologues for each facet are negligible. For the different channels, the separation between their $\langle E_{\mathrm{kin}} \rangle$ values is ~0.5 eV for all systems. Thus, for the slow channel desorption energies are lower than the thermal equilibrium energy in the system ($2k_bT_s \approx 0.08$ eV [287]).

10.2.1.10 Extrapolated Activation Energies

Using the model described in section 8.3.4.5, mean absorption probabilities for thermal gas, $\langle S_0(T_s) \rangle$, were calculated from the state selected RPCs using eqs. (8.48) and (8.49).
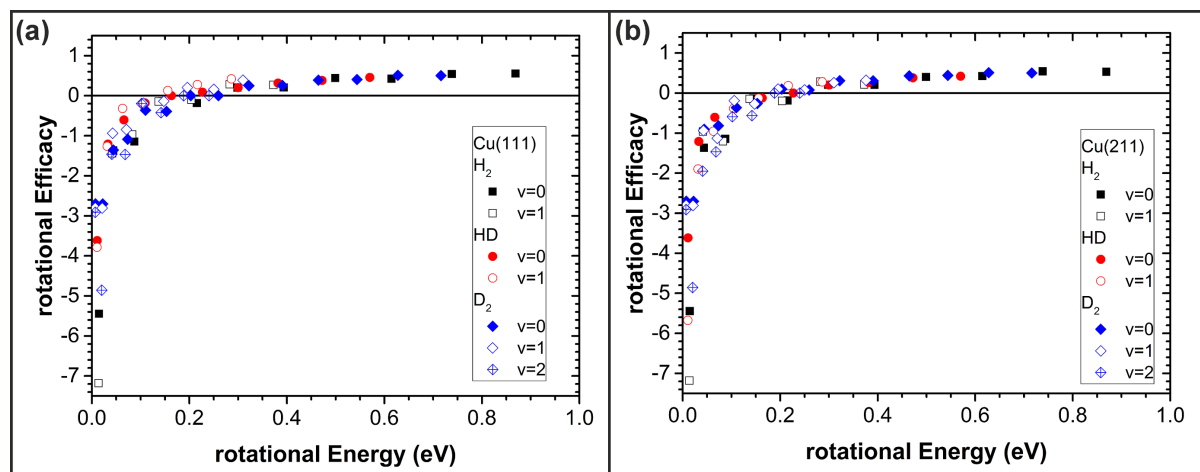
Figure 10.24: Summary of rotational efficacies (ξ_{rot}) for all isotopologues plotted as function of internal molecular energy. Panel (a) gives results for Cu(111) and (b) for Cu(211).
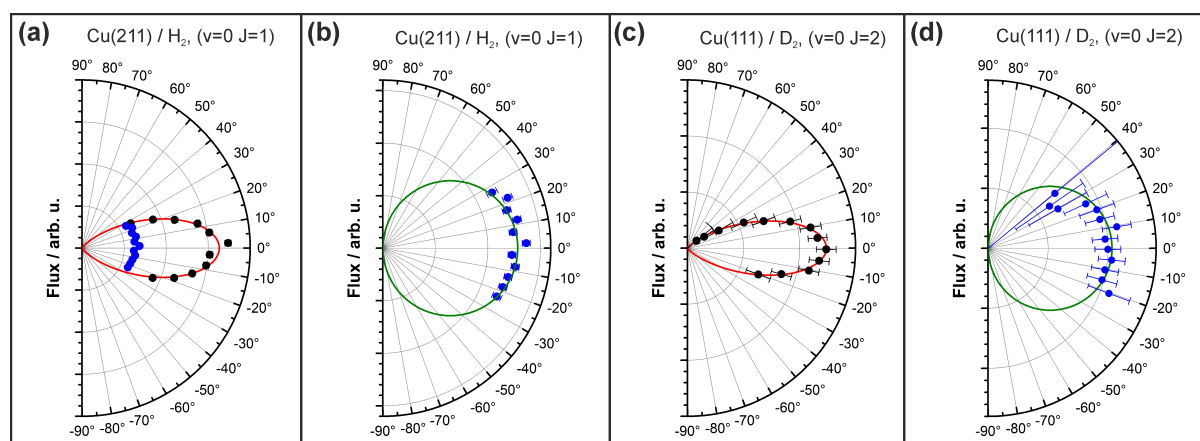
Figure 10.25: Illustrative angular distributions measured from both copper facets. Panels (a) and (b) show data obtained from H_2 ($v = 0$, $J = 1$)/Cu(211), and (c) and (d) from D_2 ($v = 0$, $J = 2$)/Cu(111). In (a) and (c), the integrated fast channel flux is indicated by black points and the corresponding fitted models as red lines. Blue points indicate the integrated flux of the slow channel. For comparison, the green lines in panels (b) and (d) show cosine distributions instead of the fitted models. Additionally, panel (a) gives the fluxes of both channels on the same scale to illustrate how the relative partitioning to the total fluxes varies with the detection angle.

Table 10.10: Mean desorption energies for both copper facets, obtained by averaging over internal states. Results are differentiated for surface facet, isotopologue and into total flux as well as both reaction channels separately.

	Mean desorption energy, $\langle E_{\mathrm{kin}} \rangle$ / meV
	\multicolumn{3}{c}{Cu(111)}	\multicolumn{3}{c}{Cu(211)}
Channel	H_2	HD	D_2	H_2	HD	D_2
total flux	0.526	0.506	0.523	0.505	0.534	0.511
fast channel	0.594	0.578	0.599	0.585	0.595	0.592
slow channel	0.102	0.088	0.098	0.096	0.110	0.103

Table 10.11: Activation Energies as determined by the model in section 8.3.4.5, using the data obtained for the hydrogen/copper systems. Parameters from fitting an Arrhenius like relationship (eq. (8.47)) to simulated $\langle S_0(T_s) \rangle$ as well as the reduced χ-square value $\left(\chi_r^2\right)$ of the fits are presented.

Surface	**Isotopologue**	A_{pre} / **Arb.u.**	E_{act} / **eV**	χ_r^2 / **Arb.u.**
	H_2	0.426 ± 0.031	0.525 ± 0.006	1.086×10^{-3}
Cu(111)	HD	0.325 ± 0.025	0.522 ± 0.006	1.138×10^{-3}
	D_2	0.355 ± 0.029	0.536 ± 0.007	1.322×10^{-3}
	H_2	0.104 ± 0.011	0.532 ± 0.008	2.043×10^{-3}
Cu(211)	HD	0.147 ± 0.014	0.530 ± 0.007	1.626×10^{-3}
	D_2	0.118 ± 0.012	0.559 ± 0.008	1.959×10^{-3}

Here, the integrations in eq. (8.48) were done numerically, by using a resolution of 3° for θ, 10 meV for E_{kin}, and an upper integration limit of 2.5 eV. The use of less restrictive limits was tested and gave simulation results for E_{act} with deviations on the order of 0.1 meV, which is well below the accuracy of the underlying model (see section 11.2.2.2). $\langle S_0(T_s) \rangle$ values were calculated for six temperatures in the range 800–1050 K, which allowed the fitting of eq. (8.47), and resulting parameters are presented in table 10.11. It is pointed out, that the given standard deviations represent the uncertainties of the fit to the Arrhenius model and not the accuracy of the model itself. Furthermore, for this model only the fast channel contribution was included.

Additionally to the many assumptions made in the model itself, it has been shown[186] that the results depend strongly on other calculation parameters. A comparison of the obtained results to literature is shown in section 10.3.1.5, and a detailed discussion is given in section 11.2.2.2.

10.2.2 Gold Surface

In the following subsections the obtained Au(111) data will be analyzed in several aspects, a part of which have already been published elsewhere[220]. In contrast to the copper data sets, the ERF model (eq. (8.4)) alone was sufficient to describe the RPCs obtained for Au(111). But due to the higher desorption energies, problems with the significance and the correlation of the obtained parameters arose, which will be discussed in section 11.2.2.1.

It is pointed out that due to problems with the experimental heating device (cf. section 9.1.1.2), not all data was obtained at the same surface temperature. While most data was acquired at $1061\,K$, the rotational sequences for H_2 ($v = 1$), HD ($v = 1$) and D_2 ($v = 2$) were measured at temperatures in the range of 1093–$1109\,K$, corresponding to a deviation of less than $+4.5\,\%$. Repeated measurements of the D_2 ($v = 2$) sequence with a repaired setup were conducted to verify the results and showed no significant differences. Temperature dependent data could not be obtained over a wide range, since the permeation flux was insufficient at lower temperatures. At higher temperatures, the mechanical stability of the sample was too low to prevent deformation of the thin membrane by the probe gas at $1\,bar$ backing pressure. This deformed sample still showed a LEED pattern corresponding to a (111) facet, despite the dome shaped elevation of $\lesssim 0.5\,mm$ in its center. Also, obtained TOF traces were still indistinguishable from those of the flat surface within experimental accuracy.

10.2.2.1   Time of Flight Distributions

Typical TOF distributions and fitted model results are presented in fig. 10.26, for all three isotopologues and different vibrational states with the subpanels (i-iii) corresponding to the vibrational states $v = 0 - 2$. Panel (a) gives data for H_2 $J = 1$, (b) for HD $J = 4$ and (c) for D_2 $J = 2$. Each of the subpanels is presented on the same TOF scale to illustrate the effect for vibrational excitation on the distributions. The desorption peaks are shifted significantly to later TOFs and thus lower kinetic energies. It is pointed out, that the fitted model (see section 8.3.1.2) is not affected by the occurring TB signals (panels (i)) due to the clear separation to the permeation signals.

In order to show also the influence of rotational state, fig. 10.27 presents the obtained data for D_2 ($v = 0$)/Au(111). Each TOF trace is normalized and plotted offset on the vertical axis, with an orange line added as guide for the eye. Despite the SNR apparently lower than found for Cu(111) (fig. 10.9), the peak positions are in the range of 8.8–$9.0\,\mu s$ for $J < 8$ and shift to longer times only for higher J states.

10.2.2.2   Kinetic Energy Distributions

Figure 10.28 presents kinetic energy distributions obtained by conversion of the presented TOF data (see section 8.3.4) which was already presented in fig. 10.26. Here, the converted data (black) was rebinned with a resolution of $20\,meV$, and the fit functions (red) result from eq. (8.29) and the fitted RPC parameters. The panel layout is the same as in fig. 10.26, separating the isotopologues in panels (a-c) and vibrational states ($v = 0 - 2$) in the according subpanels (i-iii). Vibrational energy strongly reduces the reaction barrier distributions, as can be deduced from the shift of the peaks in fig. 10.28 to lower energies.

In the kinetic energy distributions, the TB is clearly visible in the low kinetic energy regions for all ($v = 0$) data (panels (i)). While panels (ii-iii) also show small signals for
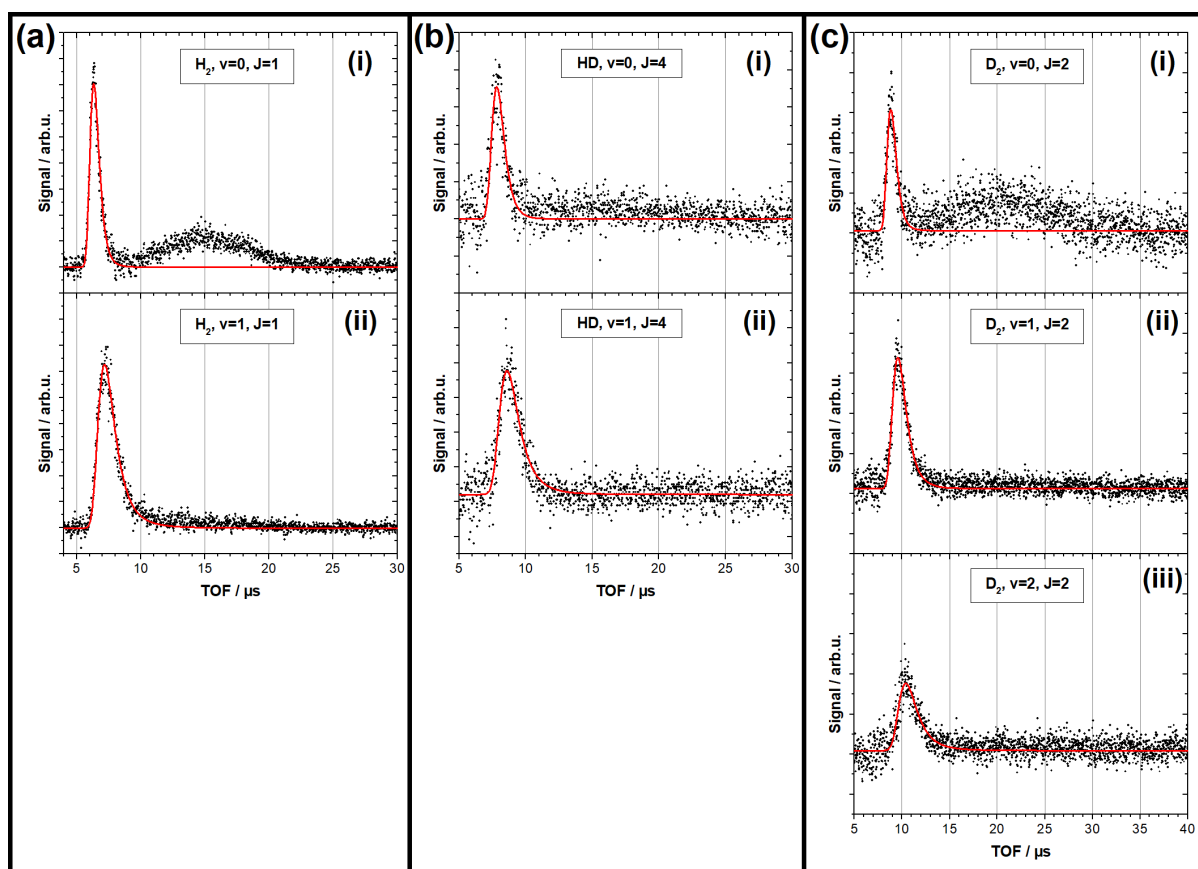
Figure 10.26: Typical TOF distributions (black points) and fit results (red lines) for hydrogen/Au(111). The panels show data of the three isotopologues, each with the rotational state chosen to present data with appropriate SNR: H_2 $J = 1$ (a), HD $J = 4$ (b) and D_2 $J = 2$ (c). Three subpanels separate the data for vibrational states: ($v = 0$) (i), ($v = 1$) (ii) and ($v = 2$) (iii). Reprinted in part with permission from [220]. Copyright 2017 American Chemical Society.

data below $0.1\,\text{eV}$, only negligible TB was expected here. These small signals therefore must result from the noise of the signal above the fixed baseline level (cf. section 8.3.2.1). This can be demonstrated by comparing the fit to the data points, e.g. panel (c, ii) in fig. 10.26 for TOFs $>15\,\mu\text{s}$.

Additionally to the presented fits using the detailed balance model, Gaussian fits to all obtained kinetic energy distributions were conducted, and those results are presented in appendix D.2. But these will not be discussed in detail, because there is no underlying model justifying such an approach. It is rater intended to allow comparison and reproduction of the measured distributions for future analysis efforts, e.g. testing other functional forms representing the RPCs. Illustrative results are given in fig. 10.29, including results for both copper facets as well.

10.2.2.3   Obtained RPC Parameters

For analysis of the obtained Au(111) data additional restrictions in the fitting process were required to prevent strong variations and uncertainties in the results. This was
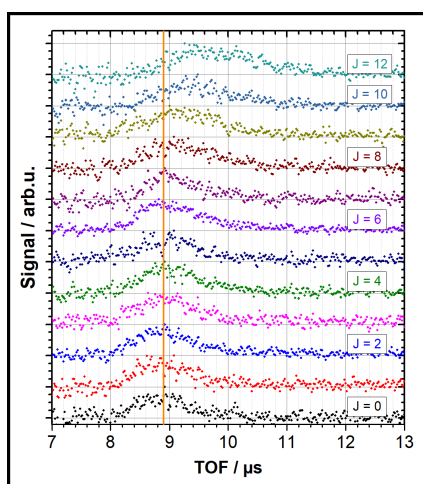
Figure 10.27: Normalized TOF traces for the J-sequence of the D_2 ($v = 0$) /Au(111) data set. Each trace is plotted offset on the vertical axis and a orange line is inserted as guide for the eye. An analogue representation for Cu(211) was shown in fig. 10.9. Here, for $J = 11$ the SNR was not sufficient to be acquired in a reasonable measurement time. Therefore, the offset for the $J = 12$ line is not linear. Due to the general low SNR, TOF shifts are unrecognizable for $J < 7$ and quantitative analysis is necessary to determine rotational effects.
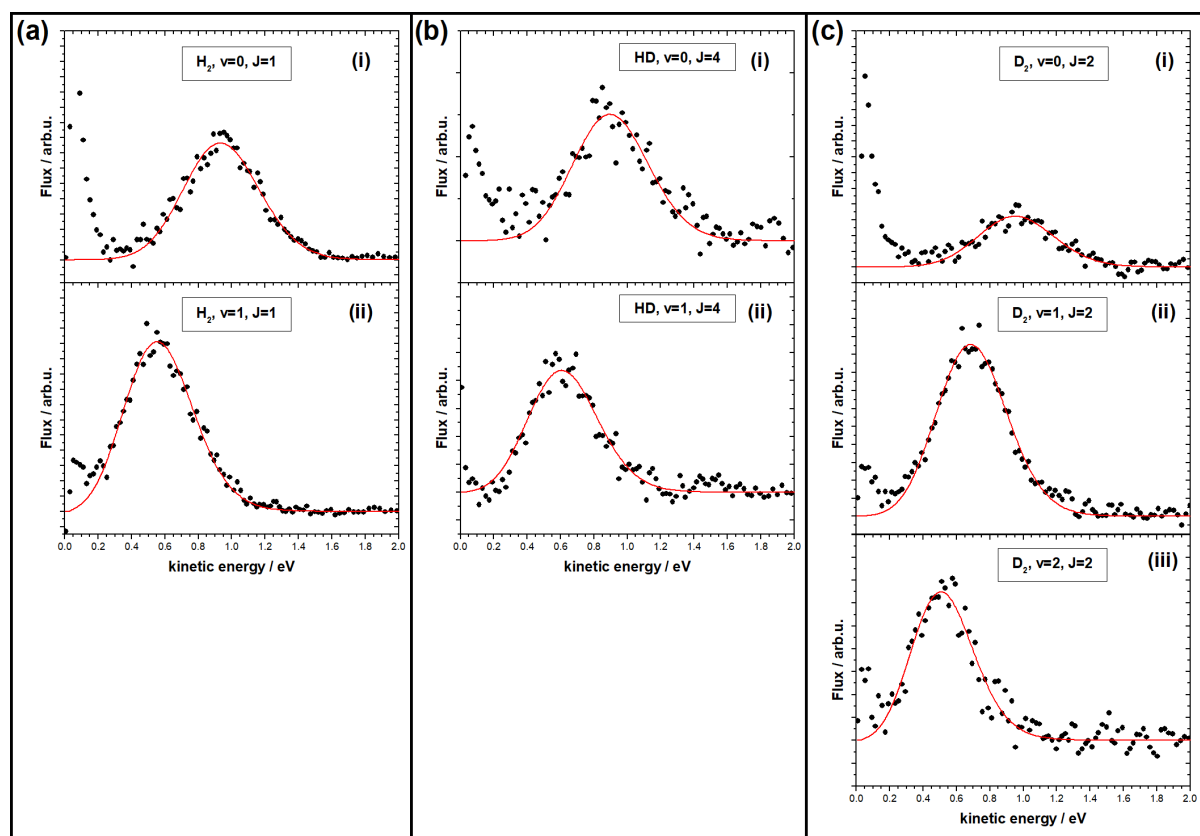
Figure 10.28: Typical kinetic energy distributions (black points) and fit results (red lines) for hydrogen/Au(111), obtained from the TOF data presented in fig. 10.26 according to section 8.3.4. Here, the panel layout is the same as in fig. 10.26: H_2 $J = 1$ (a), HD $J = 4$ (b) and D_2 $J = 2$ (c), with the subpanels (i-iii) for $v = 0 - 2$, respectively. The converted points (black) have been rebinned with $20\,\text{meV}$ bins, while the fit function (red) was simply obtained from eq. (8.29).
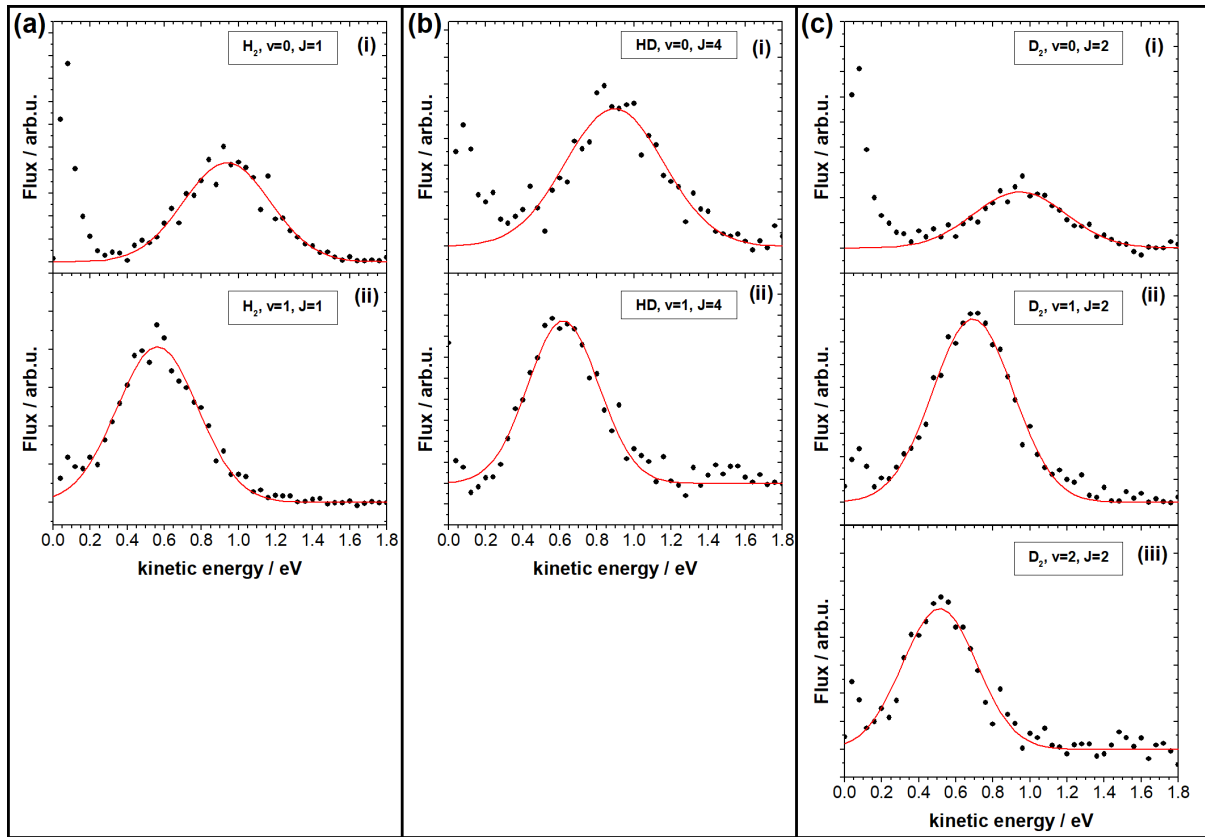
Figure 10.29: Illustrative Gaussian fits to the Au(111) results presented in fig. 10.28. Here, the panel layout is the same as in fig. 10.28, but the data points (black) have been rebinned to 40 meV and the fits (red lines) show the Gaussian model, as described in detail in appendix D.2.

induced partly by the poor SNR of most of the obtained data sets and partly by the high kinetic energy ranges sampled. The RPCs for high barrier distributions suffer from significant parameter correlation (section 11.2.2.1). Instead of analysing each quantum state individually, the W of the ERF was taken as a global parameter for data in the same vibrational state, irrespective of rotational state and isotopologue.

This approach was justified by a preceding analysis, where data for each quantum state was fitted individually. This yielded strong deviations in the resulting RPC parameters in between the individual states, and the resulting W values were averaged for each isotopologue and vibrational state. This allowed comparison of these W between the three isotopologues, showing deviations much lower than the individual uncertainties. It is pointed out, that in the TOF data no strong deviations in the individual widths of the distributions was observed, as can be seen in fig. 10.27, despite the evidently poor SNR. In conclusion, the approach of W global for all isotopologues in the same vibrational state was reasonable. This method showed an increase of the overall fit reliability while not degrading the quality notably. In the following paragraphs, the results for the three ERF parameters will be presented, but it is pointed out that the results are additionally given in tabular form in appendix D.1.4.

E_0 **Parameters**   Figure 10.30 summarizes all E_0 values acquired in this work. Each panel (a-c) gives the results for a certain isotopologue (H_2, HD, D_2), with the symbol color representing the vibrational state: ($v = 0$) (black), ($v = 1$) (red) and ($v = 2$) (blue). Here, the error bars result from the fitting model. Clearly, the barrier distribution functions shift to lower energies with increasing vibrational excitation. Furthermore, rotational energy has the same effect, but smaller in magnitude, which can be seen best in the H_2 ($v = 0$) sequence. A quantitative analysis will be presented in section 10.2.2.6. Here, it is pointed out that the E_0 values are significantly higher than for both copper facets (see section 10.2.1.3), as expected for the Au(111) system. Such high values lead to a problem with accuracy in the fitted parameters, since the observed desorption distributions do not sample the saturation regime of the RPCs sufficiently. For example, the E_0 value of the data shown in panel (a, i) in fig. 10.28 is $(1.312 \pm 0.006)\,\mathrm{eV}$, but the amplitude of the desorbing flux is already $\approx 25\,\%$.

Width Parameters   Es elaborated above, the W was obtained as global parameter depending only on vibrational state but not on rotational state or isotopologue. Results of this analysis for the whole Au(111) data set are presented in table 10.12, where the uncertainties were obtained from the fitting procedure. Due to the global approach and the large data set fitted, these uncertainties are smaller than expected. The obtained W parameters decrease for higher vibrational states, as for both copper data sets (see table 10.4). But the values for Au(111) are significantly larger, more than expected from
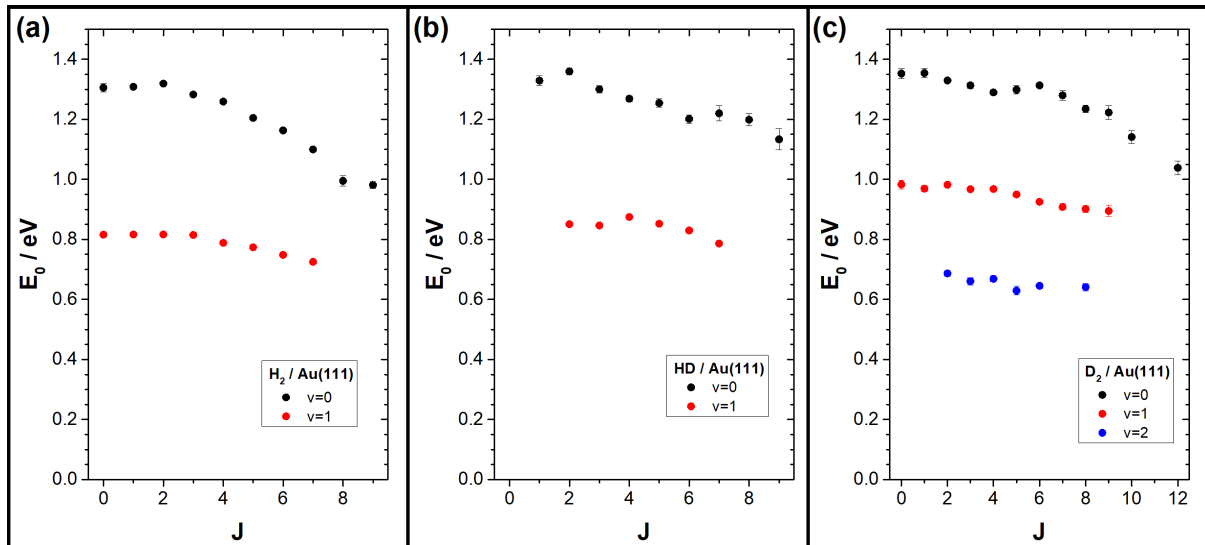
Figure 10.30: Summary of obtained E_0 values for the hydrogen/Au(111) system. Symbol colors represent data from different vibrational states with v=0-2 as black, red and blue, respectively. Panels (a-c) separate the results for the isotopologues H_2, HD and D_2. The error bars represent the uncertainties from the fitted model as explained in the text.

Table 10.12: Global W-parameters obtained for all datasets desorbing from Au(111). The parameters and the uncertainties of the fitting procedure are presented. It is pointed out, that for $(v = 2)$ only six D_2 traces are available. Reprinted in part with permission from [220]. Copyright 2017 American Chemical Society.

v	$W(v)$/ eV	$\Delta W(v)$/ eV
0	0.3084	0.0019
1	0.2859	0.0011
2 [a]	0.2504	0.0042

[a]Only data for D_2 available.

the higher surface temperature of these measurements.

Saturation Parameters A rotational state resolved summary of the A_{erf} parameters is given in fig. 10.31. Here, it is apparent that all values range in between 0–2.3 and for D_2 also agree well in between different vibrational states. In contrast, the sequences for H_2 and HD $(v = 1)$ are significantly higher than for $(v = 0)$, for all rotational states. Additionally, table 10.13 gives A_{flux} and A_{erf} values obtained from this data with the A_{erf} averaged over the whole rotational sequences. Both these analyses give clear isotopic-dependent trends for higher vibrational excitation of H_2 and HD than for D_2.

10.2.2.4 Quantum State Population Distributions

Figure 10.32 presents the obtained quantum state population distributions. Common for all isotopologues and vibrational states are the deviations from the thermally expected distributions for high J states. For the vibrational state dependence, only the D_2 data set shows no strong anomalies. In contrast the H_2 $(v = 1/v = 0)$ ratio is enhanced, as apparent
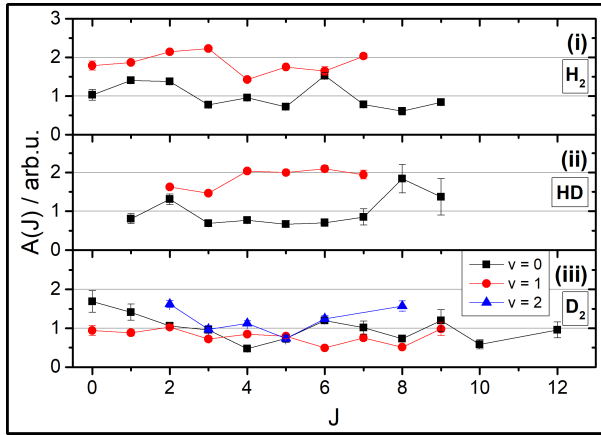
Figure 10.31: Summary of obtained A_{erf} values for the hydrogen/Au(111) system. Subpanels (i-iii) separate the results for H_2, HD and D_2, and colors for vibrational state: black squares ($v = 0$), red circles ($v = 1$) and blue triangles ($v = 2$). Data in each panel has been normalized to give an average value of unity for each ($v = 0$) sequence. Reprinted in part with permission from [220]. Copyright 2017 American Chemical Society.

Table 10.13: Vibrational state population distributions for the Au(111) system, presented as population relative to ($v = 0$). The A_{flux} and A_{erf} values are directly compared, calculated as described in section 8.3.3.4.

Isotopologue	v	relative population	A_{flux}	A_{erf}
H_2	0	1.00 ± 0.07	0.55 ± 0.06	1.00
H_2	1	0.51 ± 0.02	1.00 ± 0.06	1.86
HD	0	1.00 ± 0.18	0.43 ± 0.14	1.00
HD	1	1.00 ± 0.05	1.00 ± 0.09	1.86
D_2	0	1.00 ± 0.13	0.80 ± 0.18	1.00
D_2	1	0.34 ± 0.03	0.62 ± 0.09	0.79
D_2	2	0.13 ± 0.02	1.00 ± 0.20	1.21

from section 10.2.2.3. However, the HD data set gives an even stronger anomaly with an almost equal partition of ($v = 1$) and ($v = 0$).

It should be pointed out, that despite the partly poor SNR, especially for the HD ($v = 0$) sequence, the quantum state population distributions analysis is based on the integrated fluxes and thus more reliable than the individual RPC parameters. This argument also extends to the A_{flux} parameters in comparison to the A_{erf} values. A comparison for these parameters is presented in table 10.13. Despite some variations between the individual values, isotopologue-dependent effects are clearly discernible. While for D_2 the saturation parameters range around unity for ($v = 1$) a huge enhancement is obtained for both H_2 and HD. Such isotopic-dependent effects have not been observed for any copper facet.

10.2.2.5 Threshold Reduction

Analogue to the copper data sets (section 10.2.1.6) the obtained TOF traces were numerically converted to RPCs. From these, ΔS parameters have been determined (cf. fig. 10.33). For the HD data set it was unfortunately not possible to obtain data for all quantum states. Especially ($v = 0, J = 0$) is missing, which usually was used as the reference state. Hence, ($v = 0, J = 2$) was the state with lowest internal energy that had been acquired and was henceforth used as reference. Interestingly, ΔS resulted as $-0.06\,\text{eV}$ for both H_2

and D_2 $(v = 0, J = 2)$. By simply assuming the same shift for HD$(v = 0, J = 2)$ relative to HD$(v = 0, J = 0)$ all resulting ΔS values for HD relative to $(v = 0, J = 2)$ were added -0.06 eV. Henceforth, these results were used to compare values betwwen the different isotopologues.

Figure 10.34 summarizes these results by plotting them against the internal energy of the molecule. In panel (a) the subpanels separate the results of the isotopologues, again in the order of H_2 (i, squares), HD (ii, circles) and D_2 (iii, diamonds). Symbol fills represent the vibrational states, with the filled for $(v = 0)$, open for $(v = 1)$ and open with crosses inside for D_2 $(v = 2)$. Panel (a, ii) gives the results for HD relative to $(v = 0, J = 2)$ (black) as well as shifted by -60 meV (red) as described above. Using this shifted data then allows comparison by plotting the complete data set on the same scale, which is done in panel (b) of fig. 10.23. Subsequently, a green line was fitted through the available $(v = 0, J = 0)$ data points, yielding a slope of 0.84 ± 0.03, which corresponds to an isotopologue-averaged vibrational efficacy. In contrast to the copper data sets, for Au(111) this is based on only two data points of vibrationally excited states $(v = 1)$.

10.2.2.6   Efficacies based on ΔS parameters

Also analogue to the copper data sets (section 10.2.1.7), the ΔS values allow a RPC-model independent determination of efficacies. Unfortunately the Au(111) data set is incomplete, so that vibrational efficacies have to be calculated from $J = 2$ states for HD and D_2 $(v = 2)$. These results are presented in table 10.14, where they are well around 0.85 except for HD, which shows almost unity. An isotopologue averaged vibrational efficacy was also obtained from fig. 10.34, with 0.84 ± 0.03. This latter analysis and the missing HD$(J = 0)$ data indicate an isotopologue independent efficacy in the Au(111) system. Section 10.3.2.4 will present rotational state resolved efficacies, which support this hypothesis further.

Rotational efficacies are presented in fig. 10.35. Here, the low SNR of some results leads to huge scatter of the data in the energy region <0.2 eV, but the general trends are similar to both copper facets. The ξ_{rot} results are almost isotopologue and vibrational state independent, crossing over from negative to positive numbers above ~0.2 eV. Also, for higher energies the values reach the range ~0.5–0.7 eV asymptotically.

Efficacies based on E_0 parameters have not been calculated for the Au(111) data set. Due to problems arising from the very high E_0 values, incomplete data sets and the general dependence on the RPC model, such an analysis was not considered reasonable. In contrast to H_2/copper, no experimental literature is available for comparison for Au(111). Comparison to theoretical results will be presented in section 10.3.2.4.

10.2.2.7   Angular Desorption Distribution

For the Au(111) system, only the angular distribution of D_2 $(v = 1, J = 2)$ has been measured. Figure 10.36 shows the analyzed results where the data was fitted with the
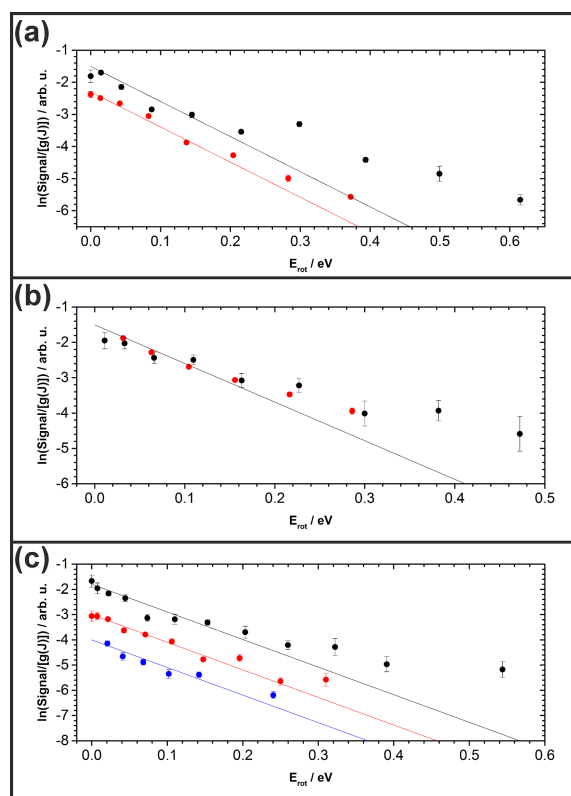
Figure 10.32: Boltzmann plots showing the quantum state population distributions of the Au(111) data sets, with the subpanels (a-c) separating for the isotopologues (H_2, HD, D_2). Colors represent data of different vibrational states, with $v = 0-2$ as black, red and blue. Solid lines give the slope expected from the T_s, but offset as guide for the eye. Reprinted in part with permission from [220]. Copyright 2017 American Chemical Society.
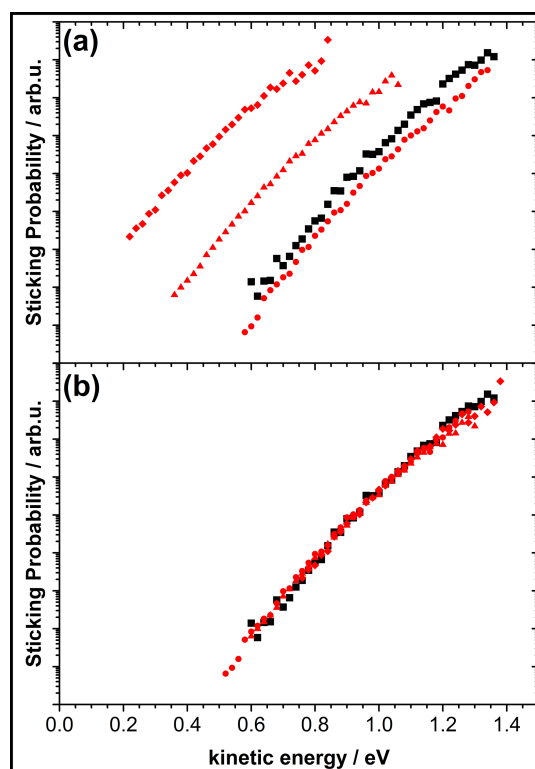
Figure 10.33: Instructive numerically derived RPCs from D_2/Au(111) (panel (a)). Presented points show the results for different quantum states on the same relative scale: $v = 0, J = 0$ (black squares), $v = 0, J = 2$ (red circles), $v = 1, J = 2$ (red triangles) and $v = 2, J = 2$ (red diamonds). Each curve has been limited to include only data points with significant obtained signal, as described in section 8.3.4.2. In panel (b), these curves have been shifted in energy to agree best with the chosen reference state ($v = 0, J = 0$), as described in section 10.2.2.5, to yield ΔS parameters. Reprinted in part with permission from [220]. Copyright 2017 American Chemical Society.

model described in section 8.3.2.3 and eq. (8.33) and obtained $n = 12.9 \pm 0.8$. Thus, a significantly narrower distribution is found than for all copper data (e.g. $n[D_2 \, (v = 1, J = 2)/\text{Cu}(211)] = 5.9 \pm 0.9$). While the high reaction barrier distributions found in the hydrogen/Au(111) system leads to an expectation of narrower distributions (cf. section 8.3.2.3), the effect of higher T_s (+138 K) works in the opposite direction. No measurements at various temperatures have been obtained, and the mentioned sample deformation (see section 10.2.2) might have led to perturbations.

10.2.2.8 Averaged Desorption Energies

Analogue to section 10.2.1.9, the state averaged mean desorption energies have been determined from the RPCs. Here, the calculation is easier than for the copper systems, because
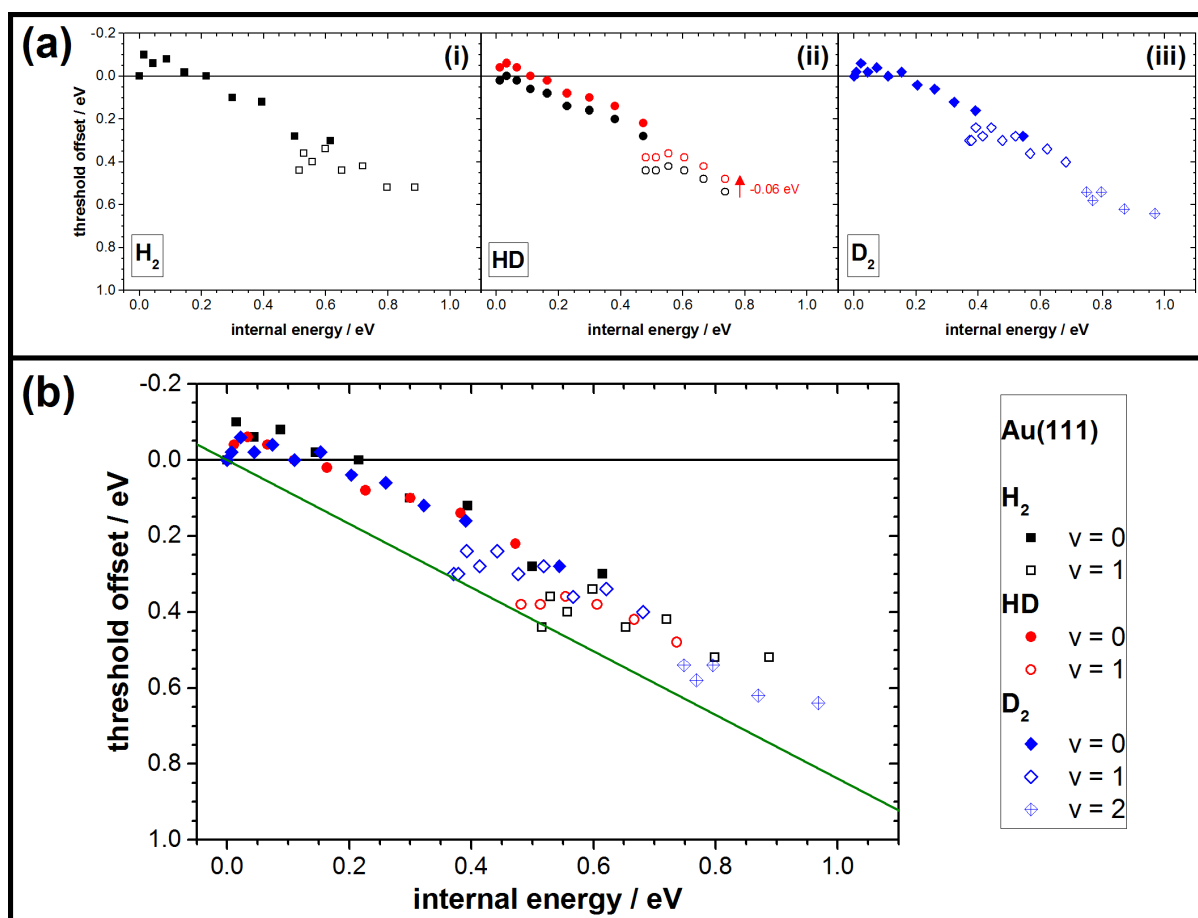
Figure 10.34: ΔS parameters obtained for the hydrogen/Au(111) system. Panel (a) shows the ΔS values as dependent on their internal energy, with the subpanels corresponding to H_2 (i), HD (ii) and D_2 (iii). Filled symbols show $(v = 0)$ data, open symbols for $(v = 1)$. For D_2 $(v = 2)$ data was also acquired, shown as open diamonds with cross inside. In subpanel (ii) the HD data is shown as two sets, with the black circles with the ΔS relative to HD $(v = 0, J = 2)$. Since HD $(v = 0, J = 0)$ had not been acquired, this was the reference with lowest internal energy. Thus, the red circles are shifted by -60 meV, which is the ΔS obtained for both H_2 $(v = 0, J = 2)$ and D_2 $(v = 0, J = 2)$ relative to their respective $(v = 0, J = 0)$ states. Panel (b) combines the data from panel (a) in a single plot with the same color coding and symbols. Here, the green line is a linear fit through the origin all $J = 0$ data, giving an estimate for the isotopologue-averaged vibrational efficacy, yielding a slope of 0.84 ± 0.03.

there is only one reaction channel, which is well described by the ERF model. Assuming normal energy scaling, the resulting values are: $\langle E_{\mathrm{kin}} \rangle (H_2) = 0.806$ eV, $\langle E_{\mathrm{kin}} \rangle (HD) = 0.801$ eV and $\langle E_{\mathrm{kin}} \rangle (D_2) = 0.897$ eV. Here, a strongly increased value ($\sim$0.1 eV) for D_2 is apparent. Additionally, a comparison to theory-based values is presented in section 10.3.2.5.

10.2.2.9 Extrapolated Activation Energies

Activation energies have been simulated for the hydrogen/Au(111) system with the model presented in section 8.3.4.5. Using the same numerical accuracies as for hydrogen/coppers (see section 10.2.1.10), values for $\langle S_0(T_s) \rangle$ were calculated for six temperatures in the range 925–1175 K. Resulting parameters from the Arrhenius model (see eq. (8.47)) are presented in table 10.15. Again, the given standard deviations represent the uncertainties
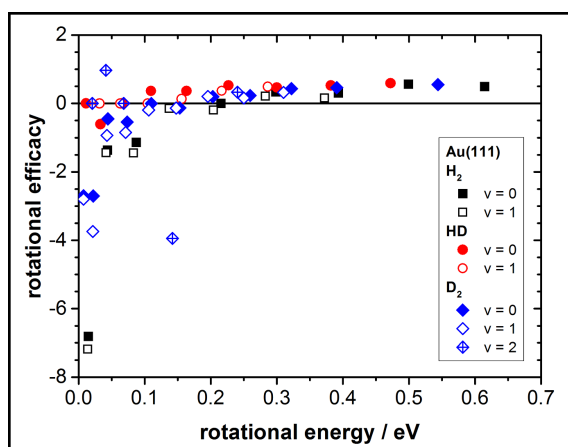
Figure 10.35: Rotational Efficacies for the Au(111) surface, with the symbols and colors as in fig. 10.34. Here, ξ_{rot} results are plotted as function of the rotational energy, showing the global effects irrespective of isotopologue or vibrational state. Due to low SNR for some data, the region $<0.2\,\mathrm{eV}$ shows significant scatter between different states.
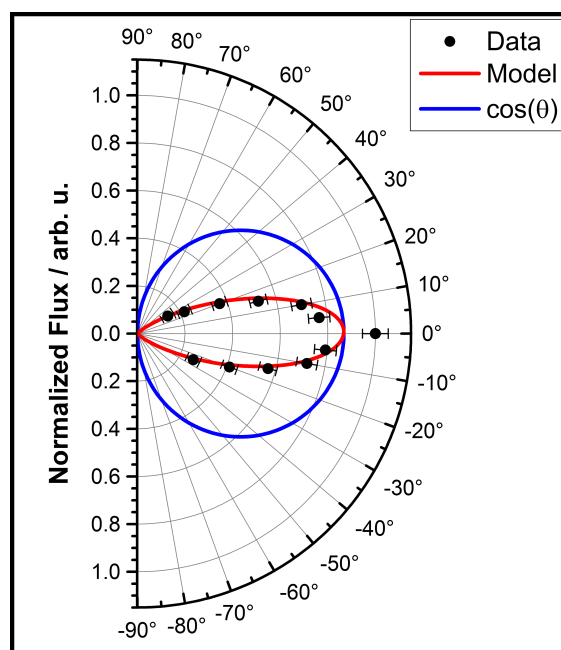
Figure 10.36: Angular desorption distribution of D_2 ($v=1, J=2$) from Au(111). Black points give the measured integrated flux and the red line is the fit result of the model as described in the text. The blue line shows a cosine distribution scaled to the same maximum. It is pointed out, that the sample was already slightly deformed (see section 10.2.2) upon acquisition of the depicted data. How this impacts the desorption distribution can only be speculated upon, and here it is only concluded that the distribution is significantly narrower than those of the studied hydrogen/copper systems.

Table 10.14: Summarized vibrational efficacies (ξ_{vib}) obtained for the Au(111) data based on ΔS values. Reprinted in part with permission from [220]. Copyright 2017 American Chemical Society.

Isotopologue	Quantum State	ξ_{vib}
H$_2$	$(v = 1, J = 0)$	0.85 ± 0.04
HD	$(v = 1, J = 2)$	0.98 ± 0.05
D$_2$	$(v = 1, J = 0)$	0.81 ± 0.06
D$_2$	$(v = 2, J = 2)$	0.84 ± 0.03

Table 10.15: Activation energies as determined by the model in section 8.3.4.5, using the data obtained for the hydrogen/Au(111) system. Presented are the parameters from fitting an Arrhenius like relationship (eq. (8.47)) to simulated $\langle S_0(T_s) \rangle$ as well as the reduced χ-square value (χ_r^2) of the fits.

Isotopologue	A_{pre} / Arb.u.	E_{act} / eV	χ_r^2 / Arb.u.
H$_2$	0.145 ± 0.013	0.827 ± 0.009	1.278×10^{-3}
HD	0.106 ± 0.010	0.825 ± 0.008	1.161×10^{-3}
D$_2$	0.147 ± 0.014	0.840 ± 0.009	1.438×10^{-3}

of the fit to the Arrhenius model and do not give a good representation of the accuracy of the model itself. A detailed discussion of the results is presented in section 11.3.2.1.

10.3 Comparison to Literature

In section 8.1 it was elaborated how theoretical models can be used to describe and predict the reactivity and dynamics of gas-surface reactions. In this section, the obtained experimental results of the fast channel will be compared to the most recent theory results available. Again, this will be done separately for copper and gold in according subsections. Where appropriate, comparison to experimental work will also be presented. Parts of this have already been published elsewhere [220].

10.3.1 Cu(111) Surface

As stated in section 7.4.1, hydrogen/Cu(111) is one of the most studied systems in gas-surface dynamics. In order to limit comparisons to a reasonable extent, only results from other desorption experiments is presented. As to theory results, only the most recent works based on SRP-DFT will be considered, namely the reports of Díaz *et al.*[167,168] and Nattino *et al.*[175]. The results of both groups are based on a six-dimensional PESs using SRP-DFT, and RPCs were obtained based on the BOSS model (see section 8.1.2). Their RPCs were mainly analysed with the FPC (eq. (8.6)), but ERF parameters were also obtained and reported.

Recently, a theoretical study of H$_2$/Cu(111) using quantum-Monte-Carlo calculation was published [288]. While this study represents a promising approach for the future of *ab initio* methods, the presented results are not yet as accurate as SRP-DFT. Thus, in this

work comparisons are only made to SRP-DFT-based studies.

Díaz *et al.*[167] kindly provided their RPC results for $H_2/Cu(111)$. Fitted FPC parameters were used for the subsequent analysis presented in the following sections. Nattino *et al.*[175] published their results for $D_2/Cu(111)$ in elaborate supplementary material. While they focused their analysis on the BOSS model results with the LGS function, they also provided ERF and FPC parameters for eight illustrative quantum states, which is sufficient for reasonable comparisons. Results from AIMD calculations were reported for those states as well.

10.3.1.1 Simulated Desorption Distributions

By using eq. (8.30) and the FPC-RPCs provided from theory, TOF distributions were simulated as they would appear in the current experimental setup. Also, this provides a comparison between experiment and theory which includes all aspects of the RPCs, in contrast to single parameters only. From this comparison, deviations can be evaluated with regard to the experimental SNR and other uncertainties. Figure 10.37 gives such comparisons for several selected signals from the Cu(111) data set, as indicated in each panel. In order to distinguish the contributions of both reaction channels, the ERF fit results corresponding to the fast channel are shown as blue lines. While ($v = 0$) signals contain also a contribution of the TB, for the remaining sgnals only the slow channel is responsible for the deviation between data points and model clearly discernible at TOF>15 µs. Calculated curves from theory are given as red lines, scaled manually to match the peak height of each ($v = 0$) signal (subpanels (i)). Curves in the other subpanels apply the same scaling factors and allow comparison to the measured ERF contributions directly. Clearly, all experimental distributions are significantly broader and shifted to longer TOF, but the peak amplitudes are similar to the modeled amplitudes.

Additionally, the same data was converted to flux vs kinetic energy distributions and is presented in fig. 10.38. Again data is indicated by black dots, the errorfunction fits by blue lines and the simulation results as red lines. Also were the amplitudes of the simulations scaled to match the fitted peak height of each ($v = 0$) signal and other signals used the same factor. This direct comparison illustrates the disagreements of the theory model, all simulated peaks roughly predict a correct amplitude, but are shifted to higher energies and are too narrow.

10.3.1.2 Obtained RPC Parameters

In this work, the use of the ERF to fit the fast channel and the occurrence of the slow channel limit the comparability to theory. By assuming complete separability of both reaction channels, the fast channel can be seen as directly comparable. Literature results for a detailed comparison of RPC parameters are available for $D_2/Cu(111)$, but not for HD. For H_2, the E_0 results of Díaz *et al.*[167] agree well with the experimental data, as was shown
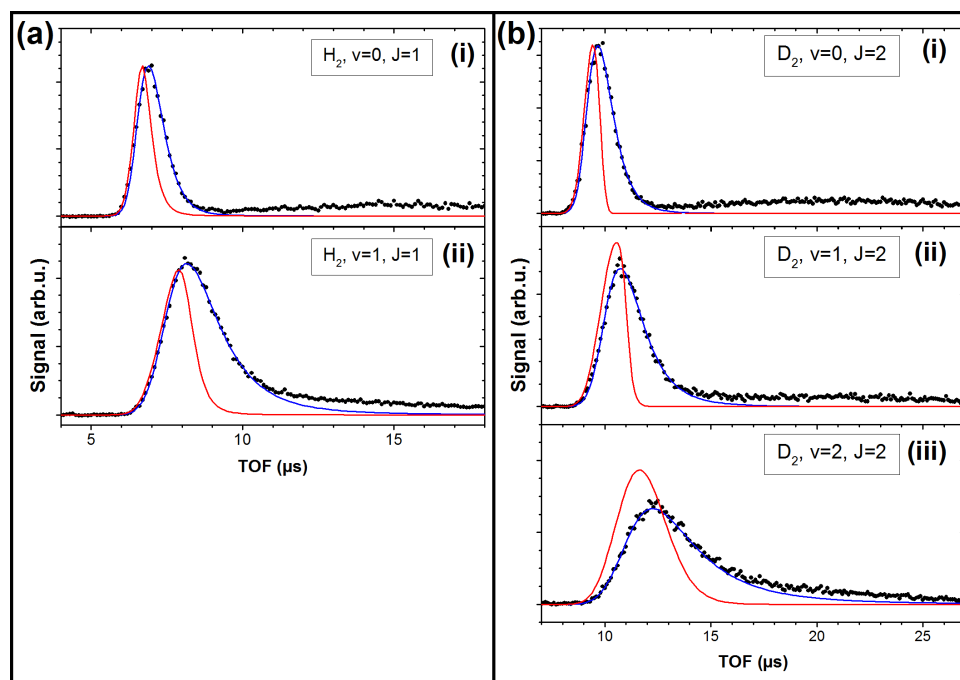
Figure 10.37: Comparison of experimental (black points) and theoretical (red lines) TOF distributions for H$_2$/Cu(111). The fit results of the ERF model are shown as blue lines to illustrate the contribution of the fast channel that the simulation is compared to. Here, the separate panels (a and b) for D$_2$ $J = 2$ and H$_2$ $J = 1$, respectively, with subpanels (i-iii) representing $v = 0 - 2$. Details on the calculation of the theoretical curves are given in the text.
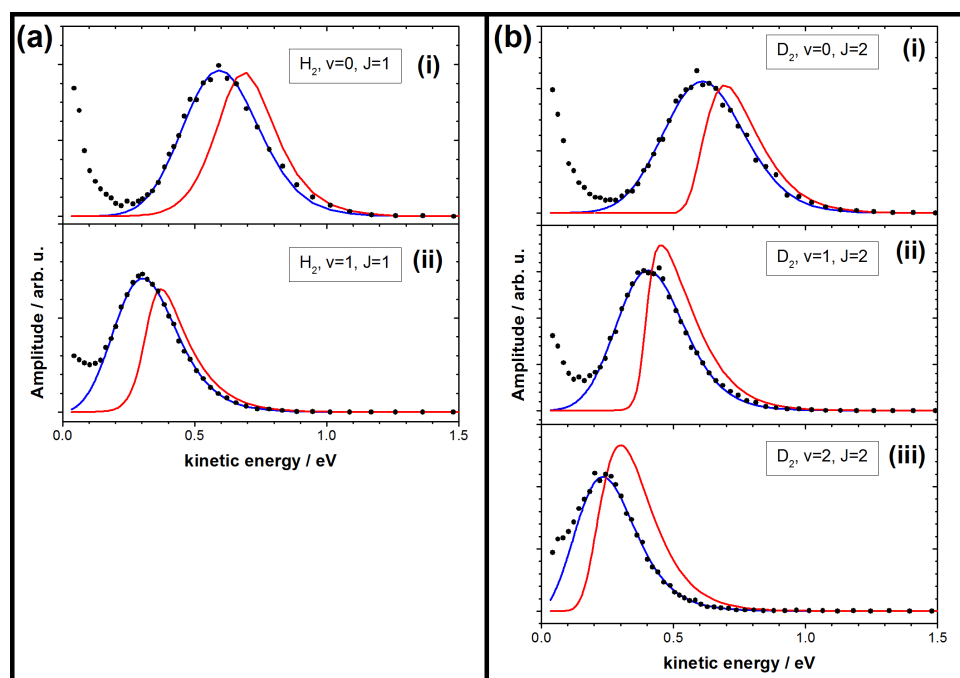
Figure 10.38: Comparison of measured and modeled flux distributions from Cu(111). Illustrative data sets are given in the panels, separated for isotopologues H$_2$ (panel (a), $J = 1$) and D$_2$ ((b), $J = 2$) as well as for vibrational states $v = 0 - 2$ (panels (i-iii)). The quantum state for each data set is also indicated in the panels. Here, the data is shwon as black points and the ERF model fit as blue line. Details on the calculation of the theoretical curves (red lines) are given in the text.

in their work (cf. figure 2 in[167]). This agreement was so good that the term chemical accuracy was formulated to describe it. Thus, a detailed comparison is not repeated here and only various experimental results are shown. For D_2, the comparisons are limited to ERF results presented by different experiments and theory values for selected quantum states as published by Nattino *et al.*[175].

E_0 **Parameters**   Figures 10.39 and 10.40 present the E_0 values for H_2 and D_2, respectively. Clearly, all data sets based on permeation (this work, Rettner *et al.*[189], and Michelsen *et al.*[182,185]) show the same qualitative behaviour with regard to rotational and vibrational state dependence. For data from Murphy and Hodgson[193], who used H-atom dosing and probed only three states of $(v = 0)$, the agreement for H_2 is very good. Deviations are <6 meV. In contrast, the energy range agrees within <45 meV for D_2, but there is a different qualitative behaviour with J.

Interestingly, between permeation experiments the E_0 values agree mostly within 50 meV, except for the $(v = 0)$ sequences. Those show significant and systematic deviations to higher values in this work, which decrease with increasing J for D_2. Starting at a difference of ~100 meV, they decrease to ~20 meV for $J = 14$. For H_2, no such effect is observed within the experimental accuracy, giving J-independent deviations on the order of ~100 meV. For vibrationally excited states deviations are reduced. For $(v = 1)$, only <50 meV is found for D_2 and <30 meV for H_2. D_2 $(v = 2)$ gives general agreement between the two experiments within their accuracy.

Comparison to theory-based D_2 results (open symbols in fig. 10.40) shows stronger differences. Actually, BOSS and AIMD results differ up to 50 meV between each other, with AIMD giving higher E_0 values for $(v = 0)$, but lower ones for $v > 0$. Unfortunately, the qualitative behaviour with J is not captured, instead a local minimum for E_0 around $J = 3 - 4$ is obtained (cf. also figure 13 in[175]). Due to the general overestimation of E_0, this leads to a fortuitous agreement of AIMD results with experimental data for $(v = 0, J = 4, 6)$ within 10 meV. For other states the deviations are higher, up to 133 meV for $[v = 0, J = 0]$. For the BOSS model results deviations in E_0 are in the range of 17–141 meV ($[v = 0, J = 4]$ and $[v = 2, J = 2]$).

Efficacies have also been calculated by Díaz *et al.*[167,168] for both H_2 and D_2, based on their E_0 results. Here it is briefly stated that those match the experimental results of Michelsen *et al.*[182,185] and Rettner *et al.*[189] quite well, and in conclusion show the same deviations to the results of this work.

Width Parameters   The obtained W parameters are compared to different experimental studies[175,189,193] in fig. 10.41 and to theory models in fig. 10.42[175]. Experimental results of the permeation studies agree very well for $v > 0$. The deviations are only up to 6 meV which is the same order of magnitude as the uncertainty. For $(v = 0)$, the discrepancies
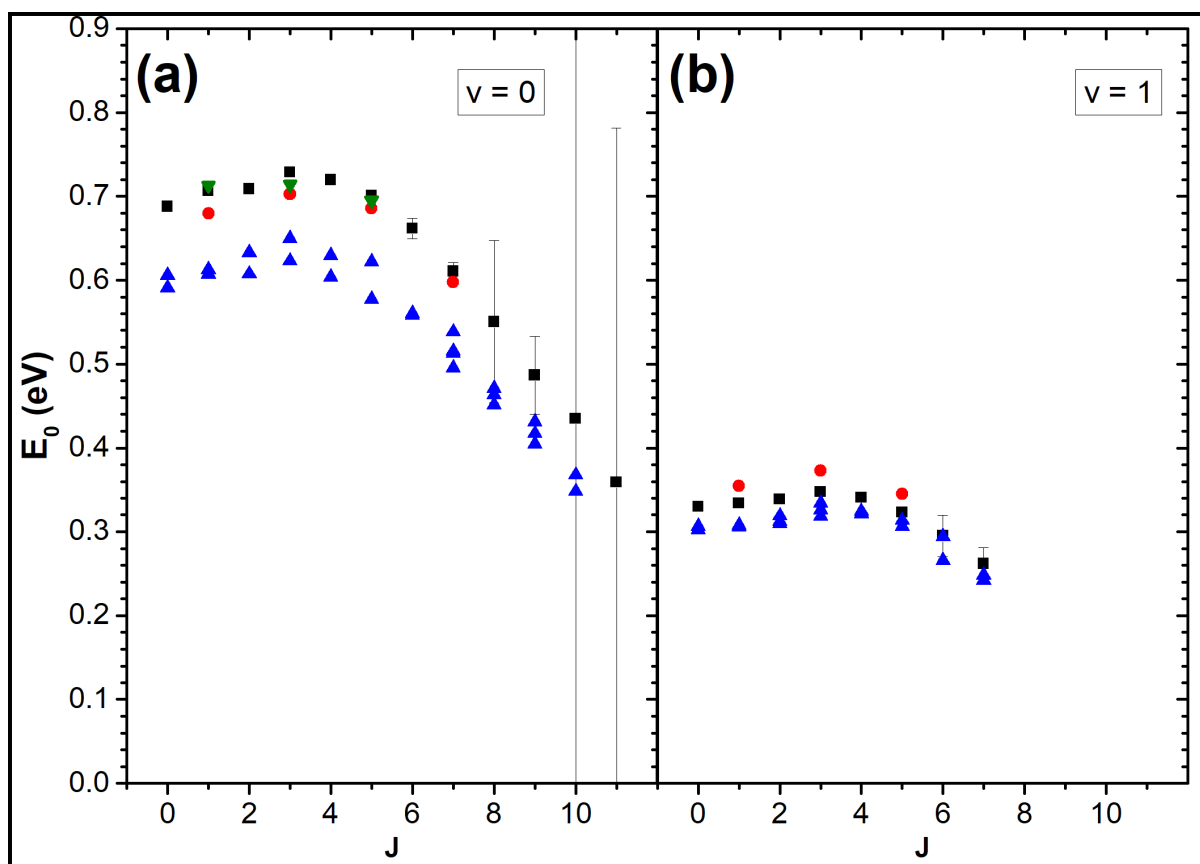
Figure 10.39: Comparison of E_0 results of H_2/Cu(111) and different works. Panels (a and b) separate vibrational states $v = 0, 1$, and the black squares and red points are results from this work which have already been presented in fig. 10.12. Up blue triangles give the results of Rettner *et al.*[189], reproduced with permission. The down green triangles ($v = 0$ only) show the reported results from Murphy and Hodgson[193].

are larger, i.e. ~-30 meV. Here, the H-atom dosing experiment shows significantly bigger deviations with 17 meV for D_2 and 35 meV for H_2.

Theoretical W values are based on the BOSS model and AIMD caluclations of Nattino *et al.*[175]. Here, their results were averaged over rotational states when in the same vibrational state. As expected, the W are significantly underestimated, due to the frozen lattice assumption in the BOSS model, except for ($v = 2$). AIMD results are in good agreement with the experimental results, except again for ($v = 2$). Both theories do not capture the narrowing effects of the RPCs with increasing vibrational state, and none of them gives a clear dependence on (v). In addition to their overestimation of $W((v = 2))$, both also gave deviations to higher E_0 values (see panel (c) of fig. 10.40).

Saturation Parameters   In table 10.16 saturation parameters for D_2/Cu(111) are compared to literature results. Michelsen *et al.*[185] analysed their experiment to obtain A_{flux} parameters with the same methodology as in this work. Furthermore, Nattino *et al.*[175] reported the ERF analysis of their SRP43 calculations in their supplementary material. Here, these were averaged for the rotational states and scaled to obtain the result for
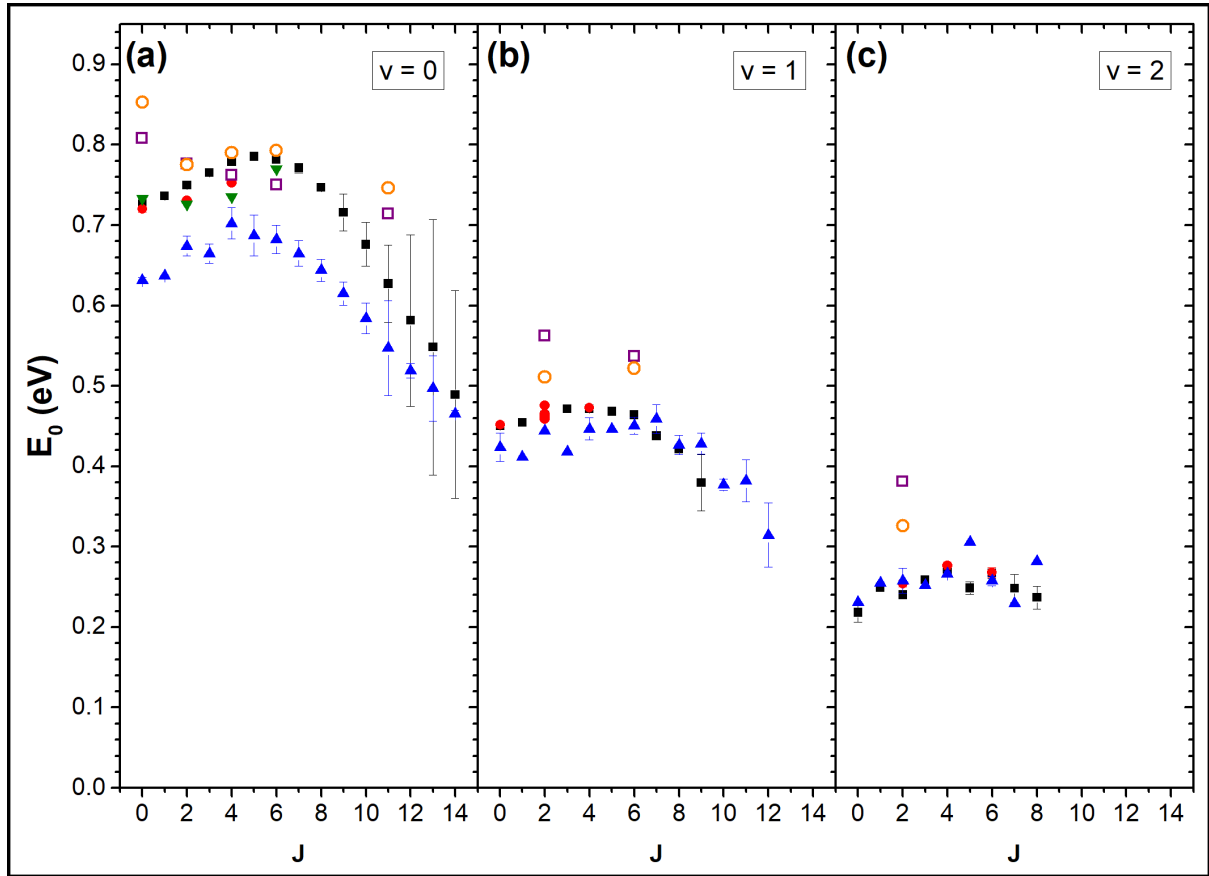
Figure 10.40: Comparison of E_0 results of D_2/Cu(111) from different experimental works as well as theory. Panels (a-c) separate for vibrational states $V = 0 - 2$, respectively. Black squares and red points show results from this work, which have already been presented in fig. 10.14. Blue up triangles give the results of Michelsen et al.[182,185], reproduced with permission. Green down triangles ($v = 0$ only) represent results from Murphy and Hodgson[193]. Open symbols show results from theory, with purple squares representing BOSS model and orange circles AIMD calculations, both from Nattino et al.[175].

($v = 0$) as unity, in order to allow comparison to the A_{erf} values reported here. For H_2/Cu(111), Rettner et al.[189] yielded saturation parameters as almost unity and from the SRP43 results of Díaz et al.[167] a similar result for A_{erf} was obtained. Therefeore, H_2 values are not included in table 10.16.

The deviations found between the experiments are significantly larger than the individual uncertainties, for both isotopologues considered. A_{flux} results for H_2 in this work yield 0.77 ± 0.05 for ($v = 1$), in contrast to unity. For D_2, this work shows the maximum value for ($v = 0$) and a decrease with v, while in literature the lowest value is found for ($v = 0$) and the maximum for ($v = 1$). Considering the theory results for D_2, the A_{erf} values agree well for the BOSS model and ($v = 0, 1$), but ($v = 2$) is overestimated. In the AIMD model no strong dependence on vibrational state is observed, while the BOSS model shows a clear increase with v state.
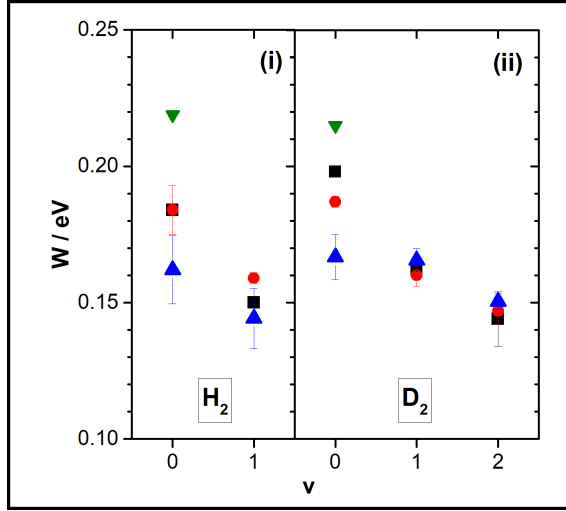
Figure 10.41: Comparison of W results of Cu(111) from different experimental works. The panels (i) and (ii) separate the results for H_2 and D_2. Again, black squares and red points show results from this work and blue up triangles give the results of Rettner *et al.*[189] and Nattino *et al.*[175], reproduced with permission. Finally, the green down triangles ($v = 0$ only) represent results from Murphy and Hodgson[193].
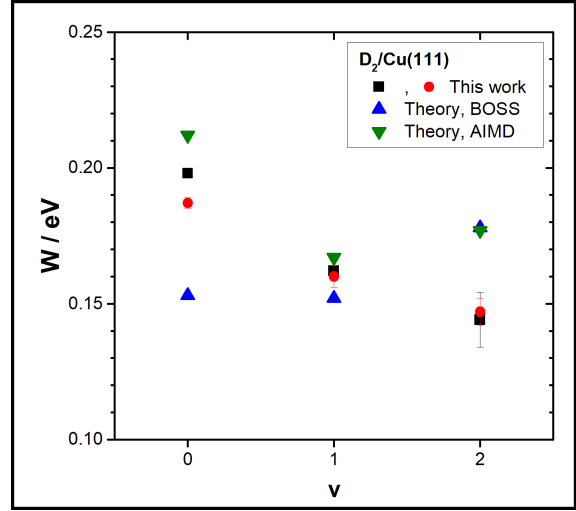
Figure 10.42: Comparison of W results of D_2/Cu(111) to theory. Here, black squares and red points show the experimental results from this work. Theory results from Nattino *et al.*[175] are shown as blue up triangles for the BOSS model and green down triangles for AIMD calculations. Both have been analysed with the ERF model.

Table 10.16: Comparison to literature saturation parameters for the D_2/Cu(111) system. Literature A_{flux} values are taken from Michelsen *et al.*[185], because their analysis was also based on the ERF model using the same methodology. Additionally, results are given for A_{erf} which were caluclated from the reported ERF fits to the SRP43 results of Nattino *et al.*[175], averaged over rotational states and scaled to obtain ($v = 0$) as unity.

-	A_{flux}		A_{erf}		
v	This work	Michelsen *et al.*	This work	Theory, BOSS	Theory, AIMD
0	1.00 ± 0.05	0.54 ± 0.16	1.00	1.00	1.00
1	0.76 ± 0.03	1.00	1.23	1.28	0.96
2	0.55 ± 0.07	0.77 ± 0.18	1.24	1.40	1.02

10.3.1.3 Simulated Quantum State Population Distributions

Figure 10.43 gives direct comparison of experimentally obtained and simulated quantum state population distributions for the fast channel, i.e. panel (a) for H_2/Cu(111) with the theory results of Díaz *et al.*[167], and panel (b) for D_2/Cu(111) and the incomplete set from Nattino *et al.*[175]. Here, the overall agreement is very good. The biggest deviations are observed for the lowest two J states, which is conclusive with the deviations seen in the E_0 parameters to higher values.

10.3.1.4 Averaged Desorption Energies

Analogue to the analysis of experimental RPCs, theoretical values can be used to estimate a quantum state averaged desorption energy. The methodology has been presented in section 8.3.3.6 and was applied using the reported FPC parameters from the work of Díaz
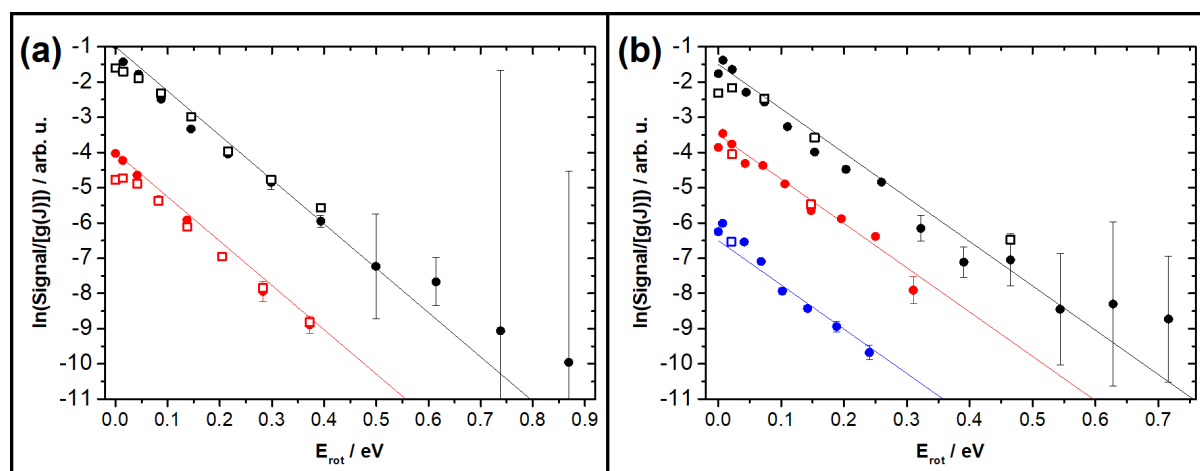
Figure 10.43: Quantum state population distributions of H_2 (panel (a)) and D_2 (b) desorbing from Cu(111) compared to SRP based theory. Filled circles show the data already presented in fig. 10.20 (panel (a)), in direct comparison to simulation results (open squares) as described in the text. Colors represent vibrational states $v = 0 - 2$ as black, red and blue.

Table 10.17: Comparison of mean kinetic energies for Cu(111) between experiment and theory [167,175]. Results are presented as total as well as separate for each vibrational state where possible. Results of this study are limited to the fast reaction channel. Reprinted in part with permission from [220]. Copyright 2017 American Chemical Society.

Isotopologue	Partition	Experimental / eV	Theory / eV	Difference / eV
H_2	total	0.594	0.670	0.076
	$v = 0$	0.608	0.683	0.075
	$v = 1$	0.336	0.413	0.077
D_2	total	0.599	0.710 [a]	0.111
	$v = 0$	0.625	-	-
	$v = 1$	0.426	-	-

[a]As reported directly from Nattino *et al.*[175] based on the BOSS model.

et al.[167] for H_2/Cu(111). For the D_2/Cu(111) system Nattino *et al.*[175] reported a $\langle E_{kin} \rangle$ directly, based on the BOSS model. With the current experiment, the problem of two observed reaction channels arises, of which the slow one is not included in any theory. Table 10.17 compares the current results for the fast channel to the theoretical results. Here, the theory deviates to higher values, for H_2 on the order of $75\,meV$ and $111\,meV$ for D_2. This shows the high level of quality of the theories to describe the reactivity in the H_2/Cu(111) system.

A further comparison of the D_2 result to several experiments is presented in table 10.18. Here, the current work gives a $\langle E_{kin} \rangle$ value well in the range of the published literature for the fast reaction channel. For the total flux, a significantly smaller result is obtained, but these values are not comparable to this literature since the slow channel was not reported in those studies.

Table 10.18: Comparison of mean kinetic energies for D_2/Cu(111) obtained from several experiments. Sources are Comsa and David[176], Nattino *et al.*[175], and Michelsen *et al.*[185]. Results of this study are given for the fast reaction channel and total flux.

Source	Surface temperature / K	Comment	$\langle E_{kin} \rangle$/ eV
This work	923	total flux	0.523
This work	923	fast channel	0.599
Michelsen *et al.*	923	Ref.[185]	0.559
Nattino *et al.*	923	Ref.[175]	0.572
Comsa and David	1000	Ref.[176]	0.63

10.3.1.5 Extrapolated Activation Energies

For the D_2/Cu(111) system Rettner *et al.*[186] introduced the methodology to extract an activation energy from dynamical data. Thus, the results presented in section 10.2.1.10 can be compared directly to their results, despite minor differences in the assumptions (cf. section 11.2.2.2). Rettner *et al.* found an activation energy of ~0.5 eV in the temperature range 500–1000 K. Here, ~0.54 eV was reported for the range of 800–1050 K, which is slightly higher. Considering all assumptions taken in derivation of these numbers, the agreement is very reasonable.

10.3.1.6 Angular Distributions

From the analysis of the angular distributions it is apparent that the fast channel flux agrees well with the literature, showing strongly peaked distributions. Unfortunateley was the data in the literature mostly obtained without quantum state resolution.

Rettner *et al.*[196] measured the desorption of H_2, HD and D_2 from Cu(111) at several temperatures. While no isotopologue dependence was obtained, they characterized the broadening effects with increasing surface temperature. Thus, their result of ($n = 10$) at 800 K agrees well with ($n \approx 9$) for 923 K found in this work. Comsa and David[176] found ($n \approx 8$) at 1000 K for a Cu(100) surface. Balooch and Stickney[243] studied desorption at 1100 K and found facet-dependent results: ($n \approx 6$) for Cu(111) and Cu(100), but ($n \approx 2$–3) for Cu(110).

State resolved data has been obtained by Schröter *et al.*[276] for Cu(100) at 885 K. They observed slightly broader distributions for molecules in vibrationally excited states, similar to the results found in this study. Murphy and Hodgson[193] acquired state-resolved desorption data, but they only simulated their angular distributions. Finally, adsorption experiments also obtained angular distributions, but were conducted at lower surface temperatures (e.g. ref. 178,181,195) and thus yielded sharper distributions.

Considering the slow channel flux, the distributions are generally broad and yield n values in the range 0.4–4.0, in part with large individual uncertainties. Systematic trends have not been observed for the surface facets, and all obtained slow channel results are

also well explained by a cosine distribution ($n = 1$).

10.3.2 Au(111) Surface

Recently, Wijzenbroek *et al.*[201] provided an extensive study, in which they predicted the dynamics of the hydrogen/Au(111) system. While they presented results for several DFT functionals, here comparisons will be limited to their SRP48 results. The disagreement with experimental data is worse than for other functionals (e.g. PBE), but the SRP48 was assumed to best predict the reactivity of hydrogen with coinage metals. This was achieved by tailoring the SRP to best describe molecular beam sticking experiments of D_2/Cu(111) at 120 K[167]. Therefore, the FPC results reported for the SRP48 were used for all subsequent analyses presented below.

Unfortunately, experimental data to compare to is scarce for associative desorption of hydrogen from gold surfaces. Where available, these references will be directly compared to in the following sections.

10.3.2.1 Simulated Desorption Distributions

As for Cu(111) the theory RPCs were used to simulate TOF profiles for direct comparison to the obtained data. Results are presented as TOF and flux vs kinetic energy distributions in figs. 10.44 and 10.45. Here, the amplitude of the simulations was scaled to match the peak height of the ($v = 0$) signals (subpanels (i)) for each isotopologue, in both figures. For the other subpanels the same factors were used accordingly. This allowed the determination of the expected amplitude from the detailed balance model, resulting in a significant underestimation of the observed H_2 ($v = 1$) signal. For D_2, only the ($v = 2$) signal shown is underestimated while for ($v = 1$) the agreement in amplitude is good. All simulated peaks are clearly too narrow and shifted to higher kinetic energies or shorter TOF accordingly. In both figures, the TB contribution is discernible in the ($v = 0$) data.

10.3.2.2 Obtained RPC Parameters

A quantitative comparison of the RPCs between theory and experiment is not as easy as for Cu(111), since the best available theory was analysed using the FPC model. Wijzenbroek *et al.*[201] also provided values denoted with E_0, but used a different definition. They denoted the energy where the absolute reactivity reached 0.25. While this is a reasonable procedure, it does not give good comparability with the analysis results presented in this work. Furthermore this arbitrary choice neglects the variation in saturation values between the curves. Simply extracting this quantity for $R = 0.5$ to compare to the E_0 parameters from this work would also suffer from the same disadvantage. Another problem is the non-trivial variation on FPC curves with temperature. In contrast, in the ERF model the E_0 is unvaried while the W correlates with temperature[185,186]. In conclusion the analysis
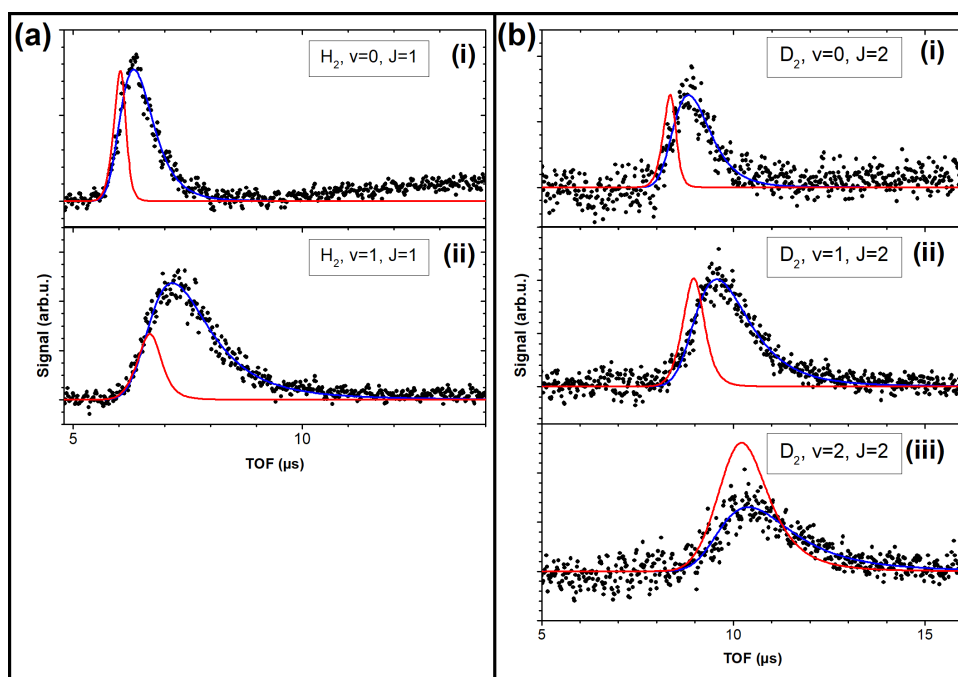
Figure 10.44: Comparison of measured (points) and simulated (red lines) TOF distributions. Fitted ERF results are shown as well (blue lines). The panels give results for H_2 $J = 1$ (a) and D_2 $J = 2$ (b), with subpanels (i-iii) for vibrational states $v = 0 - 2$. Simulated curves are based on the SRP functional, as described in the text. Reprinted in part with permission from [220]. Copyright 2017 American Chemical Society.
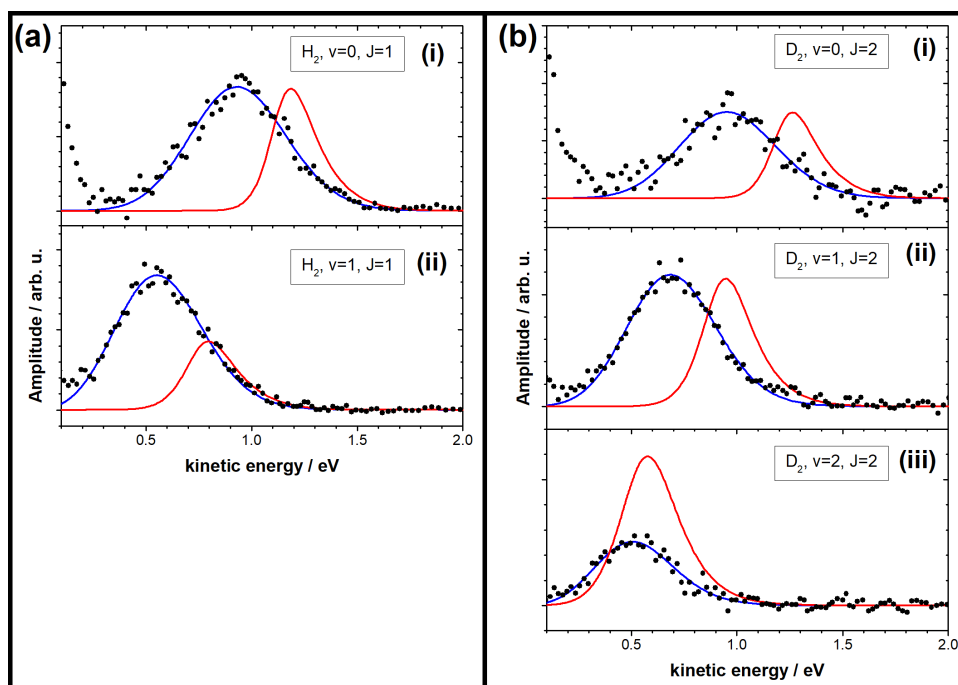
Figure 10.45: Comparison of measured and modeled flux distributions from Au(111). Illustrative data sets are given in the panels, separate for isotopologues H_2 (panel (a), $J = 1$) and D_2 ((b), $J = 2$) as well as for vibrational states $v = 0 - 2$ (panels (i-iii)). The quantum state for each data set is also indicated in the panels. Here, the data is shwon as black points and the ERF model fit as blue line. The simulation results based on the SRP [175] are presented by red lines. Reprinted in part with permission from [220]. Copyright 2017 American Chemical Society.

of the theoretical results with the ERF model is considered as the most valid option for comparison.

Wijzenbroek *et al.*[201] kindly provided their raw RPC results. Those were then fitted using the ERF model, also with W as global parameter for the rotational sequences of each vibrational state. The following paragraphs present those results in comparison to experimental ones.

E_0 **Parameters**   Panel (a) of fig. 10.46 illustrates the ERF fits to the RPC points of Wijzenbroek *et al.*[201]. Clearly, the fitted model is insufficient to describe the results accurately, but the discrepancies are similar for all depicted quantum states and the general features of the curves are captured. Therefore, the obtained E_0 values are presented in panels (b, H_2) and (c, D_2) together with the experimental results already presented in fig. 10.30. Theory gives significantly higher values for the whole system, with the differences ranging between 40–220 meV. The average deviations are lowest for ($v = 0$) and highest for ($v = 2$). Also, the reported decrease of E_0 with increasing J is seen in this analysis and the experimental data. Efficacies will be discussed in section 10.3.2.4

Width Parameters   Figure 10.47 presents the resulting W parameters of the fitting method described above. For direct comparison the experimental results are also given, which have been obtained as global parameters for all three isotopologues (see table 10.12). Generally, the W values are higher for the theory, which is contradicting the first assumptions regarding the BOSS model, which was expected to result in too narrow widths. Comparing the results for both isotopologues yields negligible differences on the order of the fitting uncertainty. Interestingly, the calculations show an increase of the W parameter with v state, while experimental results show the opposite behaviour. Thus, the deviation of theoretical to experimental W parameters increases with v from 47 meV ($v = 0$) to 110 meV ($v = 2$). An obvious explanation would be that the ERF model does not sufficiently describe the theoretical RPCs (cf. panel (a) of fig. 10.46). But despite the more complex shape of the theory results the slopes of the fitted ERF model are matching well in the reactivity ranges of 0.2–0.6. Thus, the resulting W parameters represent a reasonable quantity to compare to, despite the strong differences in curve shape between the ERF and FPC models.

Saturation Parameters   Also resulting from the ERF fits to the SRP48 results of Wijzenbroek *et al.*[201] are the saturation parameters. In order to compare, for both the experimental and theoretical results, the mean values of each rotational sequence were caluclated and those were scaled to obtain unity for ($v = 0$). These A_{erf} values are presented in table 10.19. While theory-based results are almost unity for all considered systems, the differences in experimental results are significant. Here, the deviations found for D_2 are four times smaller than for H_2 and HD.
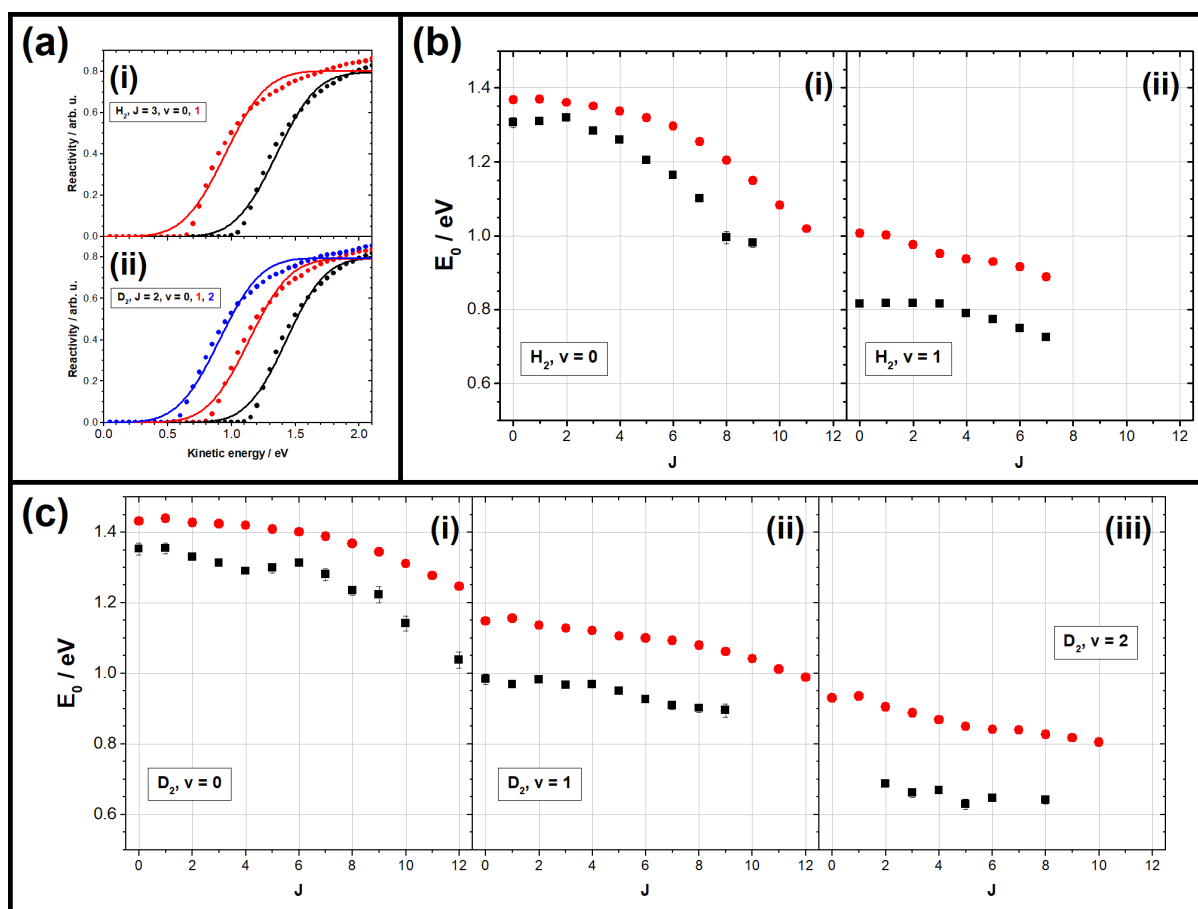
Figure 10.46: Detailed comparison of E_0 values for Au(111) between experiment and theory. Panel (a) shows how the ERF parameters were obtained from fitting (lines) eq. (8.4) to theory RPC points (filled circles). Presented are illustrative data sets for H_2 $J = 3$ in subpanel (i) and D_2 $J = 2$ in subpanel (ii). The colors (black, red and blue) indicate the vibrational states $v = 0 - 2$. The E_0 values obtained from this procedure (red dots) are compared to experimental results (black squares) of H_2 in panel (b) and D_2 in panel (c), with the subpanels (i-iii) for the vibrational states $v = 0 - 2$.

Figure 10.47: Comparison of measured W values to those estimated in theory[201]. The latter were obtained from simulated RPCs as described in the text, and these results are shown as red circles for H_2 and blue triangles for D_2. Experimental values (black squares) were obtained as global parameters for all three isotopologues.
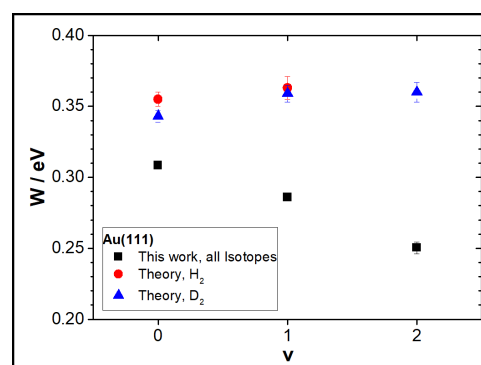
Table 10.19: Comparison of A_{erf} parameters for Au(111) between experiment and theory. All values represent the mean of the roational sequences and were scaled to obtain unity for ($v = 0$). For theoretical values the SRP48 results of Wijzenbroek *et al.* [201] were analyzed with the ERF model.

Isotopologue	v	This work	Theory
H_2	1	1.86	1.02
HD	1	1.86	-
D_2	1	0.79	1.02
D_2	2	1.21	1.03

Table 10.20: Comparison of measured and simulated vibrational state partitions for Au(111). All numbers are given as relative to the vibrational ground state and the temperature is 1061 K. Details are given in the text. Reprinted in part with permission from [220]. Copyright 2017 American Chemical Society.

System	Experiment	Theory	Difference
H_2 (v=1)	0.511 ± 0.007	0.293	-0.218
HD (v=1)	0.996 ± 0.020	-	-
D_2 (v=1)	0.340 ± 0.011	0.396	0.056
D_2 (v=2)	0.133 ± 0.007	0.086	-0.047

10.3.2.3   Simulated Quantum State Population Distributions

Figure 10.48 gives a comparison of measured and simulated quantum state population distributions based on the FPC results. Here, the general agreement with the D_2 data set is very good. In the rotational sequences, the mismatch to thermally expected populations (lines) for high J states is of the same degree for simulated as for the measured populations. Vibrational distributions agree quite well. Only D_2 ($v = 2$) is slightly underestimated. For H_2 the rotational sequences in experiment and theory agree. But the measured H_2 ($v = 1$) partition significantly exceeds the estimate, for all J states. Such an isotopologue-specific effect was not observed for copper.

Table 10.20 summarizes the vibrational state population distributions obtained from experimental data and compares them to the results of the simulation presented above. While the agreement with theory is reasonably good for D_2, the H_2 result deviates significantly. For HD an almost equal partition of ($v = 0$) and ($v = 1$) was found, but no theoretical prediction is available. The very high partitions found for H_2 and HD are unexpected, and such an isotopologue effect was not observed in associative desorption systems previously.

10.3.2.4   Simulated Efficacies

From the work of Wijzenbroek *et al.* [201] vibrational efficacies were also obtained. In their work they reported calculated RPCs as fitted with the FPC model (eq. (8.6)). Similar to the description in section 8.3.3.5, individual RPCs were compared by the kinetic energies at an arbitrary point of reaction probability (R). In their work, vibrational efficacies (η)
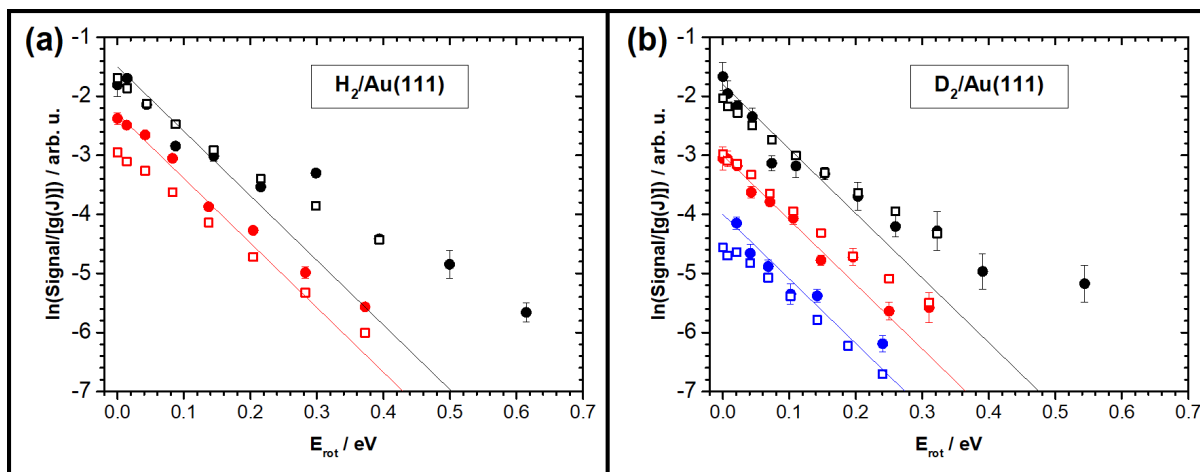
Figure 10.48: Quantum state population distributions of H_2 (panel (a)) and D_2 (b) desorbing from Au(111) compared to SRP-based theory. The filled circles show the data already presented in fig. 10.32 in direct comparison to simulation results (open squares) based on the SRP functional as described in the text. Black, red and blue colors represent vibrational states $v = 0-2$. Reprinted in part with permission from [220]. Copyright 2017 American Chemical Society.

were reported using $R = 0.25$ and yielding: $\eta_{H_2(v=1)} = 0.81$, $\eta_{H_2(v=2)} = 0.65$, $\eta_{D_2(v=1)} = 0.81$ and $\eta_{D_2(v=2)} = 0.67$.

In order to give a more comprehensive analysis, the vibrational efficacies were also calculated, for the individual rotational states, which allowed direct comparison to experimental results. Figure 10.49 summarizes these rotational state-resolved efficacies in different panels: (a) for H_2 ($v = 1$), (b) for D_2 ($v = 1$) and (c) D_2 ($v = 2$). In all panels, black squares show experimental results. Red points and blue triangles have been calculated from SRP theory using different reactivity parameters: $R = 0.25$ and $R = 0.5$, respectively.

Here, the experimental results scatter around an average value for all data sets, showing no clear J dependence and indicating an isotopologue-independent vibrational efficacy on the order of ~0.85. Theoretical results show lower η values at low J states, with this effect being stronger for $R = 0.5$. In general, only the D_2 ($v = 1$) results agree with the experiment, while for the other two sets theory underestimates the efficacies.

Rotational efficacies were only reported for the ($v = 0$) results and for specifically chosen high J states (cf. eq. (3) of [201]), similar to the Cu(111) ones. Using the SRP48 functional the values were given as 0.58 for H_2 and 0.50 for D_2, which is well in the range of the asymptotic limit determined in this work.

10.3.2.5 Averaged Desorption Energies

From the extensive set of FPC parameters provided by Wijzenbroek *et al.*[201], the state-averaged desorption energy for Au(111) was determined analogous to section 10.3.1.4. Results are presented in table 10.21, and includes a separation for vibrational levels of each subset. Clearly, the theory overestimates $\langle E_{kin} \rangle$ in all cases by >0.23 eV. Furthermore,
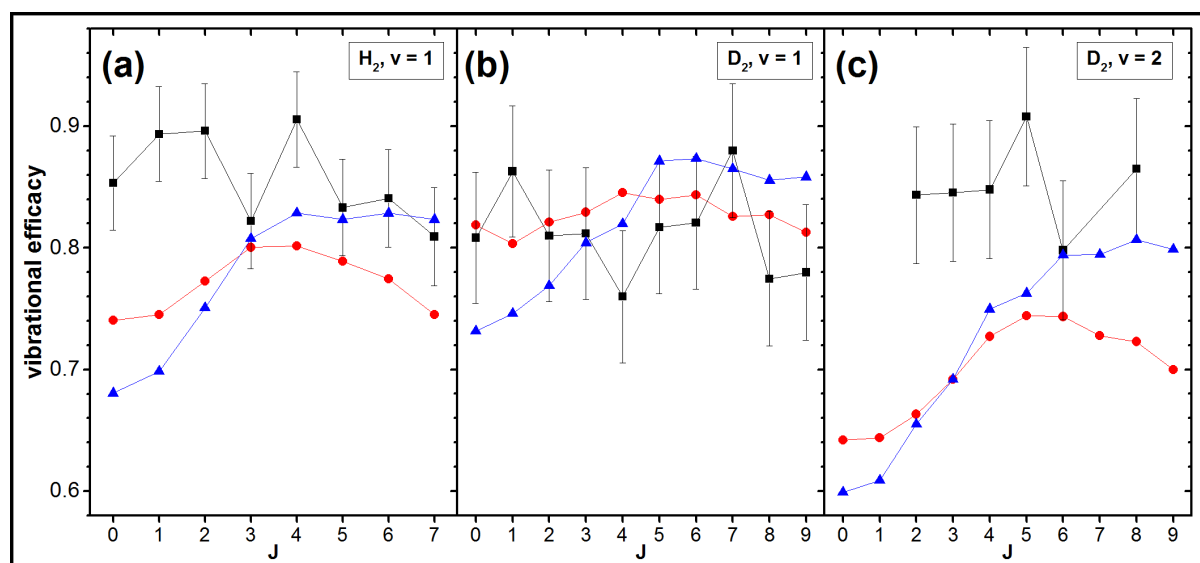
Figure 10.49: Direct comparison of ξ_{vib} results for Au(111), given as dependent on J state and using eq. (8.46). Here, the panels show ξ_{vib} of different systems: (a) H_2 ($v=1$), (b) D_2 ($v=1$) and (c) D_2 ($v=2$). Black squares have been obtained from experimental data in this work. Red points and blue triangles have been calculated from SRP theory[201] for different reactivity parameters ($R=0.25$ and $R=0.5$, respectively.), as described in the text.

Table 10.21: Comparison of mean kinetic energies for Au(111) between experiment and theory[201]. Results are presented as total as well as separated for each vibrational state, and the surface temperature was 1061 K. Reproduced with permission from[220]. Copyright 2017 American Chemical Society.

Isotopologue	Partition	Experimental / eV	Theory / eV	Difference / eV
	total	0.806	1.121	0.315
H_2	$v=0$	0.924	1.178	0.254
	$v=1$	0.576	0.806	0.230
	total	0.897	1.177	0.280
D_2	$v=0$	0.961	1.254	0.293
	$v=1$	0.691	0.964	0.273

the deviations are similar for D_2 and both vibrational states, while the higher partition of ($v=1$) measured for H_2 leads to a larger deviation in the total energy. Therefore, the total differences are bigger than for the Cu(111) system, which also does not show such an isotopologue effect.

10.3.2.6 Extrapolated Activation Energies

For the hydrogen/gold system, activation energies for the associative desorption have been reported by Stobiński and Duś[202,203]. They measured adsorption and TPD from amorphous gold surfaces and obtained coverage-dependent activation energies. For low coverages (~0.01 ML), they report an activation energy of 0.59 eV for H_2 desorption and an activation energy of 0.37 eV for dissociative adsorption. For coverages >0.01 ML, they reported desorption energies in the range of 0.56–0.32 eV and attributed those to a new adsorbed species. In contrast are the values obtained in this work for the activation energy

of adsorption ~0.83 eV for all isotopologues (section 10.2.2.9), thus by a factor more than two larger.

Chapter 11

Discussion

In this chapter, the presented work will be discussed, and the results will be examined critically. In a first section, the experimental aspects will be treated before in the second sectiont the analysis, methodology and theory models are debated. Finally. the third section presents a discussion of the obtained results and gives interpretations for the observed features.

11.1 Experimental Aspects

In the following sections the various aspects of the experimental apparatus and procedures will be discussed in detail.

11.1.1 Calibration

For ion velocity measurements (see section 8.2.4) an accurate calibration is essential. As elaborated in section 8.2.4.3, the Knudsen cell methodology is a well established way to achieve this. In this work the procedure was even more restricted, due to the additional method for independent determination of the t_{shift} parameter (section 8.2.4.3). For worsening FCA conditions, the increased flexibility of the fitted model including the cutoff function (eqs. (8.15) and (8.21)) could lead to non-physical calibration results. Therefore, as presented in section 10.1.1, the calibrations conducted with a sophisticated global model for data from two isotopologues at several temperatures. This procedure then gave reproducible results with high precision.

In order to judge the accuracy of this procedure, typical permeation data sets were analysed with regard to the uncertainty of the calibration parameters. Here, permeation data was fitted several times with the calibration parameters set to upper and lower limits of the obtained uncertainties, and the yielded deviations in the ERF results were analysed. It turned out that the results are affected percental, yielding deviations in the range 9.9–12.7 %, which henceforth is the estimated uncertainty of the calibration procedure.

An explanatory test was conducted using the D_2/Cu(111) results, in order to determine the necessary variation in the t_{shift} parameter and thus to explain the deviations between different experiments (see section 10.3.1.2). In this test, the $(v = 0, J = 6)$ data was fitted for t_{shift}, with E_0 and W fixed to the results of Nattino *et al.*[175], resulting in $t_{\text{shift}}^{H_2} = 3.06\,\mu\text{s}$. This corresponds to a difference of $-0.14\,\mu\text{s}$, which is only slightly larger than the determined uncertainty of $0.1\,\mu\text{s}$. Subsequently, $t_{\text{shift}}^{H_2} = 3.06\,\mu\text{s}$ was used to analyse the D_2 $(v = 1)$/Cu(111) data set, which yielded E_0 parameters decreased by ~50 meV relative to the nominal parameters. Conclusively, this variation of the calibration gives a too large effect, such that this alone cannot cause the deviations between experimental studies.

11.1.2   TOF Measurements

Ion velocity measurements by a nominally field-free drift region have some disadvantages, which will be presented and discussed in the following paragraphs.

Space Charge   Repulsive interaction between the generated ions can lead to severe distortions in the TOF distributions. As shown in section 8.2.6.1, these do not necessarily amount to simple broadening effects. The use of the presented method to determine an upper limit of ions should prevent such distortions. An advantageous fact is that this limit was determined for ions with low kinetic energy, which are supposed to be affected more strongly by space charge. But it can be argued that this limit was checked only for the total average over the 50 k laser pulses of each acquisition. Variations in the laser power between single pulses could therefore yield an average below this limit, while still containing a certain portion of disturbed distributions. However, this is estimated to be improbable because the limit was generally undershot significantly.

Cutoff   While the cutoff function was mostly well characterized by the calibration there are some disadvantages. Most striking is the lack of an accurate underlying model to describe the form of the cutoff. This also led to problems when the FCA perturbations became stronger and the fitted form was insufficient to model the TOF distributions. Furthermore, the cutoff could not be determined when the internal calibration method was used. Here, the cutoff was simply assumed to be constant over a few days, as long as no distortions were observed. Such distortions would significantly influence the slow channel observed for copper surfaces, while the main desorption feature would remain almost unaffected. A reduction of the general detection efficiency is improbable considering this discrimination effect.

Detection Efficiency   Ionization of particles inside a field-free drift region affects the detection efficiency in several ways. The desorption is a steady state process, which produces molecules with a distinctive velocity distribution. The laser pulse ionizes the

molecules of this distribution inside its focal region proportional to their number density. Therefore, this favors molecules with lower velocity (see section 8.3.4). In contrast, the free-drift method discriminates for faster molecules since slow ions are dispersed over a large TOF interval, which reduces the SNR in counting experiments. Fast ions are compressed into fewer TOF bins, increasing their SNR at the expense of the energy resolution.

Detection Geometry   How different detection geometries affect the obtained TOF distributions has been described in sections 8.2.6.3, 8.2.7, 9.1.1.9 and 10.1.5. The considerations included limiting apertures in the setup, the active surface area for desorption as well as the laser focal volume. Therefore, the obtained TOF distributions would deviate from the actual distributions only if those considerations were insufficient. For example, if the active crystal areas were smaller than estimated, the angular distribution assumptions would deviate. The effects, however, would be small (see section 8.2.7). In contrast to that changes in the laser focal volume woukd have stronger effects, especially due to the nonlinearity of the REMPI process. But this was excluded by checking several signals for reproducibility. These signals included daily measurements of the internal calibration standard and selected acquisitions from the Cu(111) sample.

11.1.3   Desorption Experiments

In this section, specific aspects of the associative desorption technique and the analysis procedure will be discussed.

Reaction Mechanism   As elaborated in section 7.1, a desorption process can proceed via different mechanisms. While the permeation technique gives absolute restriction to the LH type, the pulsed H-atom dosing method suffers from the competition of ER and HA-ER contributions, which even vary in time. In principle, this allows separation of the LH mechanism by simply waiting until no H-atoms impinge on the surface any more before the ionization step. But it also reduces the SNR and affects the range of investigable surface temperatures and H-atom coverages.

Active Surface Area   The desorption area of the samples varied between the experimental studies compared in section 10.3.1. While in this work it is estimated to a circular area of ~3 mm $\varnothing$, Michelsen *et al.*[182,185] used a crystal with a 10 mm $\varnothing$. Murphy and Hodgson[193] also estimated the surface area dosed with their H-atom beam to be ~3 mm. All these estimates do not take into account inhomogeneities, like variations in membrane thickness for permeation experiments or a certain beam profile in H-atom dosing. In principle those inhomogeneities would affect the detection geometry (section 9.1.1.9), but diffusion on the surface would limit their severity. When considering the low coverages

and high reaction barriers, the LH mechanism might be limited by H-atom diffusion. Thus, the discussed inhomogeneities are assumed to have only marginal effects.

Surface Coverage   In permeation experiments, H-atom surface coverages have been estimated, but not measured. As elaborated in section 8.3.1.1, the coverages are on the order of 1×10^{-3} ML. between experiments the surface coverages vary, which can be estimated by simple assumptions, like membrane thickness. Therefore, the steady state surface coverage in this work should be approximately twice as high as in Michelsen *et al.*[182,185].

In contrast, H-atom dosing techniques (see section 8.2.2) will produce dynamical coverages. Directly after dosing, the coverage is highest and starts to decrease. If dosing produces islands, these also start to diffuse and alter the coverage, resulting in various surface areas with different coverages and reaction geometries. Furthermore, all these processes vary with surface temperature.

Effects of TB   As described in section 9.2.2.6 the influences of TB gas have been considered. The direct contribution to the acquired signals can be discerned and subtracted. Also, other effects on the TOF profiles of desorbing molecules have been determined as insignificant. It can be concluded that the energy transfer to adsorbates by impinging gas phase molecules can be neglected here and do not affect the detailed balance model analysis.

Surface Structure   Due to the high surface temperatures in permeation experiments ($>900\,\text{K}$), the surface morphology varies from the nominal surface cuts. Each crystal atom is in motion around its equilibrium position, diffusion is ongoing and defects can be formed or repaired dynamically. Also, more severe surface variations are known at such high temperatures (see section 8.2.1) like varying interlayer distances, lifting of surface reconstruction or even surface pre-melting. Furthermore, the (211) facet is assumed to be thermally less stable than the (111) facet. The observations described in section 9.2.1.2 also hint towards a variation or even vanishing of the (211) structure at the experimental temperature, while the (111) structure remains stable.

An increased surface disorder will affect the distribution of possible geometries for associative desorption reactions, which then differ from the ones assumed in theory for ideal facets (see section 8.1). This assumedly results in a depletion of reaction sites with low barrier, thus shifting the RPCs to higher energies accompanied by broadening.

Even more, rough surfaces are expected to have an effect on the energy scaling law. Rettner *et al.*[186] assumed that for polycrystalline surfaces total energy scaling would be a reasonable assumption. Therefore, rough surfaces would experience an increase in reactivity by this change, regardless of the possible influences on the actual RPC.

Sample Temperature   The influence of the surface temperature on the desorption distri-
bution is complex since the temperature simultaneously affects the detailed balance model,
quantum state and angular distributions, permeation and desorption rates, and the RPCs.
Fortunately variations around few K only amount to deviations of a few percent, which
should attenuate the impact. For permeation experiments the sample heater envelopes
the crystal and leaves the active surface area open. Due to thermal radiation losses the
temperature profile on the surface should be inhomogeneous and yield a minimum in
the center of the sample surface, which is the active area. Even in the steady state of
the experiment this could account for systematic deviations, which cannot be quantified
without major effort. Possibly diffusion is counteracting any effects in this regard.

It is pointed out, that for the slow channel parameters no temperature dependence was
found within the range of $\pm 10\,\%$. Experimentally, the temperature range is limited by the
sample material properties, with the lower boundary given by a sufficient permeation flux
necessary for detection. An upper limit is determined by the mechanical stability of the
sample because the temperature must be low enough to prevent the crystal from melting
and that its vapor pressure is negligible, and the surface does not deform mechanically
due to the hydrogen pressure behind the sample.

11.1.4   Unverified Properties

Some aspects of the desorbing molecules could not be investigated in the course of this
work.

Rotational Alignment   Despite the existence of experimental evidence for the influence
of rotational state alignment on reactivity (see 190–192) this aspect could not be probed in
the present study. Here, the utilized ionization technique (section 8.2.5.2) is not sensitive
to rotational alignment[289] and the saturation of the transition would further reduce
any dependences[290]. Here, differently aligned rotational states of desorbing molecules
have been detected with almost equal probability, as in other studies relying on the same
technique (e.g. ref. 182,185,189,193).

Highly Excited Quantum States   While the probed range of molecular states can al-
ready be considered large in comparison to thermally expected populations it was still
limited. Actually, for all surfaces it was tried to acquire H_2 ($v = 2, J = 1$), which is
on the edge of the achievable wavelength range. Unfortunately the SNRs were too low
for acquisitions, and partition of molecules in even higher states is assumed to be low,
due to the detailed balance model. Nevertheless, no tests for higher quantum states were
conducted and electronically excited molecules were not considered at all.

Excitation of Electrons   All the assumptions above are very reasonable, unless non-adiabatic interactions are considered to participate in the reaction (see section 7.3). But how these affect the desorption distributions can only be speculated upon. Possible excitations of electrons in the metal cannot be detected with this setup, which is a severe disadvantage since chemicurrents have been observed on the three coinage metals (see section 11.2.3). Furthermore, if charged molecules desorbed they could not be characterized in the detection setup due to the lack of the laser ionization step, no TOF information would be provided. Such a constant flux would simply result in a rise of the noise level and possibly a broadening of the regular TOF distributions.

11.2   Analysis Aspects

In this section theory models will be discussed with regard to their comparability to presented results. Also, general challenges for the applied analysis methods, assumptions therein and other fundamental problems will be discussed. In a third section, non-adiabatic effects on hydrogen-metal surface systems will be reviewed.

11.2.1   Theoretical Methods

The presented results have been compared directly to theoretical models produced to describe the dissociative adsorption reaction. Unfortunately, hydrogen metal interactions are complex systems with a size that can be described only approximately by modern models. Some of these necessary assumptions will be discussed here, with regard of the deviations to the presented data.

Functional Comparison   In fig. 11.1 several DFT results for the coinage metals are compared[113,167,175,201,291]. Symbols represent the minimum reaction barriers (right hand y-scale) at the bridge to hollow site of (111) facets as function of the internuclear H-atom separation. These include copper (orange circles), silver (grey diamond) and gold (golden squares). For reference the PEC for gas-phase H_2 is given[292] (blue line, left hand y-scale). This representation illustrates how the H_2/surface interaction reduces the energy necessary for elongation of the H_2 bond at the transition state. It is pointed out, that the presented theories still overestimate the minimum barrier height for gold significantly. Wijzenbroek *et al.*[201] presented results for several other DFT functionals with their minimum barriers spanning the range of 1.175–1.566 eV. This demonstrates the relative freedom in the choice of the functional, which is a fundamental problem in DFT. Here, the main argument to choose the SRP approach for the comparison was the fact that SRP was tailored specifically to predict the reactivity for coinage metals.
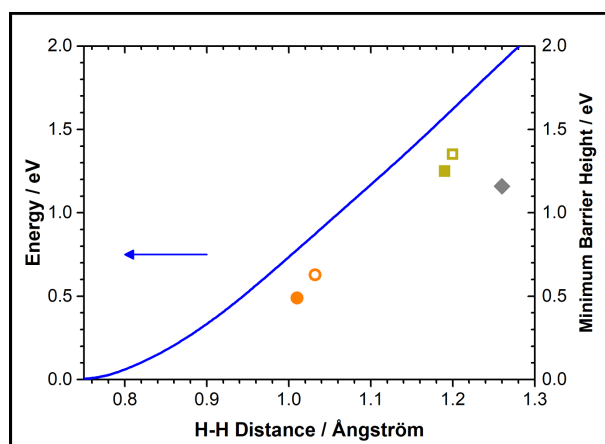
Figure 11.1: Comparison of the PEC of free H_2 (blue line, left y-axis) to various minimum reaction barriers obtained by DFT (symbols, right y-axis). The H_2 curve was taken from Kołos et al.[292]. Each symbol represents a different minimum reaction barrier for H_2 dissociation at the bridge to hollow site. Orange circles represent Cu(111), with the filled circle from Díaz et al.[167] (PW91) and the open circle from Nattino et al.[175] (SRP). The other three results are all based on PBE, with Ag(111) represented by the grey diamond, taken from Jiang et al.[113]. Au(111) results (golden squares) were taken from Wijzenbroek et al.[201] (filled) and Libisch et al.[291] (open).

SRP   One fundamental problem of the SRP approach (see section 8.1.1) is the necessity for experimental benchmark data to which the model is tailored. This makes SRP-DFT a semi-empirical model which can result in further problems. For example, the "calibration" data set could contain non-adiabatic interactions which are not described by the functionals. Then, the resulting SRP would also be adjusted to mask these interactions, instead of representing the system in its entirety.

Temperature Mismatch   While the BOSS model simulates a frozen lattice, which corresponds to a surface temperature of $0\,K$, permeation experiments were conducted at high temperatures ($>900\,K$). Therefore, the simulated surface structure differs from the expected structure (see section 11.1.3). This results in a vastly different distribution of reaction geometries, and thus barriers to reaction. For the ERF model, this was assumed to influence only the width parameter (W)[167,181,195]. But for the FPC model[175,201] there is no simple assumption on how the shape of the RPCs is affected. In general, it is assumed that the RPCs broaden, but the evolution of the shape cannot be predicted without further major efforts.

Especially for Au(111), an asymmetric variation could reduce the discrepancies to experimental results. Due to the predicted RPCs showing reaction barriers for very high energies their overlap to the MBD is governed by the rising edge of the curves. Thus, the saturation regime is probed insufficiently, which reduces the significance of shape variations in this region.

AIMD   In contrast to BOSS calculations the AIMD method treats the motion of surface atoms. Advantages have been demonstrated with regard to the description of surface temperature effects and the rotational alignment[170,175,293]. Studies directly comparing BOSS to AIMD results[294] showed that the effective barriers are lower by $\lesssim 0.1\,eV$ for AIMD in the H_2/Cu(111) system. This was attributed to the thermal surface motion and thus gives the order of magnitude at which the reaction barriers are overestimated by the BOSS model.

11.2.2 Detailed Balance

Most problems and assumptions of the detailed balance model have already been presented in section 8.3.1.1. Here, the discussion is extended to include problems of the fitting model, subsequent analysis methods and system specific challenges.

11.2.2.1 Correlation of Function Parameters

In general, sigmoidal functions experience a certain degree of parameter correlation when fitted to data. This challenge for the analysis was already discussed briefly[171,193] for the hydrogen/copper system. But because the RPCs found for the hydrogen/gold system show reaction barriers at even higher energies, a more detailed description will be presented here. The underlying problem is the limited energy range probed in post-permeation desorption experiments, where the weighting is given by the MBD at the surface temperature. Measured TOF distributions are fitted according to the detailed balance model (section 8.3.1), which describes the desorption flux as product of the MBD and the quantum state resolved RPC (section 8.1.3). Because the exponential decay of the MBD exceeds the rising slope of the sigmoidal RPCs at some point, this results in a diminution of measured signal at high kinetic energies. For strongly activated systems, the high energy part of the RPC cannot be probed sufficiently and thus is missing constraint in its saturation regime. Additionally, the free ion drift technique applied in this study enhances this effect due to the quadratic TOF to energy conversion (cf. section 8.3.4): The increased point density at low kinetic energies results in a stronger weighting of this regime during the fitting process.

For the ERF model, the three parameters of saturation (A_{erf}), width (W) and point of inflection (E_0) are all positively correlated. Their values rise or decrease simultaneously which results in curves with similar shape in their rising part, while the saturation regime is affected tremendously. In fig. 11.2 an illustrative data set is shown where the effects are perceptible and the correlations of the three sticking function parameters are investigated. As dataset $D_2/Au(111)$ ($v = 1, J = 4$) was chosen, where the SNR is adequate and the reaction barrier distribution peaks at high energies [$E_0 = (0.969 \pm 0.006)\,\mathrm{eV}$]. Furthermore, TB is not apparent in this quantum state and the RPC is described well with the ERF model. TOF data was fitted with the model minimizing the sum of square errors (SSE) between data points (black dots) and model. The result is shown as the red line in fig. 11.2. Successively, the data was fitted again, now with E_0 fixed to a manually varied value, such that the resulting SSE was increased by $5\,\%$ relative to the free fit. The result for changing the E_0 parameter to higher (lower) values is depicted as solid green (blue) lines, respectively, showing degraded but still reasonable results. Associated RPCs (eq. (8.4)) are shown as dotted lines in the corresponding colors. At TOF $>9\,\mu s$ the three RPCs converge, while their progression diverges at shorter TOF before leveling off at their A_{erf} values.

Panel (b) of fig. 11.2 shows the same data and curves converted from the TOF to the

kinetic energy domain and re-binned (see section 8.3.4). Additionally, pink dots show the corresponding E_0 points. Here, it is apparent that the sticking curves overlap for energies lower than ~0.9 eV - close to the E_0 value of the free fit - and the divergence only starts at higher energies. It is also clear that the measured flux is already decreasing and rapidly approaches the baseline above this energy. Therefore, only little more than half of the sticking curve is sampled with adequate weighting. For the curves fitted to the upper/lower boundaries, the obtained parameters deviate relative to the free fit result. For E_0 the deviation ranges from $-8\,\%$ to $+16\,\%$ and for W from $-10\,\%$ to $+19\,\%$, while the relative amplitude A_{erf} spans from $-34\,\%$ to $+121\,\%$. The use of other datasets with even higher barrier distribution functions (e.g. $D_2/Au(111)$ ($v = 0, J = 4$)) yields similar results, while data sets with lower barrier distributions are better defined and the size of the variations is reduced. Since the ERF model is only an approximation based on the assumption that the actual barrier distribution function would be Gaussian-shaped (section 8.1.3), no reliable information can be extracted for energies higher than ~1.0 eV from the presented data. Because the amplitude of the measured distribution diminishes around ~1.3 eV, there is only an upper limit for A_{erf}. More flexible RPC forms (e.g. eqs. (8.5) and (8.6)) can therefore only reliably be applied to datasets which are better defined in the probed energy region, as in the hydrogen/copper system.

Moreover, in the detailed balance model two more parameters of the MBD also affect the fitting, independent of the sticking function: the temperature and the absolute amplitude of the desorbing flux. Therefore, the experimentally obtained amplitude results from the unknown equilibrium concentration of H-atoms adsorbed on the surface and the involved kinetics, as well as the RPC parameters. For permeation experiments it is impossible to disentangle these contributions, and thus quantum state population distributions information as well as A_{erf} parameters can only be obtained on a relative scale (section 8.3.3.4). Additionally, changes in the surface temperature will directly affect all these contributions differently, resulting in a complex system which cannot be predicted easily. To illustrate this, the signal shown in fig. 11.2 was fitted with the ERF model at surface temperatures deviating by $\pm 10\,\%$. This resulted in a change of mainly the A_{erf} parameter by a factor of 2–5 while E_0 and W varied only within $10\,\%$.

It is pointed out that for more flexible functions, like LGS or FPC, these effects would be even stronger. Hence, the analysis in this work was restricted to the ERF model for the fast channel.

11.2.2.2   Advanced Analysis Methods

Starting from the state resolved RPCs advanced analysis methods were conducted to obtain information of the dynamical properties of the systems. Also, the methods to obtain state averaged desorption energies and extrapolate to thermal activation energies include further assumptions.
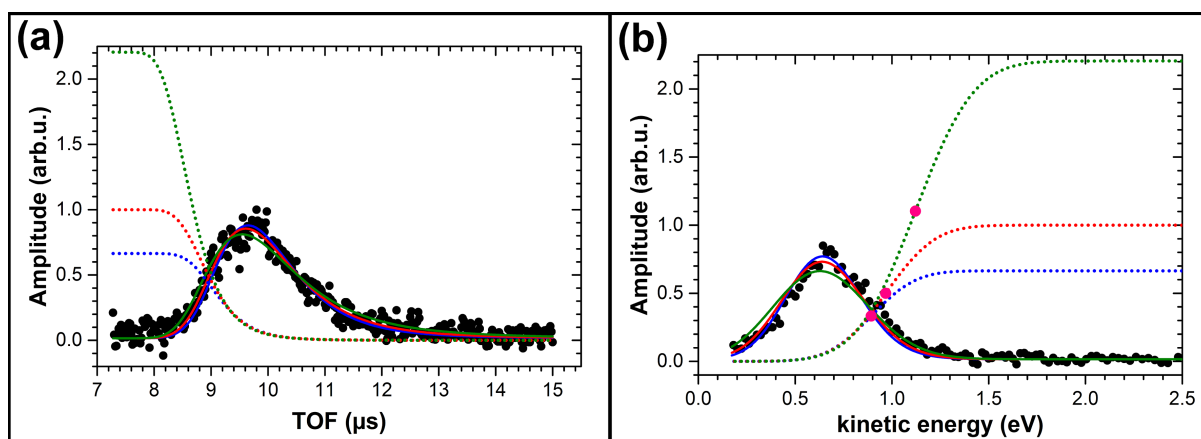
Figure 11.2: Illustration of the origin of parameter correlation. Panel (a): TOF distribution measured for $D_2/Au(111)$ ($v = 1, J = 4$) (black dots) and three fit results of the detailed balance model (solid lines) as well as their corresponding sticking functions (dotted lines). The red lines are results when fitting all three parameters unrestrained over the shown TOF range. Lower (blue) boundary results are achieved by fixing the E_0 parameter to a lower value, until the SSE of the fit is increased by 5 %. An upper (green) boundary result is determined accordingly. Panel (b): the plots from panel (a) converted to the kinetic energy scale, with the experimental data re-binned. As additional information the E_0 points are shown as pink dots.

Threshold Reduction and Efficacies The presented method (section 8.3.4.3) to determine the influence of internal molecular energy on the RPC has some advantages but also includes some assumptions. It is independent of the form of the RPCs and therefore does not rely on a fitting process, only conversion of measured TOF distributions and assumption of detailed balance. But this can also be a disadvantage, because when the ΔS values are determined the form of the two RPCs does not need to match, as can already be seen in the variation of the W parameter between vibrational states. For sigmoidal shaped functions this should be a minor problem, but for more complex ones unwanted shifts could arise. Also, for overlapping reaction channels this problem appears, as is apparent in panel (b) of fig. 10.22. But in contrast to the established methodology (section 8.3.3.5), this one also considers the relative scale and shape of the RPCs. It is concluded that the introduced method is more reliable and efficacies should henceforth be determined based on ΔS values.

Mean Desorption Energies In section 8.3.3.6, the calculation of $\langle E_{\mathrm{kin}} \rangle$ was described. In principle, this number gives a weighted average of the obtained RPC information, which would be observed in experiments without quantum state resolution. While no further assumptions are necessary for $H_2/Au(111)$ the situation is more complex for the copper facets due to the observed two reaction channels. Despite the assumed normal energy scaling for both, the question arises if the slow channel contribution would be observed in other experiments or at least with the same weighting. Thus, in the presented comparison to literature results (section 10.3.1.4), only the fast channel was considered, which was in good agreement.

Extrapolated Activation Energies As presented in section 8.3.4.5, the applied model for the estimate of the activation energy to adsorption relies on many assumptions. Additionally to those are the results strongly dependent on the calculation parameters. While the influence of numerical accuracy was simply tested and can henceforth be neglected below a certain limit, the impact of other parameters is enormous. One example is the simulated temperature range, to which the Arrhenius model is subsequently fitted. Rettner *et al.*[186] found that a variation of this range was directly correlated to the activation energy results. They obtained deviations of $\lesssim 20\,\%$ on the activation energy, while the pre-factor even changes by an order of magnitude. Therefore, the presented results were obtained by simulating a temperature range of $\sim\pm 125\,\mathrm{K}$ around the T_s at which the data had been acquired.

More complex are the effects of temperature on the ERF model. Assuming its validity, one needs to include temperature dependence of the W parameters. In principle, lower temperatures would lead to narrower RPCs and therefore higher activation energies. Since this is coupled to the previous argument, the exact effects need to be simulated, which was actually neglected because the variations of W were not verified here. More sophisticated simulations would also need to include exact information of the energy scaling law, especially in connection to the surface roughness as discussed in section 11.1.3. Also, for the copper surfaces the slow reaction channel was treated with the same scaling law as the fast one, despite the lack of information in this regard.

In conclusion, the many assumptions of this method result in a huge uncertainty of the obtained results, which is estimated to be on the order of $\sim 20\,\%$.

11.2.2.3 System Specific Features

Due to the observed desorption features in this work system specific problems with the detailed balance model arise, which will be described in the following sections. Furthermore, it is pointed out that all presented results lack absolute scaling. RPCs can be compared only for the ro-vibrational states of a given isotopologue and surface facet on a relative scale. Thus, all comparisons only involve the shape of the RPCs, but not the absolute reactivity of the systems.

Copper Two distinct reaction channels were observed in the desorption off copper. The presented analysis of the slow channel was based on the assumption of clear separability to the fast channel. While possible explanations for the slow channel will be given in section 11.3.1.4, here the critical assumptions and necessities will be pointed out. First, energy exchange between both channels must be impossible. Considering the low surface coverages, combined with the short residence times expected of nascent molecules on the surface, this is a reasonable assumption. Second, the energy scaling law was not determined for the slow channel. Dependent on the actual process, this could deviate from the normal

energy scaling assumed in the presented analysis. For example a steering effect would be more efficient for molecules with low kinetic energies, which would increase the impact of parallel kinetic energy for the reaction.

Gold For the hydrogen/gold system the recently published high-level theory results allowed direct and detailed comparisons. The deviations can be summarized in systematic and isotopologue-specific effects. For the hydrogen/gold system, non-adiabatic effects have been predicted and also observed previously, and those will be discussed in detail in section 11.2.3. In the model of detailed balance such effects are not included and how they would affect the desorption distributions can only be speculated upon. Here, it is pointed out that the hydrogen/Au(111) results presented in this study show clear isotopologue dependent effects, which are not explained within the adiabatic theoretical predictions. Possible interpretations will be presented in section 11.3.2.3.

11.2.3 Non-Adiabatic Effects

In this section, non-adiabatic effects observed in literature will be presented and discussed. This is restricted to studies which treat hydrogen interaction with coinage metals, since those were studied in this work.

In contrast to post-permeation associative desorption experiments, chemicurrent experiments are tailored to probe directly for non-adiabatic effects. Chemicurrents have been observed on all three coinage metals using metal-insulator-metal devices[19,20,58,133,143] and for silver and copper via Schottky diodes[18,131,142,295]. In these experiments H-atoms are dosed to the surface and induced steady-state currents are measured. But it is not easy to distinguish the exact reaction mechanism in such experiments and possibilities include the atomic chemisorption, the recombination reaction or other processes. Furthermore the surface structure of such devices is not well-defined and detailed knowledge of the electron transport properties would be necessary for the analysis of the reaction kinetics. An elaborate analysis of the kinetics strongly hinted to an LH desorption mechanism as cause of the chemicurrents on gold-based metal-insulator-metal devices[58]. But in contrast chemicurrents measured via Schottky diodes[18,131] have successfully been explained by electronic friction theory for the impinging H-atoms[296]. An isotopologue effect has also been observed in those experiments, which showed ~2–5 times smaller chemicurrents[142,295] for D-atom chemisorption, which also is in accordance with friction theory[296].

Furthermore, the interactions of several metal surfaces with H-atoms have been studied in scattering experiments[24,61–63]. For all studied metals, including Au(111) and Cu(111), strong non-adiabatic energy dissipation and isotopologue effects were observed, which were conclusively explained by electronic friction theory[24,141]. Since H-atoms have no internal degrees of freedom the kinetic energy distributions of the scattered atoms were affected. But electron-hole-pair (ehp) excitation or hydrogen molecule formation could

not be probed in these experiments. Thus, high-level theory was necessary to determine the most probable reaction mechanism involved, which argued for electronic friction while ignoring molecule formation[24,141].

While these combined results prove that non-adiabatic interactions of hydrogen atoms with metals are associative desorption reactions not necessarily affected. For example, the H_2/Cu(111) system currently has the status of a model system for adiabatic behaviour[146–149], which is supported by the good agreement between experiments and adiabatic SRP-DFT[167,168,175]. Nevertheless, Luntz and Persson[146] calculated ehp excitation probabilities for this system by electronic friction theory. They estimated an averaged energy loss to electron hole pairs of ~20 meV, i.e. negligibly small. Notwithstanding, the occurrence of chemicurrents on copper and electronic friction results show that theories describing the hydrogen/copper system as entirely adiabatic cannot be able to grasp the dynamics on the surface in its entirety.

Generally, for the H_2/Au(111) system more studies included and proved non-adiabatic effects, although they vary strongly in their details. For example Mukherjee *et al.*[144] studied the dissociation of H_2 molecules physisorbed on gold nanoparticles. Here, laser illumination induced plasmons in nanoparticles, which then decayed efficiently into ehps. Mukherjee *et al.* suggested electron transfer from the metal to the H_2 molecule to induce the dissociation reaction, which is also supported by theory[144,291]. In contrast to the previously described experiments the ehps in their study were produced intentionally and resulted in the chemical reaction. Thus, the mechanism for dissociation of physisorbed H_2 into chemisorbed H-atoms might be entirely different from the mechanism of the associative desorption. Takagi *et al.*[145] published DFT calculations for the dissociative adsorption reaction that predicted an at least fractional electron transfer from the H_2 molecule to the Au(111) surface. More general, recent calculations on H_2/Ag(111)[137] further suggested that the widely used method of electronic friction underestimates directional effects in molecule-surface interactions. Similar problems in theoretical methodologies have also been disputed previously[148,149].

Nevertheless all these studies show the occurrence of non-adiabatic effects in hydrogen-metal interactions. But how such effects would impact the distributions obtained from post-permeation associative desorption remains speculative, since electronic degrees of freedom cannot be probed in these experiments.

11.3   Interpretation of Results

In the following sections the obtained results will be discussed and interpreted. As in the preceding chapters, the different metals are treated in separate sections.

11.3.1 Copper Surfaces

From the presented results of the hydrogen/copper system three major results were obtained. First, an improved dataset for the benchmark system hydrogen/Cu(111) was measured, which yielded small but significant differences to the established literature. Second, a direct comparison between the (111) and (211) facets was conducted. Surprisingly, this yielded only small differences in reactivity, despite the vastly different step densities. Third, a second channel for reaction was observed and quantified here for the first time. This desorption feature is apparent on both facets and for all isotopologues studied. In order to discuss these aspects appropriately, each of the following subsections focuses on one aspect of these results.

11.3.1.1 Activated Desorption from Cu(111)

In this section the properties of the fast desorption channel for Cu(111) will be discussed. This channel corresponds to the activated associative desorption, which served as benchmark for theory models[167,168,175]. Here, this channel was characterized by the ERF model and the obtained RPC parameters allowed detailed comparisons to literature results from experimental as well as theoretical studies. With the improved calibration procedure in this work (see section 11.1.1) the obtained results show small but significant differences to the established literature which used the same methods[182,185,189].

Dynamics from RPC Parameters In the ERF model the quantum state specific E_0 values contain the majority of the dynamical information and variations between those values are generally used to describe the system dynamics, while deviations in W and A_{erf} are relatively small. Vibrational energy shifts the E_0 significantly to lower values, which is based on the elongation of the molecular bond being coupled to the reaction coordinate for dissociation[117,155,159,161,166,167,179,180,194]. This effect is quantified by the vibrational efficacy (ε_{vib}) which will be discussed in a paragraph below.

Rotational effects have been quantified by an efficacy as well (ε_{rot}), but the complex interactions prevented a straightforward analysis. In the rotational sequences two counteracting effects lead to a turnover of the variation in E_0. At low J the effect of misalignment from the minimum energy path outweighs the induced bond elongation at high rotational energies[155,182,185,189,190,193,197]. Consequently, ε_{rot} values have been obtained by analysis of results for high J states only, where the latter effect becomes linear in first approximation and the former effect is negligible[175,182,185,189,201].

Variation of the second parameter in the ERF model, W, indicates a change of the slope in the barrier distribution and is generally observed to depend only weakly on the ro-vibrational state. Therefore, W was treated as global variable for data in the same vibrational state for each isotopologue, in accordance with literature[182,185,189]. In all results a decrease of W was observed for excited v states, for all isotopologues and facets.

The saturation level (A_{erf}) is the last parameter of the ERF model and determines the relative scaling of the RPCs for individual quantum states. Those obtained in theory models vary only marginally, while the experimental ones show deviations up to a factor of two (table 10.16). It should be pointed out that the parameter correlation in the ERF model (section 11.2.2.1) influences the A_{erf} values, but not the A_{flux} results, because those were obtained from model-independent integrated fluxes. The obtained quantum state population distributions, which are also based on the integrated fluxes are similarly affected. These distributions show the effects of the whole RPCs in contrast to the individual parameters and also circumvent parameter correlation effects.

Comparison to Experimental Results   Differences between the results of various permeation experiments for Cu(111) can be summarized as small (see section 10.3.1.2). The individual RPC parameters deviate mostly within the experimental accuracy, at least for vibrationally excited molecules. Here, the differences of E_0 and W are on the order of $<50\,\mathrm{meV}$. But for the vibrational ground state these deviations are larger, up to $100\,\mathrm{meV}$ for E_0, which is reflected in the vibrational efficacies discussed in a later paragraph. For the A_{flux} parameters, the deviations to other experiments are significant but devoid of any systematic, for H_2 and D_2. Instead considering the A_{erf} results yields partial agreement to BOSS, but not AIMD results.

The E_0 vlaues are in good agreement with the results of Murphy and Hodgson[193]. For the W parameter the deviations are of the same order of magnitude as to the permeation experiments, but into the opposite direction. Unfortunately, saturation parameters were not reported which severely limits the comparability. Thus, the problem of parameter correlation arises and cannot be checked, which has also been pointed out by Wijzenbroek et al.[171]. Furthermore, only seven quantum states have been studied by Murphy and Hodgson[193] and exclusively for the vibrational ground state.

The obtained vibrational state population distributions for Cu(111) disagree with literature (table 10.6). While the H_2 ($v = 1$) partition is well between the values obtained by Kubiak et al.[177] and Rettner et al.[189], the measured D_2 partitions for ($v = 1, 2$) are lower than in the literature studies[181,185]. Such non-systematic behaviour hints towards a dependence on sample quality, since all studies applied the same methodology as in this work.

From the RPCs averaged desorption energies, $\langle E_{\mathrm{kin}} \rangle$, were obtained that could be separated for both reaction channels (table 10.10), and the D_2/Cu(111) data set was compared to literature results in table 10.18. Because other experiments observed only the fast channel contribution, this comparison is reasonable and shows that the value from this study lies well between the results of Michelsen et al.[182,185] and Comsa and David[176]. Since the result of the latter group was obtained at a higher surface temperature their $\langle E_{\mathrm{kin}} \rangle$ value should be higher, but a quantification is not easily possible.

Comparison to Theory Results   Deviations to comparable theoretical work differ between both isotopologues. For H_2 theory agreed well with the previous experiments[167,189] and therefore all deviations found in this study are the same as described in the paragraph above for the experimental results. But for D_2 the present experiment reduces the deviations of E_0 values to the theory results, where a slightly different SRP functional was used[175]. In contrast, the W results are strongly underestimated by the BOSS model, except for $(v = 2)$ where the only obtained value overestimates the experimental result significantly. The AIMD theory always overestimates W, but less severely. Also, the $(v = 2)$ value is very similar to the BOSS result.

As stated in section 11.2.1, BOSS model results are expected to overestimate barrier heights by $\lesssim 0.1\,\mathrm{eV}$. Considering the differences in E_0 parameters between experiment and the BOSS results, such a shift would lead to a better agreement. Interestingly, the AIMD results are directly compared to BOSS results and experimental data for the $D_2/Cu(111)$ system in fig. 10.40. Here, the agreement is better for the AIMD than for the BOSS values, but for both a general overestimation to experiment is observed and these differences are smaller than to literature data[182,185] for $(v = 0)$. The found deviations are of the same order of magnitude for both theory models, which indicates that other effects than lattice motion might be their origin.

Finally, the rotational state averaged A_{erf} values show better agreement to the current experiment, especially the BOSS model. Since the AIMD model gives unity saturation values for all vibrational states, the discrepancy to experiment increases with v. In conclusion, the differences between both theory models are marginal. While both describe the experimental properties sufficiently there are still deviations in the single aspects of the RPCs, showing that the methodical differences between AIMD and BOSS are not the cause of the differences to experiment.

Furthermore, by simulation of the desorption distributions (figs. 10.37 and 10.38) from the theory-based RPCs, the BOSS model can be judged in its entirety. Here, the interplay of the single parameters is taken into account, revealing the differences to experiment in a qualitative manner. For $Cu(111)$ the quantum state population distributions of the fast channel were also compared to simulations, which agree well (section 10.3.1.3). Only the results for low rotational states show qualitatively different behaviour. Such agreement is interesting when considering the discussed differences in RPCs. Conclusively, the BOSS model has problems in the description of the experimental RPCs, but succeeds in the characterization of most dynamical effects. While the behaviour for low J states is described qualitatively wrong, the more general relations between the quantum states are correct, resulting in the shown agreement.

The obtained $\langle E_{\mathrm{kin}} \rangle$ results for $Cu(111)$ were compared to BOSS model results in table 10.17, where the values are subdivided for vibrational states. For H_2, the theory overestimates the results by only ~75 meV and shows no vibrational state dependence in

contrast to the Au(111) results. The D_2 values deviate stronger, by 111 meV, contrary to expected improvements from the varied SRP functional[175]. In conclusion, this method offers a good representation of the overall quality of the theory model rather than the comparison of single RPC aspects.

Efficacy Calculations   This paragraph will evaluate the efficacies derived from the RPCs and compare them to the literature results (table 10.7). Efficacies based on the E_0 parameter ($\varepsilon_{\mathrm{vib}}$, $\varepsilon_{\mathrm{rot}}$) are mostly affected by the discrepancy found for the ($v = 0$) sequences. Thus, the $\varepsilon_{\mathrm{vib}}$ were found to range from 0.55 to 0.76 in this study, which is significantly higher than the 0.51–0.54 reported in literature[185,189]. For $\varepsilon_{\mathrm{rot}}$, the results of this study (0.59–0.16) decrease more for higher v states than in the literature results, which varied only weakly (0.45–0.32). It is pointed out that the individual scatter in E_0 and the arbitrary choice of the linear fit range can affect these results significantly.

Using ΔS values to obtain efficacies (ξ_{vib}, ξ_{rot}) is advantageous to the E_0 based method, since it neglects the fitting model and instead includes the relative amplitudes (A_{erf}) and shapes (W) of the RPCs.

Figure 10.24 presented the ξ_{rot} results as function of rotational energy and thus reveals the universality of both counteracting effects. Even the Au(111) data agree with the qualitative behavior (fig. 10.35), despite the large scatter of <0.15 eV for the data. In the graphs for all three studied surfaces neither the isotopologue nor the vibrational state of the desorbing molecules changes the qualitative aspects. For low rotational energy the ξ_{rot} values are large negative numbers, which cross the boundary to positive values above ~0.2 eV rotational energy. Finally, the values approach the region around 0.5–0.7 exponentially for higher rotational energies.

The ξ_{vib} results (table 10.8) ranged from 0.70 to 0.95. This marks a significant increase relative to the literature results of ~0.5 and indicates that vibrational energy is more effective than assumed previously. Values above 0.90 were obtained for both D_2 ($v = 2$) data sets, which indicates that this effectivity increases even more with v-state. But Díaz et al.[297] already pointed out, that the concept of vibrational efficacy neglects dynamical information and thus should be considered cautiously.

Other Properties   For the fast reaction channel of Cu(111) angular desorption distributions and an estimate for the activation energy for adsorption were obtained. Comparison to literature results yielded generally good agreement. Thus, detailed discussion of these aspects will be given in section 11.3.1.2, with the focus on differences between the surface facets.

11.3.1.2   Surface Structure Influence

This section focuses on the dependence of the hydrogen recombination reaction on the surface structure, namely the two studied copper crystals with (111) and (211) facets.

RPC Parameters   For the fast reaction channel the three RPC parameters of the ERF model show significant differences between the two studied facets. But the resulting desorption distributions differ only marginally between the facets (see fig. 10.8), which shows the interconnection of the single RPC parameters in the model.

Here, for the Cu(211) facet the E_0 parameters are higher by 30–130 meV than the Cu(111) results and the W values by 7–13 %. For the third parameter, A_{erf}, an interesting dependence was observed for the Cu(211) data (fig. 10.16 and table 10.5). Deviation of the A_{erf} values from unity to higher numbers correlates with the vibrational energy, in the order D_2 ($v = 1$) [0.37 eV], HD($v = 1$) [0.45 eV], H_2 ($v = 1$) [0.52 eV] and D_2 ($v = 2$) [0.73 eV]. Such an effect was not observed on Cu(111), thus excluding systematic errors in the methodology. Parameter correlation (section 11.2.2.1) causing the discrepancies seems reasonable, since all three ERF parameters are increased simultaneously relative to Cu(111). But then, the A_{erf} would be largest for the ($v = 0$) sequences, since those data contain the highest E_0 values. Because the opposite behavior is observed, these deviations must be reliable.

Results for the slow reaction channel are mostly independent of the surface facet, with the exception of higher relative fluxes for H_2/Cu(211). These similarities are unexpected when considering the differences in surface structure, especially the huge variation in step density. As reported for e.g. D_2/Pt[99–101] the reactivity is often enhanced for stepped surfaces, due to lowered reaction barriers at step sites. For platinum, reaction on steps is not activated in contrast to terraces and thus the overall surface reactivity correlates directly with the step density.

To explain the different behavior found in the hydrogen/copper system, it has to be considered that the barriers to reaction are considerably higher. These might be lowered at step sites[198] but will still be substantial and therefore the effects on reactivity will be smaller. Another argument is based on the surface structures at high temperatures. As described in section 11.1.3 thermal motion alters the (211) facet more than the (111) facet, and thus it can be assumed that the (211) step density is reduced at permeation temperatures. Strong broadening effects for the RPCs would also be observed, as is seen for the (211) facet.

These surface structure considerations can be expanded to reactivity at defect sites. Thermal energy at permeation temperatures (~0.08 eV) is high enough to produce a significant fraction of defects on the surface, e.g. ~0.1 eV kink formation energy on steps[298], 0.22–0.31 eV step formation energy[298–300] and ~0.67 eV adatom-vacancy pair formation energy[301] for Cu(111), respectively. DFT-based reaction barriers for various defect sites

suggest that the reactivity is highest at kink sites[198], which makes them the dominant sites for reactions. Since these sites are a product of the dynamical surface structure the expected variation with underlying facet should actually be small, which agrees with the temperature-dependent observations of Murphy and Hodgson[193].

Efficacy Calculations ξ_{vib} values have been determined to agree with the uncertainties between both copper samples, with the biggest deviation found for H_2 ($v = 1$). In contrast to that the $\varepsilon_{\mathrm{vib}}$ results show significantly lower values for Cu(211) for H_2 and HD, while for D_2 the values still agree. This illustrates the differences between the two methods, of which ξ_{vib} includes all RPC properties. In contrast the $\varepsilon_{\mathrm{vib}}$ method ignores the saturation and width parameters, thus masking important system properties. Consequently, the precision of $\varepsilon_{\mathrm{rot}}$ values is estimated to be insufficient compared to ξ_{rot} values. Especially since the dynamics quantified by ΔS values are very similar for both facets, as demonstrated in figs. 10.23 and 10.24.

Angular Distributions The separation of the measured distributions into two reaction channels yields good agreement for the fast channel in comparison to angular distributions in the literature, as presented in section 10.3.1.6. In contrast to that the broad distributions found for the slow channel are a previously unreported feature and will be discussed in section 11.3.1.3. The obtained distributions for both copper facets show no systematic differences, but the actual structure of the Cu(211) surface at 923 K is a point of discussion, as elaborated in the paragraphs above.

Quantum State Population Distributions As shown in section 10.2.1.4 the measured relative partition of both reaction channels is approximately the same for all vibrational and rotational states of each isotopologue on the Cu(111) facet. But for high J, the slow channel partitioning is often reduced and the uncertainties become larger than the order of magnitude of the values themselves. It is pointed out that the quantum state population distributions were obtained using the integrated fluxes, thus excluding any parameter correlation in the ERF model itself. In contrast, some correlation between the two reaction channels is possible which cannot be quantified or corrected. But the quantum state population distributions for both reaction channels were normalized independently to a total partition of unity and thus the resulting agreement is astonishing. Because the rotational sequences show no facet-dependent behavior only the vibrational partitioning will be discussed further (table 10.6). Here, the results show generally higher partition of vibrationally excited states on the Cu(211) facet, which reflects the variations observed in the A_{erf} parameters of the fast channel. In contrast to Cu(111) the Cu(211) sample also shows different vibrational partitions for the two reaction channels, with significant lower values for the slow channel. This indicates that vibrational energy enhances only

the reactivity for the fast channel, while the slow channel results are more similar to those of the Cu(111) facet.

Quantum State Averaged Properties $\langle E_{\mathrm{kin}} \rangle$ values were compared between both surface facets and for all studied isotopologues (table 10.10), which yielded no systematic variations and generally agreed within $<30\,\mathrm{meV}$. Also the subdivision into both reaction channels revealed no facet dependencies, as will be discussed in section 11.3.1.3.

Also averaged over quantum states were the extrapolated activation energies (see section 10.2.1.10). When taking into account the huge uncertainty of the methodology, which is estimated to $20\,\%$ (section 11.2.2.2), the result for $D_2/Cu(111)$ agrees well with the value of Rettner *et al.*[186]. While the method in itself is imprecise, it allows comparison of both studied facets in terms of reactivity because the calculations are based on the same numerics and assumptions. For all isotopologues, the E_{act} results are higher for the (211) facet by 1.3–$4.3\,\%$. This indicates a slightly higher reactivity for the Cu(111) facet, if one assumes that the absolute A_{erf} values are comparable.

11.3.1.3 Slow Channel Description

In the following paragraphs the observed properties of the slow channel will be described and the dynamics results discussed. Also, this reaction channel will be compared to similar features observed in the literature.

General Properties   The RPCs of the slow channel were quantitatively described by an exponential decay in the detailed balance model. This function uses only two fittable parameters: γ_{slow} and A_{slow} (cf. eq. (8.7)). The first parameter describes the kinetic energy width of the reaction probability curve and the latter parameter allows determination of the relative contribution of both channels to the total flux from the surface. The variation of those parameters with isotopologue and quantum state will be discussed in a following paragraph. But from the measured RPCs the average kinetic desorption energies $\langle E_{\mathrm{kin}} \rangle$ were determined separately for the two reaction channels. The results for the slow channel do not depend systematically on isotopologue or surface facet and the values range between 0.09–$0.11\,\mathrm{eV}$ (table 10.10). This is in the same range as the thermal equilibrium energy in the system ($\sim 0.08\,\mathrm{eV}$) and on the order of magnitude expected for physisorbed molecules.

The measured vibrational state population distributions of the slow channel mostly agree with those for the fast channel of Cu(111) (table 10.6). Deviations larger than the uncertainty are only found for $HD(v = 1)/Cu(211)$ to lower and D_2 $(v = 2)/Cu(211)$ to higher values. The sequences for rotational states of both channels for Cu(111) mostly agree, while for Cu(211) the population of the slow channel deviates to lower values with increasing J-state. This was already discussed in connection with the A_{erf} values obtained for the fast channel (section 11.3.1.2).

The broad angular distributions of the slow channel can be interpreted by a weak or non-activated desorption process and furthermore offer an explanation why this channel has not been reported previously, except by Murphy and Hodgson[193]. These broad distributions render the detectability of the slow channel dependent on the solid angle for detection in the experiment. For example, detected the setup of Comsa and David[176] molecules in a very small solid angle of <1°. Therefore their sensitivity was good for the strongly peaked fast channel but discriminated against the broad slow channel. Experiments comparable to the present study (e.g. ref. 182,185,189,192) used a half-cone angle of ~20°, but relied on the free ion drift method. This dispersed the signal over a long TOF range, thus reducing the SNR. In contrast to those experiments Murphy and Hodgson[193] detected ions within a similar angle, but used a weak extraction field to circumvent this signal reduction.

But due to the similarities of the current setup to said other permeation experiments (cf. fig. 8.7), some other attributes of the slow channel must be the cause of the differences in observed flux. As presented in section 10.2.1.3 the total partition of the slow channel to the flux off the surface is ~0.3 in this work. This hints towards a significant difference in the system properties to the other experiments which reported a similar feature. For example, one possible property would be the hydrogen surface coverage, which is estimated to be significantly higher than in the experiments of Michelsen et $al.$[182,185] (see section 11.1.3).

With the normalization method applied for fig. 10.11 one can compare the RPCs in between surface facets and isotopologues. This relies on the assumption of similar saturation values for all quantum states, as is found in theory[167,168,175]. Then, in the limit of zero kinetic energy and for the vibrational ground state H_2 is more reactive than D_2 by a factor of ~2–3. Such an isotopologue dependent effect hints towards tunneling through a barrier.

Dynamics Description In the detailed balance model the RPCs of the slow channel are described by an exponential decay. Such a decrease of the reaction probability with kinetic energy represents unusual dynamics when compared to other systems of dissociative chemisorption of hydrogen. Here, the reaction probability is highest for low incidence translational energies, which strongly supports the argumentation of a second reaction channel with a completely different transition state. Furthermore, for both H_2 and D_2 vibrational excitation enhances the reactivity by 2–3 orders of magnitude, as shown in fig. 10.11.

The exponential decay parameter γ_{slow} corresponds to the energy width of the function. Larger γ_{slow} values correspond to a less steep RPC decrease, thus extending the slow channel to higher kinetic energies and broadening the peak in the TOF distribution. While a general trend of increasing γ_{slow} with increasing J state could be observed for the $(v = 0)$ data, the residual results are independent of J. Surface facet dependencies could not be obtained and a vibrational state dependence was obtained only for H_2. An increase

of γ_{slow} with rotation hints towards a misalignment effect, similar to that observed for the fast channel at low rotational states. Rotation of molecules counteracts dynamical steering (e.g. ref. 101,221–225) and thus those molecules encounter a different barrier distribution. These distributions contain more geometries with higher reaction barriers, thus extending to higher energies while at the same time decreasing the fraction of sites with lower barriers. Hence, the slope of the RPCs is reduced and γ_{slow} values increase.

The γ_{slow} variation with v-state in the H_2 data indicates a compression of the barrier distribution to lower kinetic energies for vibrationally excited molecules. Combined with the strongly increased total flux (see fig. 10.18) for H_2 ($v = 1$), this hints towards a very specific reaction geometry where vibrational energy overcomes the barrier easily but dynamical steering is hindered even for moderate kinetic energies.

Results for relative fluxes of the slow channel show no significant variations with quantum state for D_2, while for H_2 the values decrease for higher J states, similar as the γ_{slow} results. Furthermore, the relative slow channel flux is higher for H_2 on the Cu(211) facet. This indicates a surface morphology dependence of the mechanism, but this argument is weakened since no such effect was observed for D_2. But this could be linked to the higher molecular mass, leading to an extend of the TOF signals over a larger range. This reduces the SNR and increases the overlap between the channels and the TB, thus leading to stronger parameter correlations and increased uncertainties.

This supports the above assumption of higher barriers encountered due to misalignment, which reduces the total amount of molecules which can react. Also, this argument agrees with the differences found between the isotopologues, where the larger mass of D_2 leads to decreased angular frequencies. Therefore, dynamical steering effects would affect D_2 stronger and possibly mask alignment effects.

Comparison to Literature   No quantitative description of the observed slow channel is available in the literature. However, Murphy and Hodgson[193] studied the desorption of H_2 and D_2 from Cu(111) using H-atom dosing, the same REMPI technique as in this work, and weak electric field extraction of the ions. Studying the temperature range of 370–900 K, their RPCs also contained a feature for kinetic energies $\lesssim 0.2\,\text{eV}$ that could not be explained with the ERF model. Murphy and Hodgson interpreted this as a second reaction channel emerging from thermally generated reaction sites with no or only negligible barriers.

Since the relative flux they obtained was $<3\,\%$, no elaborate characterization was conducted and neither was the angular distribution studied. But from the angular desorption distributions obtained in this study (section 10.2.1.8) and the interconnection to the total flux (section 10.2.1.3), their reported flux might be a strong underestimation.

Furthermore, the sticking probabilities they obtained for $\lesssim 0.2\,\text{eV}$ kinetic energy increased over several orders of magnitude with the surface temperatures over the large range they studied. This also agrees with direct adsorption studies of hydrogen on cop-

per, conducted at surface temperatures below 200 K (e.g. ref. 178,181,189,195), where the obtained sticking probabilities for ≲0.2 eV were negligible. When compared to the reported reaction probabilities from this study (cf. fig. 10.11), this supports a dependence of the reaction mechanism on the surface morphology.

Since this channel was already observed at 370 K, it should also be apparent in post-permeation desorption experiments conducted at higher temperatures. But as already discussed in section 11.3.1.3, the detection efficiency depends on the solid angle of the experiment. Furthermore, the detectability of slow ions is reduced by additional factors, e.g. for many quantum states the TB overlaps with the signal and has to be subtracted very carefully. Also, ion drift methods disperse the signal over a long TOF range which reduces the SNR. Furthermore, this leads to the detection efficiency of the slow channel being strongly dependent on the FCA conditions.

Conclusively, such a feature was not reported in most experiments, but it might have been observed. Some published data contains relevant flux at long TOF, which was not explained with the respective fitted models, e.g. Hou *et al.*[192] (figure 1, TOF>7 µs). Furthermore, the results of Michelsen *et al.*[185] (figure 6, TOF>10 µs) could also contain a similar feature, but Nattino *et al.*[175] sucessfully described these deviations by asymmetric RPCs. Another possible study which observed a slow channel contribution is the work of Rettner *et al.*[189], where the reported RPC curves also deviate from the ERF model (figure 6b, ≲0.2 eV). While this is clear for $(v = 1)$, is the data for $(v = 0)$ less conclusive, possibly due to background subtraction. All these studies illustrate how elusive the slow channel is, and that for quantification of its properties specifically designed experiments are necessary.

11.3.1.4 Slow Channel Discussion

Several reaction mechanism will be discussed in this section based on the unusual dynamics observed for the slow channel. For some of these argumentations it is easier to describe the reverse process of dissociative chemisorption based on the detailed balance model.

A first model consistent with the observations would be the physisorption of a hydrogen molecule on the surface and subsequent dissociation after a certain residence time. Over a range of 1–100 ps the physisorbed molecule would even experience movement of the copper lattice, possibly forming new reaction geometries, e.g. kinks or other defects[198]. Such a trapped molecule could then dissociate by tunneling through or passing over a large reaction barrier, before its vibrational energy is dissipated. At the surface temperatures considered here adatom and vacancy formation[301,302], diffusion, kink formation and other mechanisms will alter the surface morphology dynamically. Therefore, several defect sites will be formed, which are not available at low or cryogenic temperatures. Although, from the temperature dependencies measured here, only adatom-vacancies can be ruled out.

This proposed mechanism is consistent with many of the reported properties of the

slow channel. The low mean desorption energies and broad angular distributions agree with physisorption. Internal molecular energy of hydrogen is known to be retained over many collisions[117], thus over a long residence time on the surface. This leads to a long effective reaction time, where the copper lattice is able to form new reaction sites not considered previously.

Another possible mechanism for the slow channel could involve H-atoms in subsurface sites, as has been shown for example for the hydrogenation of acetylene on nickel[303]. Subsurface hydrogen will be apparent in experiments employing either the permeation technique or H-atom dosing, where the hydrogen atoms are known to be able to penetrate the surface layer and absorb subsurface[123,304]. Furthermore, on copper adsorbed hydrogen is known to diffuse to subsurface sites at temperatures below ~250 K in a reversible process, even for low coverages[305–308]. Also accompanied by subsurface H-atom adsorption could be a reordering of the surface structure (e.g. ref. 307,309,310), which could be involved in the transition state geometry. In any reaction mechanisms involving subsurface H-atoms in the transition state, the reactive flux will strongly depend on the subsurface concentration. When H-atom dosing is used the surface temperature will not be an important factor for this. This is in agreement with the observed small deviations of relative slow channel flux by Murphy and Hodgson[193]. In permeation experiments the sample is in a steady state, where the desorbing flux is equal to the supply of new hydrogen from the reservoir. Therefore, all factors influencing the permeation rate would also alter the subsurface H-atom concentration (see section 8.2.3). In this mechanism the slow channel flux would scale directly with this concentration, and the estimated increase of a factor of two relative to the literature[182,185,189] (see section 11.1.3) would be consistent with the low observed slow channel fluxes in previous studies. Also, systems with lower permeation rates, e.g. gold, would not show such a slow channel, as was observed in this work (cf. section 10.2.2).

A third possible mechanism involves ehp interactions, which were already discussed in section 11.2.3. For the hydrogen/copper system, electronic friction suggested energy dissipation to ehps on the order of only ~20 meV, while *H-atom* interactions with copper showed large effects[63]. In this study ehp excitations cannot be probed directly and a calculated energy dissipation for dissociative chemisortpion is only ~20 meV[146]. Now, when considering a large reaction barrier for the molecule formation over the transition state of the slow channel, a strong kinetic energy dissipation channel would be required to obtain the observed distributions. Here, ehp interactions would offer a previously unconsidered channel. Notwithstanding, the occurrence of non-adiabatic effects in the interactions of *H-atoms* with copper show that theories describing the system as entirely adiabatic cannot grasp the dynamics on the surface in its entirety.

In conclusion, the mechanism leading to the observed slow channel could not be identified unambiguously, and further experimental as well as theoretical work is required for this task.

11.3.2 Gold

For the hydrogen/Au(111) system only one desorption feature was observed, as expected. This corresponds to molecules with high kinetic energies and those are well described within the detailed balance model using the ERF to represent the RPCs. Wijzenbroek *et al.*[201] provided SRP-based DFT results to which the current data was compared extensively, revealing strong deviations. Unfortunately, experimental data for comparison is scarce for desorption of hydrogen from gold surfaces. In the following subsections the results for the hydrogen/Au(111) system will be discussed with regard to the observed properties and their comparison to literature as well as its dynamics. Interpretations and explanations of the observed differences to theory will be presented and some of this material has already been published[220].

11.3.2.1 System Properties

The properties of the dissociative chemisorption in the H_2/Au(111) system were characterized extensively, although not for all quantum states that have been obtained for the H_2/Cu(111) system. In this work, the RPCs of three hydrogen isotopologues have been acquired based on the model of detailed balance and the ERF form. The resulting RPCs revealed barrier distributions which require high incidence energies for dissociative chemisorption.

Experimentally, such high barriers also reduce the flux of molecules from the surface, which leads to low SNRs in the measurements. This limited the number of quantum states that could be acquired and caused problems in the analysis procedure, e.g. the correlation of the single ERF parameters (section 11.2.2.1). Therefore, the obtained kinetic energy distributions were also analysed with Gaussian fits, which represents an independent method to describe these desorption distributions.

Fortunately, Wijzenbroek *et al.*[201] recently provided extensive theory results for this system. Here, the presented comparisons (section 10.3.2) were limited to the SRP48 results since this DFT functional had been tailored to predict the reactivity on coinage metals. This allows discussion of the obtained results in a larger context, e.g. the purely adiabatic description of the reactivity.

In the following paragraphs individual aspects of the system will be discussed in comparison to the available literature results. The dynamics of the system will be treated in the next section.

Comparison to Theory Results   A good overview of the comparison between experiment and the theory model is given by the simulated desorption distributions (fig. 10.45). For Au(111) the simulated peaks are shifted to higher energies and are too narrow, which is qualitatively similar as found for Cu(111). These deviations are larger for Au(111) and in contrast to Cu(111) the relative amplitudes deviate significantly as well. For H_2 ($v = 1$)

theory underestimates the experimental values by a factor of approximately two and for D_2 ($v = 2$) those are overestimated by a similar factor. Such an isotopologue-dependent effect has not been observed in the Cu(111) system.

From the comparisons for the three RPC parameters these effects could not be determined directly. For example, the ERF-W parameters are fitted to theoretical RPCs larger than determined in the experiment. This shows the complex interconnection of the single parameters and the detailed balance model as well as the differences between ERF and FPC. As illustrated in panel (a) of fig. 10.46, the ERF curves extend to lower kinetic energies while the FPCs are asymmetric and cut off fast at low energies. The A_{erf} results (fig. 10.31 and table 10.19) also show smaller deviations from unity than for example the Cu(211) results. And while the E_0 parameters from theory are systematically higher than experimental values these deviations are not the same magnitude for all quantum states. Thus, only comparisons including the whole RPCs should be considered, like the presented desorption distributions.

A second method for such a comparison are the simulated quantum state population distributions (fig. 10.48). Here, the systematic deviations are quite clear and strong for vibrational states, but not for the rotational sequences. Thus, the argumentation can be limited to the vibrational partitions presented in table 10.20. Here, for D_2 ($v = 1$) a too high partition was simulated and for D_2 ($v = 2$) a too low partition, both by the same order of magnitude. But for H_2 ($v = 1$) the simulation deviated significantly stronger.

The third property which includes the full model is the averaged desorption energy. From table 10.21 it is obvious that the energy of desorbing molecules is overestimated by theory and a similar result for $\langle E_{kin} \rangle$ is obtained for both H_2 and D_2. In the experimental results, the isotopologue effect leads to $\langle E_{kin} \rangle$ values for H_2 ~0.1 eV lower than the $\langle E_{kin} \rangle$ for D_2. Due to the measured high partition of H_2 ($v = 1$) the deviations in $\langle E_{kin} \rangle$ between the theoretical model are 0.23–0.25 eV for the individual vibrational states, but for the averaged value the deviation is increased to 0.32 eV. For D_2 the predictions deviate by 0.27–0.29 eV, for both vibrational states as well as the total value.

It is pointed out, that the BOSS model neglects thermal surface motion, which leads to an overestimation of reaction barriers by $\lesssim$0.1 eV (see section 11.2.1). This is clearly too small to explain these differences between experiment and theory for the hydrogen/gold system.

Extrapolated Activation Energy Comparison of the energy barrier for dissociative adsorption reported by Stobiński and Duś[202,203] and the value obtained here yields a deviation by a factor of more than two. Since in this work the desorption is studied, the prediction of adsorption probabilities relies on the principle of detailed balance and the rather crude method to extrapolate from RPC parameters to activation energy (section 11.2.2.2). On the other hand, the chemisorption of H_2 on gold was predicted to be endothermic

by DFT (section 7.2.1), but Stobiński and Duś[203] described it as exothermic. These additional discrepancies might be related to the amorphous structure they studied, in contrast to the ideal Au(111) facet surveyed here and assumed in DFT. Furthermore, there are vast differences in the H-atom coverage and temperatures between the studies. These deviations show that the surface structure and H-atom coverage must be important factors in the reaction, but cannot be quantified.

Angular Distribution   Only for D_2 ($v = 1, J = 2$)/Au(111) the angular desorption distribution was obtained. Analysis of the measured flux with eq. (8.33) yielded good agreement with the parameter $n = 12.9 \pm 0.8$, thus significantly narrower than results for the hydrogen/copper systems. Because the surface temperature was higher for Au(111) by $138\,\mathrm{K}$ (or $15\,\%$) a counteracting broadening effect was actually expected (section 8.3.2.3). Thus, the obtained narrow distribution reflects the high barrier for reaction, but no information about the energy scaling law could be obtained from the experiment.

11.3.2.2   Dynamics Description

The following paragraphs summarize the dynamical properties for the hydrogen/Au(111) system.

Influence of Vibration   As for the hydrogen/copper system vibrational energy couples to the reaction coordinate for dissociative chemisorption of hydrogen on Au(111). Thus, a shift of RPCs to lower kinetic energies has been observed. The quantification of this effect by a vibrational efficacy was presented in detail in sections 10.2.2.6 and 10.3.2.4. Experimental results yielded isotopologue-independent ξ_{vib} values around ~0.84, except for HD, where only ($J = 2$) data was available. Here it is pointed out, that the SNR of the HD data sets was lower than for the other two isotopologues, and that no theory predictions are available for HD. The rotational state dependent analysis presented in fig. 10.49 revealed that the obtained values could scatter between individual signals up to ~0.1, but not systematically. However, the theory based ξ_{vib} values showed a correlation with rotational states that is not supported by the experiment. Furthermore, the predictions agree with experiment only for the D_2 ($v = 1$) sequence.

Influence of Rotation   For the Au(111) sample the effect of rotational energy is less obvious than for the copper facets. In fig. 10.27 no shift in the TOF peak is observable for $J < 7$. Also, the variation in the E_0 values for the rotational sequences (fig. 10.30) are small and show unsystematic scatter around constant values before decreasing for higher J states. Similar behaviour was also predicted by the theory of Wijzenbroek *et al.*[201]. But the quantitative analysis based on the ΔS parameters actually reveals the same effect found for both copper facets (see sections 10.2.1.7 and 10.2.2.6). For low J states the

rotational efficacies are negative and with increasing rotational energy a threshold value is approached asymptotically. For the Au(111) data the lower SNR leads to a larger scatter in these values, but does not change the general outcome (fig. 10.35). These results hint towards a general dynamic effect for associative desorption because it correlates directly with rotational energy, irrespective of isotopologue, surface facet and even metal.

11.3.2.3 Interpretation of Results

In this section the properties of the hydrogen/Au(111) system will be interpreted in regard to the observed deviations to adiabatic theory. As for the H_2/Cu(111) system, adiabatic SRP-DFT overestimates the barriers for reaction. Despite the systematically higher discrepancies between experiment and theory in the Au(111) system isotopologue-specific deviations are found as well (see section 11.3.2.1). These isotopologue effects manifest in the vibrational state population distributions and the quantum state averaged desorption energies and are not captured by the theory. Previously, isotopologue-dependent effects have been considered to manifest in the widths of obtained RPCs[117,193,311], induced e.g. by tunneling. But this was not observed, neither in this study nor in the experimental literature[182,185,189,193].

Considering the very good agreement of the same adiabatic SRP model for the Cu(111) system, non-adiabatic interactions are considered the most probable explanation for these isotopologue effects. But the exact impact of non-adiabatic effects on the distributions obtained in desorption experiments remains speculative. As stated in[220], the H-H bond distance at the transition state is expected to be longer for Au(111) than Cu(111), corresponding to a "later" reaction barrier for absorption in terms of the Polanyi rules[85,312–314]. Thus, the transition state geometry more closely resembles separated H-atoms, which can readily interact non-adiabatically with metal surfaces, as discussed in section 11.2.3. Possibly, this allows an additional energy dissipation channel and thus would result in lower desorption energies. Consistently, the direct comparison of experimental results to SRP-DFT predictions shows that the discrepancies are larger for Au(111) than for Cu(111). However, such an energy dissipation cannot explain the observed isotopologue effect. Unfortunately, the isotopologue-dependent electronic friction contribution as well as directional effects during the reaction remain unquantified in current theoretical work[137]. Furthermore, several studies hinted to at least partial electron transfer accompanying the reaction[58,144,145,291], thus extending the number of possible reaction mechanisms. It is concluded that further theoretical work is necessary, possibly including directional non-adiabatic effects, in order to describe and understand the hydrogen/Au(111) system.

Chapter 12

Conclusion and Outlook

12.1 Conclusions

In this study the associative desorption of three hydrogen isotopologues on three metal surfaces has been studied in great detail. Via detailed balance the obtained distributions were related to the reverse process of dissociative adsorption, which yielded initial quantum state resolved reaction probability curves.

For the well-studied Cu(111) surface an extensive data set with improved calibration has been provided. With small but significant differences to the established literature, this new set should henceforth be used as benchmark for theory models which aim to describe the interactions in the hydrogen/Cu(111) system. Although such theories already describe the reactivity within chemical accuracy some dynamics are described qualitatively wrong.

Additionally the Cu(211) facet was studied, which revealed systematic variations in the RPCs but with a smaller extent than expected for a surface with a high step-density. For all isotopologues and ro-vibrational states studied the RPCs are broader and shifted to higher kinetic energies on the Cu(211) facet. However, the desorption distributions vary only marginally between the facets and the averaged desorption energies are higher by less than 4 % for the Cu(211) facet. While absolute reactivities cannot be determined by this experimental method a lower reactivity for the Cu(211) surface would be predicted by these results. The small variations found between the facets might be explained by the increased thermal surface disorder at the permeation temperatures, which blurs out the differences between the facets.

A most interesting aspect of these results is the desorption feature observed on both copper facets at low kinetic energies and with unsusual dynamics. This is attributed to an additional reaction channel, which is analysed quantitatively here for the first time. A similar feature has been reported only once before by Murphy and Hodgson[193], but was also observed at least partially in some of the many other studies of the H_2/Cu(111) system. It is argued, that the broad angular distribution of this feature reduces its detectability significantly. While several possible explanations are presented here the underlying

mechansim remains ambiguous. Clearly, further experimental information and supporting theoretical work is necessary to determine the origin of this mechanism.

As a third system, hydrogen/Au(111) was studied and compared to recent adiabatic theory results. The deviations found are significantly larger than for hydrogen/Cu(111), where the same SRP-DFT model yielded agreement within chemical accuracy. Furthermore, for Au(111) isotopologue-dependent effects were measured, which are not reproduced by the theory altogether. Considered as most probable explanation are non-adiabatic effects, which have been observed in other systems studying the interaction of hydrogen with gold.

12.2 Outlook

For future work, several reasonable research goals are possible and also achievable with reasonable effort. Also, some properties of the desorbing H_2 have not been probed in this study, e.g. the rotational alignment of the molecules (e.g. ref. 190–192).

In general, the temperature range of permeation experiments could be extended to lower temperatures by variation of the H-atom supply method. Direct H-atom dosing of the rear of the samples would increase the hydrogen inventory in the bulk, thus the gradient for diffusion and the resulting surface coverage. This method has been termed "superpermeation" (e.g. ref. 304,315,316) and various H-atom supply techniques are available for such an approach (see section 8.2.2).

Regarding the H_2/Cu(111) system, further effort should be focused on an improved detection of the slow channel to allow for reliable quantitative analysis of the remaining properties, which also needs to be accompanied by theoretical work. One way to enhance the detection of the slow channel would be to change from free ion drift to a well-defined weak extraction field, like it was used by Murphy and Hodgson[108,110,193] or Sementa et al.[250]. Another viable experiment to study this in more detail would involve variation of the surface H-atom coverage, either by changing the crystal thickness or backing pressures or by completely different supply methods as described above. Accompanying measurements of the steady-state H-atom coverage by spectroscopic methods would be interesting but challenging to conduct. Furthermore, studying the hydrogen desorption from copper over a wide range of surface temperatures after dosing with cold molecular beams would be a completely different approach. Due to the differences in the angular desorption distributions for both reaction channels such studies might reveal a thermal dependence of the slow channel.

For Au(111), the large deviations to theoretical predictions and the observed isotopologue effect challenge the current understanding of associative desorption processes. High-level theory fails to predict the interactions in the H_2/Au(111) system (see section 7.3), irrespective of the adiabaticity of the treatment (see ref. 145,201). Clearly, the presented

data provides a useful benchmark for focused theoretical work on this system.

Additional systems of interest are Ag(111) and Co(0001), since for both high-level theory predictions are available[105,106,113]. Silver is the third coinage metal in the row and currently under experimental investigation. In contrast to that, cobalt has the peculiarity of a phase transition. Above $693\,\mathrm{K}$ cobalt changes from a hcp to a fcc structure[317,318]. Furthermore, previous hydrogen chemisorption and TPD measurements[105,319] predicted low reaction barriers, rendering this a weakly activated system.

In conclusion, the associative desorption of hydrogen from metal surfaces is not fully understood despite the considerable progress in the last decades. This study provided extensive data sets, which can serve as benchmark for high-level theoretical work to improve the fundamental understanding of hydrogen metal interactions.

Part III

Bibliography

References

[1] S. Kaufmann, D. Schwarzer, C. Reichardt, A. M. Wodtke, and O. Bünermann, "Generation of ultra-short hydrogen atom pulses by bunch-compression photolysis." Nature communications **5**, 5373 (2014).

[2] L. R. Khundkar and A. H. Zewail, "Ultrafast Molecular Reaction Dynamics in Real-Time - Progress Over a Decade," Annual Review of Physical Chemistry **41**, 15–60 (1990).

[3] F. F. Crim, "State-Selected and Bond-Selected Unimolecular Reactions," Science **249**, 1387–1392 (1990).

[4] X. D. Zhu, T. Rasing, and Y. R. Shen, "Surface-Diffusion of CO on Ni(111) Studied by Diffraction of Optical Second-Harmonic Generation off a Monolayer Grating," Physical Review Letters **61**, 2883–2885 (1988).

[5] M. Bonn, C. Hess, S. Funk, J. H. Miners, B. N. J. Persson, M. Wolf, and G. Ertl, "Femtosecond surface vibrational spectroscopy of CO adsorbed on Ru(001) during desorption," Physical Review Letters **84**, 4653–4656 (2000).

[6] T. Hertel, E. Knoesel, M. Wolf, and G. Ertl, "Ultrafast electron dynamics at Cu(111): Response of an electron gas to optical excitation," Physical Review Letters **76**, 535–538 (1996).

[7] G. Sciaini and R. J. D. Miller, "Femtosecond electron diffraction: heralding the era of atomically resolved dynamics," Reports on Progress in Physics **74** (2011), 10.1088/0034-4885/74/9/096101.

[8] A. H. Zewail, "Four-Dimensional Electron Microscopy," Science **328**, 187–193 (2010).

[9] P. Bianchini, C. Peres, M. Oneto, S. Galiani, G. Vicidomini, and A. Diaspro, "STED nanoscopy: a glimpse into the future," Cell and Tissue Research **360**, 143–150 (2015).

[10] T. van Oudheusden, P. L. E. M. Pasmans, S. B. van der Geer, M. J. de Loos, M. J. van der Wiel, and O. J. Luiten, "Compression of Subrelativistic Space-Charge-Dominated Electron Bunches for Single-Shot Femtosecond Electron Diffraction," Physical Review Letters **105**, 264801 (2010).

[11] M. Gulde, S. Schweda, G. Storeck, M. Maiti, H. K. Yu, A. M. Wodtke, S. Schäfer, and C. Ropers, "Ultrafast low-energy electron diffraction in transmission resolves polymer/graphene superstructure dynamics," Science **345**, 200–204 (2014).

[12] B. Schröder, T. Weber, S. V. Yalunin, T. Kiel, C. Matyssek, M. Sivis, S. Schäfer, F. von Cube, S. Irsen, K. Busch, C. Ropers, and S. Linden, "Real-space imaging of nanotip plasmons using electron energy loss spectroscopy," Phys. Rev. B **92**, 85411 (2015).

[13] G. Storeck, S. Vogelgesang, M. Sivis, S. Schäfer, and C. Ropers, "Nanotip-based photoelectron microgun for ultrafast LEED," Structural Dynamics **4**, 44024 (2017).

[14] A. P. Mills Jr., "Time bunching of slow positrons for annihilation lifetime and pulsed laser photon absorption experiments," Applied physics **22**, 273–276 (1980).

[15] F. Herfurth, J. Dilling, A. Kellerbauer, G. Bollen, S. Henry, H.-J. Kluge, E. Lamour, D. Lunney, R. B. Moore, C. Scheidenberger, S. Schwarz, G. Sikler, and J. Szerypo, "A linear radiofrequency ion trap for accumulation, bunching, and emittance improvement of radioactive ion beams," Nuclear Instruments and Methods in Physics Research Section A: Accelerators, Spectrometers, Detectors and Associated Equipment **469**, 254–275 (2001).

[16] H. Iijima, T. Asonuma, T. Hirose, M. Irako, K. Kadoya, T. Kumita, B. Matsumoto, K. Wada, and M. Washio, "Time bunching of slow positrons for lifetime and time-of-flight measurements of ortho-positronium," Nuclear

Instruments and Methods in Physics Research Section A: Accelerators, Spectrometers, Detectors and Associated Equipment **483**, 641–648 (2002).

[17] C. T. Rettner, "Reaction of an H-atom beam with Cl/Au(111): Dynamics of concurrent Eley–Rideal and Langmuir–Hinshelwood mechanisms," The Journal of Chemical Physics **101**, 1529–1546 (1994).

[18] H. Nienhaus, H. S. Bergh, B. Gergen, A. Majumdar, W. H. Weinberg, and E. W. McFarland, "Electron-Hole Pair Creation at Ag and Cu Surfaces by Adsorption of Atomic Hydrogen and Deuterium," Physical Review Letters **82**, 446–449 (1999).

[19] B. Mildner, E. Hasselbrink, and D. Diesing, "Electronic excitations induced by surface reactions of H and D on gold," Chemical Physics Letters **432**, 133–138 (2006).

[20] B. Schindler, D. Diesing, and E. Hasselbrink, "Electronic Excitations in the Course of the Reaction of H with Coinage and Noble Metal Surfaces: A Comparison," Zeitschrift für Physikalische Chemie **227**, 1381 (2013).

[21] L. Schnieder, K. Seekamprahn, F. Liedeker, H. Steuwe, and K. H. Welge, "Hydrogen-Exchange Reaction H + D_2 in Crossed Beams," Faraday Discussions **91**, 259–269 (1991).

[22] T. N. Kitsopoulos, A. Buntine, D. P. Baldwin, R. N. Zare, and D. W. Chandler, "Application of Ion Imaging to the Study of Unimolecular and Bimolecular Reactions," SPIE **1858**, 2–14 (1993).

[23] K. Kotaki, Y. Sakurai, and T. Arikawa, "Rempi Doppler Spectroscopy of H Atoms with tunable VUV Radiation around Lyman a Line," Journal of the Mass Spectrometry Society of Japan **43**, 351–363 (1995).

[24] O. Bünermann, H. Jiang, Y. Dorenkamp, A. Kandratsenka, S. M. Janke, D. J. Auerbach, and A. M. Wodtke, "Electron-hole pair excitation determines the mechanism of hydrogen atom adsorption," Science **350** (2015).

[25] D. B. Cassidy, S. H. M. Deng, R. G. Greaves, and J. A. P. Mills, "Accumulator for the production of intense positron pulses," Review of Scientific Instruments **77**, 73106–73108 (2006).

[26] M. Gao, H. Jean-Ruel, R. R. Cooney, J. Stampe, M. de Jong, M. Harb, G. Sciaini, G. Moriena, and R. J. Dwayne Miller, "Full characterization of RF compressed femtosecond electron pulses using ponderomotive scattering," Optics Express **20**, 12048–12058 (2012).

[27] V. Grill, J. Shen, C. Evans, and R. G. Cooks, "Collisions of ions with surfaces at chemically relevant energies: Instrumentation and phenomena," Review of Scientific Instruments **72**, 3149–3179 (2001).

[28] W. Ketterle and D. E. Pritchard, "Trapping and focusing ground state atoms with static fields," Applied Physics B **54**, 403–406 (1992).

[29] B. Friedrich and D. Herschbach, "Alignment and Trapping of Molecules in Intense Laser Fields," Phys. Rev. Lett. **74**, 4623–4626 (1995).

[30] B. Friedrich and Herschbach, "Manipulating Molecules via Combined Static and Laser Fields," The Journal of Physical Chemistry A **103**, 10280–10288 (1999).

[31] J. A. Maddi, T. P. Dinneen, and H. Gould, "Slowing and cooling molecules and neutral atoms by time-varying electric-field gradients," Physical Review A **60**, 3882–3891 (1999).

[32] E. Maréchal, S. Guibal, J.-L. Bossennec, R. Barbé, J.-C. Keller, and O. Gorceix, "Longitudinal focusing of an atomic cloud using pulsed magnetic forces," Phys. Rev. A **59**, 4636–4640 (1999).

[33] H. Sakai, C. P. Safvan, J. J. Larsen, K. M. Hilligsøe, K. Hald, and H. Stapelfeldt, "Controlling the alignment of neutral molecules by a strong laser field," The Journal of Chemical Physics **110**, 10235–10238 (1999).

[34] H. L. Bethlem, G. Berden, F. M. H. Crompvoets, R. T. Jongma, A. J. A. van Roij, and G. Meijer, "Electrostatic trapping of ammonia molecules," Nature **406**, 491–494 (2000).

[35] S. D. Hogan, D. Sprecher, M. Andrist, N. Vanhaecke, and F. Merkt, "Zeeman deceleration of H and D," Physical Review A **76**, 23412 (2007).

[36] N. Vanhaecke, U. Meier, M. Andrist, B. H. Meier, and F. Merkt, "Multistage Zeeman deceleration of hydrogen atoms," Physical Review A **75**, 31402 (2007).

[37] S. Marx, D. Adu Smith, M. J. Abel, T. Zehentbauer, G. Meijer, and G. Santambrogio, "Imaging Cold Molecules on a Chip," Phys. Rev. Lett. **111**, 243007 (2013).

References

[38] S. Y. T. van de Meerakker, H. L. Bethlem, N. Vanhaecke, and G. Meijer, "Manipulation and Control of Molecular Beams," Chemical Reviews **112**, 4828–4878 (2012).

[39] A. G. Kostenbauder, "RAY-PULSE MATRICES - A RATIONAL TREATMENT FOR DISPERSIVE OPTICAL-SYSTEMS," Ieee Journal of Quantum Electronics **26**, 1148–1157 (1990).

[40] S. Akturk, X. Gu, P. Gabolde, and R. Trebino, "The general theory of first-order spatio-temporal distortions of Gaussian pulses and beams," Optics Express **13**, 8642–8661 (2005).

[41] C. Cohen-Tannoudji and S. Reynaud, "Dressed-atom description of resonance fluorescence and absorption spectra of a multi-level atom in an intense laser beam," Journal of Physics B: Atomic and Molecular Physics **10**, 345 (1977).

[42] J. H. Posthumus, "The dynamics of small molecules in intense laser fields," Reports on Progress in Physics **67**, 623 (2004).

[43] M. R. Thompson, M. K. Thomas, P. F. Taday, J. H. Posthumus, A. J. Langley, L. J. Frasinski, and K. Codling, "One and two-colour studies of the dissociative ionization and Coulomb explosion of with intense Ti:sapphire laser pulses," Journal of Physics B: Atomic, Molecular and Optical Physics **30**, 5755 (1997).

[44] J. H. Posthumus, J. Plumridge, P. F. Taday, J. H. Sanderson, A. J. Langley, K. Codling, and A. W. Bryan, "Sub-pulselength time resolution of bond softening and Coulomb explosion using polarization control of laser-induced alignment," Journal of Physics B: Atomic, Molecular and Optical Physics **32**, L93–L93 (1999).

[45] C. E. Moore, "Atomic Energy Levels, Natl. Stand. Ref. Data Ser." (1971).

[46] R. G. Bray and R. M. Hochstrasser, "Two-photon absorption by rotating diatomic molecules," Molecular Physics **31**, 1199–1211 (1976).

[47] S. A. Wright and J. D. McDonald, "Multiphoton ionization spectroscopy of hydrogen iodide," The Journal of Chemical Physics **101**, 238 (1994).

[48] J. F. Ogilvie, "Semi-experimental determination of a repulsive potential curve for hydrogen iodide," Transactions of the Faraday Society **67**, 2205–2215 (1971).

[49] R. D. Clear, S. J. Riley, and K. R. Wilson, "Energy partitioning and assignment of excited states in the ultraviolet photolysis of HI and DI," Journal of Chemical Physics **63**, 1340 (1975).

[50] S. R. Langford, P. M. Regan, A. J. Orr-Ewing, and M. N. R. Ashfold, "On the UV photodissociation dynamics of hydrogen iodide," Chemical Physics **231**, 245–260 (1998).

[51] A. B. Alekseyev, H.-P. Liebermann, D. B. Kokh, and R. J. Buenker, "On the ultraviolet photofragmentation of hydrogen iodide," The Journal of Chemical Physics **113**, 6174 (2000).

[52] S. Manzhos, H.-P. Loock, B. L. G. Bakker, and D. H. Parker, "Photodissociation of hydrogen iodide in the A-band region 273–288 nm," Journal of Chemical Physics **117**, 9347–9352 (2002).

[53] C. E. Brion, M. Dyck, and G. Cooper, "Absolute photoabsorption cross-sections (oscillator strengths) for valence and inner shell excitations in hydrogen chloride, hydrogen bromide and hydrogen iodide," Journal of Electron Spectroscopy and Related Phenomena **144–147**, 127–130 (2005).

[54] R. S. Mulliken, "Low Electronic States of Simple Heteropolar Diatomic Molecules: III. Hydrogen and Univalent Metal Halides," Physical Review **51**, 310–332 (1937).

[55] S. C. Hurlock, R. M. Alexander, K. N. Rao, and S. N. Dreska, "INFRARED BANDS OF HI AND DI," Journal of Molecular Spectroscopy **37**, 373–and (1971).

[56] S. Kaufmann, *Multi Photon Ionization Spectroscopy of Molecular and Atomic Hydrogen and Deuterium*, Master's thesis, University of Goettingen, Goettingen (2011).

[57] F. Wang, I. C. Lu, K. Yuan, Y. Cheng, M. Wu, D. H. Parker, and X. Yang, "Photodissociation dynamics of HI and DI at 157 nm," Chemical Physics Letters **449**, 18–22 (2007).

[58] B. Schindler, D. Diesing, and E. Hasselbrink, "Electronically Nonadiabatic Processes in the Interaction of H with a Au Surface Revealed Using MIM Junctions: The Temperature Dependence," The Journal of Physical Chemistry C **117**, 6337–6345 (2013).

[59] D. Diesing and E. Hasselbrink, "Chemical energy dissipation at surfaces under UHV and high pressure conditions studied using metal-insulator-metal and similar devices," Chemical Society Reviews **45**, 3747–3755 (2016).

[60] M. Neupane, S.-Y. Xu, Y. Ishida, S. Jia, B. M. Fregoso, C. Liu, I. Belopolski, G. Bian, N. Alidoust, T. Durakiewicz, V. Galitski, S. Shin, R. J. Cava, and M. Z. Hasan, "Gigantic Surface Lifetime of an Intrinsic Topological Insulator," Phys. Rev. Lett. **115**, 116801 (2015).

[61] H. Jiang, *Dynamics of Hydrogen Atoms Scattering from Surfaces*, Ph.D. thesis, University of Goettingen (2016).

[62] N. Hertl, *Hydrogen atom scattering from Ni(111)*, Master's thesis, University of Goettingen, Goettingen (2016).

[63] O. Bünermann, H. Jiang, and Y. Dorenkamp, "unpublished results," (2015-2016).

[64] J. A. Serri, M. J. Cardillo, and G. E. Becker, "A molecular beam study of the NO interaction with Pt(111)," The Journal of Chemical Physics **77**, 2175–2189 (1982).

[65] J. A. Serri, J. C. Tully, and M. J. Cardillo, "The influence of steps on the desorption kinetics of NO from Pt(111)," The Journal of Chemical Physics **79**, 1530–1540 (1983).

[66] R. J. Buss, P. Casavecchia, T. Hirooka, S. J. Sibener, and Y. T. Lee, "REACTIVE SCATTERING OF $O(^1D)+H_2$," Chemical Physics Letters **82**, 386–391 (1981).

[67] M. Appel, *"Ammonia", Ullmann's Encyclopedia of Industrial Chemistry* (WILEY-VCH Verlag, Weinheim, 2005).

[68] U. S. Department of the Interior, *Mineral commodity summaries*, Tech. Rep. (U.S. Geological Survey, Reston, VA, 2016).

[69] G. Ertl, "Primary steps in catalytic synthesis of ammonia," Journal of Vacuum Science & Technology A: Vacuum, Surfaces, and Films **1**, 1247–1253 (1983).

[70] G.-J. Kroes and C. Díaz, "Quantum and classical dynamics of reactive scattering of H_2 from metal surfaces," Chemical Society Reviews **45**, 3658–3700 (2016).

[71] B. Jiang, M. Yang, D. Xie, and H. Guo, "Quantum dynamics of polyatomic dissociative chemisorption on transition metal surfaces: mode specificity and bond selectivity," Chemical Society Reviews **45**, 3621–3640 (2016).

[72] G. Comsa, R. David, and B.-J. Schumacher, "The angular dependence of flux, mean energy and speed ratio for D_2 molecules desorbing from a Ni(111) surface," Surface Science **85**, 45–68 (1979).

[73] G. Comsa and R. David, "Dynamical Parameters of Desorbing Molecules," Surface Science Reports **5**, 145–198 (1985).

[74] H. A. Aleksandrov, S. M. Kozlov, S. Schauermann, G. N. Vayssilov, and K. M. Neyman, "How Absorbed Hydrogen Affects the Catalytic Activity of Transition Metals," Angewandte Chemie International Edition **53**, 13371–13375 (2014).

[75] K. W. Kolasinski, W. Nessler, A. de Meijere, and E. Hasselbrink, "Hydrogen adsorption on and desorption from Si: Considerations on the applicability of detailed balance," Physical Review Letters **72**, 1356–1359 (1994).

[76] K. W. Kolasinski, W. Nessler, K.-H. Bornscheuer, and E. Hasselbrink, "Beam investigations of D_2 adsorption on Si(100): On the importance of lattice excitations in the reaction dynamics," The Journal of Chemical Physics **101**, 7082–7094 (1994).

[77] Y. G. Ptushinskiı̆, "Low-temperature adsorption of gases on metal surfaces (Review)," Low Temperature Physics **30**, 1–26 (2004).

[78] A. F. Carlsson and R. J. Madix, "The Extrinsic Precursor Kinetics of Methane Adsorption onto Ethylidyne-Covered Pt(111)," The Journal of Physical Chemistry B **105**, 3261–3268 (2001).

[79] R. Bisson, M. Sacchi, T. T. Dang, B. Yoder, P. Maroni, and R. D. Beck, "State-Resolved Reactivity of $CH_4(2\nu_3)$ on Pt(111) and Ni(111): Effects of Barrier Height and Transition State Location," The Journal of Physical Chemistry A **111**, 12679–12683 (2007).

References

[80] A. L. Utz, "Mode selective chemistry at surfaces," Current Opinion in Solid State and Materials Science **13**, 4–12 (2009).

[81] H. Ueta, L. Chen, R. D. Beck, I. Colon-Diaz, and B. Jackson, "Quantum state-resolved CH4 dissociation on Pt(111): coverage dependent barrier heights from experiment and density functional theory," Phys. Chem. Chem. Phys. **15**, 20526–20535 (2013).

[82] S. B. Donald, J. K. Navin, and I. Harrison, "Methane dissociative chemisorption and detailed balance on Pt(111): Dynamical constraints and the modest influence of tunneling," The Journal of Chemical Physics **139**, 214707 (2013).

[83] V. L. Campbell, N. Chen, H. Guo, B. Jackson, and A. L. Utz, "Substrate Vibrations as Promoters of Chemical Reactivity on Metal Surfaces," The Journal of Physical Chemistry A **119**, 12434–12441 (2015).

[84] E. Dombrowski, E. Peterson, D. D. Sesto, and A. L. Utz, "Precursor-mediated reactivity of vibrationally hot molecules: Methane activation on Ir(1 1 1)," Catalysis Today **244**, 10–18 (2015).

[85] H. Chadwick and R. D. Beck, "Quantum state resolved gas-surface reaction dynamics experiments: a tutorial review," Chemical Society Reviews **45**, 3576–3594 (2016).

[86] G. Rovida, F. Pratesi, M. Maglietta, and E. Ferroni, "Chemisorption of oxygen on the silver (111) surface," Surface Science **43**, 230–256 (1974).

[87] C. T. Rettner, L. A. DeLouise, and D. J. Auerbach, "Effect of incidence kinetic energy and surface coverage on the dissociative chemisorption of oxygen on W(110)," The Journal of Chemical Physics **85**, 1131 (1986).

[88] H. Brune, J. Wintterlin, R. J. Behm, and G. Ertl, "Surface Migration of Hot Adatoms in the Course of Dissociative Chemisorption of Oxygen on Al(111)," Physical Review Letters **68**, 624–626 (1992).

[89] C. Badan, M. T. M. Koper, and L. B. F. Juurlink, "How Well Does Pt(211) Represent Pt[n(111) × (100)] Surfaces in Adsorption/Desorption?" The Journal of Physical Chemistry C **119**, 13551–13560 (2015).

[90] G. Comsa, R. David, and B.-J. Schumacher, "Fast Deuterium Molecules Desorbing From Metals," Surface Science **95**, L210–L216 (1980).

[91] L. Schröter, G. Ahlers, M. Zacharias, and R. David, "Internal State Selected Velocity and Population Distribution of D$_2$ Desorbing From Clean Pd(100)," Journal of Electron Spectroscopy and Related Phenomena **45**, 403–411 (1987).

[92] L. Schröter, R. David, and H. Zacharias, "Vibrational Activation in Recombinative Hydrogen Desorption From Pd(100)," Journal of Electron Spectroscopy and Related Phenomena **54/55**, 143–151 (1990).

[93] L. Schröter, R. David, and H. Zacharias, "Rotational state distribution of recombinatively desorbing hydrogen from clean and S-covered Pd(100)," Surface Science **258**, 259–268 (1991).

[94] L. Schröter, S. Küchenhoff, R. David, W. Brenig, and M. Zacharias, "Vibrational activation in associative desorption of hydrogen from Pd(100)," Surface Science **261**, 243–250 (1992).

[95] A. Lozano, A. Gross, and H. F. Busnengo, "Adsorption dynamics of H$_2$ on Pd(100) from first principles," Physical Chemistry Chemical Physics **11**, 5814–5822 (2009).

[96] J. M. Boereboom, M. Wijzenbroek, M. F. Somers, and G. J. Kroes, "Towards a specific reaction parameter density functional for reactive scattering of H2 from Pd(111)," The Journal of Chemical Physics **139**, 244707 (2013).

[97] B. Hammer and J. K. Nørskov, "Why gold is the noblest of all the metals," Nature **376**, 238–240 (1995).

[98] A. T. Gee, B. E. Hayden, C. Mormiche, and T. S. Nunney, "The role of steps in the dynamics of hydrogen dissociation on Pt(533)," The Journal of Chemical Physics **112**, 7660–7668 (2000).

[99] B. Poelsema, K. Lenz, and G. Comsa, "The dissociative adsorption of hydrogen on defect-'free' Pt(111)." Journal of physics. Condensed matter : an Institute of Physics journal **22**, 304006 (2010).

[100] B. Poelsema, K. Lenz, and G. Comsa, "The dissociative adsorption of hydrogen on Pt(111): actuation and acceleration by atomic defects." The Journal of chemical physics **134**, 74703 (2011).

[101] I. M. N. Groot, A. W. Kleyn, and L. B. F. Juurlink, "The Energy Dependence of the Ratio of Step and Terrace Reactivity for H$_2$ Dissociation on Stepped Platinum," Angewandte Chemie International Edition **50**, 5174–5177 (2011).

217

[102] I. M. N. Groot, H. Ueta, M. J. T. C. van der Niet, A. W. Kleyn, and L. B. F. Juurlink, "Supersonic molecular beam studies of dissociative adsorption of H2 on Ru(0001)," The Journal of Chemical Physics **127**, 244701 (2007).

[103] G. Füchsel, S. Schimka, and P. Saalfrank, "On the Role of Electronic Friction for Dissociative Adsorption and Scattering of Hydrogen Molecules at a Ru(0001) Surface," The Journal of Physical Chemistry A **117**, 8761–8769 (2013).

[104] M. Wijzenbroek and G. J. Kroes, "The effect of the exchange-correlation functional on H2 dissociation on Ru(0001)," The Journal of Chemical Physics **140**, 84702 (2014).

[105] P. van Helden, J.-A. van den Berg, and C. J. Weststrate, "Hydrogen Adsorption on Co Surfaces: A Density Functional Theory and Temperature Programmed Desorption Study," ACS Catalysis **2**, 1097–1107 (2012).

[106] B. Jiang, X. Hu, S. Lin, D. Xie, and H. Guo, "Six-dimensional quantum dynamics of dissociative chemisorption of H_2 on Co(0001) on an accurate global potential energy surface," Physical Chemistry Chemical Physics **17**, 23346–23355 (2015).

[107] F. Healey, R. N. Carter, and A. Hodgson, "The recombinative desorption of D_2 from Ag(111): temperature-programmed desorption and low energy electron diffraction," Surface Science **328**, 67–79 (1995).

[108] M. J. Murphy and A. Hodgson, "Internal state distributions for D_2 recombinative desorption from Ag(111)," Surface Science **368**, 55–60 (1996).

[109] C. Cottrell, R. N. Carter, A. Nesbitt, P. Samson, and A. Hodgson, "Vibrational state dependence of D_2 dissociation on Ag(111)," The Journal of Chemical Physics **106**, 4714 (1997).

[110] M. J. Murphy and A. Hodgson, "Role of Surface Thermal Motion in the Dissociative Chemisorption and Recombinative Desorption of D_2 on Ag(111)," Physical Review Letters **78**, 4458–4461 (1997).

[111] M. J. Murphy and A. Hodgson, "Translational energy release in the recombinative desorption of H-2 from Ag(111)," Surface Science **390**, 29–34 (1997).

[112] P. Ferrin, S. Kandoi, A. U. Nilekar, and M. Mavrikakis, "Hydrogen adsorption, absorption and diffusion on and in transition metal surfaces: A DFT study," Surface Science **606**, 679–689 (2012).

[113] B. Jiang and H. Guo, "Six-dimensional quantum dynamics for dissociative chemisorption of H_2 and D_2 on Ag(111) on a permutation invariant potential energy surface," Physical Chemistry Chemical Physics **16**, 24704–24715 (2014).

[114] D. A. King, "Thermal desorption from metal surfaces: A review," Surface Science **47**, 384–402 (1975).

[115] S. J. Lombardo and A. T. Bell, "A review of theoretical models of adsorption, diffusion, desorption, and reaction of gases on metal surfaces," Surface Science Reports **13**, 3–72 (1991), arXiv:0708.1647v2 .

[116] K. Christmann, "Interaction of hydrogen with solid surfaces," Surface Science Reports **9**, 1–163 (1988).

[117] H. A. Michelsen and D. J. Auerbach, "A critical examination of data on the dissociative adsorption and associative desorption of hydrogen at copper surfaces," The Journal of Chemical Physics **94**, 7502 (1991).

[118] A. Hodgson, "State resolved desorption measurements as a probe of surface reactions," Progress in Surface Science **63**, 1–61 (2000).

[119] I. Langmuir, "The mechanism of the catalytic action of platinum in the reactions $2Co + O_2 = 2Co_2$ and $2H_2 + O_2 = 2H_2O$," Trans. Faraday Soc. **17**, 621–654 (1922).

[120] D. D. Eley and E. K. Rideal, "Parahydrogen Conversion on Tungsten," Nature **146**, 401–402 (1940).

[121] C. Rettner, "Dynamics of the direct reaction of hydrogen atoms adsorbed on Cu(111) with hydrogen atoms incident from the gas phase," Physical Review Letters **69**, 383–386 (1992).

[122] C. T. Rettner and D. J. Auerbach, "Quantum-state distributions for the HD product of the direct reaction of H(D)/Cu(111) with D(H) incident from the gas phase," The Journal of Chemical Physics **104**, 2732–2739 (1996).

[123] T. Kammler and J. Küppers, "Interaction of H atoms with Cu(111) surfaces: Adsorption, absorption, and abstraction," The Journal of Chemical Physics **111**, 8115 (1999).

References

[124] J.-Y. Kim and J. Lee, "Spatial and Kinetic Separation of Eley-Rideal Plus Primary Hot Atom and Secondary Hot Atom Mechanisms in H Atom Abstraction of Adsorbed D Atoms on Pt(111)," Phys. Rev. Lett. **82**, 1325–1328 (1999).

[125] J. E. Lennard-Jones, "Processes of adsorption and diffusion on solid surfaces," Trans. Faraday Soc. **28**, 333–359 (1932).

[126] M. J. Cardillo, M. Balooch, and R. E. Stickney, "Detailed Balancing and Quasi-Equilibrium in the Adsorption of Hydrogen on Copper," Surface Science **50**, 263–278 (1975).

[127] D. R. Lide, *CRC Handbook of Chemistry and Physics, Internet Version 2005*, 85th ed., edited by D. R. Lide (CRC Press, Boca Raton, FL, 2005).

[128] J. W. Gadzuk and H. Metiu, "Theory of electron-hole pair excitations in unimolecular processes at metal surfaces. I. X-ray edge effects," Phys. Rev. B **22**, 2603–2613 (1980).

[129] H. Metiu and J. W. Gadzuk, "Theory of rate processes at metal surfaces. II. The role of substrate electronic excitations," The Journal of Chemical Physics **74**, 2641–2653 (1981).

[130] B. Gumhalter and S. G. Davison, "Effect of electronic relaxation on covalent adsorption reaction rates," Phys. Rev. B **30**, 3179–3190 (1984).

[131] H. Nienhaus, "Electronic excitations by chemical reactions on metal surfaces," Surface Science Reports **45**, 1–78 (2002).

[132] A. M. Wodtke, D. Matsiev, and D. J. Auerbach, "Energy transfer and chemical dynamics at solid surfaces: The special role of charge transfer," Progress in Surface Science **83**, 167–214 (2008).

[133] E. Hasselbrink, "Non-adiabaticity in surface chemical reactions," Surface Science **603**, 1564–1570 (2009).

[134] N. Bartels, K. Golibrzuch, C. Bartels, L. Chen, D. J. Auerbach, A. M. Wodtke, and T. Schäfer, "Dynamical steering in an electron transfer surface reaction: Oriented NO(v = 3, 0.08 < Ei < 0.89 eV) relaxation in collisions with a Au(111) surface," The Journal of Chemical Physics **140**, 54710 (2014).

[135] K. Golibrzuch, N. Bartels, D. J. Auerbach, and A. M. Wodtke, "The Dynamics of Molecular Interactions and Chemical Reactions at Metal Surfaces: Testing the Foundations of Theory," Annual Review of Physical Chemistry **66**, 399–425 (2015).

[136] A. M. Wodtke, "Electronically non-adiabatic influences in surface chemistry and dynamics," Chemical Society Reviews **45**, 3641–3657 (2016).

[137] R. J. Maurer, B. Jiang, H. Guo, and J. C. Tully, "Mode Specific Electronic Friction in Dissociative Chemisorption on Metal Surfaces: H_2 on Ag(111)," Phys. Rev. Lett. **118**, 256001 (2017).

[138] M. Pavanello, D. J. Auerbach, A. M. Wodtke, M. Blanco-Rey, M. Alducin, and G. J. Kroes, "Adiabatic Energy Loss in Hyperthermal H Atom Collisions with Cu and Au: A Basis for Testing the Importance of Nonadiabatic Energy Loss," Journal of Physical Chemistry Letters **4**, 3735–3740 (2013).

[139] G.-J. Kroes, M. Pavanello, M. Blanco-Rey, M. Alducin, and D. J. Auerbach, "Ab initio molecular dynamics calculations on scattering of hyperthermal H atoms from Cu(111) and Au(111)," The Journal of Chemical Physics **141**, 54705 (2014).

[140] S. M. Janke, D. J. Auerbach, A. M. Wodtke, and A. Kandratsenka, "An accurate full-dimensional potential energy surface for H-Au(111): importance of nonadiabatic electronic excitation in energy transfer and adsorption," Journal of Chemical Physics **143**, 124708 (2015).

[141] S. M. Janke, *Theoretical Description of Hydrogen Atom Scattering off Noble Metals*, Ph.D. thesis, University of Goettingen (2016).

[142] D. Krix, R. Nünthel, and H. Nienhaus, "Generation of hot charge carriers by adsorption of hydrogen and deuterium atoms on a silver surface," Physical Review B **75**, 73410 (2007).

[143] B. Schindler, D. Diesing, and E. Hasselbrink, "Electronic excitations induced by hydrogen surface chemical reactions on gold," J Chem Phys **134**, 34705 (2011).

[144] S. Mukherjee, F. Libisch, N. Large, O. Neumann, L. V. Brown, J. Cheng, J. B. Lassiter, E. A. Carter, P. Nordlander, and N. J. Halas, "Hot electrons do the impossible: plasmon-induced dissociation of H_2 on Au," Nano Letters **13**, 240–247 (2013).

[145] S. Takagi, J.-i. Hoshino, H. Tomono, and K. Tsumuraya, "Electron Transfer from Hydrogen Molecule to Au(111) During Dissociative Adsorption: A First-Principles Study," Journal of the Physical Society of Japan **77**, 54705 (2008).

[146] A. C. Luntz and M. Persson, "How adiabatic is activated adsorption/associative desorption?" The Journal of chemical physics **123**, 74704 (2005).

[147] P. Nieto, E. Pijper, D. Barredo, G. Laurent, R. A. Olsen, E.-J. Baerends, G.-J. Kroes, and D. Farías, "Reactive and Nonreactive Scattering of H2 from a Metal Surface Is Electronically Adiabatic," Science **312**, 86–89 (2006).

[148] J. I. Juaristi, M. Alducin, R. D. Muiño, H. F. Busnengo, and A. Salin, "Role of Electron-Hole Pair Excitations in the Dissociative Adsorption of Diatomic Molecules on Metal Surfaces," Physical Review Letters **100**, 116102 (2008).

[149] A. C. Luntz, I. Makkonen, M. Persson, S. Holloway, D. M. Bird, and M. S. Mizielinski, "Comment on "Role of Electron-Hole Pair Excitations in the Dissociative Adsorption of Diatomic Molecules on Metal Surfaces"," Phys. Rev. Lett. **102**, 109601 (2009).

[150] U. Nielsen, D. Halstead, S. Holloway, and J. K. Nørskov, "The dissociative adsorption of hydrogen: Two-, three-, and four-dimensional quantum simulations," The Journal of Chemical Physics **93**, 2879 (1990).

[151] G. R. Darling and S. Holloway, "Translation-to-vibrational excitation in the dissociative adsorption of D_2," The Journal of Chemical Physics **97**, 734 (1992).

[152] J. Sheng and J. Z. H. Zhang, "Quantum dynamics studies of adsorption and desorption of hydrogen at a Cu(111) surface," The Journal of Chemical Physics **99**, 1373 (1993).

[153] J. Dai, J. Sheng, and J. Z. H. Zhang, "Symmetry and rotational orientation effects in dissociative adsorption of diatomic molecules on metals: H_2 and HD on Cu(111)," The Journal of Chemical Physics **101**, 1555 (1994).

[154] J. Dai and J. Z. H. Zhang, "Steric effect in dissociative chemisorption of hydrogen on Cu," Surface Science **319**, 193–198 (1994).

[155] G. R. Darling and S. Holloway, "Rotational motion and the dissociation of H_2 on Cu(111)," The Journal of Chemical Physics **101**, 3268 (1994).

[156] G. R. Darling and S. Holloway, "Surface temperature effects in the dissociative adsorption of D2/Cu(111) revisited," Surface Science **321**, L189–L194 (1994).

[157] G. R. Darling and S. Holloway, "Dissociation thresholds and the vibrational excitation process in the scattering of H_2," Surface Science **307**, 153–158 (1994).

[158] A. Forni, G. Wiesenekker, E. J. Baerends, and G. F. Tantardini, "The chemisorption of hydrogen on Cu(111): A dynamical study," International Journal of Quantum Chemistry **52**, 1067–1080 (1994).

[159] A. Gross, B. Hammer, M. Scheffler, and W. Brenig, "High-dimensional quantum dynamics of adsorption and desorption of H_2 at Cu(111)." Physical review letters **73**, 3121–3124 (1994).

[160] B. Hammer, M. Scheffler, K. W. Jacobsen, and J. K. Nørskov, "Multidimensional potential energy surface for H_2 dissociation over Cu(111)." Physical review letters **73**, 1400–1403 (1994).

[161] J. Dai and J. Z. H. Zhang, "Quantum adsorption dynamics of a diatomic molecule on surface: Four-dimensional fixed-site model for H_2 on Cu(111)," The Journal of Chemical Physics **102**, 6280 (1995).

[162] A. Forni, G. Wiesenekker, E. J. Baerends, and G. F. Tantardini, "A dynamical study of the chemisorption of molecular hydrogen on the Cu(111) surface," Journal of Physics: Condensed Matter **7**, 7195–7207 (1995).

[163] J. Dai and J. C. Light, "Six dimensional quantum dynamics study for dissociative adsorption of H_2 on Cu(111) surface," The Journal of Chemical Physics **107**, 1676 (1997).

[164] J. Dai and J. C. Light, "The steric effect in a full dimensional quantum dynamics simulation for the dissociative adsorption of H_2 on Cu(111)," The Journal of Chemical Physics **108**, 7816 (1998).

[165] M. F. Somers, S. M. Kingma, E. Pijper, G. J. Kroes, and D. Lemoine, "Six-dimensional quantum dynamics of scattering of (v=0,j=0) H_2 and D_2 from Cu(1 1 1): test of two LEPS potential energy surfaces," Chemical Physics Letters **360**, 390–399 (2002).

References

[166] S. Nave, D. Lemoine, M. F. Somers, S. M. Kingma, and G.-J. Kroes, "Six-dimensional quantum dynamics of (v=0,j=0)D_2 and of (v=1,j=0)H_2 scattering from Cu111." The Journal of chemical physics **122**, 214709 (2005).

[167] C. Díaz, E. Pijper, R. A. Olsen, H. F. Busnengo, D. J. Auerbach, and G. J. Kroes, "Chemically accurate simulation of a prototypical surface reaction: H_2 dissociation on Cu(111)," Science **326**, 832–834 (2009).

[168] C. Díaz, R. A. Olsen, D. J. Auerbach, and G. J. Kroes, "Six-dimensional dynamics study of reactive and non reactive scattering of H_2 from Cu(111) using a chemically accurate potential energy surface," Physical Chemistry Chemical Physics **12**, 6499–6519 (2010).

[169] M. Bonfanti, C. Díaz, M. F. Somers, and G.-J. Kroes, "Hydrogen dissociation on Cu(111): the influence of lattice motion. Part I," Physical Chemistry Chemical Physics **13**, 4552–4561 (2011).

[170] F. Nattino, C. Díaz, B. Jackson, and G.-J. Kroes, "Effect of surface motion on the rotational quadrupole alignment parameter of D_2 reacting on Cu(111)." Physical review letters **108**, 236104 (2012).

[171] M. Wijzenbroek and M. F. Somers, "Static surface temperature effects on the dissociation of H_2 and D_2 on Cu(111)." The Journal of chemical physics **137**, 54703 (2012).

[172] A. S. Muzas, J. I. Juaristi, M. Alducin, R. Díez Muiño, G. J. Kroes, and C. Díaz, "Vibrational deexcitation and rotational excitation of H_2 and D_2 scattered from Cu(111): adiabatic versus non-adiabatic dynamics." The Journal of chemical physics **137**, 64707 (2012).

[173] M. Bonfanti, M. F. Somers, C. Díaz, H. F. Busnengo, and G.-J. Kroes, "7D Quantum Dynamics of H2 Scattering from Cu(111): The Accuracy of the Phonon Sudden Approximationy," Zeitschrift für Physikalische Chemie **227**, 1397 (2013).

[174] S. B. Donald and I. Harrison, "Rice–Ramsperger–Kassel–Marcus Simulation of Hydrogen Dissociation on Cu(111): Addressing Dynamical Biases, Surface Temperature, and Tunneling," The Journal of Physical Chemistry C **118**, 320–337 (2014).

[175] F. Nattino, A. Genova, M. Guijt, A. S. Muzas, C. Díaz, D. J. Auerbach, and G.-J. Kroes, "Dissociation and recombination of D_2 on Cu(111): ab initio molecular dynamics calculations and improved analysis of desorption experiments," J Chem Phys **141**, 124705 (2014).

[176] G. Comsa and R. David, "The purely "fast" distribution of H_2 and D_2 molecules desorbing from Cu(100) and Cu(111) surfaces," Surface Science **117**, 77–84 (1982).

[177] G. D. Kubiak, "Dynamics of recombinative desorption of H_2 and D_2 from Cu(110), Cu(111), and sulfur-covered Cu(111)," Journal of Vacuum Science and Technology A: Vacuum, Surfaces, and Films **3**, 1649 (1985).

[178] G. Anger, A. Winkler, and K. D. Rendulic, "Adsorption and desorption kinetics in the systems H_2/Cu(111), H_2/Cu(110) and H_2/Cu(100)," Surface Science **220**, 1–17 (1989).

[179] B. E. Hayden and C. L. Lamont, "Coupled translational-vibrational activation in dissociative hydrogen adsorption on Cu(110)." Physical review letters **63**, 1823–1825 (1989).

[180] B. E. Hayden and C. L. A. Lamont, "Vibrational and translational energy partition and the barrier to dissociative H_2 and D_2 adsorption on Cu(110)," Surface Science **243**, 31–42 (1991).

[181] H. A. Michelsen, C. T. Rettner, and D. J. Auerbach, "On the influence of surface temperature on adsorption and desorption in the D_2/Cu(111) system," Surface Science **272**, 65–72 (1992).

[182] H. A. Michelsen, C. T. Rettner, and D. J. Auerbach, "State-specific dynamics of D_2 desorption from Cu(111): The role of molecular rotational motion in activated adsorption-desorption dynamics." Physical review letters **69**, 2678–2681 (1992).

[183] C. T. Rettner, D. J. Auerbach, and H. A. Michelsen, "Role of vibrational and translational energy in the activated dissociative adsorption of D_2 on Cu(111)," Physical Review Letters **68**, 1164–1167 (1992).

[184] C. T. Rettner, D. J. Auerbach, and H. A. Michelsen, "Observation of direct vibrational excitation in collisions of H_2 and D_2 with a Cu(111) surface," Physical Review Letters **68**, 2547–2550 (1992).

[185] H. A. Michelsen, C. T. Rettner, D. J. Auerbach, and R. N. Zare, "Effect of rotation on the translational and

vibrational energy dependence of the dissociative adsorption of D_2 on Cu(111)," The Journal of Chemical Physics **98**, 8294 (1993).

[186] C. T. Rettner, H. A. Michelsen, and D. J. Auerbach, "From quantum-state-specific dynamics to reaction rates: the dominant role of translational energy in promoting the dissociation of D_2 on Cu(111) under equilibrium conditions," Faraday Discussions **96**, 17–31 (1993).

[187] C. T. Rettner, H. A. Michelsen, and D. J. Auerbach, "Determination of quantum-state-specific gas—surface energy transfer and adsorption probabilities as a function of kinetic energy," Chemical Physics **175**, 157–169 (1993).

[188] C. T. Rettner and D. J. Auerbach, "Distinguishig the Direct and Indirect Products of a Gas-Surface Reaction," Science **263**, 365–367 (1994).

[189] C. T. Rettner, H. A. Michelsen, and D. J. Auerbach, "Quantum-state-specific dynamics of the dissociative adsorption and associative desorption of H_2 at a Cu(111) surface," The Journal of Chemical Physics **102**, 4625 (1995).

[190] S. J. Gulding, A. M. Wodtke, H. Hou, C. T. Rettner, H. A. Michelsen, and D. J. Auerbach, "Alignment of D_2(v, J) desorbed from Cu(111): Low sensitivity of activated dissociative chemisorption to approach geometry," The Journal of Chemical Physics **105**, 9702 (1996).

[191] D. Wetzig, M. Rutkowski, R. David, and H. Zacharias, "Rotational corrugation in associative desorption of D_2 from Cu(111)," Europhysics Letters (EPL) **36**, 31–36 (1996).

[192] H. Hou, S. J. Gulding, C. T. Rettner, A. M. Wodtke, and D. J. Auerbach, "The Stereodynamics of a Gas-Surface Reaction," Science **277**, 80 LP–82 (1997).

[193] M. J. Murphy and A. Hodgson, "Adsorption and desorption dynamics of H_2 and D_2 on Cu(111): The role of surface temperature and evidence for corrugation of the dissociation barrier," The Journal of Chemical Physics **108**, 4199 (1998).

[194] M. J. Murphy, J. F. Skelly, and A. Hodgson, "Nitrogen recombination dynamics at Cu(111): Rotational energy release and product angular distributions," The Journal of Chemical Physics **109**, 3619 (1998).

[195] C. T. Rettner, "Dynamical studies of the interaction of D_2 with a Cu(111) surface," Journal of Vacuum Science and Technology A: Vacuum, Surfaces, and Films **10**, 2282 (1992).

[196] C. T. Rettner, H. A. Michelsen, D. J. Auerbach, and C. B. Mullins, "Dynamics of recombinative desorption: Angular distributions of H_2, HD, and D_2 desorbing from Cu(111)," The Journal of Chemical Physics **94**, 7499 (1991).

[197] D. Wetzig, M. Rutkowski, W. Etterich, R. David, and H. Zacharias, "Rotational alignment in associative desorption of H_2 from Pd(100)," Surface Science **402-404**, 232–235 (1998).

[198] Ž. Šljivančanin and B. Hammer, "H_2 dissociation at defected Cu: Preference for reaction at vacancy and kink sites," Physical Review B **65**, 85414 (2002).

[199] I. M. N. Groot, A. W. Kleyn, and L. B. F. Juurlink, "Separating Catalytic Activity at Edges and Terraces on Platinum: Hydrogen Dissociation," The Journal of Physical Chemistry C **117**, 9266–9274 (2013).

[200] D. A. McCormack, R. A. Olsen, and E. J. Baerends, "Mechanisms of H_2 dissociative adsorption on the Pt(211) stepped surface," The Journal of Chemical Physics **122**, 194708 (2005).

[201] M. Wijzenbroek, D. Helstone, J. Meyer, and G.-J. Kroes, "Dynamics of H_2 dissociation on the close-packed (111) surface of the noblest metal: H_2 + Au(111)," The Journal of Chemical Physics **145**, 144701 (2016).

[202] L. Stobiński and R. Duś, "Atomic hydrogen adsorption on thin gold films," Surface Science **269**, 383–388 (1992).

[203] L. Stobiński and R. Duś, "Model of atomic hydrogen adsorption on thin gold film surface," Vacuum **45**, 299–301 (1994).

[204] M. Pan, A. J. Brush, Z. D. Pozun, H. C. Ham, W. Y. Yu, G. Henkelman, G. S. Hwang, and C. B. Mullins, "Model studies of heterogeneous catalytic hydrogenation reactions with gold," Chem Soc Rev **42**, 5002–5013 (2013).

References

[205] J. A. White, D. M. Bird, M. C. Payne, and I. Stich, "Surface Corrugation in the Dissociative Adsorption of H_2 on Cu(100)," Phys. Rev. Lett. **73**, 1404–1407 (1994).

[206] J. P. Perdew, J. A. Chevary, S. H. Vosko, K. A. Jackson, M. R. Pederson, D. J. Singh, and C. Fiolhais, "Atoms, molecules, solids, and surfaces: Applications of the generalized gradient approximation for exchange and correlation," Phys. Rev. B **46**, 6671–6687 (1992).

[207] J. Perdew, J. Chevary, S. Vosko, K. Jackson, M. Pederson, D. Singh, and C. Fiolhais, "Erratum: Atoms, molecules, solids, and surfaces: Applications of the generalized gradient approximation for exchange and correlation," Physical Review B **48**, 4978–4978 (1993).

[208] J. P. Perdew, K. Burke, and M. Ernzerhof, "Generalized Gradient Approximation Made Simple," Phys. Rev. Lett. **77**, 3865–3868 (1996).

[209] B. Hammer, L. B. Hansen, and J. K. Nørskov, "Improved adsorption energetics within density-functional theory using revised Perdew-Burke-Ernzerhof functionals," Phys. Rev. B **59**, 7413–7421 (1999).

[210] Y.-Y. Chuang, M. L. Radhakrishnan, P. L. Fast, C. J. Cramer, and D. G. Truhlar, "Direct Dynamics for Free Radical Kinetics in Solution: Solvent Effect on the Rate Constant for the Reaction of Methanol with Atomic Hydrogen," The Journal of Physical Chemistry A **103**, 4893–4909 (1999).

[211] R. Car and M. Parrinello, "Unified Approach for Molecular Dynamics and Density-Functional Theory," Phys. Rev. Lett. **55**, 2471–2474 (1985).

[212] M. D and H. J, *Ab Initio Molecular Dynamics: Basic Theory and Advanced Methods* (Cambridge Univ. Press, Cambridge, UK, 2009).

[213] M. Karplus, R. N. Porter, and R. D. Sharma, "Exchange Reactions with Activation Energy. I. Simple Barrier Potential for (H, H$_2$)," The Journal of Chemical Physics **43**, 3259–3287 (1965).

[214] M. Karikorpi, S. Holloway, N. Henriksen, and J. K. Nørskov, "Dynamics of molecule-surface interactions," Surface Science **179**, L41 – L48 (1987).

[215] K. Gundersen, K. W. Jacobsen, J. K. Nørskov, and B. Hammer, "The energetics and dynamics of H$_2$ dissociation on Al(110)," Surface Science **304**, 131–144 (1994).

[216] H. E. Pfnür, C. T. Rettner, J. Lee, R. J. Madix, and D. J. Auerbach, "Dynamics of the activated dissociative chemisorption of N2 on W(110): A molecular beam study," The Journal of Chemical Physics **85**, 7452 (1986).

[217] P. M. Holmblad, J. Wambach, and I. Chorkendorff, "Molecular beam study of dissociative sticking of methane on Ni(100)," The Journal of Chemical Physics **102**, 8255 (1995).

[218] A. C. Luntz, "CH4 dissociation on Ni(100): Comparison of a direct dynamical model to molecular beam experiments," The Journal of Chemical Physics **102**, 8264 (1995).

[219] P. M. Hundt, B. Jiang, M. E. van Reijzen, H. Guo, and R. D. Beck, "Vibrationally Promoted Dissociation of Water on Ni(111)," Science **344**, 504–507 (2014).

[220] Q. Shuai, S. Kaufmann, D. J. Auerbach, D. Schwarzer, and A. M. Wodtke, "Evidence for Electron–Hole Pair Excitation in the Associative Desorption of H2 and D2 from Au(111)," The Journal of Physical Chemistry Letters **5**, 1657–1663 (2017), weblink: http://pubs.acs.org/doi/full/10.1021/acs.jpclett.7b00265.

[221] A. Gross, S. Wilke, and M. Scheffler, "Six-Dimensional Quantum Dynamics of Adsorption and Desorption of H$_2$ at Pd(100): Steering and Steric Effects," Physical Review Letters **75**, 2718–2721 (1995).

[222] M. Kay, G. R. Darling, S. Holloway, J. A. White, and D. M. Bird, "Steering effects in non-activated adsorption," Chemical Physics Letters **245**, 311–318 (1995).

[223] M. Gostein and G. O. Sitz, "Rotational state-resolved sticking coefficients for H$_2$ on Pd(111): Testing dynamical steering in dissociative adsorption," The Journal of Chemical Physics **106**, 7378–7390 (1997).

[224] G. R. Darling, M. Kay, and S. Holloway, "The steering of molecules in simple dissociation reactions," Surface Science **400**, 314–328 (1998).

[225] N. Shenvi, S. Roy, and J. C. Tully, "Dynamical Steering and Electronic Excitation in NO Scattering from a Gold Surface," Science **326**, 829–832 (2009).

[226] P. Kisliuk, "The Sticking Probabilities of Gases Chemisorbed on the Surfaces of Solids," Journal of Physics and Chemistry of Solids **3**, 95–101 (1957).

[227] J. V. Barth, H. Brune, G. Ertl, and R. J. Behm, "Scanning tunneling microscopy observations on the reconstructed Au(111) surface: Atomic structure, long-range superstructure, rotational domains, and surface defects," Physical Review B **42**, 9307–9318 (1990).

[228] K. G. Huang, D. Gibbs, D. M. Zehner, A. R. Sandy, and S. G. J. Mochrie, "Phase behavior of the Au(111) surface: Discommensurations and kinks," Physical Review Letters **65**, 3313–3316 (1990).

[229] A. R. Sandy, S. G. J. Mochrie, D. M. Zehner, K. G. Huang, and D. Gibbs, "Structure and phases of the Au(111) surface: X-ray-scattering measurements," Physical Review B **43**, 4667–4687 (1991).

[230] A. R. Sandy, S. G. J. Mochrie, D. M. Zehner, G. Grübel, K. G. Huang, and D. Gibbs, "Au(111) and Pt(111) surface phase behavior," Surface Science **287**, 321–324 (1993).

[231] V. R. Lecoeur, J. M. Berroir, S. Rousset, and J, "Interaction between steps and reconstruction on Au(111)," EPL (Europhysics Letters) **47**, 435 (1999).

[232] S. Narasimhan and D. Vanderbilt, "Elastic stress domains and the herringbone reconstruction on Au(111)," Physical Review Letters **69**, 1564–1567 (1992).

[233] G. M. Watson, D. Gibbs, S. Song, A. R. Sandy, S. G. J. Mochrie, and D. M. Zehner, "Faceting and reconstruction of stepped Au(111)," Physical Review B **52**, 12329–12344 (1995).

[234] P. Kowalczyk, W. Kozlowski, Z. Klusek, W. Olejniczak, and P. K. Datta, "STM studies of the reconstructed Au(111) thin-film at elevated temperatures," Applied Surface Science **253**, 4715–4720 (2007).

[235] Y. Liu and V. Ozolins, "Self-Assembled Monolayers on Au(111): Structure, Energetics, and Mechanism of Reconstruction Lifting," The Journal of Physical Chemistry C **116**, 4738–4747 (2012).

[236] F. Hanke and J. Björk, "Structure and local reactivity of the Au(111) surface reconstruction," Physical Review B **87**, 235422 (2013).

[237] A. Hoss, M. Nold, P. von Blanckenhagen, and O. Meyer, "Roughening and melting of Au(110) surfaces," Phys. Rev. B **45**, 8714–8720 (1992).

[238] K. H. Chae, H. C. Lu, and T. Gustafsson, "Medium-energy ion-scattering study of the temperature dependence of the structure of Cu(111)," Phys. Rev. B **54**, 14082–14086 (1996).

[239] H. Häkkinen and M. Manninen, "Computer simulation of disordering and premelting of low-index faces of copper," Phys. Rev. B **46**, 1725–1742 (1992).

[240] A. N. Al-Rawi, A. Kara, and T. S. Rahman, "Comparative study of anharmonicity: Ni(111), Cu(111), and Ag(111)," Phys. Rev. B **66**, 165439 (2002).

[241] T. D. Daff, I. Saadoune, I. Lisiecki, and N. H. de Leeuw, "Computer simulations of the effect of atomic structure and coordination on the stabilities and melting behaviour of copper surfaces and nano-particles," Surface Science **603**, 445–454 (2009).

[242] W. Van Willigen, "Angular distribution of hydrogen molecules desorbed from metal surfaces," Physics Letters A **28**, 80–81 (1968).

[243] M. Balooch and R. E. Stickney, "Angular Distributions of H_2 Desorbed From The (100), (110), And (111) Faces of Copper Crystals," Surface Science **44**, 310–320 (1974).

[244] I. Čadež, R. I. Hall, M. Landau, F. Pichou, and C. Schermann, "The influence of a thin gold film on vibrational excitation of hydrogen molecules," The Journal of Chemical Physics **106**, 4745–4752 (1997).

[245] S. A. Steward, *Review of Hydrogen Isotope Permeability Through Materials*, Tech. Rep. (Lawrence Livermore National Laboratory, Livermore, 1983).

[246] O. D. Gonzales, "-," Transactions of the Metallurgical Society of AIME **239**, 929 (1967).

[247] W. G. Perkins and D. R. Begeal, "Permeation and diffusion of hydrogen in ceramvar, copper, and ceramvar-copper laminates," Berichte der Bunsengesellschaft für physikalische Chemie **76**, 863 (1972).

[248] R. B. McLellan, "Solid solutions of hydrogen in gold, silver and copper," Journal of Physics and Chemistry of Solids **34**, 1137–1141 (1973).

References

[249] D. R. Begeal, "Hydrogen and deuterium permeation in copper alloys, copper–gold brazing alloys, gold, and the in situ growth of stable oxide permeation barriers," Journal of Vacuum Science and Technology **15**, 1146–1154 (1978).

[250] L. Sementa, M. Wijzenbroek, B. J. van Kolck, M. F. Somers, A. Al-Halabi, H. F. Busnengo, R. A. Olsen, G. J. Kroes, M. Rutkowski, C. Thewes, N. F. Kleimeier, H. Zacharias, B. J. van Kolck, M. F. Somers, A. Al-Halabi, H. F. Busnengo, R. A. Olsen, G. J. Kroes, M. Rutkowski, C. Thewes, N. F. Kleimeier, and H. Zacharias, "Reactive scattering of H_2 from Cu(100): Comparison of dynamics calculations based on the specific reaction parameter approach to density functional theory with experiment," The Journal of Chemical Physics **138**, 44708 (2013).

[251] J. M. Hollas, *Modern Spectroscopy*, 4th ed. (WILEY-VCH Verlag, Chippenham, 2010).

[252] E. E. Marinero, C. T. Rettner, and R. N. Zare, "Quantum-state-specific detection of molecular hydrogen by three-photon ionization," Physical Review Letters **48**, 1323–1326 (1982).

[253] W. M. Huo, K. Rinnen, and R. N. Zare, "Rotational and vibrational effects in the E 1Σ+g–X 1Σ+g two-photon transitions of H2, HD, and D2," The Journal of Chemical Physics **95**, 205–213 (1991).

[254] K.-D. Rinnen, M. A. Buntine, D. A. V. Kliner, and R. N. Zare, "Quantitative determination of H_2, HD, and D_2 internal-state distributions by (2+1) resonance-enhanced multiphoton ionization," The Journal of Chemical Physics **95**, 214–225 (1991).

[255] A. E. Pomerantz, F. Ausfelder, R. N. Zare, and W. M. Huo, "Line strength factors for E,F$^1\Sigma_g^+$ $(v' = 0, J'' = J')$ − X$^1\Sigma_g^+$ (v'', J'') $(2 + 1)$ REMPI transitions in molecular hydrogen," Canadian Journal of Chemistry **82**, 723–729 (2004).

[256] W. Demtröder, *Laserspektroskopie: Grundlagen und Techniken*, 5th ed. (Springer Verlag, Berlin, 2007).

[257] M. R. Cervenan and N. R. Isenor, "Multiphoton ionization yield curves for gaussian laser beams," Optics Communications **13**, 175–178 (1975).

[258] J. A. Arnaud, W. M. Hubbard, G. D. Mandeville, B. de la Clavière, E. A. Franke, and J. M. Franke, "Technique for Fast Measurement of Gaussian Laser Beam Parameters," Applied Optics **10**, 2775–2776 (1971).

[259] P. B. Chapple, "Beam waist and M^2 measurement using a finite slit," Optical Engineering **33**, 2461–2466 (1994).

[260] F.-W. Sheu and C.-H. Chang, "Measurement of the intensity profile of a Gaussian laser beam near its focus using an optical fiber," American Journal of Physics **75**, 956–959 (2007).

[261] M. A. de Araújo, R. Silva, E. de Lima, D. P. Pereira, and P. C. de Oliveira, "Measurement of Gaussian laser beam radius using the knife-edge technique: improvement on data analysis," Appl. Opt. **48**, 393–396 (2009).

[262] I. C. M. Littler, E. G. Atkinson, and P. J. Manson, "Non-contact aperture area measurement by occlusion of a laser beam," Metrologia **50**, 596 (2013).

[263] Y. Qin, T. Nakajima, H. Zen, X. Wang, T. Kii, and H. Ohgaki, "Characterization of non-Gaussian mid-infrared free-electron laser beams by the knife-edge method," Infrared Physics and Technology **66**, 146–151 (2014).

[264] D. J. Manura and D. A. Dahl, *SIMION Version 8.0/8.1 User Manual*, revision 5 ed. (Scientific Instrument Services, Inc., Ringoes, NJ, 2011).

[265] "Autodesk Inventor Professional," (2015).

[266] G. R. Darling and S. Holloway, "The role of parallel momentum in the dissociative adsorption of H_2 at highly corrugated surfaces," Surface Science **304**, L461 – L467 (1994).

[267] J. D. Beckerle, A. D. Johnson, and S. T. Ceyer, "Observation and Mechanism of Collision-Induced Desorption: CH_4 on Ni(111)," Phys. Rev. Lett. **62**, 685–688 (1989).

[268] "Python, v.3.5.1 64bits," (2015).

[269] K. Levenberg, "A Method for the Solution of Certain Non-Linear Problems in Least Squares," The Quarterly of Applied Mathematics , 164–168 (1944).

[270] D. Marquardt, "An Algorithm for Least-Squares Estimation of Nonlinear Parameters," Journal of the Society for Industrial and Applied Mathematics **11**, 431–441 (1963).

[271] M. Newville, T. Stensitzki, D. B. Allen, and A. Ingargiola, "LMFIT: Non-Linear Least-Square Minimization and Curve-Fitting for Python," (2014).

[272] Parametric Technology Corporation, "Mathcad, v.15.0," (2011).

[273] OriginLab Corporation, "OriginPro, v.9.1.0 (64bit)," (2013).

[274] Corel Corporation, "CorelDRAW X6, v.16.0.0.707," (2012).

[275] W. L. Schaich, "Energy and Angle Dependence of Desorption Spectra," Physics Letters **64A**, 133–135 (1977).

[276] L. Schroter, C. Trame, J. Gauer, H. Zacharias, R. David, and W. Brenig, "State-selective studies of the associative desorption of hydrogen from Pd(100) and Cu(100)," Faraday Discussions **96**, 55–65 (1993).

[277] M. Kummer and J. R. Kirchhoff, "Graphite-coated metal mesh optically transparent electrodes," Analytical Chemistry **65**, 3720–3725 (1993).

[278] L. H. Jenkins and M. F. Chung, "LEED and Auger investigations of Cu (111) surface," Surface Science **24**, 125–139 (1971).

[279] R. W. Joyner and M. W. Roberts, "Auger electron spectroscopy studies of clean polycrystalline gold and of the adsorption of mercury on gold," J. Chem. Soc.{,} Faraday Trans. 1 **69**, 1242–1250 (1973).

[280] K. D. Childs, B. A. Carlson, L. A. LaVanier, J. F. Moulder, D. F. Paul, W. F. Stickle, and D. G. Watson, *Handbook of Auger Electron Spectroscopy*, 3rd ed., edited by C. L. Hedberg (Physical Electronics, Inc., 1995).

[281] A. T. D'Agostino and P. N. Ross, "LEED/electrochemical analysis of Au single crystals: Stability of the UHV prepared surfaces of Au(111) and Au(100) in aqueous electrolyte," Surface Science **185**, 88–104 (1987).

[282] J. S. Tsay, A. B. Yang, C. N. Wu, and F. S. Shiu, "Investigations of surface structure for thermally evaporated silicon on a Cu(111) surface," Thin Solid Films **515**, 8285–8289 (2007).

[283] G. M. McGuirk, H. Shin, M. Caragiu, S. Ash, P. K. Bandyopadhyay, R. H. Prince, and R. D. Diehl, "Au(111) surface structures induced by adsorption: {LEED} I(E) analysis of (1 × 1) and (5 × 5) Au(111)–S phases," Surface Science **610**, 42–47 (2013).

[284] A. Riemann, B. N. Satterwhite, and B. E. Owens, "Metallic thin film growth on vicinal Cu substrates," Surface Science **604**, 2157–2162 (2010).

[285] V. F. Sears and S. A. Shelley, "Debye-Waller factor for elemental crystals," Acta Crystallographica Section A **47**, 441–446 (1991).

[286] W. L. Wiese and J. R. Fuhr, "Accurate Atomic Transition Probabilities for Hydrogen, Helium, and Lithium," Journal of Physical and Chemical Reference Data **38**, 565–720 (2009).

[287] U. Leuthäusser, "Kinetic theory of desorption: Energy and angular distributions," Zeitschrift für Physik B Condensed Matter **50**, 65–69 (1983).

[288] K. Doblhoff-Dier, J. Meyer, P. E. Hoggan, and G.-J. Kroes, "Quantum Monte Carlo Calculations on a Benchmark Molecule–Metal Surface Reaction: H_2 + Cu(111)," Journal of Chemical Theory and Computation **13**, 3208–3219 (2017).

[289] N. C. M. Bartlett, D. J. Miller, R. N. Zare, D. Sofikitis, T. P. Rakitzis, and A. J. Alexander, "Preparation of oriented and aligned H2 and HD by stimulated Raman pumping," The Journal of Chemical Physics **129**, 84312 (2008).

[290] D. C. Jacobs, R. J. Madix, and R. N. Zare, "Reduction of 1+1 resonance enhanced MPI spectra to population distributions: Application to the NO A 2Σ+–X 2Π system," The Journal of Chemical Physics **85**, 5469–5479 (1986).

[291] F. Libisch, J. Cheng, and E. A. Carter, "Electron-Transfer-Induced Dissociation of H2 on Gold Nanoparticles: Excited-State Potential Energy Surfaces via Embedded Correlated Wavefunction Theory," Zeitschrift für Physikalische Chemie **227**, 1455 (2013).

References

[292] W. Kołos, K. Szalewicz, and H. J. Monkhorst, "New Born–Oppenheimer potential energy curve and vibrational energies for the electronic ground state of the hydrogen molecule," The Journal of Chemical Physics **84**, 3278–3283 (1986).

[293] A. Mondal, M. Wijzenbroek, M. Bonfanti, C. Díaz, and G.-J. Kroes, "Thermal Lattice Expansion Effect on Reactive Scattering of H2 from Cu(111) at Ts = 925 K," The Journal of Physical Chemistry A **117**, 8770–8781 (2013).

[294] A. Marashdeh, S. Casolo, L. Sementa, H. Zacharias, and G.-J. Kroes, "Surface Temperature Effects on Dissociative Chemisorption of H$_2$ on Cu(100)," The Journal of Physical Chemistry C **117**, 8851–8863 (2013).

[295] D. Krix, R. Nünthel, and H. Nienhaus, "Chemical interaction of H and D atoms with Ag/H:p-Si(111) thin film diodes," Journal of Vacuum Science and Technology A: Vacuum, Surfaces, and Films **25**, 1156–1160 (2007).

[296] J. R. Trail, D. M. Bird, M. Persson, and S. Holloway, "Electron–hole pair creation by atoms incident on a metal surface," The Journal of Chemical Physics **119**, 4539–4549 (2003).

[297] C. Díaz and R. A. Olsen, "A note on the vibrational efficacy in molecule-surface reactions," The Journal of Chemical Physics **130**, 94706 (2009).

[298] P. J. Feibelman, "First-principles step- and kink-formation energies on Cu(111)," Physical Review B **60**, 11118–11122 (1999).

[299] D. C. Schlößer, L. K. Verheij, G. Rosenfeld, and G. Comsa, "Determination of Step Free Energies from Island Shape Fluctuations on Metal Surfaces," Physical Review Letters **82**, 3843–3846 (1999).

[300] G. Schulze Icking-Konert, M. Giesen, and H. Ibach, "Novel Method for the Experimental Determination of Step Energies," Physical Review Letters **83**, 3880–3883 (1999).

[301] J.-M. Zhang, Y.-N. Wen, and K.-W. Xu, "Calculation of the formation energies of isolated vacancy and adatom–vacancy pair at low-index surfaces of fcc metals with MAEAM," Applied Surface Science **253**, 3779–3784 (2007).

[302] G. Grochola, J. du Plessis, I. K. Snook, and S. P. Russo, "On the computational calculation of adatom, vacancy and early stage surface nucleation island free energies on the (111) copper surface," Surface Science **591**, 32–37 (2005).

[303] K. L. Haug, T. Bürgi, T. R. Trautman, and S. T. Ceyer, "Distinctive Reactivities of Surface-Bound H and Bulk H for the Catalytic Hydrogenation of Acetylene," Journal of the American Chemical Society **120**, 8885–8886 (1998).

[304] P. B. Lloyd, M. Swaminathan, J. W. Kress, and B. J. Tatarchuk, "Temperature programmed desorption study of the adsorption and absorption of hydrogen on and in Cu(111)," Applied Surface Science **119**, 267–274 (1997).

[305] M. F. Luo, D. A. MacLaren, I. G. Shuttleworth, and W. Allison, "Preferential sub-surface occupation of atomic hydrogen on Cu(111)," Chemical Physics Letters **381**, 654–659 (2003).

[306] M. F. Luo, D. A. MacLaren, and W. Allison, "Migration and abstraction of H-atoms from the Cu(1 1 1) surface," Surface Science **586**, 109–114 (2005).

[307] M. F. Luo and G. R. Hu, "Coverage-dependent absorption of atomic hydrogen into the sub-surface of Cu(111) studied by density-functional-theory calculations," Surface Science **603**, 1081–1086 (2009).

[308] K. Mudiyanselage, Y. Yang, F. M. Hoffmann, O. J. Furlong, J. Hrbek, M. G. White, P. Liu, and D. J. Stacchiola, "Adsorption of hydrogen on the surface and sub-surface of Cu(111)," The Journal of Chemical Physics **139**, 44712 (2013).

[309] A. Hellman, K. Svensson, and S. Andersson, "Hydrogen-Induced Reconstruction of Cu(100): Two-Dimensional and One-Dimensional Structures of Surface Hydride," The Journal of Physical Chemistry C **118**, 15773–15778 (2014).

[310] T. M. T. Huynh and P. Broekmann, "From In Situ towards In Operando Conditions: Scanning Tunneling Microscopy Study of Hydrogen Intercalation in Cu(111) during Hydrogen Evolution," ChemElectroChem **1**, 1271–1274 (2014).

[311] M. Hand and S. Holloway, "The scattering of H_2 and D_2 from Cu(100): Vibrationally assisted dissociative adsorption," Surface Science **211**, 940–947 (1989).

[312] J. C. Polanyi and W. H. Wong, "Location of energy barriers. I. Effect on the dynamics of reactions A + BC," The Journal of Chemical Physics **51**, 1439–1450 (1969).

[313] J. C. Polanyi, "Concepts in reaction dynamics," Accounts of Chemical Research **5**, 161–168 (1972).

[314] J. C. Polanyi, "Some concepts in reaction dynamics," Science **236**, 680–690 (1987).

[315] O. V. Ogorodnikova, "Comparison of hydrogen gas–, atom– and ion–metal interactions," Journal of Nuclear Materials **277**, 130–142 (2000).

[316] M. L. Zheludkevich, A. G. Gusakov, A. G. Voropaev, E. N. Kozyrski, S. A. Raspopov, and A. A. Vecher, ""Superpermeability" and "pumping" of atomic hydrogen through palladium membranes," Journal of Membrane Science **320**, 528–532 (2008).

[317] V. J. Kehrer and H. J. R. Leidheiser, "The Phase Transformation of Cobalt as Observed on Single Crystals," The Journal of Chemical Physics **21**, 570 (1953).

[318] G. L. P. Berning, "LEED studies on the (0001) surface of cobalt," Surface Science **61**, 673–677 (1976).

[319] M. E. Bridge, C. M. Comrie, and R. M. Lambert, "Hydrogen chemisorption and the carbon monoxide-hydrogen interaction on cobalt (0001)," Journal of Catalysis **58**, 28–33 (1979).

[320] I. Dabrowski, "The Lyman and Werner bands of H_2," Canadian Journal of Physics **62**, 1639–1664 (1984).

[321] K. P. Huber and G. Herzberg, "Constants of Diatomic Molecules," (1979).

[322] D. Bailly, E. J. Salumbides, M. Vervloet, and W. Ubachs, "Accurate level energies in the $EF^1\Sigma_g^+$, $GK^1\Sigma_g^+$, $H^1\Sigma_g^+$, $B^1\Sigma_u^+$, $C^1\Pi_u$, $B'^1\Sigma_u^+$, $D^1\Pi_u$, $I^1\Pi_g$, $J^1\Delta_g$ states of H_2," Molecular Physics **108**, 827–846 (2010).

[323] P. J. Mohr, D. B. Newell, and B. N. Taylor, "CODATA recommended values of the fundamental physical constants: 2014," Rev. Mod. Phys. **88**, 35009 (2016).

Part IV

Appendices

Appendix A

List of Figures

Appendix B

List of Tables

Appendix C

Spectroscopic Constants

The values of the spectroscopic constants relevant for this work (cf. section 8.2.5.1) are given in tables C.1 and C.2. These quantities are used to describe the energies in the model of the molecules as linear rotor, including centrifugal distortion and the inharmonic oscillator model: electronic energy in equilibrium position (T_{eq}), rotational constant in equilibrium position (B_{eq}), first anharmonic term in equilibrium position (a_{eq}), centrifugal distortion constant in equilibrium position (D_{eq}), vibrational constant in equilibrium position - first term (w_{eq}), vibrational constant in equilibrium position - second term $(w_{eq}x_{eq})$ and vibrational constant in equilibrium position - third term $(w_{eq}y_{eq})$.

Table C.1: Spectroscopic constants of hydrogen isotopologues in their electronic ground state, X $^1\Sigma_g^+$.[320,321]. All values are given in cm^{-1}.

Constant	H$_2$	HD	D$_2$
B_{eq}	60.853	45.655	30.443
a_{eq}	3.062	1.986	1.0786
D_{eq}	0.0471	0.026	0.01141
w_{eq}	4401.21	3813.1	3115.5
$w_{eq}x_{eq}$	121.33	91.65	61.82
$w_{eq}y_{eq}$	0	0	0.562

Table C.2: Spectroscopic constants of hydrogen isotopologues for the E,F $^1\Sigma_g^+$ double-well state [320–322]. All values are given in cm^{-1}.

Constant	H$_2$	HD	D$_2$
T_{eq}	97893.962	100104	99461.44
B_{eq}	32.68	24.568	16.369
a_{eq}	1.818	1.288	0.6764
D_{eq}	0.0228	0.0123	0.0054
w_{eq}	2588.9	2204.4	1784.42
$w_{eq}x_{eq}$	130.5	81.6	48.1
$w_{eq}y_{eq}$	0	0	0

Appendix D

Tables of Obtained Parameters

e

D.1 Comprehensive Tables of Parameters Obtained from Fitting

In the following section the parameters describing the measured distributions are reported. Results for different samples are presented in according subchapters.

The obtained quantum state specific TOF distributions were analyzed in terms of detailed balance, see section 8.3.1. Adsorption probability functions were fitted with the error function eq. (8.4) for the fast channel, with an exponential function eq. (8.7) for the slow channel, and the thermal background contribution (see section 10.1.5) for ($v = 0$) states. The corresponding amplitudes are denoted A_{Erf}, A_{Exp} and A_{BG}, respectively. It is noted that A_{Erf}-parameters are on a relative scale for each isotopologue and sample. A_{Exp} and A_{BG} parameters are scaled relative to A_{Erf}. All resulting parameters are reported with their standard deviations (1σ, denoted by Δ). The algorithm used was the "lmfit" [271] module in python.

D.1.1 Cu(111)

The surface temperature (T_s) for all values reported in these tables was $(923 \pm 2)\,\mathrm{K}$. The calibration was done by the Knudsen cell method (cf. section 9.2.2.1. Due to poor signal to noise ratio for some of the obtained data, strong parameter variation and uncertainties were found when fitting those individually. This was circumvented by restricting W as a global parameter for data in the same vibrational state, irrespective of rotational state. This resulted in an increase of the overall fit reliability while not degrading the quality notably.

Table D.1: Error function parameters obtained for H_2 ($v = 0$)/Cu(111).

J	E_0/ eV	ΔE_0/ eV	W/ eV	ΔW/ eV	A_{Erf}/ arb.u.	ΔA_{Erf}/ arb.u.
0	0.6878	0.0030	0.184 [a]	fixed	1.5931	0.0541
1	0.7066	0.0005	0.184 [a]	fixed	1.4442	0.0089
2	0.7087	0.0014	0.184 [a]	fixed	1.4902	0.0235
3	0.7286	0.0007	0.184 [a]	fixed	1.5856	0.0122
4	0.7193	0.0036	0.184 [a]	fixed	1.2575	0.0512
5	0.7006	0.0021	0.184 [a]	fixed	1.2319	0.0280
6	0.6616	0.0123	0.184 [a]	fixed	1.0192	0.1336
7	0.6105	0.0107	0.184 [a]	fixed	0.6586	0.0742
8	0.5503	0.0967	0.184 [a]	fixed	0.3682	0.3796
9	0.4865	0.0463	0.184 [a]	fixed	0.5415	0.2575
10	0.4349	0.5245	0.184 [a]	fixed	0.3898	2.0090
11	0.3591	0.4224	0.184 [a]	fixed	0.4204	1.5868

[a]Quantity fixed to value obtained in table D.29, due to the better calibration.

Table D.2: Exponential function and background parameters obtained for H_2 ($v = 0$)/Cu(111).

J	A_{Exp}/ arb.u.	ΔA_{Exp}/ arb.u.	γ/ eV	$\Delta\gamma$/ eV	A_{BG}/ arb.u.	ΔA_{BG}/ arb.u.
0	2.999×10^{-3}	1.576×10^{-3}	0.087	0.032	1.261×10^{-4}	6.144×10^{-5}
1	1.534×10^{-3}	1.339×10^{-4}	0.128	0.011	1.122×10^{-4}	6.924×10^{-6}
2	9.692×10^{-4}	1.892×10^{-4}	0.237	0.074	1.028×10^{-4}	1.359×10^{-5}
3	4.792×10^{-4}	3.591×10^{-5}	99.803	4950.817	7.226×10^{-5}	4.126×10^{-6}
4	9.251×10^{-4}	2.305×10^{-4}	0.296	0.167	1.000×10^{-10} [a]	fixed
5	7.639×10^{-4}	1.321×10^{-4}	0.495	0.305	1.000×10^{-10} [a]	fixed
6	7.127×10^{-4}	1.084×10^{-3}	0.672	4.903	1.000×10^{-10} [a]	fixed
7	1.124×10^{-3}	2.291×10^{-3}	0.214	0.808	1.000×10^{-10} [a]	fixed
8	1.000×10^{-10} [a]	fixed	1.000 [a]	fixed	1.000×10^{-10} [a]	fixed
9	1.000×10^{-10} [a]	fixed	1.000 [a]	fixed	1.000×10^{-10} [a]	fixed
10	1.000×10^{-10} [a]	fixed	1.000 [a]	fixed	1.000×10^{-10} [a]	fixed
11	1.000×10^{-10} [a]	fixed	1.000 [a]	fixed	1.000×10^{-10} [a]	fixed

[a]Quantity fixed to a negligible value.

Table D.3: Error function parameters obtained for H_2 ($v = 1$)/Cu(111).

J	E_0/ eV	ΔE_0/ eV	W/ eV	ΔW/ eV	A_{Erf}/ arb.u.	ΔA_{Erf}/ arb.u.
0	0.3300	0.0040	0.1500	0.0020	1.7160	0.0530
1	0.3340	0.0010	0.1500	0.0020	1.7440	0.0110
2	0.3390	0.0020	0.1500	0.0020	1.6950	0.0210
3	0.3480	0.0010	0.1500	0.0020	1.5390	0.0110
4	0.3410	0.0050	0.1500	0.0020	1.6100	0.0380
5	0.3230	0.0040	0.1500	0.0020	1.1350	0.0220
6	0.2950	0.0250	0.1500	0.0020	0.8850	0.1670
7	0.2620	0.0200	0.1500	0.0020	0.8080	0.1400

Table D.4: Exponential function parameters obtained for H_2 ($v = 1$)/Cu(111).

J	A_{Exp}/ arb.u.	ΔA_{Exp}/ arb.u.	γ/ eV	$\Delta\gamma$/ eV
0	1.175×10^{-1}	2.741×10^{-2}	0.052	0.010
1	8.763×10^{-2}	3.143×10^{-3}	0.060	0.003
2	5.632×10^{-2}	6.033×10^{-3}	0.082	0.010
3	2.972×10^{-2}	1.458×10^{-3}	0.296	0.055
4	3.058×10^{-2}	4.365×10^{-3}	1.000×10^4	4.903×10^8
5	3.448×10^{-2}	3.998×10^{-3}	99.971	1.059×10^5
6	5.125×10^{-2}	3.247×10^{-2}	50.286	2.631×10^4
7	5.760×10^{-2}	3.089×10^{-2}	1.816	34.089

Table D.5: Error function parameters obtained for HD($v = 0$)/Cu(111).

J	E_0/ eV	ΔE_0/ eV	W/ eV	ΔW/ eV	A_{Erf}/ arb.u.	ΔA_{Erf}/ arb.u.
0	0.7400	0.0030	0.1980	0.0040	1.3420	0.0330
1	0.7350	0.0020	0.1980	0.0040	0.7700	0.0130
2	0.7330	0.0020	0.1980	0.0040	0.9100	0.0120
3	0.7270	0.0020	0.1980	0.0040	0.9990	0.0130
4	0.7310	0.0020	0.1980	0.0040	1.3750	0.0170
5	0.7270	0.0020	0.1980	0.0040	1.5130	0.0230
6	0.7180	0.0030	0.1980	0.0040	1.2880	0.0350
7	0.6940	0.0050	0.1980	0.0040	1.1770	0.0570
8	0.6600	0.0150	0.1980	0.0040	0.6910	0.0990
9	0.6110	0.0240	0.1980	0.0040	0.6010	0.1510
10	0.5510	0.0730	0.1980	0.0040	0.3340	0.2540

Table D.6: Exponential function and background parameters obtained for HD($v = 0$)/Cu(111).

J	A_{Exp}/ arb.u.	ΔA_{Exp}/ arb.u.	γ/ eV	$\Delta\gamma$/ eV	A_{BG}/ arb.u.	ΔA_{BG}/ arb.u.
0	3.942×10^{-3}	1.259×10^{-3}	0.062	0.011	8.093×10^{-5}	3.582×10^{-5}
1	1.914×10^{-3}	3.443×10^{-4}	0.100	0.014	1.078×10^{-4}	1.476×10^{-5}
2	1.382×10^{-3}	2.087×10^{-4}	0.107	0.014	6.555×10^{-5}	9.436×10^{-6}
3	9.892×10^{-4}	1.263×10^{-4}	0.161	0.025	5.224×10^{-5}	7.451×10^{-6}
4	7.985×10^{-4}	9.334×10^{-5}	0.224	0.041	1.878×10^{-5}	6.463×10^{-6}
5	7.631×10^{-4}	1.076×10^{-4}	0.334	0.103	5.458×10^{-6}	8.589×10^{-6}
6	6.904×10^{-4}	1.794×10^{-4}	0.805	1.027	2.295×10^{-6}	1.714×10^{-5}
7	7.348×10^{-4}	4.091×10^{-4}	1.107	4.163	1.555×10^{-5}	3.991×10^{-5}
8	1.025×10^{-3}	1.693×10^{-3}	2.000	31.930	1.000×10^{-9}	2.873×10^{-4}
9	1.672×10^{-4}	9.329×10^{-2}	$0.050\,^a$	11.482	1.000×10^{-9}	2.168×10^{-3}
10	2.471×10^{-8}	1.393×10^{-1}	$0.050\,^a$	8.081×10^4	7.296×10^{-8}	4.884×10^{-3}

[a] Boundary condition of value.

Table D.7: Error function parameters obtained for $HD(v = 1)/Cu(111)$.

J	E_0/ eV	ΔE_0/ eV	W/ eV	ΔW/ eV	A_{Erf}/ arb.u.	ΔA_{Erf}/ arb.u.
0	0.3980	0.0020	0.1540	0.0040	2.7780	0.0450
1	0.3980	0.0010	0.1540	0.0040	2.6710	0.0210
2	0.3870	0.0010	0.1540	0.0040	2.1280	0.0140
3	0.3790	0.0010	0.1540	0.0040	1.6870	0.0120
4	0.3810	0.0020	0.1540	0.0040	1.5590	0.0170
5	0.3800	0.0010	0.1540	0.0040	1.8260	0.0230
6	0.3550	0.0050	0.1540	0.0040	1.3320	0.0300
7	0.3300	0.0130	0.1540	0.0040	1.0010	0.0420

Table D.8: Exponential function parameters obtained for $HD(v = 1)/Cu(111)$.

J	A_{Exp}/ arb.u.	ΔA_{Exp}/ arb.u.	γ/ eV	$\Delta\gamma$/ eV
0	4.829×10^{-2}	6.813×10^{-3}	0.063	0.008
1	3.852×10^{-2}	1.806×10^{-3}	0.075	0.003
2	3.436×10^{-2}	1.751×10^{-3}	0.082	0.004
3	2.860×10^{-2}	2.270×10^{-3}	0.088	0.007
4	1.803×10^{-2}	1.926×10^{-3}	0.263	0.065
5	1.670×10^{-2}	2.324×10^{-3}	1.779	1.966
6	2.475×10^{-2}	5.462×10^{-3}	1.787	8.714
7	3.385×10^{-2}	1.389×10^{-2}	1.999	16.229

Table D.9: Error function parameters obtained for D_2 $(v = 0)/Cu(111)$.

J	E_0/ eV	ΔE_0/ eV	W/ eV	ΔW/ eV	A_{Erf}/ arb.u.	ΔA_{Erf}/ arb.u.
0	0.7260	0.0040	0.1980	0.0010	0.8660	0.0290
1	0.7360	0.0020	0.1980	0.0010	1.5460	0.0250
2	0.7500	0.0020	0.1980	0.0010	1.6530	0.0160
3	0.7650	0.0020	0.1980	0.0010	1.3560	0.0230
4	0.7790	0.0020	0.1980	0.0010	1.7230	0.0190
5	0.7850	0.0030	0.1980	0.0010	1.4520	0.0390
6	0.7820	0.0030	0.1980	0.0010	1.1720	0.0280
7	0.7710	0.0060	0.1980	0.0010	1.1930	0.0760
8	0.7470	0.0040	0.1980	0.0010	1.2980	0.0530
9	0.7160	0.0230	0.1980	0.0010	0.5500	0.1410
10	0.6760	0.0280	0.1980	0.0010	0.3270	0.0990
11	0.6270	0.0480	0.1980	0.0010	0.5290	0.2750
12	0.5810	0.1070	0.1980	0.0010	0.2210	0.2350
13	0.5480	0.1590	0.1980	0.0010	0.5270	0.8450
14	0.4890	0.1300	0.1980	0.0010	0.5870	0.7090

Table D.10: Exponential function and background parameters obtained for D_2 $(v = 0)/Cu(111)$.

J	A_{Exp}/ arb.u.	ΔA_{Exp}/ arb.u.	γ/ eV	$\Delta\gamma$/ eV	A_{BG}/ arb.u.	ΔA_{BG}/ arb.u.
0	1.861×10^{-3}	6.929×10^{-4}	0.110	0.035	1.332×10^{-4}	2.999×10^{-5}
1	1.730×10^{-3}	2.915×10^{-4}	0.107	0.016	1.012×10^{-4}	1.244×10^{-5}
2	1.237×10^{-3}	7.327×10^{-5}	0.135	0.009	7.584×10^{-5}	3.774×10^{-6}
3	9.535×10^{-4}	1.304×10^{-4}	0.173	0.030	8.494×10^{-5}	7.460×10^{-6}
4	8.164×10^{-4}	5.232×10^{-5}	0.193	0.017	5.354×10^{-5}	3.246×10^{-6}
5	5.609×10^{-4}	1.313×10^{-4}	0.329	0.157	5.521×10^{-5}	1.349×10^{-5}
6	5.473×10^{-4}	1.154×10^{-4}	0.342	0.152	5.667×10^{-5}	1.202×10^{-5}
7	5.291×10^{-4}	3.200×10^{-4}	0.469	0.794	6.116×10^{-5}	3.620×10^{-5}
8	6.573×10^{-4}	3.404×10^{-4}	0.279	0.256	6.119×10^{-5}	3.272×10^{-5}
9	1.000×10^{-7} [a]	fixed	1.000 [a]	fixed	1.000×10^{-11} [a]	fixed
10	1.000×10^{-7} [a]	fixed	1.000 [a]	fixed	1.000×10^{-11} [a]	fixed
11	1.000×10^{-7} [a]	fixed	1.000 [a]	fixed	1.000×10^{-11} [a]	fixed
12	1.000×10^{-7} [a]	fixed	1.000 [a]	fixed	1.000×10^{-11} [a]	fixed
13	1.000×10^{-7} [a]	fixed	1.000 [a]	fixed	1.000×10^{-11} [a]	fixed
14	1.000×10^{-7} [a]	fixed	1.000 [a]	fixed	1.000×10^{-11} [a]	fixed

[a]Quantity fixed to a negligible value.

Table D.11: Error function parameters obtained for D_2 $(v = 1)/Cu(111)$.

J	E_0/ eV	ΔE_0/ eV	W/ eV	ΔW/ eV	A_{Erf}/ arb.u.	ΔA_{Erf}/ arb.u.
0	0.4500	0.0040	0.1620	0.0010	0.9050	0.0280
1	0.4550	0.0020	0.1620	0.0010	1.5420	0.0230
2	0.4640	0.0020	0.1620	0.0010	1.4930	0.0120
3	0.4720	0.0020	0.1620	0.0010	1.2130	0.0190
4	0.4710	0.0020	0.1620	0.0010	1.6340	0.0130
5	0.4680	0.0020	0.1620	0.0010	1.4560	0.0250
6	0.4640	0.0020	0.1620	0.0010	1.1040	0.0170
7	0.4380	0.0040	0.1620	0.0010	1.2430	0.0410
8	0.4210	0.0030	0.1620	0.0010	1.2700	0.0310
9	0.3800	0.0350	0.1620	0.0010	0.3990	0.0750

Table D.12: Exponential function parameters obtained for D_2 $(v = 1)/Cu(111)$.

J	A_{Exp}/ arb.u.	ΔA_{Exp}/ arb.u.	γ/ eV	$\Delta\gamma$/ eV
0	6.498×10^{-2}	1.323×10^{-2}	0.053	0.008
1	4.195×10^{-2}	4.510×10^{-3}	0.062	0.006
2	2.980×10^{-2}	1.422×10^{-3}	0.070	0.003
3	2.022×10^{-2}	2.434×10^{-3}	0.087	0.011
4	1.704×10^{-2}	8.440×10^{-4}	0.105	0.006
5	1.805×10^{-2}	2.412×10^{-3}	0.104	0.015
6	2.272×10^{-2}	2.124×10^{-3}	0.115	0.013
7	1.619×10^{-2}	4.689×10^{-3}	0.167	0.079
8	3.118×10^{-2}	4.618×10^{-3}	0.141	0.030
9	6.209×10^{-3}	3.225×10^{-2}	2.000	27.783

Table D.13: Error function parameters obtained for D_2 $(v = 2)$/Cu(111).

J	E_0/ eV	ΔE_0/ eV	W/ eV	ΔW/ eV	A_{Erf}/ arb.u.	ΔA_{Erf}/ arb.u.
0	0.2180	0.0120	0.1440	0.0100	1.0560	0.0330
1	0.2490	0.0050	0.1440	0.0100	1.8330	0.0560
2	0.2400	0.0020	0.1440	0.0100	1.1980	0.0140
3	0.2590	0.0030	0.1440	0.0100	1.7940	0.0220
4	0.2720	0.0020	0.1440	0.0100	1.6130	0.0130
5	0.2490	0.0080	0.1440	0.0100	0.8840	0.0300
6	0.2670	0.0060	0.1440	0.0100	1.0250	0.0380
7	0.2480	0.0180	0.1440	0.0100	0.9520	0.0260
8	0.2370	0.0150	0.1440	0.0100	0.8030	0.1270

Table D.14: Exponential function parameters obtained for D_2 $(v = 2)$/Cu(111).

J	A_{Exp}/ arb.u.	ΔA_{Exp}/ arb.u.	γ/ eV	$\Delta\gamma$/ eV
0	9.994×10^{-2}	3.289×10^{-2}	0.130	0.127
1	6.405×10^{-2}	1.138×10^{-2}	0.510	0.943
2	9.998×10^{-2}	1.735×10^{-2}	0.124	0.025
3	8.095×10^{-2}	1.367×10^{-2}	0.123	0.039
4	7.786×10^{-2}	5.587×10^{-3}	0.227	0.076
5	9.965×10^{-2}	5.874×10^{-2}	0.095	0.070
6	8.551×10^{-2}	1.129×10^{-2}	0.648	1.375
7	8.791×10^{-2}	4.829×10^{-2}	0.285	0.532
8	7.551×10^{-2}	3.059×10^{-2}	1.993	39.541

D.1.2 Cu(211)

The T_s for all values reported in these tables was (923 ± 2) K. The calibration was done by the Knudsen cell method (cf. section 9.2.2.1. Due to poor signal to noise ratio for some of the obtained data, strong parameter variation and uncertainties were found when fitting those individually. This was circumvented by restricting W as a global parameter for data in the same vibrational state, irrespective of rotational state. This resulted in an increase of the overall fit reliability while not degrading the quality notably.

Table D.15: Error function parameters obtained for H_2 $(v = 0)$/Cu(211).

J	E_0/ eV	ΔE_0/ eV	W/ eV	ΔW/ eV	A_{Erf}/ arb.u.	ΔA_{Erf}/ arb.u.
0	0.7450	0.0020	0.2070	0.0010	2.3900	0.0400
1	0.7510	0.0020	0.2070	0.0010	0.9810	0.0090
2	0.7540	0.0020	0.2070	0.0010	0.9170	0.0160
3	0.7650	0.0020	0.2070	0.0010	0.9090	0.0100
4	0.7570	0.0040	0.2070	0.0010	0.7820	0.0290
5	0.7500	0.0020	0.2070	0.0010	1.0240	0.0190
6	0.7130	0.0090	0.2070	0.0010	0.9490	0.0850
7	0.6770	0.0100	0.2070	0.0010	0.6710	0.0580
8	0.6230	0.0360	0.2070	0.0010	1.0370	0.3340
9	0.5590	0.0390	0.2070	0.0010	0.6410	0.2240
10	0.5060	0.3330	0.2070	0.0010	0.7420	1.8820
11	0.4500	0.4570	0.2070	0.0010	0.9570	1.6330

Table D.16: Exponential function and background parameters obtained for H_2 $(v = 0)$/Cu(211).

J	A_{Exp}/ arb.u.	ΔA_{Exp}/ arb.u.	γ/ eV	$\Delta\gamma$/ eV	A_{BG}/ arb.u.	ΔA_{BG}/ arb.u.
0	2.549×10^{-3}	3.516×10^{-4}	0.089	0.009	2.161×10^{-4}	1.246×10^{-5}
1	1.077×10^{-3}	4.903×10^{-5}	0.225	0.017	3.716×10^{-4}	5.272×10^{-6}
2	1.093×10^{-3}	1.540×10^{-4}	0.161	0.027	1.401×10^{-4}	8.075×10^{-6}
3	5.440×10^{-4}	3.085×10^{-5}	1.184	0.479	1.216×10^{-4}	3.798×10^{-6}
4	5.707×10^{-4}	1.884×10^{-4}	0.471	0.468	5.470×10^{-5}	1.434×10^{-5}
5	4.555×10^{-4}	8.076×10^{-5}	$2.000\,^a$	2.839	5.108×10^{-5}	9.718×10^{-6}
6	5.457×10^{-4}	6.465×10^{-4}	$2.000\,^a$	9.514	3.957×10^{-5}	7.608×10^{-5}
7	5.361×10^{-4}	1.196×10^{-3}	$2.000\,^a$	39.098	6.871×10^{-7}	2.334×10^{-4}
8	1.288×10^{-3}	1.323×10^{-2}	0.329	6.939	1.000×10^{-7}	5.375×10^{-4}
9	4.815×10^{-3}	6.165×10^{-2}	0.126	1.503	2.031×10^{-4}	5.501×10^{-3}
10	5.000×10^{-3}	4.752×10^{-1}	0.152	22.556	6.424×10^{-4}	6.423×10^{-2}
11	4.898×10^{-3}	7.363×10^{-1}	1.997	178.169	8.427×10^{-4}	5.854×10^{-2}

^{a}Boundary condition of value.

Table D.17: Error function parameters obtained for H_2 $(v = 1)$/Cu(211).

J	E_0/ eV	ΔE_0/ eV	W/ eV	ΔW/ eV	A_{Erf}/ arb.u.	ΔA_{Erf}/ arb.u.
0	0.4590	0.0030	0.2030	0.0020	6.2870	0.1340
1	0.4670	0.0020	0.2030	0.0020	6.3240	0.0400
2	0.4750	0.0010	0.2030	0.0020	5.9970	0.0860
3	0.4820	0.0010	0.2030	0.0020	6.0250	0.0350
4	0.4700	0.0050	0.2030	0.0020	3.9390	0.1340
5	0.4690	0.0040	0.2030	0.0020	2.9510	0.0640
6	0.4350	0.0130	0.2030	0.0020	3.9880	0.3360
7	0.4110	0.0210	0.2030	0.0020	3.1320	0.1710

Table D.18: Exponential function parameters obtained for H_2 $(v = 1)$/Cu(211).

J	A_{Exp}/ arb.u.	ΔA_{Exp}/ arb.u.	γ/ eV	$\Delta\gamma$/ eV
0	7.716×10^{-2}	1.157×10^{-2}	0.051	0.005
1	5.506×10^{-2}	1.342×10^{-3}	0.056	0.002
2	3.405×10^{-2}	2.988×10^{-3}	0.066	0.003
3	2.338×10^{-2}	8.579×10^{-4}	0.068	0.004
4	2.276×10^{-2}	6.734×10^{-3}	0.075	0.013
5	9.556×10^{-3}	2.204×10^{-3}	0.132	0.047
6	1.299×10^{-2}	1.462×10^{-2}	0.187	0.404
7	6.014×10^{-3}	9.110×10^{-3}	1.000×10^{3} [a]	1.100×10^{7}

[a]Boundary condition of value.

Table D.19: Error function parameters obtained for HD$(v = 0)$/Cu(211).

J	E_0/ eV	ΔE_0/ eV	W/ eV	ΔW/ eV	A_{Erf}/ arb.u.	ΔA_{Erf}/ arb.u.
0	0.7880	0.0020	0.2130	0.0010	0.7910	0.0140
1	0.7880	0.0010	0.2130	0.0010	0.9780	0.0070
2	0.7780	0.0010	0.2130	0.0010	1.0560	0.0060
3	0.7730	0.0010	0.2130	0.0010	0.7640	0.0050
4	0.7770	0.0010	0.2130	0.0010	1.1030	0.0070
5	0.7760	0.0010	0.2130	0.0010	1.1270	0.0100
6	0.7910	0.0020	0.2130	0.0010	1.1540	0.0190
7	0.7710	0.0030	0.2130	0.0010	1.0240	0.0300
8	0.7320	0.0050	0.2130	0.0010	1.2260	0.0520
9	0.6800	0.0090	0.2130	0.0010	0.9940	0.0830
10	0.6420	0.0250	0.2130	0.0010	0.7830	0.1790

Table D.20: Exponential function and background parameters obtained for HD($v = 0$)/Cu(211).

J	A_{Exp}/ arb.u.	ΔA_{Exp}/ arb.u.	γ/ eV	$\Delta\gamma$/ eV	A_{BG}/ arb.u.	ΔA_{BG}/ arb.u.
0	8.491×10^{-4}	1.367×10^{-4}	0.164	0.031	2.662×10^{-4}	9.370×10^{-6}
1	8.044×10^{-4}	4.215×10^{-5}	0.164	0.010	2.161×10^{-4}	2.996×10^{-6}
2	6.738×10^{-4}	2.861×10^{-5}	0.179	0.010	1.439×10^{-4}	2.086×10^{-6}
3	4.665×10^{-4}	2.949×10^{-5}	0.305	0.039	1.020×10^{-4}	2.572×10^{-6}
4	3.510×10^{-4}	2.236×10^{-5}	0.484	0.095	4.308×10^{-5}	2.202×10^{-6}
5	3.097×10^{-4}	2.926×10^{-5}	1.004	0.571	2.189×10^{-5}	3.252×10^{-6}
6	2.749×10^{-4}	3.480×10^{-5}	99.898	5.109×10^{3}	1.000×10^{-10} [a]	fixed
7	5.589×10^{-4}	1.979×10^{-4}	0.142	0.062	1.000×10^{-10} [a]	fixed
8	4.658×10^{-4}	1.811×10^{-4}	99.961	3.279×10^{4}	1.000×10^{-10} [a]	fixed
9	6.572×10^{-4}	7.645×10^{-4}	0.574	2.774	1.000×10^{-10} [a]	fixed
10	8.385×10^{-4}	3.058×10^{-3}	0.714	14.475	1.000×10^{-10} [a]	fixed

[a]Quantity fixed to a negligible value.

Table D.21: Error function parameters obtained for HD($v = 1$)/Cu(211).

J	E_0/ eV	ΔE_0/ eV	W/ eV	ΔW/ eV	A_{Erf}/ arb.u.	ΔA_{Erf}/ arb.u.
0	0.5130	0.0030	0.2030	0.0030	2.7880	0.0630
1	0.5160	0.0020	0.2030	0.0030	3.6060	0.0440
2	0.5120	0.0020	0.2030	0.0030	3.2930	0.0370
3	0.5070	0.0020	0.2030	0.0030	2.0320	0.0180
4	0.5100	0.0020	0.2030	0.0030	3.2780	0.0410
5	0.5050	0.0040	0.2030	0.0030	3.1320	0.1190
6	0.4550	0.0040	0.2030	0.0030	2.2550	0.0530
7	0.4240	0.0040	0.2030	0.0030	1.7720	0.0590

Table D.22: Exponential function parameters obtained for HD($v = 1$)/Cu(211).

J	A_{Exp}/ arb.u.	ΔA_{Exp}/ arb.u.	γ/ eV	$\Delta\gamma$/ eV
0	2.649×10^{-2}	3.820×10^{-3}	0.079	0.010
1	2.256×10^{-2}	1.185×10^{-3}	0.076	0.004
2	1.715×10^{-2}	9.631×10^{-4}	0.081	0.005
3	1.943×10^{-2}	2.559×10^{-3}	0.068	0.008
4	1.067×10^{-2}	1.692×10^{-3}	0.087	0.014
5	8.146×10^{-3}	1.479×10^{-3}	0.134	0.032
6	1.211×10^{-2}	3.474×10^{-3}	0.144	0.063
7	1.768×10^{-2}	1.023×10^{-2}	0.142	0.142

Table D.23: Error function parameters obtained for D_2 $(v = 0)$/Cu(211).

J	E_0/ eV	ΔE_0/ eV	W/ eV	ΔW/ eV	A_{Erf}/ arb.u.	ΔA_{Erf}/ arb.u.
0	0.7900	0.0020	0.2140	0.0010	1.0720	0.0150
1	0.7890	0.0020	0.2140	0.0010	1.1760	0.0110
2	0.7930	0.0010	0.2140	0.0010	1.3290	0.0070
3	0.8040	0.0010	0.2140	0.0010	1.1470	0.0100
4	0.8140	0.0010	0.2140	0.0010	0.7000	0.0060
5	0.8210	0.0020	0.2140	0.0010	1.2610	0.0150
6	0.8130	0.0020	0.2140	0.0010	0.8650	0.0100
7	0.8050	0.0030	0.2140	0.0010	1.2940	0.0280
8	0.7820	0.0020	0.2140	0.0010	1.3590	0.0200
9	0.7510	0.0040	0.2140	0.0010	1.2950	0.0520
10	0.7060	0.0060	0.2140	0.0010	0.5900	0.0360
11	0.6750	0.0190	0.2140	0.0010	0.6020	0.1170
12	0.6330	0.0200	0.2140	0.0010	0.4760	0.0950
13	0.6030	0.0370	0.2140	0.0010	0.9490	0.3590
14	0.5520	0.0370	0.2140	0.0010	0.8860	0.3170

Table D.24: Exponential function and background parameters obtained for D_2 $(v = 0)$/Cu(211).

J	A_{Exp}/ arb.u.	ΔA_{Exp}/ arb.u.	γ/ eV	$\Delta\gamma$/ eV	A_{BG}/ arb.u.	ΔA_{BG}/ arb.u.
0	1.115×10^{-3}	1.189×10^{-4}	0.149	0.017	2.905×10^{-4}	8.026×10^{-6}
1	1.238×10^{-3}	8.270×10^{-5}	0.133	0.009	1.921×10^{-4}	4.578×10^{-6}
2	8.568×10^{-4}	2.122×10^{-5}	0.176	0.006	1.861×10^{-4}	1.811×10^{-6}
3	7.666×10^{-4}	4.349×10^{-5}	0.175	0.013	1.145×10^{-4}	2.800×10^{-6}
4	5.566×10^{-4}	3.001×10^{-5}	0.279	0.028	1.081×10^{-4}	2.670×10^{-6}
5	4.964×10^{-4}	4.006×10^{-5}	0.284	0.043	6.005×10^{-5}	3.120×10^{-6}
6	4.410×10^{-4}	3.276×10^{-5}	0.617	0.168	7.808×10^{-5}	3.524×10^{-6}
7	3.950×10^{-4}	6.379×10^{-5}	0.781	0.586	5.543×10^{-5}	6.273×10^{-6}
8	1.241×10^{-3}	8.579×10^{-5}	0.125	0.010	1.000×10^{-10} ^{a}	fixed
9	1.383×10^{-3}	3.654×10^{-4}	0.110	0.032	1.000×10^{-10} ^{a}	fixed
10	1.308×10^{-3}	5.484×10^{-4}	0.185	0.126	1.000×10^{-10} ^{a}	fixed
11	1.530×10^{-3}	3.135×10^{-3}	0.123	0.315	1.000×10^{-10} ^{a}	fixed
12	4.192×10^{-3}	6.509×10^{-3}	0.089	0.141	1.000×10^{-10} ^{a}	fixed
13	1.298×10^{-4}	4.034×10^{-1}	0.013	16.218	1.000×10^{-10} ^{a}	fixed
14	7.384×10^{-3}	4.217×10^{-2}	0.055	0.251	1.000×10^{-10} ^{a}	fixed

^{a}Quantity fixed to a negligible value.

Table D.25: Error function parameters obtained for D_2 $(v = 1)$/Cu(211).

J	E_0/ eV	ΔE_0/ eV	W/ eV	ΔW/ eV	A_{Erf}/ arb.u.	ΔA_{Erf}/ arb.u.
0	0.5070	0.0020	0.1930	0.0020	1.1280	0.0170
1	0.5030	0.0020	0.1930	0.0020	1.1100	0.0120
2	0.5170	0.0010	0.1930	0.0020	1.9620	0.0090
3	0.5180	0.0020	0.1930	0.0020	1.0820	0.0100
4	0.5330	0.0010	0.1930	0.0020	1.7720	0.0090
5	0.5250	0.0020	0.1930	0.0020	1.1620	0.0130
6	0.5260	0.0020	0.1930	0.0020	0.7490	0.0090
7	0.5080	0.0030	0.1930	0.0020	0.9920	0.0250
8	0.4920	0.0030	0.1930	0.0020	0.8750	0.0210
9	0.5030	0.0090	0.1930	0.0020	1.5270	0.0830
10	0.4480	0.0070	0.1930	0.0020	1.4810	0.0500

Table D.26: Exponential function parameters obtained for D_2 $(v = 1)$/Cu(211).

J	A_{Exp}/ arb.u.	ΔA_{Exp}/ arb.u.	γ/ eV	$\Delta\gamma$/ eV
0	4.391×10^{-2}	2.337×10^{-3}	0.060	0.003
1	4.198×10^{-2}	1.888×10^{-3}	0.055	0.002
2	3.419×10^{-2}	4.932×10^{-4}	0.056	0.001
3	2.705×10^{-2}	1.231×10^{-3}	0.056	0.002
4	1.898×10^{-2}	3.907×10^{-4}	0.075	0.002
5	1.524×10^{-2}	1.185×10^{-3}	0.072	0.007
6	1.637×10^{-2}	1.262×10^{-3}	0.079	0.007
7	1.734×10^{-2}	2.909×10^{-3}	0.077	0.012
8	1.520×10^{-2}	2.986×10^{-3}	0.078	0.015
9	6.133×10^{-3}	3.035×10^{-3}	6.176×10^{5}	1.071×10^{12}
10	8.561×10^{-3}	3.491×10^{-3}	1.773×10^{6}	1.063×10^{13}

Table D.27: Error function parameters obtained for D_2 $(v = 2)$/Cu(211).

J	E_0/ eV	ΔE_0/ eV	W/ eV	ΔW/ eV	A_{Erf}/ arb.u.	ΔA_{Erf}/ arb.u.
0	0.2910	0.0050	0.1790	0.0090	5.4250	0.1090
1	0.2950	0.0020	0.1790	0.0090	7.1660	0.0920
2	0.3100	0.0010	0.1790	0.0090	7.5980	0.0340
3	0.3260	0.0030	0.1790	0.0090	6.7450	0.0660
4	0.3280	0.0020	0.1790	0.0090	5.8220	0.0390
5	0.3320	0.0050	0.1790	0.0090	5.3100	0.0810
6	0.3310	0.0040	0.1790	0.0090	4.1890	0.1020
7	0.3120	0.0100	0.1790	0.0090	5.2530	0.1560
8	0.3140	0.0080	0.1790	0.0090	4.9310	0.0600

Table D.28: Exponential function parameters obtained for D_2 $(v = 2)$/Cu(211).

J	A_{Exp}/ arb.u.	ΔA_{Exp}/ arb.u.	γ/ eV	$\Delta\gamma$/ eV
0	1.115×10^{-1}	2.112×10^{-2}	0.102	0.027
1	9.170×10^{-2}	1.423×10^{-2}	0.052	0.004
2	4.295×10^{-2}	2.813×10^{-3}	0.146	0.020
3	3.986×10^{-2}	5.785×10^{-3}	0.152	0.044
4	3.995×10^{-2}	3.549×10^{-3}	0.153	0.018
5	1.866×10^{-2}	6.067×10^{-3}	0.659	1.987
6	3.257×10^{-2}	4.004×10^{-3}	9.790×10^{2}	3.648×10^{6}
7	2.654×10^{-2}	1.538×10^{-2}	0.395	1.372
8	3.632×10^{-2}	8.924×10^{-3}	9.989×10^{2}	6.155×10^{5}

D.1.3 Cu(111) and Cu(211) with Internal Calibration

The T_s for all values reported in these tables was (923 ± 3) K, except when indicated otherwise. The calibration was done using the internal calibration method (cf. section 9.2.2.1). However, it is noted that the amplitude parameters are on a relative scale for each sample individually. Due to poor signal to noise ratio for some of the obtained data, strong parameter variation and uncertainties were found when fitting those individually. This was circumvented by restricting W as a global parameter for data in the same vibrational state, irrespective of rotational state. This resulted in an increase of the overall fit reliability while not degrading the quality notably.

Table D.29: Error function parameters obtained for H_2 $(v = 0)$/Cu(111). Here, the sample temperature was (933 ± 1) K. Successive measurements showed no distinguishable differences to TOF data obtained at 923 K.

J	E_0/ eV	ΔE_0/ eV	W/ eV	ΔW/ eV	A_{Erf}/ arb.u.	ΔA_{Erf}/ arb.u.
1	0.6790	0.0010	0.1840	0.0090	0.9580	0.0070
3	0.7030	0.0020	0.1840	0.0090	0.6520	0.0070
5	0.6860	0.0020	0.1840	0.0090	1.2780	0.0150
7	0.5980	0.0040	0.1840	0.0090	1.1120	0.0370

Table D.30: Exponential function and background parameters obtained for H_2 $(v = 0)$/Cu(111). Here, the sample temperature was (933 ± 1) K. Successive measurements showed no distinguishable differences to TOF data obtained at 923 K.

J	A_{Exp}/ arb.u.	ΔA_{Exp}/ arb.u.	γ/ eV	$\Delta\gamma$/ eV	A_{BG}/ arb.u.	ΔA_{BG}/ arb.u.
1	2.464×10^{-3}	1.075×10^{-4}	0.109	0.005	4.579×10^{-4}	4.587×10^{-6}
3	1.088×10^{-3}	9.237×10^{-5}	0.208	0.028	1.035×10^{-4}	4.171×10^{-6}
5	6.500×10^{-4}	9.326×10^{-5}	0.630	0.373	3.809×10^{-5}	5.623×10^{-6}
7	4.762×10^{-9}	4.811×10^{-3}	0.010	3.031×10^{3}	6.501×10^{-5}	1.178×10^{-4}

Table D.31: Error function parameters obtained for H_2 ($v = 1$)/Cu(111).

J	E_0/ eV	ΔE_0/ eV	W/ eV	ΔW/ eV	A_{Erf}/ arb.u.	ΔA_{Erf}/ arb.u.
1	0.3550	0.0020	0.1590	0.0020	1.7410	0.0190
3	0.3730	0.0020	0.1590	0.0020	1.3800	0.0180
5	0.3450	0.0040	0.1590	0.0020	1.4270	0.0360

Table D.32: Exponential function parameters obtained for H_2 ($v = 1$)/Cu(111).

J	A_{Exp}/ arb.u.	ΔA_{Exp}/ arb.u.	γ/ eV	$\Delta\gamma$/ eV
1	3.220×10^{-1}	6.846×10^{-3}	0.035	0.001
3	8.390×10^{-2}	4.913×10^{-3}	0.057	0.004
5	5.085×10^{-2}	7.176×10^{-3}	0.178	0.056

Table D.33: Error function parameters obtained for D_2 ($v = 0$)/Cu(111).

J	E_0/ eV	ΔE_0/ eV	W/ eV	ΔW/ eV	A_{Erf}/ arb.u.	ΔA_{Erf}/ arb.u.
0	0.7200	0.0040	0.1870	0.0020	1.1260	0.0440
2	0.7310	0.0030	0.1870	0.0020	1.1010	0.0210
4	0.7520	0.0030	0.1870	0.0020	0.9030	0.0210
6	0.7510	0.0040	0.1870	0.0020	0.8690	0.0320

Table D.34: Exponential function and background parameters obtained for D_2 ($v = 0$)/Cu(111).

J	A_{Exp}/ arb.u.	ΔA_{Exp}/ arb.u.	γ/ eV	$\Delta\gamma$/ eV	A_{BG}/ arb.u.	ΔA_{BG}/ arb.u.
0	2.548×10^{-2}	8.869×10^{-3}	0.031	0.003	1.814×10^{-8}	4.436×10^{-5}
2	8.203×10^{-3}	7.800×10^{-4}	0.045	0.002	1.400×10^{-4}	1.294×10^{-5}
4	1.358×10^{-3}	1.752×10^{-4}	0.127	0.018	9.604×10^{-5}	6.409×10^{-6}
6	8.745×10^{-4}	1.848×10^{-4}	0.287	0.121	4.313×10^{-5}	9.264×10^{-6}

Table D.35: Error function parameters obtained for D_2 ($v = 1$)/Cu(111).

J	E_0/ eV	ΔE_0/ eV	W/ eV	ΔW/ eV	A_{Erf}/ arb.u.	ΔA_{Erf}/ arb.u.
0	0.4520	0.0040	0.1600	0.0010	1.5980	0.0730
2	0.4600	0.0010	0.1600	0.0040	2.2630	0.0190
4 [a]	0.4730	0.0020	0.1600	0.0040	1.3410	0.0230

[a]Surface temperature was 927 K.

Table D.36: Exponential function parameters obtained for D_2 ($v = 1$)/Cu(111).

J	A_{Exp}/ arb.u.	ΔA_{Exp}/ arb.u.	γ/ eV	$\Delta\gamma$/ eV
0	3.992×10^{-2}	9.393×10^{-3}	0.059	0.013
2	7.193×10^{-2}	2.059×10^{-3}	0.051	0.003
4 [a]	3.958×10^{-2}	2.490×10^{-3}	0.075	0.005

[a]Surface temperature was 927 K.

Table D.37: Error function parameters obtained for D_2 $(v = 2)$/Cu(111).

J	E_0/ eV	ΔE_0/ eV	W/ eV	ΔW/ eV	A_{Erf}/ arb.u.	ΔA_{Erf}/ arb.u.
2	0.2540	0.0050	0.1470	0.0050	4.0310	0.1110
4	0.2760	0.0050	0.1470	0.0050	4.1750	0.1270
6	0.2680	0.0060	0.1470	0.0050	4.0770	0.1730

Table D.38: Exponential function parameters obtained for D_2 $(v = 2)$/Cu(111).

J	A_{Exp}/ arb.u.	ΔA_{Exp}/ arb.u.	γ/ eV	$\Delta\gamma$/ eV
2	2.617×10^{-1}	3.206×10^{-2}	0.048	0.007
4	2.210×10^{-1}	2.374×10^{-2}	0.066	0.009
6	2.500×10^{-1}	4.877×10^{-2}	0.054	0.011

Table D.39: Error function parameters obtained for H_2 $(v = 0)$/Cu(211).

J	E_0/ eV	ΔE_0/ eV	W/ eV	ΔW/ eV	A_{Erf}/ arb.u.	ΔA_{Erf}/ arb.u.
1	0.7420	0.0020	0.2040	0.0010	1.2390	0.0150
3	0.7520	0.0030	0.2040	0.0010	0.6370	0.0110
5	0.7350	0.0030	0.2040	0.0010	1.0330	0.0250
7	0.6530	0.0070	0.2040	0.0010	1.0910	0.0680

Table D.40: Exponential function and background parameters obtained for H_2 $(v = 0)$/Cu(211).

J	A_{Exp}/ arb.u.	ΔA_{Exp}/ arb.u.	γ/ eV	$\Delta\gamma$/ eV	A_{BG}/ arb.u.	ΔA_{BG}/ arb.u.
1	2.089×10^{-3}	6.700×10^{-5}	0.139	0.006	3.841×10^{-4}	5.211×10^{-6}
3	1.345×10^{-3}	1.167×10^{-4}	0.165	0.019	1.005×10^{-4}	4.758×10^{-6}
5	8.496×10^{-4}	1.262×10^{-4}	0.546	0.288	4.687×10^{-5}	7.081×10^{-6}
7	1.300×10^{-3}	1.080×10^{-3}	0.276	0.466	2.532×10^{-5}	4.977×10^{-5}

Table D.41: Error function parameters obtained for H_2 $(v = 1)$/Cu(211).

J	E_0/ eV	ΔE_0/ eV	W/ eV	ΔW/ eV	A_{Erf}/ arb.u.	ΔA_{Erf}/ arb.u.
1	0.4410	0.0030	0.2200	0.0020	2.5000	0.0390
3	0.4600	0.0030	0.2200	0.0020	2.3640	0.0400
5	0.4350	0.0050	0.2200	0.0020	1.7040	0.0640

Table D.42: Exponential function parameters obtained for H_2 $(v = 1)$/Cu(211).

J	A_{Exp}/ arb.u.	ΔA_{Exp}/ arb.u.	γ/ eV	$\Delta\gamma$/ eV
1	2.961×10^{-1}	5.438×10^{-3}	0.037	0.001
3	1.017×10^{-1}	3.173×10^{-3}	0.048	0.002
5	5.840×10^{-2}	9.020×10^{-3}	0.064	0.010

Table D.43: Error function parameters obtained for D_2 ($v = 0$)/Cu(211).

J	E_0/ eV	ΔE_0/ eV	W/ eV	ΔW/ eV	A_{Erf}/ arb.u.	ΔA_{Erf}/ arb.u.
0	0.7700	0.0060	0.2080	0.0020	0.6220	0.0360
2	0.7950	0.0030	0.2080	0.0020	1.3760	0.0240
4	0.8200	0.0030	0.2080	0.0020	0.9770	0.0220
6	0.8110	0.0040	0.2080	0.0020	1.0250	0.0320

Table D.44: Exponential function and background parameters obtained for D_2 ($v = 0$)/Cu(211).

J	A_{Exp}/ arb.u.	ΔA_{Exp}/ arb.u.	γ/ eV	$\Delta\gamma$/ eV	A_{BG}/ arb.u.	ΔA_{BG}/ arb.u.
0	8.978×10^{-3}	3.255×10^{-3}	0.044	0.007	1.328×10^{-4}	5.229×10^{-5}
2	2.649×10^{-3}	1.827×10^{-4}	0.062	0.003	1.214×10^{-4}	4.341×10^{-6}
4	8.011×10^{-4}	8.901×10^{-5}	0.135	0.017	5.426×10^{-5}	3.363×10^{-6}
6	8.166×10^{-4}	1.344×10^{-4}	0.161	0.033	2.096×10^{-5}	5.230×10^{-6}

Table D.45: Error function parameters obtained for D_2 ($v = 1$)/Cu(211).

J	E_0/ eV	ΔE_0/ eV	W/ eV	ΔW/ eV	A_{Erf}/ arb.u.	ΔA_{Erf}/ arb.u.
0	0.5090	0.0030	0.1920	0.0010	1.9480	0.0530
2	0.5170	0.0020	0.1920	0.0010	2.1360	0.0200
4	0.5310	0.0020	0.1920	0.0010	1.8220	0.0210

Table D.46: Exponential function parameters obtained for D_2 ($v = 1$)/Cu(211).

J	A_{Exp}/ arb.u.	ΔA_{Exp}/ arb.u.	γ/ eV	$\Delta\gamma$/ eV
0	3.713×10^{-2}	3.242×10^{-3}	0.068	0.006
2	2.709×10^{-2}	7.261×10^{-4}	0.065	0.002
4	1.689×10^{-2}	7.436×10^{-4}	0.085	0.004

Table D.47: Error function parameters obtained for D_2 ($v = 2$)/Cu(211).

J	E_0/ eV	ΔE_0/ eV	W/ eV	ΔW/ eV	A_{Erf}/ arb.u.	ΔA_{Erf}/ arb.u.
2	0.3090	0.0070	0.1910	0.0060	2.8270	0.0960
4	0.3210	0.0070	0.1910	0.0060	2.4380	0.0930
6	0.3320	0.0110	0.1910	0.0060	2.2430	0.1380

Table D.48: Exponential function parameters obtained for D_2 ($v = 2$)/Cu(211).

J	A_{Exp}/ arb.u.	ΔA_{Exp}/ arb.u.	γ/ eV	$\Delta\gamma$/ eV
2	2.714×10^{-1}	1.788×10^{-2}	0.054	0.005
4	1.899×10^{-1}	1.754×10^{-2}	0.064	0.008
6	1.622×10^{-1}	2.626×10^{-2}	0.095	0.022

D.1.4 Au(111)

The T_s for all values reported in these tables was $(1061 \pm 2)\,$K. The calibration was done by the Knudsen cell method (cf. section 9.2.2.1. Due to poor SNR for some of the obtained data, we found strong parameter variation and uncertainties when fitting those individually. This was circumvented by restricting W as a global parameter for data in the same vibrational state, irrespective of rotational state as well as isotopologue (see table 10.12). This resulted in an increase of the overall fit reliability while not degrading the quality notably. It is noted that the amplitude-parameters are on a relative scale and can only be compared for each isotopologue individually. As described in section 8.3.3.1, the desorbing flux is well described by an adsorption probability function with the ERF-form. Due to clear separation from the TB, only the ERF parameters are reported in the following tables.

Table D.49: Error function parameters obtained for H_2 $(v = 0)$/Au(111).

J	E_0/ eV	ΔE_0/ eV	A_{Erf}/ arb.u.	ΔA_{Erf}/ arb.u.
0	1.307	0.020	1.027	0.140
1	1.312	0.006	1.403	0.034
2	1.323	0.008	1.373	0.058
3	1.287	0.006	0.768	0.021
4	1.262	0.009	0.957	0.051
5	1.208	0.007	0.722	0.022
6	1.167	0.009	1.526	0.075
7	1.103	0.008	0.777	0.034
8	0.996	0.025	0.608	0.099
9	0.986	0.017	0.839	0.091

Table D.50: Error function parameters obtained for H_2 $(v = 1)$/Au(111).

J	E_0/ eV	ΔE_0/ eV	A_{Erf}/ arb.u.	ΔA_{Erf}/ arb.u.
0	0.816	0.011	1.787	0.119
1	0.816	0.003	1.866	0.023
2	0.816	0.004	2.143	0.042
3	0.815	0.003	2.228	0.024
4	0.788	0.006	1.424	0.048
5	0.773	0.004	1.753	0.027
6	0.747	0.011	1.646	0.110
7	0.725	0.006	2.031	0.071

Table D.51: Error function parameters obtained for $HD(v = 0)/Au(111)$.

J	E_0/ eV	ΔE_0/ eV	A_{Erf}/ arb.u.	ΔA_{Erf}/ arb.u.
1	1.332	0.023	0.806	0.130
2	1.363	0.016	1.308	0.136
3	1.305	0.017	0.687	0.079
4	1.272	0.014	0.768	0.073
5	1.256	0.020	0.670	0.092
6	1.202	0.019	0.705	0.094
7	1.218	0.034	0.850	0.209
8	1.201	0.029	1.837	0.366
9	1.139	0.050	1.369	0.467

Table D.52: Error function parameters obtained for $HD(v = 1)/Au(111)$.

J	E_0/ eV	ΔE_0/ eV	A_{Erf}/ arb.u.	ΔA_{Erf}/ arb.u.
2	0.850	0.005	1.626	0.039
3	0.846	0.005	1.461	0.037
4	0.878	0.005	2.034	0.059
5	0.854	0.006	1.996	0.067
6	0.829	0.007	2.093	0.088
7	0.787	0.009	1.942	0.111

Table D.53: Error function parameters obtained for D_2 $(v = 0)/Au(111)$.

J	E_0/ eV	ΔE_0/ eV	A_{Erf}/ arb.u.	ΔA_{Erf}/ arb.u.
0	1.356	0.024	1.690	0.280
1	1.361	0.022	1.412	0.207
2	1.332	0.010	1.060	0.061
3	1.317	0.014	0.954	0.090
4	1.292	0.013	0.475	0.039
5	1.304	0.020	0.736	0.100
6	1.319	0.011	1.196	0.080
7	1.281	0.023	1.015	0.166
8	1.238	0.018	0.728	0.088
9	1.225	0.033	1.197	0.275
10	1.141	0.029	0.581	0.121
12	1.041	0.032	0.956	0.206

Table D.54: Error function parameters obtained for D_2 $(v = 1)$/Au(111).

J	E_0/ eV	ΔE_0/ eV	A_{Erf}/ arb.u.	ΔA_{Erf}/ arb.u.
0	0.983	0.020	0.938	0.131
1	0.969	0.014	0.882	0.084
2	0.982	0.006	1.026	0.034
3	0.966	0.010	0.719	0.051
4	0.969	0.006	0.845	0.029
5	0.950	0.010	0.794	0.056
6	0.923	0.009	0.492	0.030
7	0.908	0.014	0.751	0.074
8	0.900	0.015	0.511	0.055
9	0.899	0.026	0.981	0.172

Table D.55: Error function parameters obtained for D_2 $(v = 2)$/Au(111).

J	E_0/ eV	ΔE_0/ eV	A_{Erf}/ arb.u.	ΔA_{Erf}/ arb.u.
2	0.688	0.010	1.622	0.086
3	0.658	0.013	0.975	0.089
4	0.666	0.010	1.126	0.063
5	0.626	0.015	0.735	0.081
6	0.643	0.010	0.735	0.081
8	0.642	0.012	1.245	0.073

D.2 Tables of Gaussian Peak Parameters

This section contains tables of Gaussian parameters (eq. (D.1),[220]) describing the measured kinetic energy distributions of H_2 and D_2 formed in associative desorption. The subchapters seperate the results for the different samples.

$$f\left(E_{kin}, \mu, \sigma\right) = \frac{A_G}{\sqrt{2\sigma^2\pi}} \cdot \exp\left[\frac{-\left(E_{kin} - \mu\right)^2}{2\sigma^2}\right] \tag{D.1}$$

Here, the parameters are: A_G, the amplitude of the peak, μ, the center and σ, the standard deviation. The experimental data was converted to flux in the kinetic energy scale and re-binned into bins of $40\,\text{meV}$. The fitting procedure excluded the thermal background by restriction to kinetic energies above $0.25\,\text{eV}$ for $v = 0$ and $0.15\,\text{eV}$ for $v = 1$, respectively. For $v = 2$ no restrictions were necessary. The algorithm used was the "lmfit"[271] module in python. All tables give the resulting parameters together with their standard deviations (1σ, denoted by Δ) and the obtained reduced χ-square value (χ_r^2) of the fits. It is pointed out that the amplitude parameters are on a relative scale for each isotopologue and sample, respectively, and no corrections for degeneracies or quantum state population was applied.

D.2.1 Cu(111)

The T_s for all values reported in these tables was (923 ± 2) K. The calibration was done by the Knudsen cell method (cf. section 9.2.2.1).

Table D.56: Gaussian peak parameters describing the measured flux in kinetic energy scale for H_2(v=0)/Cu(111)

J	μ/ eV	$\Delta\mu$/ eV	σ/ eV	$\Delta\sigma$/ eV	A_G/ arb.u.	ΔA_G/ eV	χ^2_r
0	0.584	0.006	0.145	0.006	365.699	11.569	0.07
1	0.602	0.005	0.153	0.005	277.455	7.639	0.0289
2	0.604	0.005	0.154	0.005	282.820	7.780	0.0297
3	0.621	0.005	0.163	0.005	250.338	5.462	1.3733
4	0.613	0.005	0.16	0.005	216.467	4.813	1.0895
5	0.595	0.005	0.159	0.005	259.425	6.428	0.0194
6	0.559	0.005	0.157	0.005	325.839	8.110	0.0307
7	0.511	0.004	0.143	0.004	345.082	7.474	0.0287
8	0.456	0.006	0.159	0.007	384.057	11.880	0.0465
9	0.396	0.005	0.153	0.005	1085.260	29.074	0.1783
10	0.323	0.028	0.154	0.023	1472.430	224.501	2.8969
11	0.15	0.026	0.195	0.031	6125.250	2311.290	0.1086

Table D.57: Gaussian peak parameters describing the measured flux in kinetic energy scale for H_2(v=1)/Cu(111)

J	μ/ eV	$\Delta\mu$/ eV	σ/ eV	$\Delta\sigma$/ eV	A_G/ arb.u.	ΔA_G/ eV	χ^2_r
0	0.313	0.003	0.124	0.003	11567.300	190.333	0.2234
1	0.315	0.003	0.128	0.003	11511.000	168.078	0.1648
2	0.317	0.003	0.132	0.004	10985.700	209.532	0.2429
3	0.315	0.003	0.141	0.003	9951.550	156.368	0.1154
4	0.296	0.003	0.151	0.004	12511.600	210.546	0.1485
5	0.283	0.003	0.148	0.003	10263.300	152.024	0.0705
6	0.25	0.004	0.156	0.004	11206.500	246.713	0.0994
7	0.214	0.007	0.165	0.006	14616.200	492.608	0.179

Table D.58: Gaussian peak parameters describing the measured flux in kinetic energy scale for HD(v=0)/Cu(111)

J	μ/ eV	$\Delta\mu$/ eV	σ/ eV	$\Delta\sigma$/ eV	A_G/ arb.u.	ΔA_G/ eV	χ^2_r
0	0.602	0.005	0.145	0.005	97.955	2.373	0.3685
1	0.598	0.004	0.15	0.004	60.448	1.136	0.0804
2	0.596	0.004	0.152	0.005	73.391	1.694	0.1769
3	0.591	0.004	0.152	0.004	86.314	1.768	0.1923
4	0.593	0.004	0.151	0.004	114.336	2.436	0.3687
5	0.589	0.005	0.148	0.005	130.143	3.092	0.608
6	0.58	0.004	0.15	0.004	123.377	2.567	0.4096
7	0.559	0.003	0.151	0.004	146.993	2.476	0.3748
8	0.533	0.004	0.162	0.004	129.930	2.323	0.2999
9	0.493	0.006	0.148	0.007	177.293	6.015	2.1046
10	0.433	0.007	0.147	0.008	185.348	7.838	2.5772

Table D.59: Gaussian peak parameters describing the measured flux in kinetic energy scale for HD(v=1)/Cu(111)

J	μ/ eV	$\Delta\mu$/ eV	σ/ eV	$\Delta\sigma$/ eV	A_G/ arb.u.	ΔA_G/ eV	χ^2_r
0	0.364	0.003	0.125	0.004	4822.660	101.669	0.0843
1	0.363	0.003	0.128	0.003	4683.810	74.144	0.0434
2	0.354	0.003	0.131	0.003	4221.000	78.815	0.0457
3	0.346	0.003	0.13	0.003	3598.200	66.437	0.0321
4	0.343	0.003	0.136	0.003	3423.260	55.901	0.0206
5	0.334	0.003	0.145	0.003	4379.180	72.095	0.0289
6	0.307	0.003	0.147	0.003	4229.400	65.986	0.019
7	0.277	0.005	0.159	0.005	4334.140	105.457	0.0283

Table D.60: Gaussian peak parameters describing the measured flux in kinetic energy scale for D_2(v=0)/Cu(111)

J	μ/ eV	$\Delta\mu$/ eV	σ/ eV	$\Delta\sigma$/ eV	A_G/ arb.u.	ΔA_G/ eV	χ^2_r
0	0.592	0.004	0.154	0.004	78.923	1.689	0.194
1	0.602	0.004	0.155	0.004	127.099	2.790	0.5256
2	0.613	0.004	0.153	0.004	117.181	2.135	0.3129
3	0.63	0.004	0.152	0.004	81.868	1.494	0.1532
4	0.641	0.003	0.152	0.003	88.325	1.320	0.1214
5	0.647	0.004	0.152	0.004	69.755	1.336	0.1236
6	0.642	0.004	0.153	0.004	58.683	1.027	0.0724
7	0.631	0.003	0.162	0.004	69.008	1.112	0.0797
8	0.612	0.004	0.156	0.004	96.279	1.700	0.1939
9	0.585	0.004	0.162	0.004	58.019	1.145	0.0826
10	0.546	0.004	0.154	0.004	51.284	1.038	0.0697
11	0.503	0.004	0.153	0.004	141.693	2.989	0.5249
12	0.444	0.01	0.19	0.01	109.955	4.705	0.5495
13	0.432	0.005	0.15	0.006	312.028	8.975	0.0338
14	0.376	0.006	0.16	0.006	663.085	20.871	0.0774

Table D.61: Gaussian peak parameters describing the measured flux in kinetic energy scale for $D_2(v=1)/Cu(111)$

J	μ/ eV	$\Delta\mu$/ eV	σ/ eV	$\Delta\sigma$/ eV	A_G/ arb.u.	ΔA_G/ eV	χ_r^2
0	0.4	0.003	0.135	0.003	1075.870	18.212	0.2805
1	0.405	0.003	0.134	0.004	1738.860	33.015	0.9416
2	0.412	0.003	0.134	0.003	1549.400	26.818	0.6238
3	0.42	0.003	0.136	0.003	1174.560	16.272	0.2285
4	0.418	0.003	0.139	0.003	1607.580	23.081	0.4472
5	0.416	0.003	0.142	0.003	1490.130	22.912	0.4255
6	0.407	0.003	0.149	0.003	1219.280	18.290	0.2489
7	0.384	0.003	0.15	0.003	1798.130	24.055	0.4011
8	0.365	0.003	0.157	0.004	2240.680	36.937	0.8092
9	0.333	0.004	0.148	0.004	1014.770	21.915	0.2706

Table D.62: Gaussian peak parameters describing the measured flux in kinetic energy scale for $D_2(v=2)/Cu(111)$

J	μ/ eV	$\Delta\mu$/ eV	σ/ eV	$\Delta\sigma$/ eV	A_G/ arb.u.	ΔA_G/ eV	χ_r^2
0	0.15	0	0.192	0	15407.600	0.000	3.4739
1	0.238	0.004	0.125	0.004	14079.400	343.687	1.2809
2	0.231	0.002	0.132	0.003	9523.200	126.432	0.1586
3	0.245	0.002	0.137	0.002	12591.800	129.057	0.161
4	0.245	0.002	0.143	0.002	11002.400	102.138	0.0951
5	0.233	0.003	0.141	0.003	6855.900	112.829	0.1154
6	0.226	0.004	0.154	0.004	8342.760	147.103	0.1672
7	0.24	0.007	0.121	0.007	7209.780	343.892	1.2911
8	0.225	0.005	0.126	0.005	7250.400	224.659	0.5156

D.2.2   Cu(211)

The T_s for all values reported in these tables was $(923 \pm 2)\,\mathrm{K}$. The calibration was done by the Knudsen cell method (cf. section 9.2.2.1).

Table D.63: Gaussian peak parameters describing the measured flux in kinetic energy scale for $H_2(v=0)/Cu(211)$

J	μ/ eV	$\Delta\mu$/ eV	σ/ eV	$\Delta\sigma$/ eV	A_G/ arb.u.	ΔA_G/ eV	χ_r^2
0	0.592	0.003	0.157	0.003	49560.400	735.983	0.0438
1	0.598	0.003	0.161	0.003	19426.800	260.548	0.5348
2	0.599	0.003	0.161	0.003	17608.900	245.088	0.4727
3	0.608	0.003	0.171	0.003	16116.600	171.345	0.2158
4	0.601	0.003	0.166	0.003	14781.200	188.987	0.2705
5	0.594	0.003	0.17	0.003	21250.700	258.295	0.4883
6	0.56	0.003	0.173	0.003	29627.900	363.210	0.009
7	0.528	0.004	0.171	0.004	30580.400	494.498	0.0156
8	0.48	0.005	0.164	0.005	80912.700	1880.270	0.2011
9	0.421	0.005	0.164	0.005	97181.900	2133.030	0.1633
10	0.36	0.013	0.181	0.011	208679.000	12032.400	1.724
11	0.285	0.031	0.192	0.021	539137.000	74130.200	0.1376

Table D.64: Gaussian peak parameters describing the measured flux in kinetic energy scale for $H_2(v=1)/Cu(211)$

J	μ/ eV	$\Delta\mu$/ eV	σ/ eV	$\Delta\sigma$/ eV	A_G/ arb.u.	ΔA_G/ eV	χ_r^2
0	0.349	0.003	0.156	0.003	2361420	30830.100	0.6256
1	0.355	0.002	0.155	0.002	2189580	22233.400	0.3423
2	0.361	0.002	0.156	0.002	1937740	19759.800	0.276
3	0.367	0.003	0.158	0.003	1830000	23691.900	0.3972
4	0.355	0.003	0.163	0.003	1376030	19708.300	0.2405
5	0.354	0.004	0.161	0.004	1035240	18749.100	0.2223
6	0.323	0.004	0.16	0.005	1952040	41563.400	0.8987
7	0.3	0.005	0.169	0.006	2003790	50910.900	0.9394

Table D.65: Gaussian peak parameters describing the measured flux in kinetic energy scale for HD(v=0)/Cu(211)

J	μ/ eV	$\Delta\mu$/ eV	σ/ eV	$\Delta\sigma$/ eV	A_G/ arb.u.	ΔA_G/ eV	χ_r^2
0	0.62	0.003	0.167	0.003	13408.200	187.223	0.2683
1	0.62	0.003	0.167	0.003	16578.600	224.570	0.3851
2	0.611	0.003	0.165	0.003	19831.400	259.426	0.52
3	0.606	0.003	0.168	0.003	15236.600	224.373	0.378
4	0.61	0.003	0.166	0.003	20968.400	245.570	0.4607
5	0.609	0.003	0.163	0.003	21465.600	290.005	0.6581
6	0.621	0.003	0.174	0.003	19377.100	270.346	0.5311
7	0.606	0.004	0.159	0.004	20276.600	344.006	0.9522
8	0.565	0.003	0.175	0.003	39342.900	512.848	0.0176
9	0.52	0.004	0.167	0.004	53923.600	953.107	0.0592
10	0.484	0.004	0.169	0.005	64167.100	1308.220	0.0933

Table D.66: Gaussian peak parameters describing the measured flux in kinetic energy scale for HD(v=1)/Cu(211)

J	μ/ eV	$\Delta\mu$/ eV	σ/ eV	$\Delta\sigma$/ eV	A_G/ arb.u.	ΔA_G/ eV	χ_r^2
0	0.389	0.002	0.162	0.002	764035	6921.160	0.0352
1	0.393	0.003	0.162	0.003	956524	11416.700	0.0963
2	0.391	0.002	0.16	0.003	896387	9501.140	0.0684
3	0.389	0.003	0.155	0.003	569381	7752.860	0.0476
4	0.391	0.003	0.156	0.003	897145	10591.400	0.0883
5	0.385	0.002	0.159	0.003	913584	9677.220	0.0705
6	0.342	0.003	0.158	0.003	1069540	15161.100	0.1432
7	0.315	0.003	0.158	0.003	1138170	14203.800	0.1012

Table D.67: Gaussian peak parameters describing the measured flux in kinetic energy scale for D_2(v=0)/Cu(211)

J	μ/ eV	$\Delta\mu$/ eV	σ/ eV	$\Delta\sigma$/ eV	A_G/ arb.u.	ΔA_G/ eV	χ_r^2
0	0.62	0.003	0.165	0.003	7478.160	99.220	0.0764
1	0.619	0.004	0.165	0.004	8259.730	132.975	0.1369
2	0.622	0.003	0.167	0.003	9068.720	124.089	0.1177
3	0.633	0.003	0.167	0.003	6890.460	102.331	0.0808
4	0.641	0.003	0.168	0.003	3804.150	53.841	0.0223
5	0.647	0.003	0.17	0.003	6405.940	85.342	0.0552
6	0.639	0.004	0.173	0.004	4818.810	81.064	0.0486
7	0.631	0.003	0.172	0.003	7898.720	89.700	0.0599
8	0.612	0.003	0.176	0.003	10680.600	137.014	0.1334
9	0.584	0.003	0.17	0.003	13924.000	194.703	0.2729
10	0.541	0.003	0.176	0.003	10574.900	135.850	0.1157
11	0.513	0.004	0.175	0.004	14819.300	257.106	0.3822
12	0.475	0.004	0.172	0.004	18167.100	297.187	0.4415
13	0.452	0.005	0.158	0.006	47151.600	1327.210	0.0916
14	0.402	0.006	0.169	0.007	77084.600	2356.370	0.147

Table D.68: Gaussian peak parameters describing the measured flux in kinetic energy scale for $D_2(v=1)/Cu(211)$

J	$\mu/$ eV	$\Delta\mu/$ eV	$\sigma/$ eV	$\Delta\sigma/$ eV	$A_G/$ arb.u.	$\Delta A_G/$ eV	χ_r^2
0	0.401	0.003	0.156	0.003	123730	1809.880	0.2673
1	0.399	0.003	0.153	0.003	124716	1865.280	0.2918
2	0.411	0.003	0.154	0.003	193344	2573.380	0.5628
3	0.414	0.002	0.149	0.003	103161	1163.720	0.1219
4	0.424	0.002	0.157	0.003	149936	1611.060	0.2189
5	0.419	0.002	0.154	0.002	105152	1061.320	0.0973
6	0.418	0.002	0.157	0.002	68251	719.542	0.0432
7	0.402	0.003	0.159	0.003	109490	1413.520	0.157
8	0.39	0.002	0.157	0.002	111659	1069.250	0.089
9	0.385	0.003	0.17	0.003	192501	2527.460	0.4226
10	0.341	0.003	0.16	0.003	312200	3588.800	0.0077

Table D.69: Gaussian peak parameters describing the measured flux in kinetic energy scale for $D_2(v=2)/Cu(211)$

J	$\mu/$ eV	$\Delta\mu/$ eV	$\sigma/$ eV	$\Delta\sigma/$ eV	$A_G/$ arb.u.	$\Delta A_G/$ eV	χ_r^2
0	0.248	0.004	0.134	0.005	3812920	98730.300	0.1133
1	0.263	0.004	0.127	0.004	4454420	93898.000	0.1117
2	0.266	0.004	0.131	0.004	4405340	88001.300	0.0944
3	0.276	0.003	0.134	0.003	3465750	63635.800	0.0487
4	0.277	0.003	0.134	0.003	2959580	53182.700	0.0339
5	0.281	0.004	0.132	0.004	2615930	56253.300	0.0386
6	0.271	0.004	0.136	0.004	2285460	53240.100	0.0331
7	0.269	0.005	0.128	0.005	2979980	90798.300	0.1042
8	0.261	0.005	0.132	0.005	3057880	85481.300	0.088

D.2.3 Au(111)

The T_s for all values reported in these tables was in the range of $(1061 \pm 2)\,\mathrm{K}$. The calibration was done by the Knudsen cell method (cf. section 9.2.2.1).

Table D.70: Gaussian peak parameters describing the measured flux in kinetic energy scale for $H_2(\mathrm{v}{=}0)/\mathrm{Au}(111)$. Reprinted with permission from [220]. Copyright 2017 American Chemical Society.

J	$\mu/$ eV	$\Delta\mu/$ eV	$\sigma/$ eV	$\Delta\sigma/$ eV	$A_G/$ arb.u.	$\Delta A_G/$ eV	χ_r^2
0	0.927	0.017	0.26	0.018	961.495	53.935	1.4265
1	0.938	0.007	0.233	0.007	1195.130	27.102	0.4102
2	0.95	0.011	0.234	0.011	1043.330	40.659	0.9152
3	0.917	0.007	0.217	0.008	806.190	22.531	0.3071
4	0.896	0.011	0.195	0.011	1200.480	55.531	2.0809
5	0.841	0.006	0.238	0.006	1723.920	36.818	0.7391
6	0.809	0.008	0.204	0.008	4976.440	165.368	0.1762
7	0.746	0.007	0.221	0.007	4872.380	129.378	0.097
8	0.659	0.013	0.213	0.013	9751.280	494.742	1.4
9	0.639	0.007	0.224	0.008	16090.800	425.362	0.9321

Table D.71: Gaussian peak parameters describing the measured flux in kinetic energy scale for $H_2(\mathrm{v}{=}1)/\mathrm{Au}(111)$. Reprinted with permission from [220]. Copyright 2017 American Chemical Society.

J	$\mu/$ eV	$\Delta\mu/$ eV	$\sigma/$ eV	$\Delta\sigma/$ eV	$A_G/$ arb.u.	$\Delta A_G/$ eV	χ_r^2
0	0.565	0.01	0.211	0.01	2182.070	86.154	4.887
1	0.564	0.005	0.219	0.005	2317.330	41.133	1.0572
2	0.566	0.006	0.194	0.006	2473.040	62.959	2.8957
3	0.564	0.004	0.204	0.005	2635.610	44.761	1.3784
4	0.543	0.007	0.198	0.007	2055.930	54.679	2.0989
5	0.53	0.006	0.196	0.006	2775.420	65.253	2.9982
6	0.511	0.008	0.194	0.008	3109.630	99.595	0.0697
7	0.491	0.007	0.2	0.008	4604.830	137.185	0.123

Table D.72: Gaussian peak parameters describing the measured flux in kinetic energy scale for HD(v=0)/Au(111)

J	μ/ eV	$\Delta\mu$/ eV	σ/ eV	$\Delta\sigma$/ eV	A_G/ arb.u.	ΔA_G/ eV	χ_r^2
1	0.942	0.025	0.293	0.027	379.022	28.481	33.3052
2	0.99	0.019	0.244	0.019	406.413	26.332	0.3593
3	0.933	0.015	0.249	0.015	398.232	20.450	0.2164
4	0.898	0.014	0.257	0.014	619.206	27.621	0.3805
5	0.895	0.015	0.247	0.015	591.172	30.206	0.4786
6	0.841	0.016	0.197	0.016	920.209	61.049	2.4814
7	0.861	0.024	0.205	0.024	986.854	99.590	6.3643
8	0.816	0.02	0.314	0.022	3323.060	186.864	12.6952
9	0.766	0.027	0.268	0.029	4425.640	390.744	0.6942

Table D.73: Gaussian peak parameters describing the measured flux in kinetic energy scale for HD(v=1)/Au(111)

J	μ/ eV	$\Delta\mu$/ eV	σ/ eV	$\Delta\sigma$/ eV	A_G/ arb.u.	ΔA_G/ eV	χ_r^2
2	0.597	0.007	0.209	0.007	903.544	23.171	0.3637
3	0.593	0.007	0.223	0.007	860.455	21.789	0.2955
4	0.618	0.007	0.19	0.008	854.224	27.284	0.5673
5	0.598	0.007	0.214	0.007	1054.650	27.023	0.4821
6	0.58	0.008	0.22	0.009	1317.300	41.307	1.072
7	0.543	0.009	0.212	0.009	1677.280	59.201	2.243

Table D.74: Gaussian peak parameters describing the measured flux in kinetic energy scale for D_2(v=0)/Au(111). Reprinted with permission from [220]. Copyright 2017 American Chemical Society.

J	μ/ eV	$\Delta\mu$/ eV	σ/ eV	$\Delta\sigma$/ eV	A_G/ arb.u.	ΔA_G/ eV	χ_r^2
0	0.986	0.014	0.22	0.014	533.501	28.397	0.4748
1	0.969	0.018	0.248	0.019	530.649	33.363	0.5725
2	0.947	0.015	0.269	0.016	497.796	23.916	0.2666
3	0.926	0.018	0.273	0.018	551.752	30.474	0.4261
4	0.917	0.009	0.223	0.009	297.096	9.429	5.2093
5	0.914	0.019	0.261	0.02	465.605	29.139	0.4155
6	0.934	0.01	0.246	0.01	643.112	21.949	0.2529
7	0.919	0.013	0.184	0.013	625.680	37.813	1.0226
8	0.87	0.01	0.227	0.01	762.842	28.568	0.4695
9	0.86	0.016	0.269	0.017	1541.680	79.566	2.984
10	0.786	0.011	0.201	0.011	1438.670	62.862	2.5692
12	0.697	0.009	0.197	0.009	6012.870	219.542	0.3149

Table D.75: Gaussian peak parameters describing the measured flux in kinetic energy scale for $D_2(v=1)/Au(111)$. Reprinted with permission from [220]. Copyright 2017 American Chemical Society.

J	μ/ eV	$\Delta\mu$/ eV	σ/ eV	$\Delta\sigma$/ eV	A_G/ arb.u.	ΔA_G/ eV	χ_r^2
0	0.695	0.01	0.205	0.01	162.107	6.689	3.1671
1	0.682	0.008	0.201	0.008	173.366	5.633	2.2898
2	0.692	0.005	0.217	0.005	185.247	3.579	0.8531
3	0.68	0.009	0.207	0.009	145.465	4.925	1.7009
4	0.679	0.006	0.221	0.006	176.054	3.878	0.9789
5	0.667	0.008	0.186	0.008	180.018	6.059	2.8701
6	0.645	0.005	0.193	0.005	142.348	2.785	0.5827
7	0.629	0.009	0.204	0.009	260.528	9.505	6.3859
8	0.623	0.009	0.193	0.009	183.273	7.015	3.683
9	0.617	0.016	0.233	0.017	411.873	24.688	0.3649

Table D.76: Gaussian peak parameters describing the measured flux in kinetic energy scale for $D_2(v=2)/Au(111)$

J	μ/ eV	$\Delta\mu$/ eV	σ/ eV	$\Delta\sigma$/ eV	A_G/ arb.u.	ΔA_G/ eV	χ_r^2
2	0.493	0.007	0.192	0.007	3722.290	105.222	0.0948
3	0.493	0.007	0.191	0.007	3531.260	108.164	0.1003
4	0.495	0.007	0.191	0.007	3154.670	86.642	0.0646
6	0.485	0.011	0.218	0.011	3340.340	137.473	0.1402
8	0.484	0.012	0.214	0.012	4590.790	208.760	0.331

Appendix E

List of Materials

Table E.1: Materials used in this work

Name	Supplier	Comment	Application
DCM	Radiant Dyes	–	Laser dye
Rhodamine B	Lambda Physik	–	Laser dye
Rhodamine 101	Lambda Physik	–	Laser dye
H_2	Westfalen Gas	purity 99.999%	Gas for permeation experiments
D_2	Sigma Aldrich	99.96 atom% D	Gas for permeation experiments
HD	–	1:2 mixture of H_2 and D_2	Gas for permeation experiments
Ar	Westfalen Gas	purity 99.999%	Gas for spuuttering
HI	homebuilt	–	Gas for molecular beam
Tungsten mesh	Advent Research Materials	wire ∅ 25 µm 50 Mesh per inch; 90.3% open area	Mesh for design of ion optics
Boron nitride	Henze BNP AG, Deutschland	HeBoSint®	Heater body material
Tantalum wire	Goodfellow Cambridge	0.25 mm ∅; 99.9% purity	Heater filaments
Graphite spray	CRC Industries Deutschland	isopropyl graphite suspension	Spray coating of meshes
Aquadaq E	Henkel Corporation, Michigan	aqueous graphite suspension	Suspension coating of meshes
MgF_2 windows	Korth Kristalle GmbH	1.5 mm thickness; 15 mm ∅	Exchangable laser windows
UV-fused silica lens	Thorlabs Inc.	> 90% transmission, uncoated	Focusing optic for REMPI laser beam

Appendix F

List of Abbreviations

Abbreviations

AES	Auger electron spectroscopy
AIMD	*ab initio* molecular dynamics
BBO	beta-barium borate; β-BaB$_2$O$_4$
BCP	bunch-compression photolysis
BOA	Born-Oppenheimer approximation
BOSS	Born-Oppenheimer static surface
DFT	density functional theory
∅	diameter
ehp	electron-hole-pair
ER	Eley-Rideal
ERF	error function
FCA	Faraday cage assembly
fcc	face-centered cubic
FPC	five parameter curve
FTL	Fourier-transform limited
FWHM	full width at half maximum
GGA	generalized gradient approximation
HA-ER	hot atom Eley-Rideal
HAP	H-atom pulse
hcp	hexagonal close packed
HV	high voltage
LEED	low energy electron diffraction
LGS	generalized logistic function
LH	Langmuir-Hinshelwood
MAE	mean absolute error
MBD	Maxwell-Boltzmann distribution

MCP	micro channel plate
MEIS	medium energy ion scattering
MPI	multi photon ionization
Nd:YAG	neodymium-doped yttrium aluminium garnet
Nd:YLF	neodymium-doped yttrium lithium fluoride
PBE	Perdew-Burke-Ernzerhof
PEC	potential energy curve
PES	potential energy surface
PW91	Perdew and Wang 91
QCT	quasi-classical trajectory
REMPI	resonantly enhanced multi-photon ionization
RGA	regenerative amplifier
RPBE	revised Perdew-Burke-Ernzerhof
RPC	reaction probability curve
SM	shielding mesh
SNR	signal to noise ratio
SRP	specific reaction parameter
SSE	sum of square errors
TB	thermal background
TOF	time-of-flight
TPD	temperature programmed desorption
UHV	ultra high vacuum
UV	ultraviolet
1D	one-dimensional
2D	two-dimensional
3D	three-dimensional
ML	monolayer

Appendix G

List of Nomenclature

The values of the fundamental physical constants in the following list have been taken from [323].

Nomenclature

c	speed of light in vacuum
E_{kin}	kinetic energy
h	Planck constant
k_b	Boltzmann constant
T_{melt}	melting temperature
Φ	permeability
E_{Φ}	Arrhenius activation energy for permeation
R	ideal gas constant
k_g	grating constant
m_g	grating diffraction order
ν_0	center frequency
$\Delta\nu$	laser bandwidth
w_0	beam radius at waist position
X_0	nominal flight distance
D_0	dissociation energy
m_{H}	mass of hydrogen atom
m_{I}	mass of iodine atom
E_{act}	Arrhenius activation energy
A_{pre}	Arrhenius prefactor
$\langle S_0(T_s)\rangle$	mean absorption probability per collision
E_{min}	minimal kinetic energy for cutoff
E_{slope}	slope parameter for cutoff
θ	polar angle relative to the surface normal

ϕ	azimuthal angle around the surface normal
T_{Kn}	temperature of the Knudsen cell
T_s	surface temperature
t_{shift}	constant TOF of ions in the detection setup
x_0	drift length in the FCA
w_0	beam radius at waist / focus position
$w(z)$	beam radius at given z
x_c	beam center in horizontal transversal direction
x_{edge}	knife edge position in horizontal direction
y_c	beam center in vertical transversal direction
y_{edge}	knife edge position in vertical direction
z	longitudinal distance from beam waist / focus
z_0	longitudinal position of the beam waist / focus
z_R	Rayleigh length
a_{eq}	first anharmonic term in equilibrium position
B_{eq}	rotational constant in equilibrium position
D_{eq}	centrifugal distortion constant in equilibrium position
g_{ns}	nuclear spin statistical weight
T_{eq}	electronic energy in equilibrium position
w_{eq}	vibrational constant in equilibrium position - first term
$w_{eq}x_{eq}$	vibrational constant in equilibrium position - second term
$w_{eq}y_{eq}$	vibrational constant in equilibrium position - third term
A_{erf}	amplitude parameter for the error function
A_{flux}	rotational state averaged saturation parameter
A_{slow}	amplitude parameter for the exponential function
ε_{int}	internal efficacy based on E_0
ξ_{int}	internal efficacy based on ΔS
ε_{rot}	rotational efficacy based on E_0
ξ_{rot}	rotational efficacy based on ΔS
ε_{vib}	vibrational efficacy based on E_0
ξ_{vib}	vibrational efficacy based on ΔS
E_{shift}	shift in kinetic energy
E_0	point of inflection of the sticking curve
γ_{slow}	energy width parameter for the slow channel
S_{fast}	sticking function for the fast channel
S_{slow}	sticking function for the slow channel
S_0	reaction probability in the zero-coverage limit
ΔS	offset of reaction threshold
W	width parameter of the sticking curve

Appendix H

Curriculum Vitae

Personal Details

Name	Sven Kaufmann
Address	Stumpfe Eiche 15a
	37077 Goettingen
Birthday	05.08.1986
Birthplace	Neustadt a. Rbge.
Nationality	german

Education

- **Since 01.03.2012**
  Doctoral studies in the Georg-August University School of Science PhD program,
  Georg-August University of Goettingen.

- **15.11.2011**
  Graduation as Master of Science in Chemistry,
  Georg-August University of Goettingen.

- **03.08.2009**
  Graduation as Bachelor of Science in Chemistry,
  Georg-August University of Goettingen.

- **1999 − 26.06.2006**
  Grammar school, **Abitur (A-level exams)**,
  Wilhelm-Busch Gymnasium Stadthagen.

- **1997 − 1999**
  Middle school,
  Magister-Nothold-Schule Lindhorst.

- **1993 – 1997**
  Elementary school,
  Grundschule Sachsenhagen.

Further Education

- **20.11.2014**
  Graduation from correspondence course "Laser technology" at the Friedrich-Schiller University Jena, instructed by Doz. Dr. G. Staupendahl.

- **20.11.2014**
  Acquisition of the certification as laser safety representative at the Friedrich-Schiller University Jena, instructed by Doz. Dr. G. Staupendahl.

Publications

Peer-reviewed journals

- Evidence for Electron–Hole Pair Excitation in the Associative Desorption of H_2 and D_2 from Au(111), *The Journal of Physical Chemistry Letters*, **8**, 1657-1663, (2017).

- Generation of ultra-short hydrogen atom pulses by bunch-compression photolysis, *Nature Communications*, **5**, 5373, (2014).

Contributions at Conferences

- **10.–15.07.2016   Easton**, USA
  Gordon Research Seminar and Conference: Molecular Interactions and Dynamics
  Poster presentation: "Associative Desorption of Hydrogen from Metal Surfaces"

- **18.–21.05.2016   Schloss Ringberg, Tegernsee**, Germany
  Symposium on Dynamics at Surfaces
  Oral presentation: "Associative Desorption of Hydrogen from Cu(111) and Cu(211)"

- **05.–07.05.2016   Rostock**, Germany
  Bunsentagung - General Assembly of the German Bunsen Society for Physical Chemistry
  Poster presentation: "Associative Desorption of Hydrogen from Metal Surfaces"

- **17.–19.06.2015   Cahors**, France
  DRAGS-TER - <u>D</u>ynamics and <u>R</u>eactions of Hydrogen <u>A</u>toms with <u>G</u>old and <u>S</u>ilver surfaces - a <u>T</u>heoretical and <u>E</u>xperimental fundamental <u>R</u>esearch cooperation

Oral presentation: "Associative Desorption of Hydrogen Isotopes from Copper Surfaces"

- **20.–23.05.2015   Schloss Ringberg, Tegernsee**, Germany
  Symposium on Dynamics at Surfaces
  Oral presentation: "Associative Desorption of Hydrogen Isotopes from Copper Surfaces"

- **18.–21.05.2014   Schloss Ringberg, Tegernsee**, Germany
  Symposium on Dynamics at Surfaces
  Oral presentation: "Generation of ultra-short H atom pulses"

- **10.–15.03.2013   Schloss Ringberg, Tegernsee**, Germany
  Winter School on Chemical Reaction Dynamics at Surfaces
  Poster presentation: "Generation of sub-nanosecond H-atom pulses"

- **18.–22.03.2012   Prague**, Czech Republic
  PIMoP - Prague Workshop on Photoinduced Molecular Processes
  Oral presentation: "Multi Photon Ionization Spectroscopy of Molecular and Atomic Hydrogen and Deuterium"